Elastographic Reconstruction Methods for Orthotropic Materials

A thesis submitted in partial fulfilment of the requirements for the

Degree of Master of Engineering

in Mechanical Engineering

Author: Zohreh Barani Lonbani

Department of Mechanical Engineering

University of Canterbury

2010

Dedications:

To my family

For their endless love and
their warm affection

and

To all who are desperately
fighting with cancer.

Preface

"……...Whenever we do something that fills us with enthusiasm, we are following our legend. …. I ask myself: are defeats necessary? Well, necessary or not, they happen. When we first begin fighting for our dream, we have no experience and make many mistakes. The secret of life, though, is to fall seven times and to get up eight times. So, why is it so important to live our personal calling if we are only going to suffer more than other people? Because, once we have overcome the defeats – and we always do – we are filled by a greater sense of euphoria and confidence. In the silence of our hearts, we know that we are proving ourselves worthy of the miracle of life. Each day, each hour, is part of the good fight. We start to live with enthusiasm and pleasure. …….".

Paulo Coelho, "The Alchemist"

Table of Contents

Acknowledgments

My deepest gratitude goes to my dearest family, especially my mother and late father, for their unlimited love and strong support during my entire life. They understood the meaning of true love, and encouraged me to fly away far from home to reach my dreams. Thank you all.

Completion of this work was reliant upon the help of a number of individuals. Because of that I would like to thank:

Canterbury supervisory team and MRE research group including: Professor David Wall for his strong support in all circumstances, Matthew McGarry, James Fellowelen and David Weaver for their help and answering my questions.

The USA Supervisory Team during the Internship Program including: Professor Keith Paulsen and MRE Group (Dartmouth College, NH, USA), Professor John Weaver (Dartmouth-Hitchcock Medical Center NH, USA), Professor Paul Barbone (Boston University, MA, USA), Professor Assad Oberai (RPI, NY, USA).

I also would like to express my appreciation to: University of Canterbury, Scholarship Office, Mechanical Engineering Department, Dartmouth College of Engineering (NH, USA), for all their kind help and support along the way.

I also wish to thank my friends inside and outside the University of Canterbury: Mostafa Nayyerloo, Ali Ghanbari, and Chandra Baadkar and others for their help, and for always being good friends.

And last but not least, my local Wilkie family; Jeff, Heather, Bruce, Sonia and her two little sons Marshall and Carter. I am truly happy that I had a chance to meet this kind family. I am incredibly grateful to you for staying with me in all circumstances, for your help, strong support, and your warm affection during this time.

List of Figures

List of Table

List of Symbols

Subscript *i, j, k, l,* are general counting variables.

Roman Symbols:

A:	Forward FEM matrix or a symmetric, positive definite matrix in the linear CG algorithm.
A:	Bilinear operator.
C_{ijkl}:	The elasticity tensor.
$D_x F$:	Another notation for the first derivation $\frac{\partial F}{\partial x}$.
2-D:	Two dimensions.
3-D:	Three dimensions.
E:	Young's modulus.
F:	An arbitrary function.
Hz:	The frequency unit.
J:	Jacobian matrix.
K:	Bulk Modulus ($K = \frac{E}{3(1-2\upsilon)}$) or condition number (Eq. 2.16).
KPa:	The shear modulus unit (Kilo Pascal).
L:	Characteristic length.
Lx:	The length of the zone in the x direction.
Ly:	The length of the zone in the y direction.
L_1:	An expression for TV, which is the norm of the first spatial derivation of the solution.
M:	Number of iterations.
N:	Number of nodes.
R:	Regularization term.
R_e:	Real component of the complex displacements.
R_{fwd}:	RHS vector containing boundary conditions in the forward problem.
R_{inv}:	RHS vector containing boundary conditions in the inverse problem.
S_{ijkl}:	Compliance tensor.
T:	Transpose.
$T2^*$:	MR magnitude image.
U:	Strain energy function.
V:	Total Volume.
V_0:	Original volume.
ΔV:	Change in volume for a particular state of strain.
X:	Global coordinate direction or excitation direction.

Y: Global coordinate direction or excitation direction.
Z: Global coordinate direction or direct inversion matrix or excitation direction.
a: Matrix row (Eq. 2.15).
b: RHS for the linear system $Ax=b$ where x is an exact solution.
b_c: RHS for a linear system $Ax_c = b_c$ where x_c is a calculated solution.
c: Velocity of shear waves.
e: Volumetric strain.
e_k: Current error vector in the linear CG.
f: Frequency (Hz).
i: The current node number.
j: General counting variables or $\sqrt{-1}$.
k: The current sequence of iteration.
ℓ_{ij}: Transformation tensor.
p_k: The current search direction in an iterative optimization procedure.
p_i: Conjugate vector.
p_j: Conjugate vector.
r: The error due to substituting the approximate solution into the weak form of the general forward problem.
r_k: Current residual in the linear CG.
t: Time.
u: Displacement field.
u^c: Displacements calculated using the current η estimate.
u^m: Measured displacements.
u_{ap}: An approximation of the displacement.
u_c: Complex displacement amplitude.
u_i: Imaginary component of the complex displacement.
u_r: Real component of the complex displacement.
$\breve{u}$: Real-valued amplitude of displacement from MR-detected motions.
u^X Displacement component in the X direction.
u^Y Displacement component in the Y direction.
u^Z Displacement component in the Z direction.
w_j: A weighted function.
x: An exact solution to a linear system as $Ax=b$:
x_c: Calculated solution for a linear system $Ax_c = b_c$.
x_k: The value of the function in the current iteration or actual solution.
x_{k+1}: The value of the function in the new iteration.
x_0: The starting point in minimization algorithm known as initial guess.

Greek Symbols:

α_k : The step length in an iterative process selected by line search.
α_{tv} : The TV regularization parameter.
α_{TK} : Tikhonov regularization weight.
β_k : Conjugate gradient scalar.
β^{FR} : The β obtained from the Fletcher-Reeves formula (2.42).
β^{PR} : The β obtained from the Polak-Ribiere formula (2.43).
λ_s : Shear wavelengths per side.
λ : First Lam´e parameter.
θ : Argument in the Euler's formula or the function gives the angle the positive real axis and the vector position of the complex plane.
μ : Shear modulus, or second Lam´e parameter.
μ_{mag} : The orthotropic magnitude shear modulus vector at each node.
μ_{XY} : The orthotropic real shear moduli component in the X-Y plane.
μ_{ZX} : The orthotropic real shear moduli component in the Z-X plane.
μ_{ZY} : The orthotropic real shear moduli component in the Z-Y plane.
σ_{ij} : Second order isotropic stress tensor.
σ_i : Axial stresses.
ε_{kl} : Second order isotropic strain tensor.
ε_i : Axial strains.
τ_i : Shear stresses.
γ_i : Shear strains.
τ : Time domain.
υ : Poisson's ratio.
ρ : Density.
φ : Phase of MR-detected motions.
ω : Angular frequency of time-harmonic motion ($rad\ s^{-1}$).
η : A general reconstructed variable.
ϕ : Nodal basis function (shape function).
Ψ : Displacement error function.
Ψ' : First derivative of the displacement error function.
Ψ'' : Second derivative of the displacement error function.
Φ : Objective function.
Φ_{tv} : Objective function applied in the TV regularization technique.
Φ_{TK} : Objective function applied in the TK regularization technique.
Ω : Whole problem domain.
δ : The step size used for the FD approximation in the secant method.

Acronyms:

CG:	Conjugate gradient.
COR. CO:	Correlation Coefficient.
DOF:	Degree of freedom.
FD:	Finite difference.
FE:	Finite element.
FEM:	Finite element method.
GB:	Giga bytes.
HPC:	High performance super computer.
Hz:	Frequency unit (Hertz).
I.G.:	Initial guess.
MR:	Magnetic resonance.
MRE:	Magnetic resonance elastography.
MRI:	Magnetic resonance imaging.
PDE:	Partial differential equation.
RHS:	Right hand side.
STD:	Standard deviation.
TK :	Tikhonov regularization methods.
TV:	Total variation regularization methods.
$Rl.\ Err.$:	Relative Error.

Mathematical Symbols:

Δ :	Changes i.e. ΔV is the change in total volume.
∇ :	Gradient.
$\nabla \cdot$:	Divergence.
∂ :	Directional derivative.
δ :	Variation or an arbitrary small non-zero number.
ε :	Small non-zero number.
$\lvert\ \rvert$:	Absolute value.
$\lVert\ \rVert$:	Norm.
$\oint$:	Integration on the surface.
$\int_{\Omega}$:	Integration on the whole domain Ω.
$A(.,.)$:	A bilinear operator which shows the inner product between two tensors.

Abstract

To date, elastographic imaging techniques such as magnetic resonance elastography (MRE) have primarily been considered isotropic material properties, despite the fact that most biological tissues tend to have some anisotropic qualities.

In this thesis, a finite-element based orthotropic, incompressible material model is used as the basis for the *in vitro* MRE gelatin phantom. This study includes the use of biologically based orthotropic gelatin phantoms, with MRI data acquisition and boundary conditions suitable to describe the orthotropic material behavior.

Fabricating a biological gelatin phantom using pineapple for MRE *in vitro* testing is a novel technique which was developed specially for this study. Multiple motion measurements from the pineapple gelatin phantom were made by applying directionally independent boundary conditions within the 85-125 Hz frequency range. Such multiple, orthogonal excitation data is needed to provide a complete description of the mechanical properties of this anisotropic phantom, given the potential for non-uniqueness of the reconstructed property estimates.

Orthotropic image reconstructions were then carried out to map orthotropic elasticity properties in 3-D based on MR detected motion datasets captured from the pineapple gelatin phantom. The subzone based orthotropic incompressible reconstruction algorithm was based on the Conjugate Gradient optimization method, to gain computational efficiency, and used total volitional (TV) regularization techniques to constraint the solution process.

The adjoint-residual method was utilized to improve the efficiency of the gradient descent based algorithm. The elasticity image reconstruction results presented for the orthotropic incompressible phantom are also correlated with isotropic property reconstructions for the same phantom.

"Believe, when you are most unhappy, that there is something for you to do in the world. So long as you can sweeten another's pain, life is not in vain". *Helen Keller*

Chapter1

1.1 Breast Cancer

Breast cancer is a disease in which abnormal cells (cancerous) grow in an uncontrolled way inside the normal breast tissue. A malignant tumour is a group of cancer cells that attack surrounding tissues [1]. Breast cancer is the second leading cause of cancer deaths in women today and is the most common cancer among women, excluding non-melanoma skin cancers. According to the World Health Organization (WHO), more than 1.2 million people diagnosed with breast cancer in 2007 worldwide [3].

The American Cancer Society estimates that about 213,000 women in the United States will be diagnosed with invasive breast cancer each year. The chance of developing invasive breast cancer during a woman's lifetime is approximately 1 in 8 (about 13%). Though much less common, breast cancer also occurs in men. An estimated 1,720 cases were diagnosed in men in 2005.

According to the American Cancer Society, the chance that breast cancer will be responsible for a woman's death is about 1 in 33 (3%). The incidence rate of breast cancer (number of new breast cancers per 100,000 women) increased by approximately 4% during the 1980s but levelled off to 100.6 cases per 100,000 women in the 1990s. The death rates from breast cancer also declined significantly between 1992 and 1996, with the largest decreases among younger women [4, 5].

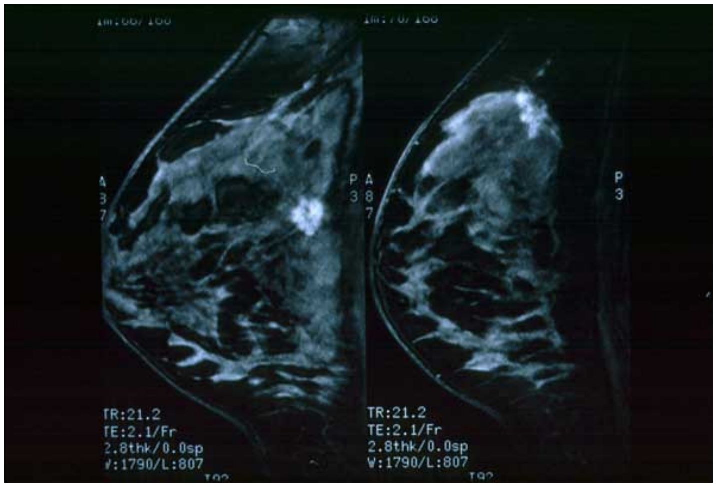

Figure 1- 1 MRI scan of the breast clearly shows two areas of abnormality, which proved to be cancer [2].

Medical experts attribute the decline in breast cancer deaths to earlier detection and more effective treatments [6, 7]. Table 1.1 shows estimated breast cancer rates in various regions of the world, with a focus on New Zealand and Australia for purpose of comparison [8]. Per 100,000 females, New Zealand has the fifth highest breast cancer incidence in the world. In this country, cancer registration figures show that 2,345 women were diagnosed with breast cancer in 2002. Each year, more than 2000 New Zealand women are diagnosed with breast cancer. A statistics report given by New Zealand Health Information Service about breast cancer illustrates that the death rate due to breast cancer is notably high among women [9, 10].

1.2 Diagnosis of Breast Cancer

Here the current diagnostic methods for breast cancer screening are classified. This classification includes two main categories; clinical breast exams and imaging studies that are explained in the next section.

1.2.1 Clinical Breast Exam

Manual palpation performed by self-examination or a physician is a traditional method for detecting abnormal lesions within the breast. The ability to detect anomalies using this method is a result of the increased stiffness of the lesion [11]. However, breast cancer symptoms can also include swelling and skin changes. Many breast cancers have no obvious symptoms [12], so manual palpation will not be able to detect the cancer accurately and thus is not reliable.

Region	New Cases (2000)	Deaths (2000)
Eastern Africa	13,615	6,119
Middle Africa	3,902	1,775
Northern Africa	18,724	8,388
Southern Africa	5,537	2,504
Western Africa	17,389	7,830
Caribbean	6,210	2,310
Central America	18,663	5,888
South America	69,924	22,735
Northern America	202,044	51,184
Eastern Asia	142,656	38,826
South-Eastern Asia	55,907	24,961
South Central Asia	129,620	62,212
Western Asia	20,155	8,459
Eastern Europe	110,975	43,058
Northern Europe	54,551	20,992
Southern Europe	65,284	25,205
Western Europe	115,308	40,443
Australia/New Zealand	12,748	3,427
Melanesia	470	209
Micronesia	62	28

Table 1-1 Estimated Breast Cancer Cases/Deaths Worldwide

1.2.2 Imaging Studies

For breast cancer diagnosis, several novel methods in the field of soft tissue imaging are currently under development, as outlined below.

1.2.2.1 Mammography

Mammography is a specific type of imaging that uses a low-dose X-ray system to examine breasts. A mammography exam, known a mammogram, is used to help in the early detection and diagnosis of breast diseases in women. There are a number of disadvantages to this method. Initial mammography images are not usually enough to determine the existence of a normal or cancer disease with certainty. Sometimes interpretations of mammograms are difficult because a normal breast can appear differently for each woman [13, 14]. While mammography is commonly used as a screening tool for breast cancer, this method is not able to detect all breast cancers. Experience show that a cancer could be indicated when there is no cancer, which is called a false-positive result. These results occur mostly in women younger than forty as the tissue of the breast is not enough dense. This method is also painful for women [15, 16].

1.2.2.2 Breast Ultrasound

In ultrasound imaging, organs are exposed by high-frequency sound waves to produce images. In this technique, sound waves will be sent through a part of body and then the reflection will be received off of soft tissues and an image is constructed based upon the interpretation of the waves' reflections. Usually a single probe both sends and receives the sound waves. The structure and movement of the internal organs can be shown in ultrasound images as the pictures are taken in real-time known as Doppler. Ultrasound imaging is a non-invasive imaging modality that it used to diagnose breast cancer [17]. Recently, three-dimensional (3D) ultrasound has been used to translate sound wave data into 3D images. An advanced ultrasound technology is four-dimensional (4D) ultrasound, which is a 3D ultrasound in motion [18].

1.2.2.3 Magnetic Resonance Imaging (MRI)

Magnetic resonance imaging (MRI) is a high quality non-invasive medical imaging modality that helps to diagnose cancer and tumours. The technique uses radiofrequency waves rather than x-rays. A strong magnetic field helps to produce high resolution images of internal organs and tissues. These detailed pictures can then be seen on a computer monitor. MRI imaging is an accurate method in comparison with other medical image modalities such as mammography and valuable to detect a wide range of disease in all tissues and organs [19, 20, 21, 22].

Figure 1- 2 A superconducting magnet from a magnetic resonance imager (MRI)

1.2.2.4 Elastographic Methods

Elastographic techniques for breast cancer screening concentrate on the elevated elastic property contrast between carcinoma and breast tissue. Separate studies completed by Krouskop et al. [23] and Samani et al. [24] measuring the elastic modules of human tissue have shown invasive ductal carcinoma to be approximately an order of magnitude stiffer than fibro glandular tissue from a healthy breast. This contrast allows carcinoma to be identified within the breast based on a tissue stiffness map.

The relatively new field of elastography has developed [25] around efforts to image the mechanical properties of soft tissue. The desire for such images has come from clinical based findings that a variety of diseases, such as breast cancer, exhibit significant changes in the stiffness of the tissue they affect [26]. The field of elastography thus involves developing image reconstruction methods for relating measured tissue motion to underlying tissue stiffness patterns [27, 28, 29, 30, 31].

As it turns out, this relation between stiffness and motion is most commonly calculated in the form of computational models of the motion behavior of materials with complex stiffness distributions. In theory, the more sophisticated these models are, the more accurate the resulting elasticity image predictions they generate will be. There several types of elastographic image modalities that are presented in below.

1.2.2.4.1 Digital–Image-Elasto-Tomography (DIET)

Digital-Image- Elasto-Tomography (DIET) is a proposed new imaging technique which uses only surface motion supplied by a set of digital cameras to describe the elastic properties within the breast volume. This novel method determines the distribution of elastic properties within the breast by utilizing surface displacements. Several calibrated digital cameras detect and picture the motion and then an inverse reconstruction algorithm allows mapping the internal elastic stiffness distribution of the breast. As the breast cancer cells are much stiffer than normal tissue, this reconstructed elastic property distribution can clarify carcinoma even with the addition of random noise based on expected calibration accuracy [32, 33].

1.2.2.4.2 Ultrasound Elastography

Ultrasound elastography is a soft tissue imaging modality based on high-frequency sound waves which is able to produce an elastogram using displacements generated by external loads [34]. This technique calculates the local elastic properties of tissue *in vitro* and *in vivo* through an estimation of strain within tissue under external load condition [35].

The procedures involved with ultrasound elastography are categorized as: ultrasound image data acquisition, image registration and elastic modulus reconstruction. In the image acquisition technique, the image dataset is obtained while the object (phantom or tissue) is deformed under compression which this load condition is usually applied by an ultrasound probe.

Then the displacement field is captured and displays as an image by processing the strain values recorded in the image dataset. In the final step, these displacements are utilized to elasticity modulus reconstruction through an inverse problem process [36, 37].

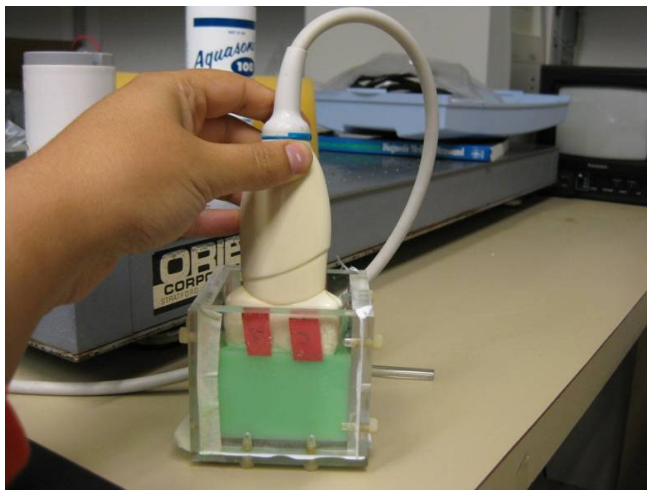

Figure 1- 3 This image shows a gelatine phantom and an ultrasound probe. The role of probe is important in an ultrasound imaging as it both sends and receives the sound's wave.

1.2.2.4.3 Magnetic Resonance Elastography (MRE)

Magnetic Resonance Elastography (MRE) is a novel imaging technique for visualization of elastic property distributions in tissue. This medical imaging modality uses harmonic mechanical displacements measured in a MRI unit to calculate mechanical properties [38, 39]. The technique has shown potential to diagnose suspicious breast lesions and it uses low-frequency mechanical waves that are sent into the tissue and visualized via an MR sequence using the phase contrast method synchronized with mechanical excitation [40, 41].

One of the advantages of the breast MRE technique is that this method can quantitatively show the elastic properties of breast tissues *in vivo* and clarifies high shear elasticity modulus of breast tumours. Further research is needed to evaluate the potential applications of MRE, such as detecting breast carcinoma and characterizing suspicious breast lesions [42, 43].

This research will mainly be conducted in the field of preventative breast cancer screening using MRE, which is expected to be a promising technique [44, 45, 46, 47], offering a potential alternative to the traditional methods of palpation and mammography [48, 49, 50, 51]. Fig 1.4 shows a general protocol of a MRE imaging technique that comprises three main steps.

First, an object that can be a phantom or a part of the body such as a breast is shaken by mechanical waves created by an actuator in a desired frequency. These mechanical waves create motion through the object (Fig. 1.4-A).

Second, a motion (displacements) map is generated through the phase contrast MRI methods. To obtain such a motion image, it is necessary that the motion encoding gradient be synchronized with actuation at the same frequency (Fig 1.4-B).

Third, the motion information is used to map the mechanical properties of the object by applying an inverse problem algorithm that reconstructs the elasticity image, known as an elastogram (Fig. 1.4-C).

1.3 Motivation and Contribution

The work specific to this research concerns the development of orthotropic phantoms, multiple displacement measurements from an orthotropic phantom and validating of the orthotropic incompressible algorithm to reconstruct a distributed orthotropic elasticity estimate from MRE detected motion data.

A

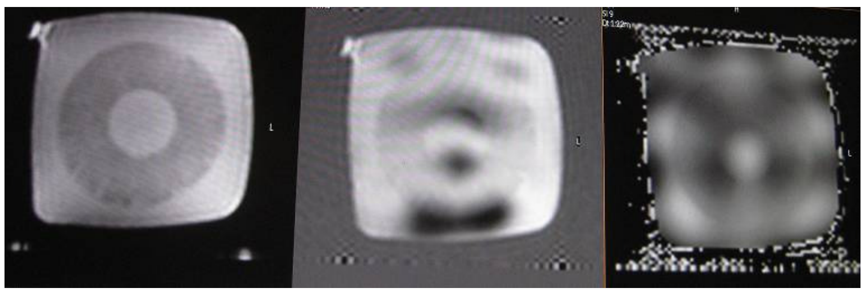

B

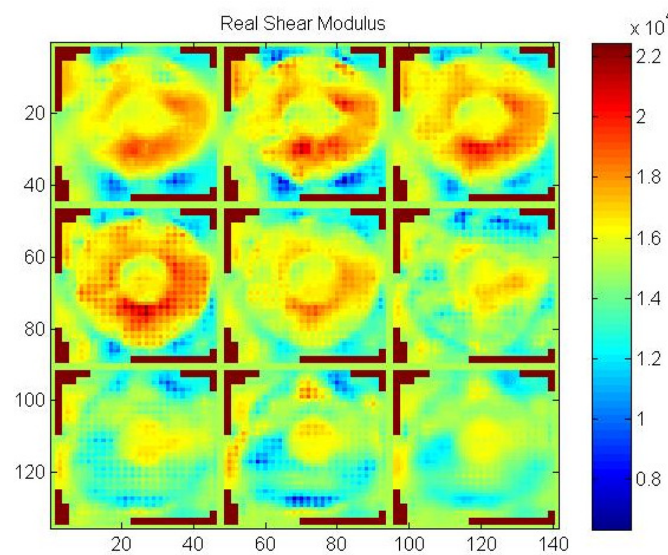

C

Figure 1- 4 This figure depicts the three main steps of an MRE imaging technique for a gelatine-pineapple phantom at frequency of 100 HZ. Phantom actuating (A), displacements map generated through phase contrast MRI (B), and reconstructed elastogram (C) are shown.

This project seeks to evaluate the capability of an existing orthotropic incompressible algorithm to differentiate three shear moduli in three different directions as well as comparing the orthotropic results with a linear elasticity isotropic. Orthotropic models have already been well developed within the mechanical and biomedical engineering literature, so the investigation will focus mostly on the performance and capabilities of imaging algorithms based on these more advanced models. Typically these imaging algorithms are formulated based on “inverse problems” which are involved optimization methods and regularization techniques.

Current models will therefore be improved in terms of anisotropy (orthotropic) that will also supply the basis for further implementations of various orthotropic nonlinearities. The correlation between the type of motion imaged by existing modalities (MRE) and the type of motion generated by forward and inverse simulations of these computational models must be accurate in order for quality images to be generated.

While MRE techniques have proven to be powerful biomedical imaging tools, most approaches assume isotropic material properties and there is little quantitative information available regarding orthotropic material behaviour. The anisotropic models available in the literature evaluate elasticity modules mostly in 2-D [41, 42, and 43]. Therefore, to study a more realistic behaviour of tissue and cancerous tumours it is necessary to develop a 3-D model with actual geometry and elasticity modules to include sufficient details regarding the orthotropic behaviour.

The analysis of the elasticity moduli for a biological orthotropic gelatine phantom (pineapple) fabricated for this study is expected to support the hypothesis that breast carcinoma might exhibit an anisotropic elasticity distribution.

In this study a 3-D model of the pineapple phantom will be developed for MRE based anisotropic elastography, and a non-linear analysis using a finite element method (FEM) will be performed. The technique is extended to three dimensions to provide sufficient information about the anisotropy of the elasticity tensor.

In terms of the finite element method (in particular for MRE algorithms), the reconstruction algorithm will be an iterative procedure, making an initial estimate of the elasticity parameter distribution.

The technique used in this research will provide an approach to further understand the orthotropic behaviour of non-linear materials such as breast tissue and hard tumour and suggests a realistic design guideline for advanced MRE.

1.4 Thesis Overview

Chapter 1 presents the necessity of the breast cancer studying as well as classifying the current diagnostic methods for breast cancer screening. While the main focus of the MRE as a powerful imaging tools is to distinguish the cancer within a benign tissue, this research was mostly concentrated working on tissue-mimicking phantoms fabricated during this project to make a fundamental basis for a modern MRE technique based on orthotropic elastography by using a novel algorithm.

Chapter 2 in general introduces theories of the MRE technique, inverse problem process based on iterative approaches, FEM implementations, Conjugate Gradient (CG) optimization method, total variation (TV) regularization technique and also adjoint gradient calculation regarding their application in this project.

Chapter 3 covers the theory behind the anisotropic and orthotropic materials, isotropic and orthotropic incompressibility and also the orthotropic elastography regarding its applications in MRE.

Chapter 4 introduces the MRE actuation systems utilized for this research and its remarks along with phantom-coil set up arrangements.

This chapter also presents the isotropic phantom manufacturing through a development of one wedge shaped inclusion phantom using silicone gel to generate a framework for the future isotropic phantom fabrication applied to MRE. Outside of the scope of this project, the role of one artifact due to actuation system and boundary conditions is evaluated by investigating several isotropic elasticity image reconstruction results obtained from two different actuation systems.

Chapter 5 presents developments of several orthotropic incompressible phantoms using different novel approaches and materials (biological and non-biological) to propose a guide line for future MRE orthotropic phantom manufacturing. This chapter also discusses boundary condition and data acquisition improvements towards multiple displacement measurements collected in one MRE set. In addition, orthotropic phantom fabrication protocols and data acquisition analysis are also evaluated regarding their remarks applied to MRE.

Chapter 6 represents orthotropic elasticity image reconstructions from a biological orthotropic phantom (pineapple) through the initial guess study to test the reliability of the new orthotropic algorithm. A range of different orthotropic reconstructions was computed and the results compared to the existing isotropic algorithm in linear elasticity. The main focus was to validate the ability of the algorithm to differentiate three shear moduli in three directions and the capability of the orthotropic phantom to mimic the orthotropic behaviour of tissue. The full MRE dataset developed for this thesis is also evaluated by Raleigh damping algorithm to obtain an optimum measurement condition regarding the frequency and directions for an advanced MRE in the future.

Chapter 7 discuses the goals achieved throughout this thesis and the future work for all three phases; orthotropic phantom developments and modifications, multiple measurements developments and modifications for orthotropic boundary conditions and orthotropic algorithm validation and suggestions in elastograpgy image analysis.

"Take the first step in faith. You don't have to see the whole staircase, just take the first step". Dr. Martin Luther King

Chapter 2

2.1 Magnetic Resonance Elastography (MRE)

As mentioned in 1.3.4.3, elasticity imaging comprises three basic steps: applying a known static or cyclic mechanical load through an object, measuring the deformation of the medium as the displacement pattern, and then calculating the elasticity modulus, or any related parameters that are worth being reconstructed. MRE has been developed to measure the elastic properties of tissue *in-vivo* [44, 45, 46, 47]. There are two different MRE styles: quasi-static and dynamic.

The dynamic method uses shear wave propagation to actuate the tissue. This method was developed as a phase-contrast technique by using harmonic shear vibrations and synchronized cyclic motion gradients to map the motion as a displacement field. These recorded data are utilized to reconstruct the image. The quasi-static technique uses the phase-contrast technique as well but the data acquisition in this method is often slow [48].

MRI applies a sequence of radiofrequency (RF) excitation pulses and a series of magnetic field gradients to produce an image by locating and encoding the spatial position of hydrogen nuclei (spins) in volume elements (voxels) within a tissue [49, 50, 51]. Furthermore, the MRE method combines a motion encoding gradient (MEG) to other magnetic field gradients at the same frequency and direction as the actuator [48].

2.2 Motion Measuring

In dynamic MRE, a piezoelectric or a voice actuator is used to actuate the sample being imaged with a sinusoidal driving signal. The MRI technique can scan the resulting harmonic motions within the volume of the sample using a phase contrast motion encoding gradients (MEGs) [49] which record the accumulated phase shift of the spins at different points along the sinusoidal signal [52].

These motions can be mapped in 3D to describe the motion at every point in space within the medium. This method generates a complex displacement value at a grid of internal points within the sample volume at each point [53]. The wavelength of shear waves produced by an actuator can be defined as:

$$\lambda_s \approx \frac{1}{f}\sqrt{\frac{\mu}{\rho}} \qquad (2.1)$$

where λ_s is the shear wavelength, f is the actuation frequency in Hz, μ is the shear modulus of the material, ρ is the density and $c = \sqrt{\frac{\mu}{\rho}}$ is the velocity of the shear waves [54].

2.3 Reconstructive Elastodynamic Imaging

MRE is a means of visualizing and quantitatively measuring the elastic property distribution in tissues or phantoms using harmonic mechanical excitation at low frequencies (10 to 1000 Hz) [49]. In this research, a phase-contrast MRI technique was used between 85-125 Hz in frequency to spatially map and measure the complete three-dimensional displacement patterns. From this data, local quantitative values of shear modulus distribution can be calculated.

2.3.1 Forward Problem

By definition, a forward problem is finding the mechanical response which is usually displacements, u in the MRE, given the material property distribution, η and boundary conditions. The general formulation of the forward problem is presented as:

$$[A(\eta)]\{u\} = \{R_{fwd}\} \tag{2.2}$$

where $A(\eta)$ is the forward matrix including terms related to material properties, η and u are unknown displacements. The term of R_{fwd} is the RHS vector containing boundary conditions in the forward problem [44, 58].

The usual forward problem in linear elasto-dynamics involves finding the domain behaviour generated by the PDE description as well as considering boundary conditions under a known (or assumed) property distribution. The solution of the forward problem provides the displacement field, $u(x,t)$, everywhere within the domain, which depends on position $x \in \Omega$ and time $t \in \tau$. In the case of elastography, the governing equation for a deformable medium is the linear elasto-dynamic equation. In the PDE form, also known as Navier's equation (see Appendix A), these relations can be presented as:

$$(\lambda + \mu)\nabla(\nabla \cdot u) + \mu\nabla^2 u + \nabla\lambda(\nabla \cdot u) + \nabla\mu \cdot \nabla u + \nabla u \cdot \nabla\mu = \rho\frac{\partial^2 u}{\partial t^2} \qquad \text{in } \Omega \tag{2.3}$$

where u is the displacement vector within the medium, μ and λ are material stiffness parameter, known as Lame's constants which depend on position, and ρ is the density of the material [211, 27]. Young's modulus of elasticity, E is related to Lame's constants through the expressions involving Poisson's ratio, υ,

$$\mu = \frac{E}{2(1+\upsilon)} \tag{2.4}$$

$$\lambda = \frac{\upsilon E}{(1+\upsilon)(1-2\upsilon)} \tag{2.5}$$

It should be noted that for nearly incompressible materials such as soft tissue, as υ is very close to 0.5, according to equation (2.5) the Lame parameter, $\lambda(x) \gg \mu(x)$. In nearly incompressible materials, $\lambda(x)$ is too high to allow a visualization of its associated wave pattern. This makes reconstruction of the $\lambda(x)$ parameter poorly conditioned based on measured data [55, 56, 57].

For imaging reconstruction, it is necessary to develop a parameter based on the model behavior which provides both a measurable response to excitation and a parameter that is worthy of being imaged. In MRE, this parameter is the shear modulus, μ. Also this PDE equation provides a measurable response pattern which is the displacement of the medium being imaged.

The most common excitation used in the elastography field is a time harmonic excitation that creates a standing wave displacement pattern. In the MRE procedure, the complex displacement from MRI scans includes amplitude and phase information which are used in the inversion code.

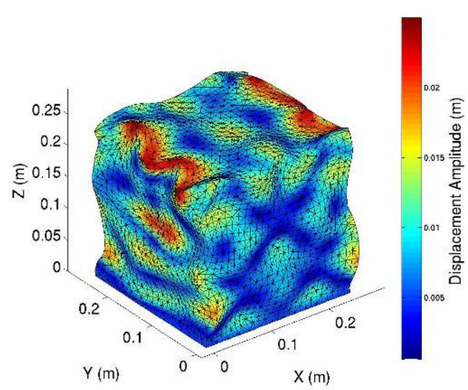

Figure 2- 1 The displacement pattern obtained from a simulation forward problem of a cubic gelatin phantom with fine mesh and shear waves.

The time harmonic displacement field takes on the form

$$u(x,t) = R_e\left\{ u_c(x)e^{j\theta}\right\} \tag{2.6}$$

where $$\theta = \omega t + \varphi \tag{2.7}$$

and $u(x,t)$ is the real-value displacement occurring at position x and time t, and u_c is complex displacement amplitude at phase φ and angular frequency ω of excitation. The real $u_r(x)$ and imaginary $u_i(x)$ components of u_c are defined as

$$u_c(x) = u_r(x) + ju_i(x) \tag{2.7}$$

where $j = \sqrt{-1}$ so the equation (2.6) can be expanded using Euler's formula, $e^{j\theta} = \cos\theta + j\sin\theta$ to give

$$R_e\left\{ u_c(x)e^{j\theta}\right\} = R_e\left\{ \left(u_r(x) + ju_i(x)\right) \left(\cos(\theta) + j\sin(\theta)\right) \right\} \tag{2.9}$$

which leads to

$$u(x,t) = u_r(x)\cos(\theta) - u_i(x)\sin(\theta) \tag{2.10}$$

This equation gives the form of the computed harmonic motions, so it is important that the measured motions are recorded as the same form.

The MR-detected motions are given as real-valued amplitude $\breve{u}(x)$ and phase $\varphi(x)$ for each point in the medium, so that the displacement field at a point x and at time t are given by

$$u\ (x,t) = \breve{u}\ (x)\cos[\omega t + \varphi(x)] \tag{2.11}$$

The displacements obtained from the harmonic motion discussed in equation (2.11) are substituted into equation (2.3), which yields

$$(\lambda+\mu)\nabla(\nabla\cdot\breve{u})+\mu\nabla^2\breve{u}+\nabla\lambda(\nabla\cdot\breve{u})+\nabla\mu\cdot\nabla\breve{u}+\nabla\breve{u}\cdot\nabla\mu=-\rho\omega^2\breve{u} \quad \text{in } \Omega \qquad (2.12)$$

This equation, with the given boundary conditions, governs the general dynamic response of a homogenous, isotropic, linearly elastic material to harmonic excitation [58, 59].

2.3.2 Inverse Problem in General View

At the heart of each elasticity imaging, there is the formulation and solution of an inverse elasticity problem. The inverse problem is essentially given one or more measured displacement fields, u inside an elastic body and boundary conditions, to determine the distribution of unknown parameters of interest, η. Inverse problem systems, arising from image reconstruction methods, are usually large and ill-conditioned.

The inverse problem formula is given as:

$$Z(u)\{\eta\}=\{R_{inv}\} \qquad (2.13)$$

where $Z(u)$ is the inverse matrix containing terms related to known measured displacements obtained from the MRE imaging procedure, unknown material properties, η and R_{inv} the direct inversion RHS vector [104, 105, 106].

This can be a conversion of the displacement solution obtained from equation (2.12) as a set of measurements into an estimate of elasticity parameters throughout the domain. The inverse problem in MRE cases mostly involves finding the shear modulus, $\mu(x)$ which can eventually satisfy the equation (2.12) by giving some measurements of the displacement field amplitude obtained from MRI at discrete locations and boundary condition data [60, 61, 62, 63].

One of the problems that arise in the solution of an inverse problem is that a very small amount of noise in data can cause large errors in the estimates. This instability phenomenon is known as ill-posedness.

By definition a problem is well posed when its solution exists and it is unique, which means, if $Ax_1 = Ax_2 \Rightarrow x_1 = x_2$. In a real image reconstruction the computed solution uniqueness suffers, as in a physical sense the solution is not exact but an approximation of the real data. The noisy experimental data increases the error which does not allow the original data to be reproduced completely. This problem is ill posed even for a small perturbation, which produces a large oscillation for a small change in the data [64].

Another factor which can be highlighted about the inverse problem is the condition number *K(A)* of a matrix A which is defined as:

$$K(A) = \|A\|_\infty \|A^{-1}\|_\infty \tag{2.14}$$

where $\|A\|_\infty$ is the size of matrix *A* given by maximum absolute row summation as:

$$\|A\|_\infty = \max_{i=1,\dots,n} \left\{ \sum_{j=1}^{n} \left| \; a_{ij} \; \right| \right\} \tag{2.15}$$

Suppose, *Ax=b,* where *x* is the exact solution to the linear system defined by *A* and *b* and $Ax_c = b_c$, where x_c is the calculated solution and b_c is the corresponding RHS. By definition, the relationship between relative error $\|x - x_c\| / \|x\|$ and relative residual $\|b - b_c\| / \|b\|$ can be shown as:

$$\frac{\|x - x_c\|}{\|x\|} \le K(A) \frac{\|b - b_c\|}{\|b\|} \tag{2.16}$$

The condition number determines the value of error. If $K(A) \approx 1$, the system is well-conditioned and it means the small inaccuracies in the residual give small errors, but if $K(A) \geq 1$, the system is ill-conditioned and with a small perturbation in the residual causes a large error [65]. In the section 2.4, the inverse problem approaches will be discussed.

2.3.3 Finite Element (FE) Approximation

One of the most efficient numerical approaches for computing the displacements in a forward solution, or the material properties in an inverse problem, is the finite element method. In the forward problem approach, this method approximates the governing equations (2.12) over a continuous medium as a mesh of elements.

Ultimately, for an N-node mesh system, the problem will reach the solution of a matrix equation of the form $[A(\eta)]\{u\} = \{R_{fwd}\}$, where $[A]$ is an n× n matrix, sparse as it is involved with basis functions which are nonzero only on each node over the domain. Usually a basis function, or a shape function, $\phi_i(x, y, z)$ is centered on each node and the magnitude of the parameter of interest is measured at every point in the meshed area as a weighted sum of these basis functions given as:

$$u_{ap}(x, y, z) = \sum_{i=1}^{N} u_i \phi_i(x, y, z) \tag{2.17}$$

where the index "*ap*" here represents the approximate functions in the finite dimensional space and $u_{ap}(x, y, z)$ is the approximate displacement value at a point (x, y, z), $\phi_i(x, y, z)$ are known FE basis functions correspond with *i*'th node and u_i is the displacement value at node *i*.

In the inverse problem approach, the FE approximation of the matrix equation $Z(u)\{\eta\} = \{R_{inv}\}$ takes the form as implementation of nodal material property distribution using basis functions for the element as:

$$\eta_{ap}(x,y,z) = \sum_{i=1}^{N} \eta_i \phi_i(x,y,z) \tag{2.18}$$

where $\eta_{ap}(x,y,z)$ is the approximate material property value at a point (x, y, z) that can be calculated as the sum of N basis functions that are valued by N constants, η_i. $\phi_i(x,y,z)$ is FE basis function correspond with *i*'th node and it is known. η_i is material parameter at node i which is unknown. The expansion of this equation for the approximation of elasticity parameters $\mu_{ap}(x,y,z)$, $\lambda_{ap}(x,y,z)$, and $\rho_{ap}(x,y,z)$ on the nodes will take the form

$$\begin{aligned} \mu_{ap}(x,y,z) &= \sum_{i=1}^{N} \mu_i \phi_i(x,y,z) \\ \lambda_{ap}(x,y,z) &= \sum_{i=1}^{N} \lambda_i \phi_i(x,y,z) \\ \rho_{ap}(x,y,z) &= \sum_{i=1}^{N} \rho_i \phi_i(x,y,z) \end{aligned} \tag{2.19}$$

where the index "*ap*" again represents the approximate functions in the finite dimensional space and μ_i, λ_i, ρ_i, u_i are the discrete parameter values at node i of the N total nodes within the FE mesh, known as shear modulus, bulk modulus, and density respectively.

The weighted residual method is a useful approach, which is widely applied in MRE finite element approximation. This method takes the weak form of the general forward problem, multiplies the error, '*r*' due to substituting the approximate solution, $\eta_{ap}(x,y,z)$, in a weighted function $w_j(x,y,z)$, then the product is integrated over the domain, Ω, and ultimately the result is set to equal zero which can be written as $\int_{\Omega} w_j(x,y,z) r dV = 0$.

One simple way to solve a FE weak form is using *Galerkin method* which chooses a linear basis function, $\phi_i(x,y,z)$ as the weighting function, ϕ_{ap} which leads to $\phi_{ap}(x,y,z) = w_{ap}(x,y,z) = \sum_{i=1}^{N} w_i \phi_i(x,y,z)$.

In the MRE time harmonic cases, the solution is naturally oscillatory, and applying fine and suitable meshes regarding the physical geometry of the problem plays an important role in accurately capturing the convergence of the solution with respect to the mesh size (Fig. 2.2), [66, 67, 68, 71].

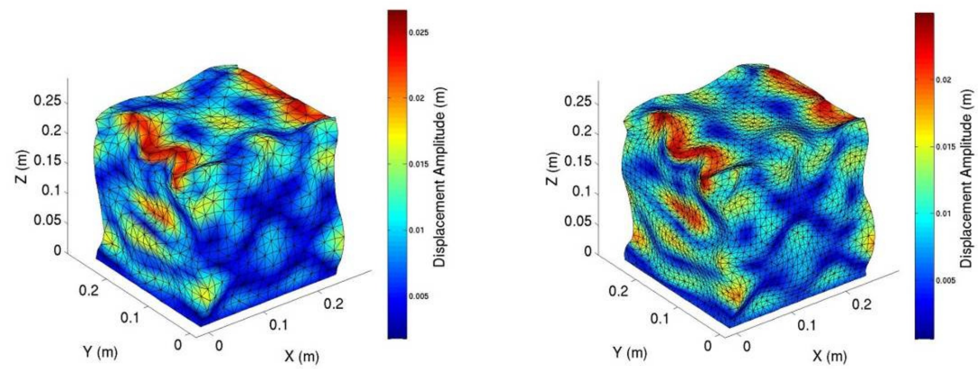

A **B**

Figure 2- 2 FE meshes size comparison between two cubic gelatin phantoms. The displacement results obtained from a simulation forward problem with shear waves in case B show a very smooth pattern with fine mesh in contrast to case A.

2.4 Optimization Algorithms

Optimization is the minimizing of an undesired, or maximizing of a desired, quantity or function that is constrained by its variables. In MRE, the goal is to minimize the objective function which depends on the variable of interest such as elasticity parameters.

The unknown parameter is usually bounded by values or constraint scalar functions related to the parameter. This constrained area known as a “feasible region”, which is the bounded area between two sets of points satisfying all the constraints boundaries, and the actual solution, which is the solution of the optimization problem [72, 73, 74].

In solving the inverse problem using an optimization method, two approaches are utilized: direct and iterative. As in this research the iterative optimization method was used, the strength and weakness points of this solution approach are described next.

2.4.1 Iterative Optimization Approach

The iterative approach refers to a wide range of techniques that solve a problem by finding successive approximation to an accurate solution starting from an initial guess. This method is used to solve nonlinear functions as well as linear problems with numerous variables [75, 76].

The strategy is that the iterative optimization algorithm begins with an "initial guess" of the parameter to be reconstructed and builds up a sequence of updated estimates until they meet the solution. In this improving sequence, the technique is to move from one iterate to the next. There are several methods to optimize an inverse problem iteratively.

Some algorithms store information obtained at previous iterations, while others utilize only local information from the current point [77, 78, 79]. Regardless of the algorithm's differences, an acceptable algorithm should have the following properties:

- **Flexibility**: it should be able to solve the problem for all reasonable choices of the initial guess.

- **Efficiency**: it should require the minimum computer run time or storage.

- **Accuracy**: it should be able to find a solution with precision, without being sensitive to errors in the data.

While these goals represent an ideal, in reality they may conflict. For example, a fast convergent technique for nonlinear programming may require too much computer memory on large problems.

Also, a robust optimization strategy may be very slow in practice. Therefore, in most optimization methods, the approach is a tradeoff between an advantage and a disadvantage, for example between convergence rate and memory storage, robustness and speed, and so on [80, 81, 82, 83].

In the MRE approach, the iterative approach solves the optimization problem that finds the nodal values of the shear modulus using given nodal displacements obtained from the real MRE data acquisition or a forward solution in a simulation study.

The method used in the reconstruction code involves an optimization approach that is more robust to measurement noise. This involves finding a material property distribution, such as shear modulus, which minimizes a displacement error function, Ψ,

$$\Psi = \int_{\Omega} (u^c - u^m)^T (u^c - u^m) d\Omega \tag{2.20}$$

where u^c is the set of the calculated displacement using an estimate of the material property distribution, and u^m is the measured displacement input data.

The advantage of an iterative approach is that it does not require filtering or differentiation of the data as it uses the data directly. The disadvantages are that the procedure is slow because the iterative nature of optimization techniques results in extremely computationally intensive problems. Also, this technique usually requires multiple full forward solutions at each iteration [84, 85, 86, 87, 88, 89].

2.4.2 Overview of Algorithms

All minimization algorithms need a starting point to be determined, x_0, known as an initial guess. This initial guess is the initial assumed value of the quantity which needs to be determined.

Knowledge about the data set and material properties in MRE reconstruction helps to estimate a reasonable value for x_0. Otherwise, the initial guess must be chosen in some arbitrary manner. In MRE, the role of the initial guess is very important in order to solve a reconstruction problem with fewer artifacts.

The technique starts at x_0, from which the optimization algorithm builds up a sequence of iterates $\{x_k\}_{k=0}^{M}$ where M is the total number of iterations and k is the current sequence of iteration. The minimization procedure is finished when there is no progress on convergence to the solution point, or when the solution has met an acceptable level of accuracy. The algorithms use information about the function at x_k, and also information from earlier iterates x_0, x_1, ..., x_{k-1} to move from x_k to x_{k+1} with a lower function value than x_k.

There are two basic strategies for moving from the current point x_k to a new iterate, x_{k+1}; "line search" and "trust region". As the trust region is not in the scope of this research, only line search strategy will be discussed in the next sections. Readers can find more information about the trust region strategy in [90, 91].

2.4.3 Line Search Methods

In general, in the line search strategy, the algorithm selects a 'search direction' p_k, from the current iterate x_k, and travel along this direction to a new iterate x_{k+1} with a lower function value as:

$$F(x_{k+1}) < F(x_k) \tag{2.21}$$

where the function, F is an arbitrary function which is expected to be minimized. The line search technique has two steps; the first step is choosing the p_k, for each iteration, which is used to update the value of the parameter that is being optimized at each iteration.

The distance to move along p_k or the update value for the k'th iteration can be found by approximately solving the following one-dimensional minimization equation in general:

$$x_{k+1} = x_k + \alpha_k p_k \tag{2.22}$$

where α_k is the step size to be found. The effective choices of two parameters; direction p_k and the step length α_k are the key factors for success in a line search method. In most minimization cases, p_k is the descent direction such that $p_k^T \nabla F_k < 0$. This property guarantees that the function F can be reduced along this direction [74, 76, 78]. By considering the material property, η as the parameter which needs to be updated, the equation (2.22) can be specialized for an MRE optimization case using line search strategy:

$$\eta_{k+1} = \eta_k + \alpha_k p_k \tag{2.23}$$

Assume the displacement error function Ψ from equation (2.20) is the function which is supposed to be minimized. At first, the p_k, should be determined in such a way that ensures that some reduction in error is happening with each iteration. This can be achieved by calculating the directional derivative of the error along p_k, at small α_k and making sure it is negative, as shown in below:

$$p_k^T \frac{\partial \Psi}{\partial \eta} < 0 \tag{2.24}$$

where $\frac{\partial \Psi}{\partial \eta}$ is the current error gradient . As the search direction is one dimension the error domain, this directions was the form of method a line, therefore this is called a line search. Next, a value for α_k must be chosen. A line search is exact or perfect when it can choose α_k to minimize $\Psi(\eta_k + \alpha_k p_k)$ by finding an actual minima in the direction given by p_k. An exact line search gives the best possible reduction in Ψ along the search direction but it can be computationally intensive to do an accurate minimization of the function on each iterate.

Weak or inexact line searches are usually preferred as this makes the method simple and reliable to use to find a value for α_k which satisfies the descent property [79, 80, 92], such as:

$$\Psi(\eta_k + \alpha_k p_k) < \Psi(\eta_k) \tag{2.25}$$

Although the α_k chosen in this way may not be the optimal value generating the best reduction in error, however, the low computational cost allows more optimization iterations in a given time. This increases the speed and efficiency of the algorithm while the perfect line search is noticeably slow [93].

2.4.4 Search Directions for Line Search Methods

The steepest descent direction is the simplest approach of the gradient methods and also a good assumption for the search direction of a line search optimization method in n variables. Among all the possible directions to move from current point η_k to minimize a function $\Psi(\eta)$, there is only one along which $\Psi(\eta)$ decreases most rapidly and this direction of steepest descent is obtained by the negative gradient $-\nabla\Psi_k$. The general steepest descent algorithm steps with an exact line search can be performed as below:

1) Selecting an initial guess, η_0 for the minimum of $\Psi(\eta)$.
2) Repeat for $k = 0,\ 1,\ 2,....$
3) Set $p_k = -\nabla\Psi(\eta_k)$
4) Calculate α_k to minimize $\Psi(\eta_k + \alpha_k p_k)$
5) Set $\eta_{k+1} = \eta_k + \alpha_k p_k$
6) Until $\|\nabla\Psi(\eta_{k+1})\|$ is sufficiently small.

The steepest descent advantage is that the method can be very simple as it requires calculation of the gradient $-\nabla\Psi_k$ but not the second derivatives, known as the Hessian.

However, this algorithm may not be efficient enough to minimize the function and proceeding along the line search can be extremely slow on difficult nonlinear problems. The fact that an algorithm can converge does not necessarily mean that it is an efficient technique. In comparison with other methods such as the Conjugate Gradient Method, shown in the next section, the steepest descent is usually inefficient [94, 91].

2.4.5 Conjugate Gradient (CG) Method

The conjugate gradient (CG) method is an efficient approach, which at its base is a modification of the simple steepest descent method. The CG method improves on the steepest descent by making a set of search directions from the gradient at each iterate, which eventually form a conjugate basis set. This technique is one of the most useful tools for solving large scale linear and nonlinear systems of equations. The advantages of CG are that it requires no matrix storage and is faster than the steepest descent method [95].

2.4.5.1 Linear Conjugate Gradient Method

In the minimization problem the gradient of the error function $-\nabla\Psi_k$ can take the general form as:

$$-\nabla\Psi_k = r_k = b - Ax_k \tag{2.26}$$

where A is an $n\times n$ matrix that is symmetric and positive definite. By introducing error vector $e_k = \eta_{k+1} - \eta_k$, which shows the distance from the actual solution, and residual r_k in equation (2.26) that represents the distance from the correct value of b, the equation (2.26) is transformed to:

$$r_k = -Ae_k \tag{2.27}$$

This shows the residual is the error transformed by A into the same space as b. As the error is unknown, it can be transformed to the known residual space.

An interesting property of the CG method is its ability to produce a set of linearly independent conjugate vectors $\{p_{0,}\ p_{1,}\ ....p_l\}$ with respect to the symmetric positive definite matrix *A*. The conjugacy property is shown as:

$$p_i^T A p_j = 0, \qquad i \neq j \tag{2.28}$$

As will be shown, linear CG is an iterative method for solving linear systems with positive definite matrices and the conjugacy property guarantees successively minimization of the function along the individual directions after *n* steps by setting the iterative sequence as $\eta_{k+1} = \eta_k + \alpha_k p_k$, where α_k is the step length along the search direction p_k. The value of α_k can be obtained using the fact that the error $e_{(k+1)}$ should be orthogonal to the previous search direction p_k because this not only avoids the skipping in the direction of p_k again, but also corresponds to the minimum point along the p_k. This leads to:

$$p_k^T e_{k+1} = 0 \tag{2.29}$$

$$p_k^T (e_k + \alpha_k p_k) = 0 \tag{2.30}$$

$$\alpha_k = -\frac{p_k^T e_k}{p_k^T p_k} \tag{2.31}$$

As the e_k is unknown so by using (2.27) the e_k can be transformed to the r_k, space which is known as:

$$\alpha_k = -\frac{p_k^T r_k}{p_k^T A p_k} \tag{2.32}$$

If the search direction p_k will be set up in the direction of gradient or r_k the value of α_k can take the form of the same value in the steepest descent, given by:

$$\alpha_k = \frac{r_k^T r_k}{p_k^T A p_k} \tag{2.33}$$

This iterative minimization is updated along both error and residual space. This leads to:

$$r_{k+1} = -Ae_{k+1} = -A(e_k + \alpha_k p_k) \tag{2.34}$$

$$r_{k+1} = r_k - \alpha_k A p_k \tag{2.35}$$

$$e_{k+1} = e_k + \alpha_k p_k \tag{2.36}$$

CG is based on conjugate direction but with a very special property that means it is able to generate the next search direction p_{k+1} using a linear combination of the current gradient, $-\nabla\Psi_k$ known as residual, r_k and the previous search direction, p_k. This advantage of the CG method is remarkable because it does not need to know all the previous elements, thus it requires little storage and computation. This conception is expressed as:

$$p_{k+1} = r_{k+1} + \beta_{k+1} p_k \tag{2.37}$$

The constant β_k is being chosen so that p_k and p_{k+1} will form as they must be conjugate with respect to *A*. By pre-multiplying (2.37) by $p_k^T A$ and applying the condition of conjugacy $p_K^T A p_{K+1} = 0$, it is found that:

$$\beta_{k+1} = \frac{r_{k+1}^T A p_k}{p_k^T A p_k} \tag{2.38}$$

As the matrix *A* is difficult to calculate, to remove it from the equation (2.38) the term Ap_k is replaced by $r_{k+1} - r_k / \alpha_k$ from equation (2.35). Now by using (2.37) and substituting the equation (2.38) and applying the two facts that each residual is orthogonal to the previous search direction, and also orthogonal to the previous residuals as they are shown in (2.39) and (2.40), leads to β_k as a ratio of a new and previous gradient norm as it is shown in (2.41).

$$r_k^T r_{k+1} = 0 \tag{2.39}$$

$$p_k^T r_{k+1} = 0 \tag{2.40}$$

$$\beta_{k+1} = \frac{r_{k+1}^T r_{k+1}}{r_k^T r_k} \tag{2.41}$$

The algorithm proceeds by producing vector sequences iteratively to approximate and update the solution, residuals, and search directions, successively. CG generates three vectors at each step, the approximate solution *x*, its residual *r*=*Ax*-*b*, and a search direction, which is based on the CG. At each step *x* is improved by searching for a better solution in the direction [96, 97, 98, 99].

The CG algorithm can be summarized as below:

1) Choose η_0 % initial estimate of the solution
2) Calculate $r_0 = b - A\eta_0$ % initial gradient
3) Set $r_0 \to p_0$, $k \to 0$ % initial search direction
4) Find $\alpha_k = \dfrac{r_k^T r_k}{p_k^T A p_k}$ % line search parameter
5) Set $\eta_{k+1} = \eta_k + \alpha_k p_k$ % update approximate solution
6) Set $r_{k+1} = r_k - \alpha_k A p_k$ % update gradient
7) Find $\beta_{k+1} = \dfrac{r_{k+1}^T r_{k+1}}{r_k^T r_k}$ % ratio of new and previous gradient norm
8) Determine $p_{k+1} = r_{k+1} + \beta_{k+1} p_k$ % update search direction
9) Put $k \to k+1$
10) Until $\|r_{k+1}\|$ is sufficiently small.

2.4.5.2 Nonlinear Conjugate Gradient Method

In the nonlinear CG method, there are several possible expressions for the value of β_k such as Fletcher-Reeves (2.42), but the most commonly used is the Polak-Ribiere formula, given by (2.43).

$$\beta_{k+1}^{FR} = \frac{r_{k+1}^T r_{k+1}}{r_k^T r_k} \tag{2.42}$$

$$\beta_{k+1}^{PR} = \max\left\{ \frac{r_{k+1}^T (r_{k+1} - r_k)}{r_k^T r_k},\ 0 \right\} \tag{2.43}$$

where the scalar β_k is used to enforce local conjugacy between p_{k+1} and p_k with respect to A. Also there are several choices for β_k and they are no longer equivalent. For example the Fletcher-Reeves method works well when the initial guess is very close to the actual result while Polak-Ribiere usually converges much more quickly. Another advantage of Polak-Ribiere is that its convergence can be guaranteed by choosing $\beta_k = \max\{\beta^{PR},\ 0\}$.

The CG algorithm in the nonlinear case becomes more complicated. These are difficulties in calculating the step length, α_k, as the line search is not linear anymore and also in computing the gradient $-\nabla\Psi\ (\eta_k + \alpha_k p_k)$. The Secant line search technique is a useful method to calculate α_k in nonlinear CG.

As the elastographic inverse problem is non-linear, the search directions will lose conjugacy as the iterations progress, therefore CG reconstructions often perform better with periodic 'restarts', where building up the set of conjugate search directions is started from scratch. This is achieved by simply setting $\beta_k = 0$. This restarting will happen when $\beta_k^{PR} < 0$, as well. Restarting the CG means ignoring all past search directions, and beginning the CG in a new direction of the steepest descent.

Therefore, the CG is very memory efficient as the only information with significant storage required for a CG algorithm are four vectors of length number of parameters (NP), r_k, r_{k+1}, p_k and p_{k+1}.

Another problem in nonlinear CG is that a general function may have many local minima and in this case CG cannot guarantee to converge to the global minimum [74, 100, 101].

In MRE, the displacement error function, Ψ, is minimized by computing the gradient of the Ψ with respect to the material property η and then setting this derivative to zero as:

$$u^c = F(\eta) \tag{2.44}$$

$$\Psi = \left\| u^m - u^c(\eta) \right\|^2 = \left\| u^m - F(\eta) \right\|^2 \tag{2.45}$$

$$\frac{\partial \Psi}{\partial \eta} = -2\left(\frac{\partial F(\eta)}{\partial \eta}\right)^T (u^m - F(\eta)) = 0 \tag{2.46}$$

where $\frac{\partial F(\eta)}{\partial \eta}$ is called the Jacobian matrix given by:

$$J = \begin{bmatrix} \frac{\partial u_1}{\partial \eta_1} & \frac{\partial u_1}{\partial \eta_2} & \cdots\cdots \frac{\partial u_1}{\partial \eta_n} \\ \frac{\partial u_2}{\partial \eta_1} & & \\ . & & \\ . & & \\ \frac{\partial u_n}{\partial \eta_1} & \cdots\cdots\cdots\cdots & \frac{\partial u_m}{\partial \eta_n} \\ & & \end{bmatrix} \tag{2.47}$$

2.4.6 Secant line search method

The Secant method is a fast exact line search technique which is used for zero-finding of a function in nonlinear CG and iteratively solves for a stationary point of the error domain. The approximation of the function $\Psi(\eta_k + \alpha_k p_k)$ using a truncated Taylor series is given by:

$$\Psi(\eta_k + \alpha_k p_k) \approx \Psi(\eta_k) + \alpha_k \left[\frac{\partial}{\partial \alpha_k} \Psi(\eta_k + \alpha_k p_k) \right]_{\alpha_k = 0} + \frac{\alpha_k^2}{2} \left[\frac{\partial^2}{\partial \alpha_k^2} \Psi(\eta_k + \alpha_k p_k) \right]_{\alpha_k = 0} \tag{2.48}$$

The objective of the line search is to minimize this function by setting its derivative to zero, so that

$$\frac{\partial}{\partial \alpha} \Psi(\eta_k + \alpha_k p_k) \approx [\Psi'(\eta_k)]^T p_k + \alpha_k p_k^T \Psi''(\eta_k) p_k = 0 \tag{2.49}$$

where $[\Psi'(\eta_k)]^T p_k$ is the directional derivative along p_k. As the calculation of the second derivative of the function $\Psi''(\eta_k)$ (also known as the Hessian matrix) is computationally expensive, a finite difference approximation of the second derivative can be used.

This can be computed by the Secant method which approximates the second derivative of $\Psi(\eta_k + \alpha_k p_k)$ by calculating the first derivative of the function at two different points $\alpha_k = 0$ and $\alpha_k = \delta$, where δ is an arbitrary small nonzero number. This leads to:

$$\frac{\partial^2}{\partial \alpha_k^2} \Psi(\eta_k + \alpha_k p_k) \approx \frac{\left[\frac{\partial}{\partial \alpha_k} \Psi(\eta_k + \alpha_k p_k) \right]_{\alpha_k = \delta} - \left[\frac{\partial}{\partial \alpha_k} \Psi(\eta_k + \alpha_k p_k) \right]_{\alpha_k = 0}}{\delta} \qquad \delta \neq 0$$

$$= \frac{[\Psi'(\eta_k + \delta p_k)]^T p_k - [\Psi'(\eta_k)]^T p_k}{\delta} \tag{2.46}$$

which calculates the second derivative of the function when α and δ approach zero. By substituting (2.46) for the third term of the Taylor series (2.44), performed as:

$$\frac{\partial}{\partial \alpha_k}\Psi(\eta_k + \alpha_k p_k) \approx [\Psi'(\eta_k)]^T p_k + \frac{\alpha_k}{\delta}\left\{ [\Psi'(\eta_k + \delta p_k)]^T p_k - [\Psi'(\eta_k)]^T p_k \right\} \quad (2.47)$$

then the α_k can be found for the line search setting this derivative to zero, which leads to:

$$\alpha_k = -\delta \frac{[\Psi'(\eta_k)]^T p_k}{[\Psi'(\eta_k + \delta p_k)]^T p_k - [\Psi'(\eta_k)]^T p_k} \quad (2.48)$$

For nonlinear problems this process is applied iteratively until a suitable stopping point is reached. The Secant method approximates the function $\Psi(\eta_k + \alpha_k p_k)$ with a parabola by finding the first derivative at two different points. It should be pointed out that this method should be ended when x_k is in the neighborhood of the actual solution, otherwise the convergence may fail and will not progress any longer, as the search direction for highly nonlinear problems will lose conjugacy quickly.

While the Secant method is simple as it only needs to calculate the first derivative of the function, this technique has some disadvantages. This method is not able to recognize minima from maxima and also it is sensitive to "initial guess" and parameter δ. Good choices of δ and the "initial guess" close to the actual solution will help this algorithm converge to the minima point successfully. Although the secant method is an exact line search, a better policy is often to use an inexact line search technique by applying a limited number of secant iterations [101, 102].

2.5 Regularization Techniques

In a general, the error function, Ψ, does not put any restrictions on the material property values or their distribution. This implies that any material property distribution which decreases this function can be acceptable as a solution, but this may not always lead to physically realistic values.

Techniques which involve modifying a function in an attempt to make the reconstruction algorithm prefer solutions which fit *a-priori* information are known as regularization techniques. This can be carried out by adding a regularization term, $R(\eta)$, known as a penalty function to the objective function, so that $\Phi = \Psi + R(\eta)$. The typical strategy is minimizing an objective function, Φ that comprises two terms: an error function Ψ, and a regularization term $R(\eta)$. Ψ is the integration of the differences between measured, u^m, and calculated, u^c, displacements over the domain and $R(\eta)$ is normally a function of the material property distribution, η.

Several regularization methods are available such as Tikhonov (TK), Total variation (TV) minimization and spatial filtering [103, 104]. The regularization of the objective function is explained in the next section regarding TK and TV. As in this research, TV was used; the focus is on this method.

2.5.1 Tikhonov (TK) Regularization Techniques

Tikhonov (TK) regularization is a technique to stabilize the inverse problem's solution. The equation to describe this method can be written as:

$$\Phi_{TK} = \frac{1}{2}\left\| u^c - u^m \right\|^2 + \frac{\alpha_{TK}}{2}\left\| \eta - \eta_0 \right\|^2 \tag{2.49}$$

where η is the current material property estimate, η_0 is the initial material property and α_{TK} is called the regularization parameter which is the weighting applied to TK [58, 105].

2.5.2 Total Variation (TV) Minimization

Total variation is a regularization technique that penalizes special variation of the reconstructed image, which leads to smoother images. Most of the regularization methods assume the data set to be smooth and continuous, but TV is sufficiently robust to deal with blocky image and discontinuities as well as being able to preserve the edge information in the reconstructed image.

If η is piecewise constant with a finite number of jump discontinuities, then TV(η) is a robust approach to penalize un-physically large variations in the modulus distribution while allowing a piecewise discontinuous solution. Overall the objective function Φ_{tv} is terms:

$$\Phi_{tv} = \Psi + R(\eta) \tag{2.50}$$

where

$$\Psi = \int_{\Omega} (u^c - u^m)(u^c - u^m) d\Omega \tag{2.51}$$

and

$$R(\eta) = \int_{\Omega} \alpha(\nabla \eta^T \nabla \eta + \delta^2) \ \ d\Omega \tag{2.52}$$

so that

$$\Phi_{tv} = \int_{\Omega} (u^c - u^m)^T (u^c - u^m) d\Omega + \alpha_{tv} \int_{\Omega} (\nabla \eta^T \nabla \eta + \delta_{tv}^2) d\Omega . \tag{2.53}$$

TV can also be expressed as L_1 norm of the first spatial derivation of the solution when δ_{tv}^2 is sufficiently small. This can be shown as:

$$\Phi_{tv} = \frac{1}{2}\left\| u^c - u^m \right\|^2 + \alpha_{tv} \int_{\Omega} \sqrt{\left| \nabla \eta \right|^2 + \delta_{tv}^2} \qquad (2.54)$$

where $\nabla \eta$ is the spatial variation of the material property, η, and α_{tv} is called the regularization parameter which is the weighting applied to TV. It controls the relative level of the regularization effect on the minimization process.

Typically, the greater the noise level in the data, the more regularization is required to obtain a good approximate solution for the equation. This parameter can play an important role in a good regularized output. The integral means that the level of total variation is the area under the $\sqrt{\left| \nabla \eta \right|^2 + \delta_{tv}^2}$ curve. The quantity $\sqrt{\left| \nabla \eta \right|^2 + \delta_{tv}^2}$ is known as gradient magnitude. This provides us with the information about the discontinuities in the image.

Here, δ_{tv} is a numerically small constant introduced to smooth the singularity that would otherwise exist at $\nabla \eta = 0$ as TV is not differentiable at zero. So to avoid this problem a small positive constant value is added to the equation [105, 106, 107, 108, 109].

2.6 Adjoint Gradient Calculation

Although the CG technique requires calculating the gradient to obtain the search direction in each iteration, calculating the Jacobian to build the residual is computationally intensive. The adjoint gradient method has been recently developed to provide a very efficient method to compute the gradient without “agonizing pain”. In gradient based optimization, the adjoint technique is widely utilized for the gradient computation when there is a problem dealing with a large number of parameters.

While other methods, such the Jacobian matrix or a finite difference approximation use as many forward solutions as there are parameters, the adjoint approach requires only two forward solutions to obtain the gradient for any number of reconstructed parameters.

Here the discrete adjoint gradient calculation for MRE is expressed. By definition the variation of a function $F(x)$ in the direction δx is denoted by δF and it is given by

$$\delta F = \frac{\partial F}{\partial x} \cdot \delta x = \frac{d}{d\varepsilon} |_{\varepsilon \to 0} \ F(x + \varepsilon \delta x) \tag{2.55}$$

where $\frac{\partial F}{\partial x}$ which also is shown by this notation $D_x F$ is a directional derivative of the function $F(x)$ and represents the perturbation rate of the function by the presence of small changes in the variable.

The general weak form of the forward problem can be defined as

$$A(w_{ap},\ u_{ap}^{c};\ \eta_{ap}) = \oint w_{ap} \cdot \sigma ds \tag{2.56}$$

where $A(\cdot,\ \cdot;\eta)$ is a bilinear operator which represents an equivalent weak form of the elasticity equation which represents the inner product between two tensors w and u respectively and depends on the elasticity parameter vector η. The discretized weighting function w is expressed as $w_{ap}(x,y,z) = \sum_{i=1}^{N} w_i \phi_i(x,y,z)$ and the approximation of the calculated displacement field can be shown as $u_{ap}^{c}\ [x,y,z,\eta\ (x,y,z)] = \sum_{i=1}^{N} u_i \phi_i(x,y,z)$. The RHS shows the traction on the boundaries obtained from Green's theorem. The inverse adjoint elasticity formulation for the TK discretized function is introduced as follows:

$$\Phi_{TK} = \frac{1}{2}\left\| u_{ap}^{c} - u^{m} \right\|^{2} + \frac{\alpha_{TK}}{2}\left\| \eta - \eta_0 \right\|^{2} + A(w_{ap},\ u_{ap}^{c};\ \eta_{ap}) - \oint w_{ap} \cdot \sigma ds \tag{2.57}$$

The variation of the equation (2.57) is computed by using the functional derivative defined in equation (2.55) and can be written as:

$$\delta \Phi_{TK} = \frac{\partial \Phi}{\partial u^{c}} \delta u^{c} + \frac{\partial \Phi}{\partial w_{ap}} \delta w_{ap} + \frac{\partial \Phi}{\partial \eta_{ap}} \delta \eta_{ap} = 0 \tag{2.58}$$

Assuming the presence of TK regularization, the variation of the equation (2.53) due to w is:

$$\frac{\partial \Phi}{\partial w_{ap}} \delta w_{ap} = A(\delta w_{ap},\ u_{ap}^c;\ \eta_{ap}) - \oint \delta w_{ap}.\sigma ds \tag{2.59}$$

Setting this variation to be equal to zero (i.e. $\frac{\partial \Phi}{\partial w_{ap}} \delta w_{ap} = 0$) leads to u_{ap}^c satisfying the weak form of the elasticity equation. On the constraint boundaries of the equation (2.59), the equation (2.57) reduces to the original objective function (2.49). Equation (2.58) can be further simplified if the weighting function is chosen so that $\frac{\partial \Phi}{\partial u^c} \delta u^c = 0$. This leads to:

$$A(w_{ap},\ \delta u_{ap}^c;\ \eta_{ap}) = -\left(u_{ap}^c - u^m\right) \tag{2.60}$$

As the elasticity operator A is self-adjoint and symmetric, thus it is equal to its transposed A^T which can be illustrated as $A(w_{ap},\ \delta u_{ap}^c;\ \eta_{ap}) = A^T(\delta u_{ap}^c,\ w_{ap};\ \eta_{ap})$. Therefore, the equation (2.60) can be rewritten as

$$A^T(\delta u_{ap}^c,\ w_{ap};\ \eta_{ap}) = -\left(u_{ap}^c - u^m\right) \tag{2.61}$$

With u_{ap}^c and w_{ap} given by (2.56) and (2.61) respectively, from (2.58) and (2.49) it is seen that:

$$\delta\Phi = \frac{\partial \Phi}{\partial \eta_{ap}} \cdot \delta\eta_{ap} = \frac{\partial}{\partial \eta_{ap}}\left[A(w_{ap},\ u_{ap}^c;\ \eta_{ap}) + \frac{\alpha_{TK}}{2}\left\|\eta - \eta_0\right\|^2\right]\delta\eta_{ap} \tag{2.62}$$

$$\delta\Phi = \frac{\partial \Phi}{\partial \eta_{ap}} \cdot \delta\eta_{ap} = A(w_{ap},\ u_{ap}^c;\ \delta\eta_{ap}) - \alpha_{TK}\left\|\eta - \eta_0\right\| \tag{2.63}$$

Now this gradient will be minimized by setting the equal to zero so that $\frac{\partial \Phi}{\partial \eta_{ap}} \delta\eta_{ap} = 0$ and this follows as:

$$A(w_{ap},\ u_{ap}^{c};\ \delta\eta_{ap}) = \alpha_{TK} \left\| \eta - \eta_0 \right\| \tag{2.64}$$

The steps required for implementing the adjoint method are given as below:

1. Solve the forward problem (2.59) for u_{ap}^{c}, the current displacement solution, using the current material property estimate.

2. Calculate the '*adjoint forcing'*; which is given by $(u_{ap}^{c} - u^{m})$, whereas u^{m} is the vector of measured displacements.

3. Solve the forward problem again for (2.60) with the *adjoint forcing* as the RHS vector, to evaluate the w_{ap}.

4. Apply u_{ap}^{c} and w_{ap} in (2.64) to calculate the gradient with respect to the i^{th} material property value [110, 111, 112, 113].

2.7 Subzone Implementation

A new and powerful method to solve an inverse problem is by using the subzone technique, which reduces the global inversion process to multiple local inversion problems. This technique works efficiently to solve an iterative inverse reconstruction across a large parameter set with reasonable computational load.

The 3D subzone procedure for the sub-domain inverse problem uses the known internal displacements to solve an iterative inversion process on small partitions of the total problem domain. This approach generates a high degree of spatial discretization and, utilizes the data-rich environment obtained from MRI.

The image reconstructions show that the zoned inversion strategy is capable of producing accurate elasticity modulus distribution images from displacement data obtained from MR even in the presence of high noise.

An advantage of the subzone reconstruction is that this method is able to use the very large MRI data for material property reconstructions. While MRI scans generate a large data set which leads to a large number of nodes in the resulting FE models, current computer systems may not be able to solve and analyze these large problems because of memory limitations. The subzone method reduces this time as it breaks the entire FE domain to small sub-regions.

In the subzone process the entire data obtained from MRI is divided into a grid of subzones where the size of these smaller subsets depends on the geometry of the original data set, based on the measured motion information, Dirichlet boundary conditions are then applied on the boundary of these subsets.

Another advantage of the subzone reconstruction method is its ability for parallel solution by sending these subsets to the different processors of a distributed computing system. The results obtained from the individual subsets can then be assembled in the whole geometry. This method has been proven successful in reconstructing stiffness distributions using MR-detected motion datasets from both gelatin phantoms and real patient data sets [114, 114, 115].

User flexibility to choose the size of the minimization problems without reducing the resolution of the reconstructed image is another positive point of the subzone approach. As each subzone inversion works independently, so the total procedure involves so many different minimizations that a failure on one of the subzones due to local error minima in the error minimization process does not mean the entire reconstruction will fail.

This advantage of the subzone technique increases the reliability of the reconstructions, because if a solution from a subzone fails, another set of subzones can be made to cover the region of the failed subzone and this subzone solution can simply be ignored.

The parallel subzone technique is built using the Message Passing Interface (MPI). One of the processors is defined by the user and manages the tasks such as dividing the problem into small regions, passing this set of subzones to the other processors for reconstruction, and receiving the completed material property solutions from them. It then assembles these reconstructions and saves them in a resulting file which can be visualized as an image of the full-volume problem.

At each global iterate, the centre point (the seed location) for the grid of overlapping subzones is determined randomly. In each round of dividing the geometry into the subzone grid, a different set of subzones will be implemented. This will reduce the boundary related artifacts in the final material property image. When the manager processor receives the solution obtained from each zone it will be located into the correct place in the global solution arrays.

There are several subzone geometry parameters which may affect the improvement of the subzone reconstruction such as zone size (subzone edge length factor), zone shape and the subzone grid overlapping (Fig. 2.4).

Experience has shown there is an optimum size for building the subzone grid for better reconstruction results. For example, by increasing the number of subzones in one domain and reducing the size of the each subzone, the time to run a reconstruction in one subzone will be decreased as the problem is being solved in a smaller area.

However, this may cause loss of accuracy of the results as most of the internal nodes inside each subzone have sufficient data to accurately determine the underlying parameter distribution. Technically, the nodes on the boundaries are less useful in the minimization process. Thus, raising the number of subzones in one grid will lead to a higher overall ratio of boundary nodes, and this means the information from internal nodes possibly lead to reduced accuracy. In fact, the sensitivity of the boundary nodes is lower than internal nodes as they receive relatively less information. The internal nodes are surrounded on all sides by motion data while the boundary nodes only have motion data on one side. This may be shown by calculating the ratio between the internal and external nodes in one grid.

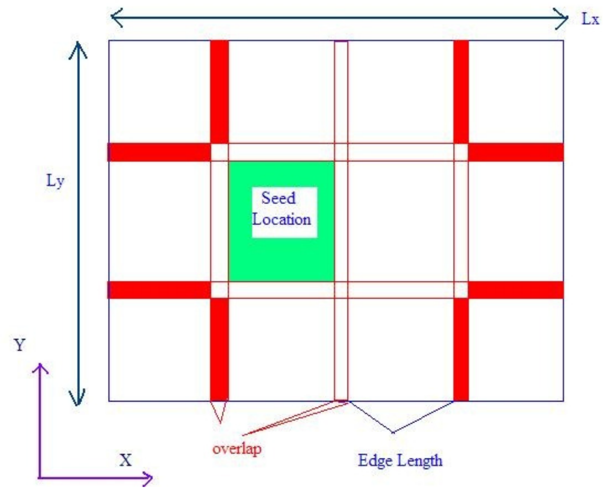

Figure 2- 3 A schematic of a zone grid in 2-D. The location of the zone center point (seed), the length of the zone in x and y coordinate system (Lx and Ly), the zone overlapping and the size of the zone (edge length) are shown.

Another factor is the geometry of the grid, especially in a 3-D case, which should be compatible with the physical geometry of the problem. The geometric size should be defined so that each subzone comprises at least a half wave length of the mechanical shear wave.

2.8 An Example Problem

Figure (2.5) shows the relationship between the number of iterations and the quality of the material property distribution image regarding the image contrast and the number of artifacts. The result illustrates that, as the number of iterations increases the image appears clearer and with fewer artifacts. The result demonstrates the real magnitude image and the shear modulus distribution of a cubic gelatin phantom which includes a stiffer cone shaped inclusion. For the inverse reconstruction, the subzone technique was used. The CG method along with TV regularization with $\alpha_{tv} = 1.d-6$ was utilized to regularize the problem.

The results below demonstrate the real magnitude image (Fig 2.4) and the shear modulus distribution (Fig. 2.5) for the CG technique after 20 iterations (Fig. 2.5, A), 30 iterations (Fig. 2.5, B), 40 iterations (Fig. 2.5, C) and 60 iterations (Fig. 2.5, D), respectively. The images show, as the number of iterations is increased from 20 to 40; the shear modulus reconstruction image demonstrates an obvious difference in the higher resolution of the images regarding the recovery of the material property and the physical shape of the inclusion with fewer artifacts in the background.

Although by raising the number of iterations from 40 to 60, the reconstruction images still illustrate a cleaner and better reconstruction result; however, this difference is small. This implies that there is an optimum number for the iteration sequences and as iterations reach this number, the image reconstruction quality increases dramatically, but after passing this number the quality remains constant. This fact helps to reduce the time and computational cost due to the number of iterations.

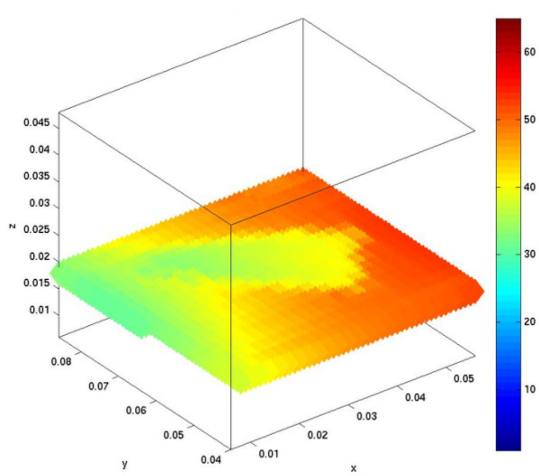

Figure 2- 4 The MR magnitude image obtained from MRE imaging is presented here. This picture shows a cubic gelatin phantom which includes one stiffer cone shaped inclusion.

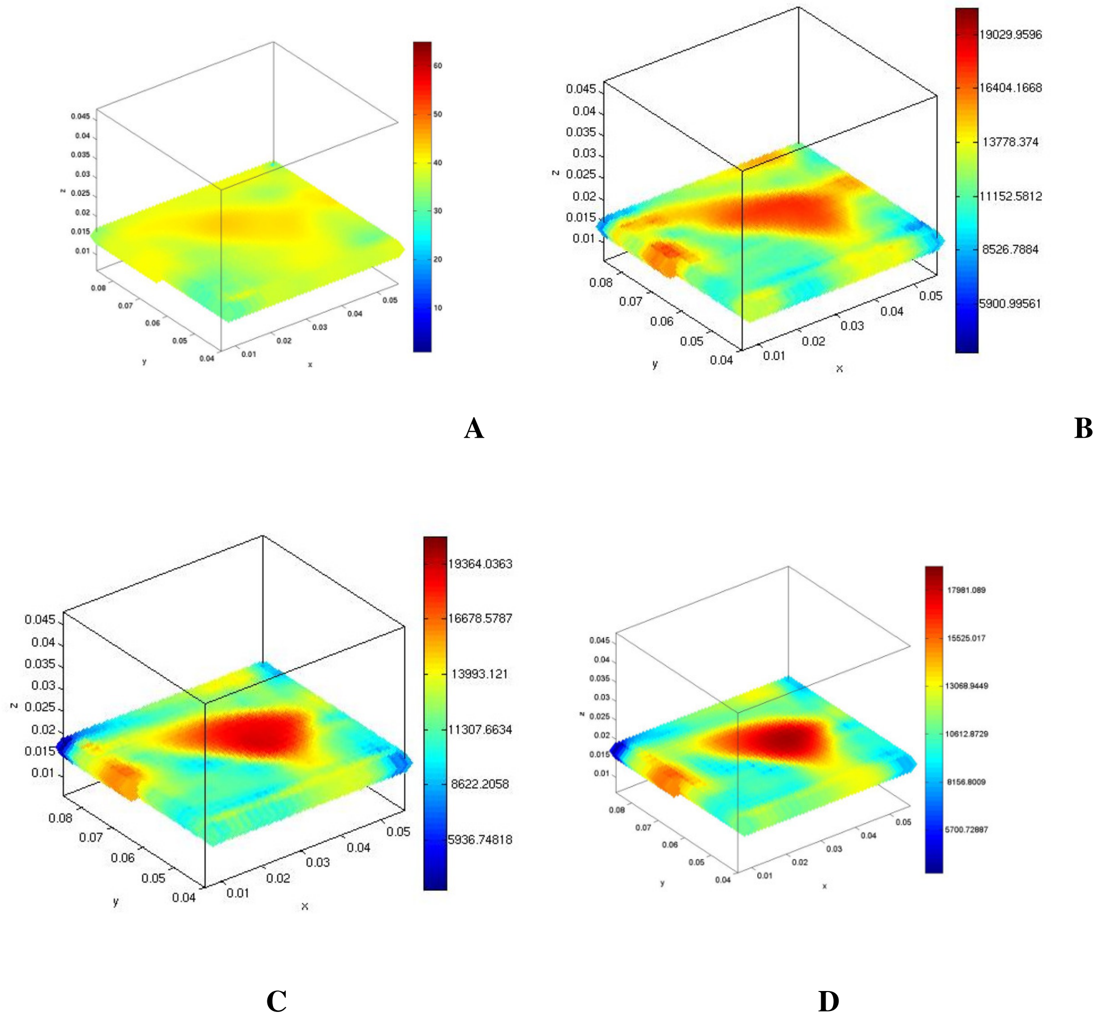

Figure 2- 5 These pictures show the shear modulus reconstructed image for a subsection of the two cone phantom. Images A, B, C and D demonstrate reconstructions for the CG method with the number of iterations 20, 30, 40 and 60, respectively. The images illustrate that, as the number of iterations increases from 20 to 40 the shear modulus reconstruction image demonstrates an obvious difference in the higher resolution of the images with low levels of artifacts in the background. Although by raising the number of iteration from 40 to 60, this reconstruction image still illustrates a cleaner and better reconstruction result; however, this difference is small.

"Never walk on the traveled path, because it only leads you where the others have been".
Graham Bell

Chapter 3

3.1 Anisotropic and Orthotropic Materials

Although elastographic imaging techniques have been introduced as powerful medical imaging modalities, most approaches consider isotropic material properties [116, 117, 118]. There is little quantitative information available in the MRE literature regarding the behavior of orthotropic materials and most anisotropic MRE reconstructions are in 2-D [119].

To study a more realistic behavior of tissue and cancerous tumors it is necessary to develop a 3-D model with actual geometry which includes sufficient details about orthotropic elasticity parameters. This chapter introduces the existing formulations for anisotropic and orthotropic material models.

In solid mechanics, there are some conditions related to equations of equilibrium which must be satisfied to solve a problem. These conditions are strain-displacement relations and material constitutive laws. The first condition does not require the material property parameters while the second one, which relates the stress to strain components at any point in the solid, is a function of elasticity modulus. Since the behavior of the real material is complex and difficult to comprehend, it is necessary to make assumptions and perform simplifications to make a mathematical model of the material's behavior by applying suitable theories and adequate experimental tests. This mathematical model can calculate a particular property to express the material behavior in a certain condition [123, 124].

In the most generalized anisotropic model, material symmetry does not exist and mechanical properties are different in all directions [125, 126]. In the condition that there are different degrees of material symmetries, the material can be categorized as, for example, orthotropic or isotropic and so on. In this chapter, certain elastic models based on the existence of elastic symmetry axes are considered. In these axes, known as elastic principal axes, the constitutive relations remain invariant.

3.2 Introduction to Anisotropic Materials

Anisotropy means the mechanical property of a material is directionally dependent. This can be expressed as a difference in a physical or mechanical property such as elasticity modulus, density, etc. In the chemical aspect, anisotropy is defined as phenomena of chemical bond strengths which are directionally dependent [127]. Fig 3.1 shows an example of two different molecular bonds which describe the difference in the mechanical behavior of a material in three directions [128].

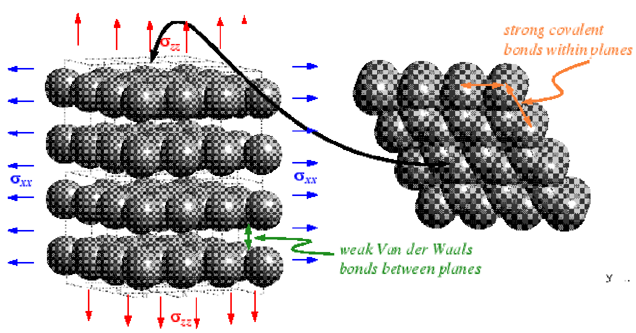

Figure 3- 1 This figure depicts the effect of applying a stress in two different directions in graphite. The elasticity properties will be anisotropic as the deformation depends on the direction of a particular stress [128].

Many biological materials, such as tissue, are anisotropic materials that display directionally variations in material properties. Inhomogeneous material property distributions can also be a pathological sign, as in the case of breast carcinomas. The discussion on tissue structures provides many micro-scale examples of mechanical behavior [120, 121].

Since most tissues are highly anisotropic and also incompressible it would be appropriate to learn more about how anisotropy influences the mechanical behavior of the tissue and tissue mimicking phantoms [122, 129].

3.3 Linear Anisotropic Elastic Solid

3.3.1 Theoretical Analysis of Anisotropic Materials

To study anisotropy it is essential to know the constitutive equation that describes the elastic behavior of the material and also determines the elasticity tensor, C_{ijkl} and its components. In the linear elasticity, the relationship between current stress and current strain remains linear. The constitutive equation which is the generalized form of Hooke's law can be written as:

$$\sigma_{ij} = C_{ijkl}\varepsilon_{kl} \tag{3.1}$$

where σ_{ij} and ε_{kl} are second order stress and strain tensors respectively, and C_{ijkl} is the fourth order elasticity or stiffness tensor. As stress is measured in units of pressure and strain is dimensionless, the entries of C_{ijkl} are also in units of pressure. The symmetric stress and strain tensors can be written as six-dimensional vectors in an orthonormal coordinate system (3.2). The anisotropic form of Hooke's law in matrix expression is shown in (3.3) in which C_{ijkl} is expressed as 6×6 symmetric matrix.

$$\{\sigma\} = \begin{Bmatrix} \sigma_{11} \\ \sigma_{22} \\ \sigma_{33} \\ \sigma_{23} \\ \sigma_{31} \\ \sigma_{12} \end{Bmatrix} = \begin{Bmatrix} \sigma_1 \\ \sigma_2 \\ \sigma_3 \\ \sigma_4 \\ \sigma_5 \\ \sigma_6 \end{Bmatrix} \quad \& \quad \{\varepsilon\} = \begin{Bmatrix} \varepsilon_{11} \\ \varepsilon_{22} \\ \varepsilon_{33} \\ 2\varepsilon_{23} \\ 2\varepsilon_{31} \\ 2\varepsilon_{12} \end{Bmatrix} = \begin{Bmatrix} \varepsilon_1 \\ \varepsilon_2 \\ \varepsilon_3 \\ \varepsilon_4 \\ \varepsilon_5 \\ \varepsilon_6 \end{Bmatrix} \tag{3.2}$$

$$\begin{Bmatrix} \sigma_1 \\ \sigma_2 \\ \sigma_3 \\ \sigma_4 \\ \sigma_5 \\ \sigma_6 \end{Bmatrix} = \begin{bmatrix} C_{11} & C_{12} & C_{13} & C_{14} & C_{15} & C_{16} \\ C_{21} & C_{22} & C_{23} & C_{24} & C_{25} & C_{26} \\ C_{31} & C_{32} & C_{33} & C_{34} & C_{35} & C_{36} \\ C_{41} & C_{42} & C_{43} & C_{44} & C_{45} & C_{46} \\ C_{51} & C_{52} & C_{53} & C_{54} & C_{55} & C_{56} \\ C_{61} & C_{62} & C_{63} & C_{64} & C_{65} & C_{66} \end{bmatrix} \begin{Bmatrix} \varepsilon_1 \\ \varepsilon_2 \\ \varepsilon_3 \\ \varepsilon_4 \\ \varepsilon_5 \\ \varepsilon_6 \end{Bmatrix} \qquad (3.3)$$

The generalized Hooke's law can be inverted to obtain a relation for the strain in terms of stress as:

$$\varepsilon_{ij} = S_{ijkl}\sigma_{kl} \qquad (3.4)$$

The tensor S_{ijkl} is called the compliance tensor. This relation is given by:

$$\begin{Bmatrix} \varepsilon_1 \\ \varepsilon_2 \\ \varepsilon_3 \\ \varepsilon_4 \\ \varepsilon_5 \\ \varepsilon_6 \end{Bmatrix} = \begin{bmatrix} S_{11} & S_{12} & S_{13} & S_{14} & S_{15} & S_{16} \\ S_{21} & S_{22} & S_{23} & S_{24} & S_{25} & S_{26} \\ S_{31} & S_{32} & S_{33} & S_{34} & S_{35} & S_{36} \\ S_{41} & S_{42} & S_{43} & S_{44} & S_{45} & S_{46} \\ S_{51} & S_{52} & S_{53} & S_{54} & S_{55} & S_{56} \\ S_{61} & S_{62} & S_{63} & S_{64} & S_{65} & S_{66} \end{bmatrix} \begin{Bmatrix} \sigma_1 \\ \sigma_2 \\ \sigma_3 \\ \sigma_4 \\ \sigma_5 \\ \sigma_6 \end{Bmatrix} \qquad (3.5)$$

where ε_i and σ_i are axial strains and stresses, respectively [130, 131].

3 .3.2 Elastic symmetry

A material has symmetry if its elastic properties are the same in certain directions. If symmetry exists in all directions, the material is called isotropic otherwise, it is anisotropic. In general, C_{ijkl} contains 81 constants, but since both stress and strain tensors are symmetrical ($\sigma_{ij} = \sigma_{ji}$ and $\varepsilon_{kl} = \varepsilon_{lk}$), and with the assumption that there exists a strain energy function U given by:

$$U = 1/2 C_{ijkl} \varepsilon_{ij} \varepsilon_{kl} \quad (3.6)$$

where, $$\sigma_{ij} = C_{ijkl} \varepsilon_{kl} = \frac{\partial U}{\partial \varepsilon_{ij}} \Rightarrow \frac{\partial^2 U}{\partial \varepsilon_{ij} \partial \varepsilon_{kl}} = C_{ijkl} \quad (3.7)$$

It is seen that the stiffness tensor must be symmetrical so that $C_{ijkl} = C_{klij}$ because of the arbitrary order of differentiation ε_{ij} and ε_{kl}. As a result, the number of elastic constants can be reduced to 21 coefficients [130, 131].

According to Love [132], Chen and Saleeb [133], the equations that govern engineering problems are related to the stored energy in a solid. Therefore, the energy developed by the external work is stored in an elastic solid and may be developed as potential elastic energy that is known as strain energy.

During this process the body is deformed, but may recover its original shape and size. An interesting point is that the presence of certain types of symmetry in an elastic body, simplify the constitutive relations. These simplifications are represented in different ways, for example those applied by Love, where the strain energy function remains unchangeable by all symmetrical coordinate system substitutions.

For instance, a corresponding substitution given by three axes of elastic symmetry, $x_i' = -x_i$ with i = 1, 2, 3, does not change U_o. In this thesis, the reduced indices form of constitutive and compliance equations are used, for example C_{ijkl} is expressed as C_{ij}.

The linear transformation of a material with elastic symmetry can be expressed as $x_i' = \ell_{ij} x_j$, where ℓ_{ij} is the transformation tensor. This requires that the constitutive tensor, either C_{rspq} or S_{rspq}, can be transformed in the following condition as (3.8), see [130, 132, 133, 134, 135].

$$C'_{rspq} = \ell_{ri} \ell_{sj} \ell_{pk} \ell_{ql} C_{ijkl} \quad (3.8)$$

3.2.1 Material Classifications by Their Elastic Symmetrical Planes

While an anisotropic or triclinic material has no plane of symmetry, there are four cases of elastic symmetry that are considered most important. These materials are categorized as:

- *Monoclinic* with one plane of elastic symmetry

- *Orthotropic* with three planes of elastic symmetry

-*Transversely isotropic* with a plane of isotropy such that every plane perpendicular to it is a plane of symmetry and

- *Isotropic* every plane is a plane of symmetry [130].

As the biological materials such as tissue and also tissue mimicking phantoms with their internal structures reveal an orthotropic pattern, so the goal of this thesis is to introduce an orthotropic model and then obtain the elastic constitutive tensor parameters.

3.4 Orthotropic Elastic Theory

Orthotropic elastic theory is defined as the behavior of elastic materials which locally exhibit three orthogonal planes of material symmetry and three corresponding orthogonal axes known as orthotropic axes.

Mechanical properties of the material are identical within these three planes. Material properties in an orthotropic material are independent in three orthogonal directions at every point and the elastic coefficients C_{ij} remain invariant at a point under rotation of 180° about any of the orthotropic axes. For example, assume $(x,\ y,\ z)$ are the orthotropic axes for an orthotropic material and $(x,\ y)$ is a plane of material symmetry.

By coordinate transformation $x \rightarrow x$, $y \rightarrow y$ and $z \rightarrow -z$, known as a reflection with respect to the (x, y) plane, the elastic parameters C_{ij} remain constant. See direction cosines for this transformation [130, 138]. As an orthotropic material has three mutually orthogonal planes of material symmetry, the 21 unknown elasticity constants of an anisotropic model can therefore be decreased to 12 elasticity coefficients in compliance equations given by:

$$\begin{Bmatrix} \varepsilon_1 \\ \varepsilon_2 \\ \varepsilon_3 \\ \gamma_4 \\ \gamma_5 \\ \gamma_6 \end{Bmatrix} = \begin{bmatrix} S_{11} & S_{12} & S_{13} & 0 & 0 & 0 \\ S_{21} & S_{22} & S_{23} & 0 & 0 & 0 \\ S_{31} & S_{32} & S_{33} & 0 & 0 & 0 \\ 0 & 0 & 0 & S_{44} & 0 & 0 \\ 0 & 0 & 0 & 0 & S_{55} & 0 \\ 0 & 0 & 0 & 0 & 0 & S_{66} \end{bmatrix} \begin{Bmatrix} \sigma_1 \\ \sigma_2 \\ \sigma_3 \\ \tau_4 \\ \tau_5 \\ \tau_6 \end{Bmatrix} \tag{3.9}$$

where ε_i and σ_i are normal strains and stresses respectively, τ_i shear stresses and γ_i shear strains. The compliance equation expansion for an orthotropic material model is also expressed as:

$$\varepsilon_1 = S_{11}\sigma_1 + S_{12}\sigma_2 + S_{13}\sigma_3 \tag{3.10}$$

$$\varepsilon_2 = S_{12}\sigma_1 + S_{22}\sigma_2 + S_{23}\sigma_3 \tag{3.11}$$

$$\varepsilon_3 = S_{13}\sigma_1 + S_{23}\sigma_2 + S_{33}\sigma_3 \tag{3.12}$$

$$\gamma_{12} = S_{44}\tau_{12} \tag{3.13}$$

$$\gamma_{23} = S_{55}\tau_{23} \tag{3.14}$$

$$\gamma_{31} = S_{66}\tau_{31} \tag{3.15}$$

The equation (3.9) can be rewritten in matrix form in terms of standard engineering constants, Young's modulus E_i, Poisson's ratio υ_{ij}, and shear modulus μ_i as:

$$\begin{Bmatrix} \varepsilon_1 \\ \varepsilon_2 \\ \varepsilon_3 \\ \gamma_4 \\ \gamma_5 \\ \gamma_6 \end{Bmatrix} = \begin{bmatrix} \frac{1}{E_1} & -\frac{\nu_{21}}{E_2} & -\frac{\nu_{31}}{E_3} & 0 & 0 & 0 \\ -\frac{\nu_{12}}{E_1} & \frac{1}{E_2} & -\frac{\nu_{32}}{E_3} & 0 & 0 & 0 \\ -\frac{\nu_{13}}{E_1} & -\frac{\nu_{23}}{E_2} & \frac{1}{E_3} & 0 & 0 & 0 \\ 0 & 0 & 0 & \frac{1}{\mu_4} & 0 & 0 \\ 0 & 0 & 0 & 0 & \frac{1}{\mu_5} & 0 \\ 0 & 0 & 0 & 0 & 0 & \frac{1}{\mu_6} \end{bmatrix} \begin{Bmatrix} \sigma_1 \\ \sigma_2 \\ \sigma_3 \\ \tau_4 \\ \tau_5 \\ \tau_6 \end{Bmatrix} \tag{3.16}$$

The equation (3.16) can be expanded as:

$$\varepsilon_1 = \frac{1}{E_1}\sigma_1 - \frac{\nu_{21}}{E_2}\sigma_2 - \frac{\nu_{31}}{E_3}\sigma_3 \tag{3.17}$$

$$\varepsilon_2 = -\frac{\nu_{12}}{E_1}\sigma_1 + \frac{1}{E_2}\sigma_2 - \frac{\nu_{32}}{E_3}\sigma_3 \tag{3.18}$$

$$\varepsilon_3 = -\frac{\nu_{13}}{E_1}\sigma_1 - \frac{\nu_{23}}{E_2}\sigma_2 + \frac{1}{E_3}\sigma_3 \tag{3.19}$$

$$\gamma_{12} = \frac{1}{\mu_4}\tau_{12} \tag{3.20}$$

$$\gamma_{23} = \frac{1}{\mu_5}\tau_{23} \tag{3.21}$$

$$\gamma_{31} = \frac{1}{\mu_6}\tau_{31} \tag{3.22}$$

These equations describe an orthotropic material model which deals with 12 unknown elastic parameters, E_i, υ_{ij}, and μ_i in three dimensions [139, 140]. These equations also show shear strains are generated by three independent shear moduli corresponding to these independent shear stresses. These direct and independent relationships between shear strains and stresses in the three directions provide a simple way to calculate the shear modulus within the orthotropic material, as compared to an anisotropic model which is more complicated and requires more coefficients to describe shear behavior [136, 137].

Another important comment from the above equations is that the Poisson's ratio of an orthotropic material is different in each direction. At this point, there are six equations with 12 unknowns, six υ_{ij}, three E_i and three μ_i. However, by considering the symmetry of the stress and strain tensors implies $S_{12} = S_{21}$, $S_{13} = S_{31}$ and $S_{23} = S_{32}$ which all the six Poisson's ratios in the equation are not independent. Therefore, the equation (3.16) can be further simplified and the number of elasticity parameters is reduced to 9 independent constants, three E_i, three υ_{ij}, and three μ_i. By introducing three new equations the remaining three Poisson's ratios can be found from the relations

$$\frac{\upsilon_{12}}{E_1} = \frac{\upsilon_{21}}{E_2} \tag{3.23}$$

$$\frac{\upsilon_{13}}{E_1} = \frac{\upsilon_{31}}{E_3} \tag{3.24}$$

$$\frac{\upsilon_{23}}{E_2} = \frac{\upsilon_{32}}{E_3} \tag{3.25}$$

The score is now nine equations (from Eq. 3-17 to Eq. 3-25) and nine unknowns (three E_i, three υ_{ij}, and three μ_i).

3.5 Incompressible Orthotropic Materials

3.5.1 Isotropic Incompressibility

Strain components of the equilibrium equations relating axial stress and strain, for a compressible, linear elastic, isotropic material are expressed as:

$$\varepsilon_1 = \frac{1}{E}(\sigma_1 - \upsilon(\sigma_2 + \sigma_3) \quad (3.26)$$

$$\varepsilon_2 = \frac{1}{E}(\sigma_2 - \upsilon(\sigma_1 + \sigma_3) \quad (3.27)$$

$$\varepsilon_3 = \frac{1}{E}(\sigma_3 - \upsilon(\sigma_1 + \sigma_2) \quad (3.28)$$

By assuming small strains, the volumetric strain, *e*, of an elastic solid is given by:

$$e = \frac{\Delta V}{V_0} = \varepsilon_1 + \varepsilon_2 + \varepsilon_3 \quad (3.29)$$

where ΔV is the change in total volume, V_0 the original volume, and ε_i are the axial strains in the *i* direction.

In an isotropic material by applying the stress in only one direction, three strain components ε_i can be easily found. For example, if an axial stress in the x direction, σ_x applies, the equation (3.29) becomes the following:

$$e = \frac{\sigma_1}{E}(1 - 2\upsilon) \quad (3.30)$$

By definition, incompressible materials are known as materials without any change in volume subjected to tensile or compressive strains [141, 142, 143, 144, 145].

This implies that in an incompressible material $e \to 0$ as, $\upsilon \to 0.5$. This can also be shown by setting equation (3.30) equal to zero and solving for υ which gives $\upsilon = 0.5$ [146, 147].

3.5.2 Orthotropic Incompressibility

One necessary point for an elastographic study of soft tissue and tissue mimicking phantoms is obtaining a suitable formulation for the incompressible or nearly incompressible orthotropic models. In an incompressible orthotropic material, however the relation between stress and strain is more complicated and this is discussed below [148].

Recall (3.29)

$$e = \frac{\Delta V}{V_0} = \varepsilon_1 + \varepsilon_2 + \varepsilon_3 = (S_{11} + S_{12} + S_{13})\sigma_1 + (S_{12} + S_{22} + S_{23})\sigma_2 + (S_{13} + S_{23} + S_{33})\sigma_3 = 0 \tag{3.31}$$

This implies:

$$(S_{11} + S_{12} + S_{13}) = (S_{12} + S_{22} + S_{23}) = (S_{13} + S_{23} + S_{33}) = 0 \tag{3.32}$$

which leads to:

$$S_{11} = -(S_{12} + S_{13}) \xrightarrow{\mathrm{Re}\,call(3-9)} \upsilon_{12} + \upsilon_{13} = 1 \tag{3.33}$$

$$S_{22} = -(S_{12} + S_{23}) \xrightarrow{\mathrm{Re}\,call(3-9)} \upsilon_{21} + \upsilon_{23} = 1 \tag{3.34}$$

$$S_{33} = -(S_{32} + S_{31}) \xrightarrow{\mathrm{Re}\,call(3-9)} \upsilon_{31} + \upsilon_{32} = 1 \tag{3.35}$$

For instance, applying σ_1 gives the following equations for each of the strain components:

$$\varepsilon_1 = \frac{\sigma_1}{E_1} \tag{3.36}$$

$$\varepsilon_2 = \frac{-\sigma_1 \upsilon_{21}}{E_2} \tag{3.37}$$

$$\varepsilon_3 = \frac{-\sigma_1 \upsilon_{31}}{E_3} \tag{3.38}$$

By substituting equations (3.36), (3.37) and (3.38) into (3.31) and setting the resulting equation equal to zero gives:

$$\frac{1}{E_1} - \frac{\upsilon_{21}}{E_2} - \frac{\upsilon_{31}}{E_3} = 0 \tag{3.39}$$

By considering equation (3.39), for other two stress components, σ_2 and σ_3 the resulting equations give the following relations:

$$\frac{1}{E_2} - \frac{\upsilon_{12}}{E_1} - \frac{\upsilon_{32}}{E_3} = 0 \tag{3.40}$$

$$\frac{1}{E_3} - \frac{\upsilon_{13}}{E_1} - \frac{\upsilon_{23}}{E_2} = 0 \tag{3.41}$$

Adding equations (3.39), (3.40) and (3.41) together leads again to equations (3.33), (3.34) and (3.35). By using the equations mentioned above, the following Poisson's ratio relationships can be obtained as:

$$\upsilon_{12} = \frac{E_1}{2}\left[\frac{1}{E_2} - \frac{1}{E_3} + 1\right] \tag{3.42}$$

$$\upsilon_{23} = \frac{E_2}{2}\left[\frac{1}{E_3} - \frac{1}{E_1} + 1\right] \quad (3.43)$$

$$\upsilon_{31} = \frac{E_3}{2}\left[\frac{1}{E_1} - \frac{1}{E_2} + 1\right] \quad (3.44)$$

This implies that with only six independent coefficients, the incompressible or nearly incompressible orthotropic elastic behavior of materials can be described. These parameters are: E_i (E_1, E_2 and E_3), in the three directions; and μ_j (μ_4, μ_5 and μ_6), within each of the three coordinate planes [149, 150].

3.6 Orthotropic Elastography

To date, most elastographic imaging techniques considered isotropic material properties in their elasticity image reconstructions [151]. The fact that most biological tissues tend to have some anisotropic qualities [120, 121, 122], there is a need to improve elastographic imaging techniques towards anisotropic image reconstructions.

Sinkus *et al*. [129] developed equations for MRE reconstruction in 2005, considering transverse isotropy for tissues. In this section, a general framework is proposed for 3-D orthotropic incompressible elastography. By orthotropic incompressible elastography, the structure properties and fiber orientations within the tissue or tissue mimicking phantoms can be detected by only six independent elasticity parameters in three dimensions.

This research uses the computational algorithm implemented for the complex orthotropic behavior which is based on MRE image modality. This approach also investigates the capability and performance of this imaging technique based on these advanced material models.

3.7 Remarks of the Orthotropic Incompressibility Applied to MRE

3.7.1 Geometry and Phantoms

In this research, several tissue mimicking gelatin phantoms were used to show the orthotropic incompressibility behavior. Experience obtained from phantom studies has shown that the average magnitude of motion gradient for the Young's modulus terms, E_1, E_2 and E_3, is several orders smaller than the corresponding sensitivities for the shear modulus terms, μ_4, μ_5 and μ_6. Therefore, in this research, the initial study was the reconstruction of the orthotropic shear properties of a tissue mimicking phantom made with a pineapple inclusion. The reason to use pineapple was that the pineapple's different fiber orientations can be a good example of an orthotropic incompressible material. The phantom making protocol, shear modulus reconstruction results and analysis will be explained in the following chapters.

3.7.2 Algorithms

The reconstruction of the orthotropic incompressible properties performed for this study was optimization based, minimizing a displacement error function quantifying difference between the calculated and observed displacements by evaluating the sensitivities of this function with respect to the six independent elastic properties being imaged.

Recall 2.4.2.9

$$u^c = f(\eta) \tag{3.45}$$

$$\Psi = \left\| u^m - u^c \right\|^2 = \left\| u^m - f(\eta) \right\|^2 \tag{3.46}$$

$$\frac{\partial \Psi}{\partial \eta} = -2\left(\frac{\partial f(\eta)}{\partial \eta}\right)^T (u^m - f(\eta)) = 0 \tag{3.47}$$

Here $\eta = E_1,\ E_2,\ E_3,\ \mu_4,\ \mu_5,\ \mu_6$ are the six independent elastic properties for incompressible orthotropic material. The adjoint method was used to calculate the gradient of the displacement error function with respect to the six elastic moduli. This technique increases the numerical efficiency significantly. In this investigation, the finite difference (FD) technique was used to numerically estimate the motion sensitivity with respect to the elastic properties for orthotropic incompressible elastography reconstruction, so that:

$$\frac{\partial \Psi}{\partial \eta_{i\,FD}} \approx \frac{\Psi(\eta + \Delta\eta_i) - \Psi(\eta)}{\Delta\eta_i} \tag{3.48}$$

and

$$\frac{\partial f(\eta)}{\partial \eta_{i\,FD}} \approx \frac{f(\eta + \Delta\eta_i) - f(\eta)}{\Delta\eta_i} \tag{3.49}$$

These FD calculations should be checked for correctness by verifying (3.50) for a reasonable numerical accuracy. This implies:

$$\frac{\partial \Psi}{\partial \eta_{FD}} = -2\left(\frac{\partial f(\eta)}{\partial \eta_{FD}}\right)^T (u^m - f(\eta)) \tag{3.50}$$

The method used in the reconstruction of the orthotropic shear properties optimization approach was based on the CG method and TV regularization technique.

3.7. 3 Multiple Sets of Measurements

As explained in the chapter 2, in MRE, material properties are reconstructed by using measured displacements. Research has shown that the material property in an isotropic case can be uniquely obtained in 2-D [152]. However, in anisotropic case, the situation is different and the elastic parameters cannot be uniquely determined in 2-D by one set of Drichilet boundary conditions [153].

The anisotropic inverse problem is non-unique in nature and one set of displacement measurement (Drichilet boundary condition) may not provide sufficient information for uniquely identify material properties in 3-D [154, 155].

To obtain a unique C_{ij} in the orthotropic case, it is important to make sure that the measurements carry enough information. Therefore, to avoid non-uniqueness problem, multiple sets of displacement measurements are essential. Investigations have shown the feasibility of using multiple displacement fields for transversely isotropic analysis [156].

In this thesis, multiple displacement measurement sets were taken in 3-D, based on the available experimental techniques. This provides sufficient information for the boundary conditions to avoid the ambiguity due to non-uniqueness problems, which can be found in any orthotropic inverse problem.

"Discovery is the ability to be puzzled by simple things". Noam Chomsky

Chapter 4

4.1 Phantom Studies

Before each new medical technique can be used *in vivo*, it is necessary to check it *in vitro*. As orthotropic elastography is a novel approach to quantitatively measure the soft tissue elasticity properties, the capability of this method needs to be verified by phantom studies to avoid any uncertainty about the factors which may affect the quantitative measurements.

For this reason, several orthotropic and isotropic phantoms were developed for the acquisition of orthotropic and isotropic datasets to map the material properties in 3-D.

Experiments in orthotropic phantom manufacturing with tissue-mimicking gelatin and muscle along with orthotropic reconstructions will be explained in the next chapters.

In this chapter, the focus is on isotropic phantoms which were designed for isotropic elasticity reconstructive imaging. This chapter presents the experiments with tissue-like silicone and gelatin phantoms and comprises:

- MRE actuation systems and remarks
- Isotropic phantoms manufacturing protocol and remarks
- Isotropic image reconstructions
- MRE artifacts

4.2 MRE Actuation Systems

In dynamic MRE, the mechanical excitation is an external mechanical load applied to the tissue or the phantom under investigation to generate time- harmonic shear waves which propagate through the sample. This excitation is usually produced by actuators coupled to the phantom or tissue. As actuating systems are used for each MRE dataset acquisition, it is essential to explain the mechanisms and phantom set up sufficiently.

Different coils are utilized to receive the displacement pattern signals of the actuation systems. Choosing these coils relates to the condition of the tests and in this investigation, the head, breast, and the surface coil were used. There are two types of actuators to induce harmonic motion in a specimen: electromechanical actuators known as pneumatic actuators and piezoelectric actuators. The research presented in this thesis involves data acquisition using both actuators as explained below.

4.2.1 Pneumatic Actuator

Fig. 4.1 shows a schematic of the pneumatic actuator setup for MRE testing. As shown the speaker drives air propagated in the coupled tube attached to the actuator. This air propagation vibrates the membrane of the actuator that provides the mechanical excitation to create shear waves within the phantom.

The phantom is located on the membrane which has covered the actuator top. The speaker can generate the cyclic force at a frequency between 50 and 1000 Hz. Displacements obtained from this system are in the order of hundreds of microns.

Figure 4.1 depicts a pneumatic actuator system with the phantom excitation due to the actuator oscillating as being in the X direction of the MRI scan coordinate system. To obtain a complete description of the material behavior in all three dimensions for orthotropic materials, multiple actuations in three directions is desired.

However, the system shown in Fig. 4.1 is unable to produce harmonic motion in multiple directions and to generate multiple excitation directions, the sample needs to be flipped 90^0. Figure 4.2 represents the voice actuator set up which has been supported by pads and sand bags to prevent the undesirable movement during the vibration. The position of the phantom and the surface coils are also shown.

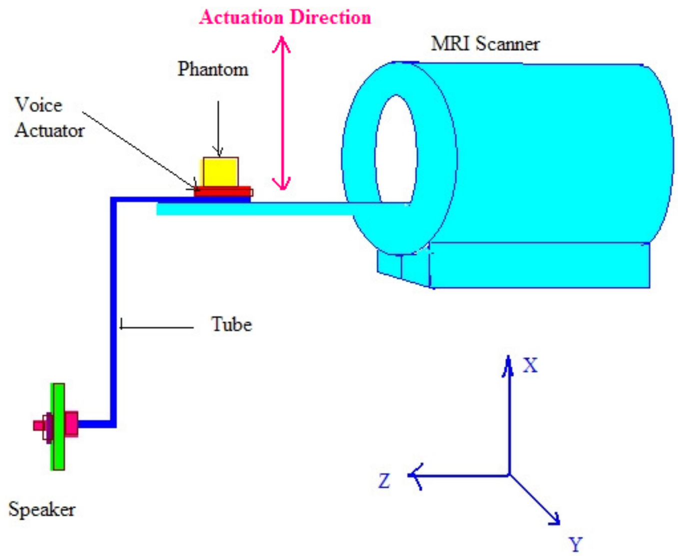

Figure 4- 1 The configuration of the Pneumatic (voice) actuating system setup. The actuation direction for this actuation system is shown along the X direction of the Cartesian coordinate system.

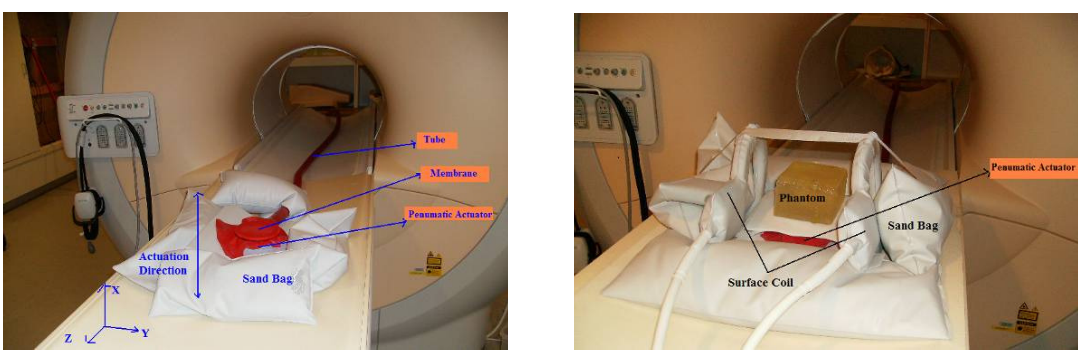

A **B**

Figure 4- 2 The experimental setup of the pneumatic actuating system. The geometry configuration regarding the actuation direction with respect to the MRI scan coordinate system (A) and the assembled apparatus with the location of the surface coils, phantom and sand bags (B) are illustrated.

4.2.2 Piezoelectric Actuators

The piezoelectric effect means that an electric charge is generated when the material is pressed or stretched. Also an applied electric field will cause a change in the dimensions of the piece of piezoelectric material [157].

Recently, piezoelectric actuation systems have been commonly used in MRE imaging to actuate the tissue or different kinds of phantom. One of the advantages of these actuators is the freedom to orient the system in any direction within the MRI scanner. In piezoelectric actuators, the axis of the piezoelectric stack represents the motion direction [158].

Different types of piezoelectric actuation systems can be classified based on their geometry and method of contact with the phantom or tissue. Three piezoelectric actuation mechanisms have been used to provide the MRE datasets described in this approach which are referred as "Type-A", "Type-B", and "Type-C". These are introduced in the following section.

4.2.2.1 Type -A

In the Type-A actuator, the gelatin phantom is built in a cubic Perspex box which is coupled to a piezoelectric actuator (P-842K022, Physic Instrument, GmbH Co. KG). The actuator has been built almost entirely from Perspex. The actuator geometry setup included three cylindrical inclusions phantom and a heavy Perspex base to prevent the actuator movement during the MRI scanning and is presented in (Fig. 4.3).

As Fig. 4.3 shows the excitation direction in this type of actuator is in the Z direction of the MRI scan coordinate system. The potential for MR artifacts was minimized by applying a distance between the actuator and the phantom being imaged. Teflon pads were also used between the phantom box and the base. For image acquisition, the actuator device was located in the head coil of the scanner. This type of actuator has been detailed by Flewellen *et al.* [159].

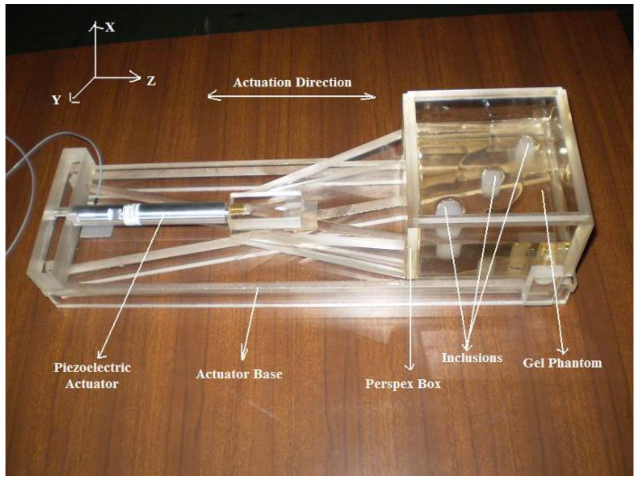

Figure 4- 3 This image depicts the assembled apparatus of a Type-A piezoelectric actuation system. The gel phantom which included three cylindrical inclusions inside the Perspex box is shown. (Images courtesy of James Flewellen)

4.2.2.2 Type-B (Lever Shaker)

The Type-B actuator is also another excitation mechanism which is applied for phantom tests and clinical tissue imaging. The geometry of the Type-B actuator, which is also known as a lever shaker, comprises a piezoelectric actuator, a motion amplifying lever arm, and a shaker-plate. The motion amplifier increases the maximum displacement achieved by the shaker plate. The piezoelectric stack is used as the actuation source.

The rectangular shaker-plate is designed to hold the samples. The excitation direction is aligned in the Y direction of the MRI coordinate system. This actuator was explained in detail by Perrinez *et al.* [158]. The phantom-actuator apparatus is performed in (Fig. 4.4).

4.2.2.3 Type-C Actuator

The Type-C actuator is an advanced generation of the piezoelectric actuators with two vertical piezoelectric bars which are located at the bottom, in front of the contact surface. A large pad is applied to stablize the other side of the plate. The driven force supplied by two actuators provides more strength to excite the phantom.

The piezoelectric bars are located inside two rectangular Perspex legs. Two thin rubber mats (red) are used underneath the legs to prevent the movement of the actuation system during the scanning. Fig. 4.5 represents the geometry of this piezoelectric prototype with a phantom on the contact plate top. As this picture shows the direction of the actuation system is in the X direction of the MRI scan coordinate system.

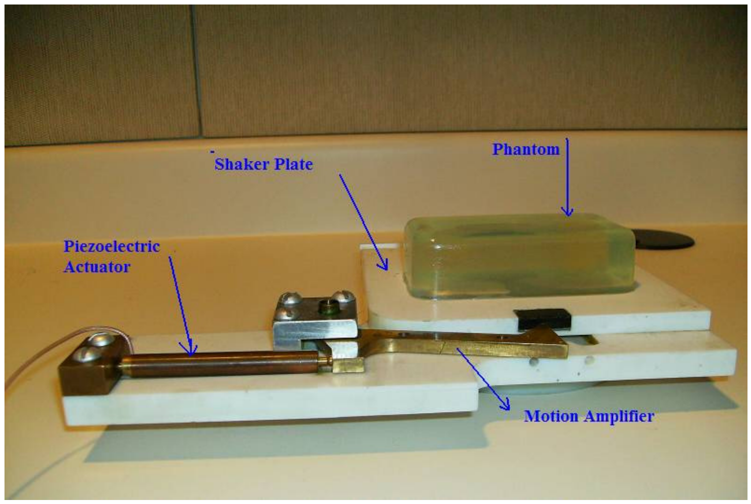

A

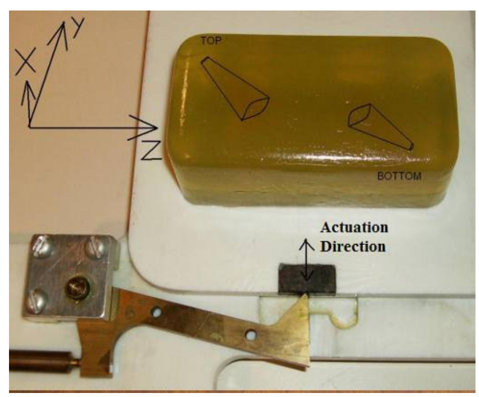

B **C**

Figure 4- 4 This image shows three views of the Type-B piezoelectric actuation system with a gel phantom on the plate surface which includes two cone shaped inclusions. The actuator geometry (A), the phantom-actuation system inside the breast coil (B), and the coordinate system alignment with a small arrow in the bottom of the picture which shows the actuation direction (C) as illustrated. (Images courtesy of MRE group, Dartmouth College).

4.2.3 MRE Actuation System Remarks

1. Although piezoelectric actuators provide relatively large displacements with respect to the thickness of the phantom, the absolute displacement achieved is small (tens of microns) compared to the pneumatic actuator (hundreds of microns). Experience has shown the datasets obtained from the pneumatic actuator involve stronger amplitudes motion signals in comparison to piezoelectric actuators.

2. In the MR scan, the actuation system should be supported by some sand bags to prevent undesirable movements which cause artifacts in the final image.

3. The receiver coil should be very close to the actuation system and even attached to the phantom to obtain a stronger motion signal throughout the phantom.

4. The phantom movement while it is being excited by an actuation mechanism should not be highly constrained as this reduces the level of motion magnitude within the phantom which may causes artifacts.

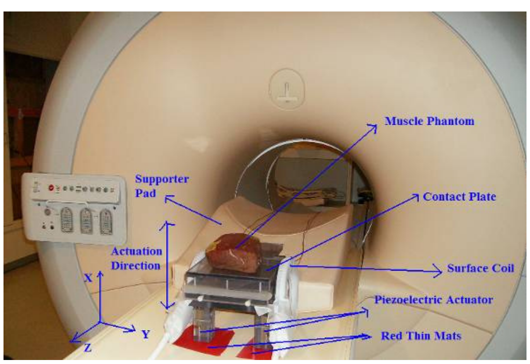

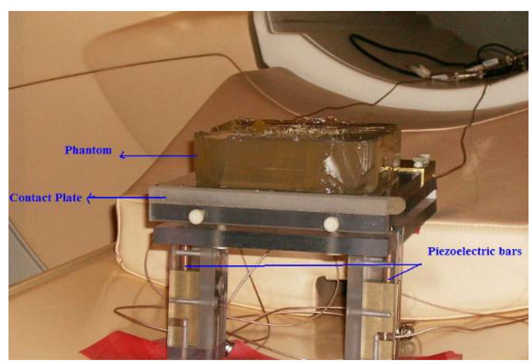

A **B**

Figure 4- 5 This picture depicts two views of the Type-C actuator. The actuator geometry setup, the coordinate system of the MRI scan, along with the actuation direction (A), and the actuation-phantom setup with a closer view (B) are presented.

5. Another artifact that can happen during the data acquisition is the motion artifact. This artifact comes from the movement of the actuation system on the MRI table while the phantom is being imaged which causes the blurring of the image. The motion artifact can come from the MRI table vibration as well. To reduce this artifact, the coil and actuation-phantom set up on the MRI table should be immobilized by using some sand bags. Applying some pads between the actuation mechanism and the MRI table is another way to prevent the MRI table vibration transferring to the system. Actuation system stabilization is a very important point to reduce the MRE artifacts.

6. Phantom location should also be considered during MRE data acquisition. Usually the best place to locate the phantom actuation set up is in the iso-centre of the magnetic bore. Experience has shown that placing the phantom-actuation system far from this point causes image distortion.

4.3 Isotropic Phantoms

Isotropic phantoms are usually developed for the acquisition of datasets to examine the efficiency of developed codes in order to map the mechanical properties of the imaged phantoms. Additionally, to validate the elasticity reconstruction results obtained from an orthotropic phantom, the isotropic phantom can be considered as a reference for comparison.

In this investigation one isotropic silicone phantom with a wedge inclusion was made and also the obtained datasets of another isotropic silicone phantom, which comprised three cylindrical inclusions, were used for the mechanical properties image reconstructions.

The procedure of the wedge inclusion phantom fabrication and the image reconstruction results obtained from the three cylindrical silicone phantom, are explained in this section.
The geometry of the isotropic phantoms was 10cm × 10cm × 10cm in volume.

These phantoms were designed for the Type-A actuator, thus they followed the geometry of the phantom cuboids Perspex box. As a result the phantom was restricted on five sides because of the phantom box walls.

4.4.1 Isotropic Phantom Manufacturing

4.4.1.1 Silicone Gel Phantom in General

Silicone gel is a rubber-like hydrophobic polymer which is being widely used in many industries such as medical research, cosmetics, breast implants, and so on [160, 161]. Research has shown that silicone can be a suitable material for elastography testing as it can mimic the mechanical properties of soft tissues [162]. This material has several advantages which make this material desirable for MRE testing. These are:

1. It can be easily molded and set into a wide variety of geometries.
2. The material is not poisonous.
3. Its physical and mechanical properties remain unchanged over the time.
4. It does not require heat for the fabrication procedure.

4.4.1.2 Wedge Shaped Inclusion Silicone Phantom

An isotropic wedge shaped inclusion silicone phantom was made during this project. This phantom was initially manufactured for MRE testing and comprised a soft background and a hard inclusion. This phantom was required to test the resolution limitations of the MRE setup.

4.4.1.3 Material and Methods

The silicone gel phantom was made in several stages. Two types of silicone gel were used to fabricate the soft base and the wedge shaped inclusion of the silicone phantom: 'soft gel' which is called 'A-341' and 'hard gel' known as 'LSR-05' made by 'Factor II, Inc., Lakeside, AZ'. The silicone gel, whether 'soft' or 'hard', has a 'hardner' which is applied to catalyze the gel. The 'soft' and 'hard' gels are called part A and their 'hardners' are known as part B. The ratio of the gel to its 'hardner' is 10 to one.

The silicone mass was found by calculating the volume of the phantom box and considering the density of the water as an estimation for the silicone gel density. This mass was weighed by an electronic scale. Before pouring the silicone liquid, all of the internal surfaces of the phantom box were lubricated by silicone spray (Silicone Star', Sta-Lube, East Tamaki, NZ). This lubricating helps to remove the phantom from its box after setting.

To make this phantom, first 270g soft silicone gel was added to the 27g of hardner and then it was prepared as the background. After the de-gassing of this mixture, it was used to fill one third of the phantom box to make the base of the phantom. The sample was then allowed to set for six hours in the room temperature. In this test, a Venturi vacuum was used to de-gas the phantom after each step of pouring the mixture.

To obtain the MRI datasets from the phantom precisely, a coordinate system should be considered for the phantom. This helps to identify the phantom orientation while it is being imaged. For this purpose four liver oil capsules were chosen as markers and then placed on the corners of the phantom box. Two of these markers were stuck on each other to represent direction Z. One marker was located in one corner of the phantom box to illustrate the X direction and the other one was arranged in the middle of one side to show direction Y. These markers can be seen as three bright spots during the MRI scanning.

The next step was creating a rectangular hole on top of the base. This hole was made by placing lubricated cubic plastic block on the base and surrounding it with more soft silicone gel. After the silicone was set the cube was removed.

In the next phase of this test, 10g hard silicone gel added to 1g of hardner and after mixing and de-gassing, it was poured inside the rectangular hole. In order to make the 'hard' silicone gel more visible some drops of colorant ('FI-200, white', Factor II, Inc., Lakeside, AZ) were used. One half of this rectangular hole was filled with this material.

To make the ramp shape for the inclusion, one side of the phantom box was located at an angle with respect to the floor (Fig. 4.6). After setting the hard silicone gel (ramp shaped inclusion), the phantom was filled with the same soft silicone gel which was made for the base and then the phantom was left to set overnight.

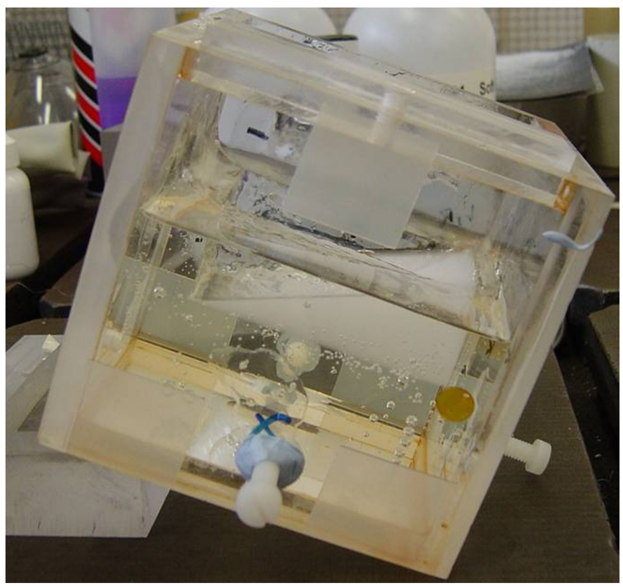

Figure 4- 6 An angle was applied to the phantom box to create the wedge shaped inclusion.

Unfortunately, after setting the phantom some air bubbles noticeably appeared as shown in (Fig. 4.7). Reducing air bubbles in MRE phantoms is a very important issue as no MR signal can be generated from air bubbles. In the resulting image they are seen as null spots which create the artifacts and significantly affect the image reconstruction results. A reason for this undesirable air bubble formation can be the silicone liquid pouring procedure inside the phantom box.

Some of the suggestions for better phantom fabrication are mentioned in the next section. These were considered for the manufacturing of the next phantoms.

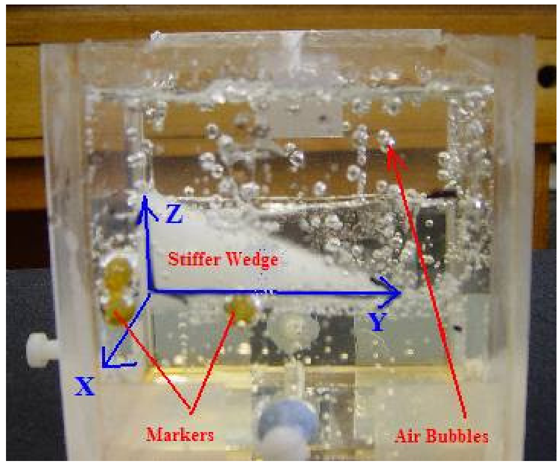

Figure 4- 7 In this picture the stiff wedge inclusion (white color), and directional markers which represent the phantom box coordinate system, and air bubbles in the background of the soft gel part are shown.

4.5 Phantom Fabrication Remarks Applied to MRE

1. Although working with silicone is easy, there are some important points that should be considered. These, as well as other gel phantom materials can create air bubbles during manufacture which cause artifacts in the obtained image. These can be solved by:

- Pouring the liquid into the mold should be carried out carefully and slowly.

- It is better that the liquid be in contact with the mold while it is being poured.

- Shaking the mold by a vibrator while the liquid is being poured can release the air bubbles to the surface of the phantom, which makes the removal of air bubbles from the phantom easier.

- A de-gassing procedure by Venturi vacuum should be carried out in each step of phantom making.

2. Phantom mass is another important factor. By increasing the mass of the phantom, the motion amplitude of the actuation system is reduced. To work more realistically regarding future clinical demands, it is suggested to fabricate the phantom in the same mass as that of a human breast.

3. While phantom markers (oil capsules) were helpful to accurately determine a coordinate system for the phantom, data acquisition experiences have shown they may cause artifacts. In order to remove this undesirable effect, fiducial markers [1] are highly recommended.

4. Phantom lubricating is another important issue which must be considered. Although silicone lubrication spray was helpful, it was still difficult to remove the phantom from the phantom box. To solve this problem, petroleum jelly was used to lubricate the internal surface of the phantom box for the next phantom manufacture. In one phantom manufacturing experience, a phantom box was used where each face could be separated and attached to another by some screws. The benefit of this method is to facilitate the removal of the set phantom from the separated phantom box. However, the disadvantage of this technique is liquid leaking from the phantom box's margins especially if the margins have not been sealed properly.

5. For successful data acquisition it is better that the actuator and the coil are located very close or even attached to the surface of the phantom under investigation.

4.6 MRE Artifacts Due to Actuation systems

An artifact is a visible distortion of an actual structure present in the image subject that can be due to a limitation or malfunction of the imaging system [49].

[1] A fiducial marker is non magnetic materials which can be appearing in the image during the MRI scan.

Knowledge of MRI, MRE artifacts, and noise producing factors is important for an image with high quality. The elimination of artifacts in cancer imaging systems is essential to limiting chances of the misrepresentation of cancerous cells or normal tissue. Artifacts may give confusing erroneous results that may be misdiagnosed as pathology. There is little quantitative information available on MRE regarding the causes of artifacts and the solutions. While MRE is expected to be a high-quality imaging modality targeted at differentiation between benign and cancerous lesions, artifacts can make this differentiating between the cancerous cells and the normal tissue difficult. Therefore, to achieve a high quality image, a more realistic behavior of tissue and cancerous tumors is necessary to evaluate the cause of artifacts in MRE.

One possible artifact in MRE imaging is due to constraints applied by the actuation system to the phantoms. Two example experiments carried out in the next sections with two different real MRI datasets obtain from the actuator Type A and Type B and then results were compared. This attempt may demonstrate a possibility of creating artifact and data interpretation due to actuator geometry and its applied boundary conditions in MRE phantom imaging.

4.7 Isotropic Elasticity Reconstructive Imaging

While it has been shown that MRE is capable of quantitatively measuring *in vivo* soft tissue elasticity, there is still some uncertainty about the factors which affect the quantitative MRE measurements. For this reason, it is necessary to determine *in vitro* how MRE measurements correspond with other quantitative parameters of measuring characteristic elasticity values.

This section presents the results of experiments with tissue-like gelatin phantoms in which the motion was measured by MRE shear waves and the resultant shear modulus distribution was compared in different phantoms vibrated by two different actuators. The shear modulus and displacement pattern of two different phantoms with different stiffer inclusions were investigated.

In this research, one artifact due to the geometry of the actuation mechanism for tissue mimicking phantoms is presented. The reconstruction results obtained from real MR data sets for these two types of actuators are compared. Periodic shear mechanical excitation coupled with phase-contrast MR-imaging was used to actuate the phantoms and image the resulting motion patterns. Two different types of piezoelectric actuators that are being utilized for the phantoms in MRE imaging are evaluated. The goal of this experiment was to compare the reconstruction results from two different real MR data sets obtained from *in vitro* tissue mimicking phantoms for these two types of actuators. As the MRE fundamental techniques for the *in vivo* and *in vitro* cases are very similar, the results from this experiment may be considered for future *in vivo* MRE testing.

Two different isotropic phantoms have been used to reconstruct the elasticity modulus image: a three cylindrical inclusions silicone phantom and the two cone inclusions phantom. The three cylindrical inclusions silicone phantom was imaged by the Type-A actuation mechanism (Fig. 4.3), while the two cone inclusions phantom was tested by the Type-B actuation system (Fig. 4.4). The measured displacements from MRE are used to compute the calculated displacement fields and the shear modulus distribution. The measured boundary displacements from the given data were then applied. In the Type-A actuator, the phantom is contained inside a box container with five sides and was constrained on those surfaces, while the Type-B actuator applied constraints only on the bottom surface of the phantom. These are explained in the following sections.

4.7.1 Three Cylindrical Inclusions of a Silicone Gel Phantom

4.7.1.1 Isotropic Reconstruction Using Real MRI Datasets

Full 3-D MRI dataset of an isotropic silicone phantom comprised three stiff cylindrical inclusions with diameters of 8, 12, and 16 mm, surrounded by a soft background which was used for isotropic elasticity modulus reconstructions. The soft silicone background can represent the benign tissue of a human breast and the inclusions simulate harder tumors.

This silicone phantom was initially used for material property reconstructions in this research. Two shear modulus image reconstructions were carried out by considering two different initial guesses, 10 KPa and 15 KPa.

The CG optimization technique along with the TV regularization method was used to minimize the objective function. Also, the subzone implementation approach was applied to reduce the global inversion process by dividing the problem into multiple local inversion problems. Figure 4.3 shows the performance of this phantom resting inside the phantom box and excited by actuation Type-A. The actuation frequency applied to this phantom by this actuator was 100 Hz.

4.7.1.2 Reconstruction Results

The results below represent the T^{2*} MRI magnitude images (Fig. 4.8-A and Fig.4.8-B), the shear modulus distribution (Fig. 4.9 and 4.10), and the displacement pattern (Fig.4.11) obtained from the real MRI datasets of the three cylindrical inclusions phantom.

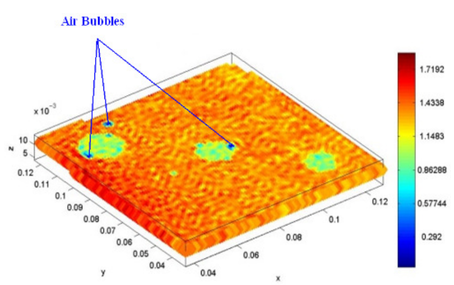

A

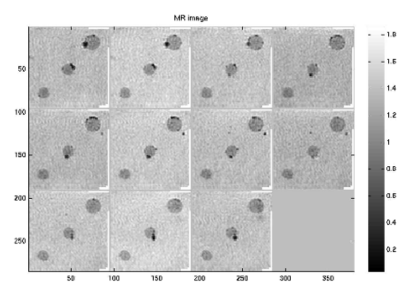

B

Figure 4- 8 Two views of $T2^*$ MR magnitude images obtained from the silicone gel phantom which includes three stiffer cylinder shaped inclusions. The resulting $T2^*$ MR magnitude image (A) and eleven slices of $T2^*$ MR magnitude image obtained from MRI imaging (B) are presented. Three cylindrical inclusions are shown in both pictures.

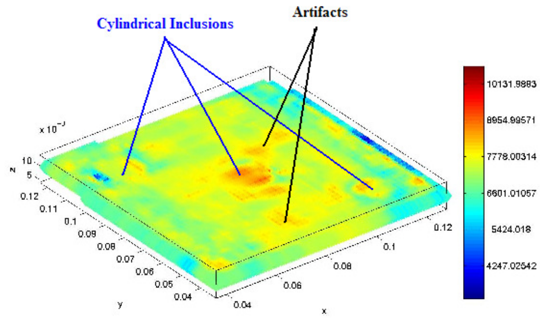

Figure 4- 9 Resulting reconstruction of the isotropic real shear modulus distribution obtained from the three cylinder silicone gel phantom with initial guess 10KPa. Unfortunately, the picture shows a high level of artifact in the background of the images and the three cylinders are barely visible.

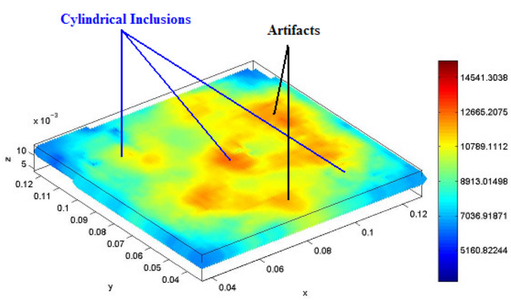

Figure 4- 10 Shear modulus reconstruction result obtained from the three cylinders isotropic silicone gel phantom with initial guess 15KPa. By increasing the initial guess the inclusions are slightly visible but the image still shows a high level of artifact in the background. The expected locations of the inclusions are shown.

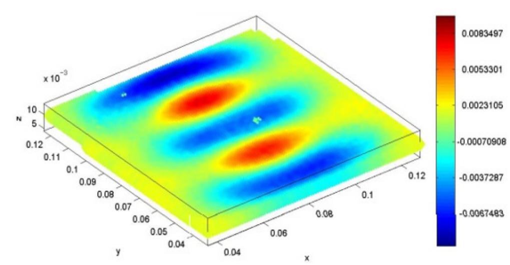

Figure 4- 11 The motion pattern for the isotropic phantom with three cylindrical inclusions which was excited by the Type-A actuator. The regularity of the displacement field without any perturbation around the inclusions is evident.

4.7.1.3 Reconstruction Results Analysis

Table 4.1 represents the mean values of the shear modulus reconstructions with two different initial guesses, 10 and15 KPa, for the three cylindrical inclusions phantom.

The Mean Values for Shear Modulus Reconstructions (KPa)		
Initial guess=10	Initial guess=15	Difference
7.1895e+003	9.8511e+003	2.6616 e+003

Table 4- 1 The mean values of the shear modulus reconstruction with two different initial guesses 10 and15 KPa for the three cylindrical inclusions phantom are presented.

As Table 4.1 shows, the mean value of the shear modulus reconstruction is raised by increasing the initial guess from 10 to 15 KPa. Also the color bars in Fig. 4.9 and Fig. 4.10 represent that the shear modulus reconstruction result with initial guess 10 KPa shows a low contrast between the stiffness of the inclusions and the image background, while this contrast in the shear modulus reconstruction result with initial guess 15 KPa is slightly raised.

The above results illustrate that although by increasing the initial guess, the shear modulus reconstruction mean value and the image contrast has slightly improved, but still the image resolution between the inclusions and the background is low, which makes the invisibility of the inclusions more sensible.

The displacement field represents a regular pattern with the mean value of 8.007e-004 μm, as it is presented in (Fig. 4.11). This regularity of the displacement field can mean that the motion magnitude level received by inclusions was unable to create a strong perturbation around the inclusions within the phantom.

Poor elasticity modulus reconstruction with a high level of artifacts (Fig. 4.9 and 4.10), which made the three inclusions barely visible, reveal that this problem cannot only be due to some air bubbles as they have been shown in Fig. 4.8-A.

One hypothesis leads to the actuation system and boundary conditions applied to the phantom by the phantom box in the Type-A actuation mechanism. Figure 4.3 implies that the phantom has been constrained on five sides and the motion pattern is heavily governed by boundary conditions. Perhaps this can describe the reason of the poor shear modulus reconstruction which may be the cause of artifacts.

4.7.2 Two Cone Shaped Inclusions Gel Phantom

4.7.2.1 Isotropic Reconstruction Using Real MRI Datasets

The second isotropic gel phantom reconstruction belonged to two stiffer conical inclusions embedded in the soft gel as a base. Figure 4.4 depicts three views of this phantom sitting on the tray of the Type-B actuation mechanism.

Figure 4.4-C also represents the position of these two cone shaped inclusions. As has been shown, one conical inclusion is located in the top left and another in the bottom right of the cubic phantom. The full volume MRI datasets obtained from this phantom were used for the isotropic elasticity modulus reconstructions. The initial guesses of 10 and 15 KPa were also chosen for the shear modulus image reconstructions of this phantom.

4.7.2.2 Reconstruction Results

Results below demonstrate the MRI and the reconstructed magnitude images (Fig. 4.15), the shear modulus distribution (Fig. 4.16), and the displacement pattern (Fig.4.17) obtained from the real MRI datasets of the two conical inclusions gel phantom.

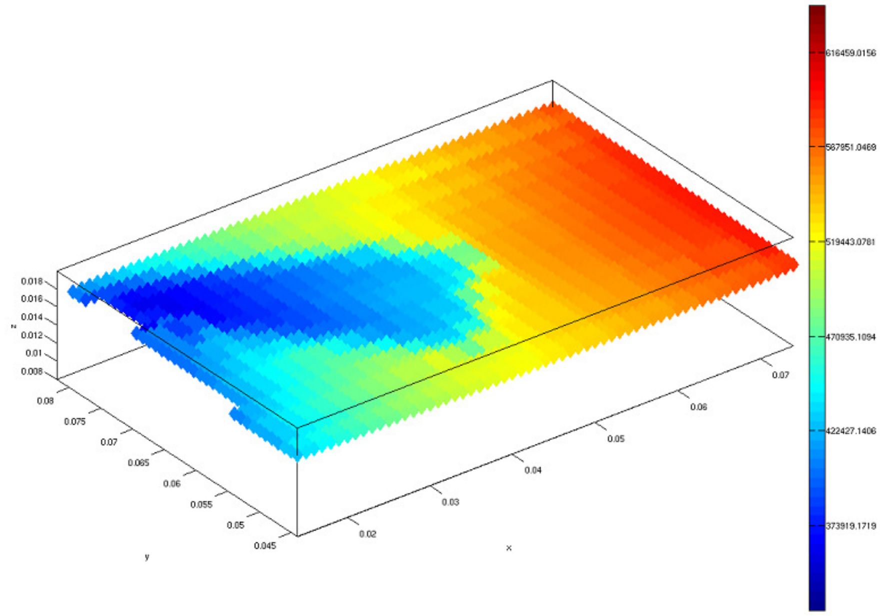

A

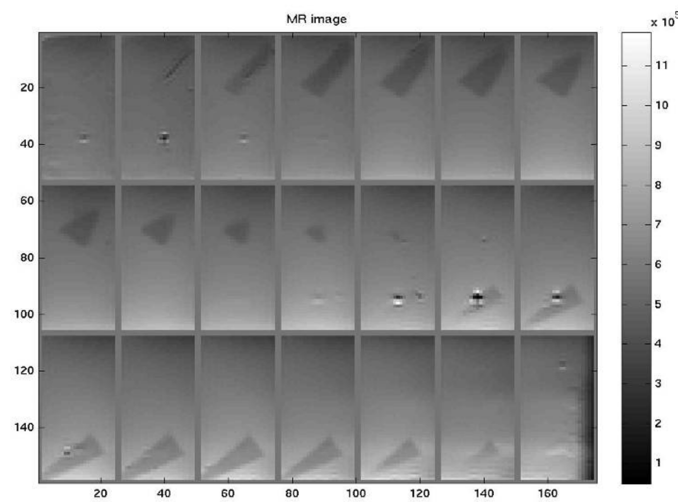

B

Figure 4- 12 Two views of magnitude images obtained from the two cone shaped inclusions gel phantom. The magnitude image from MRE reconstructions shown in one slice (A) and twenty one slices of MR magnitude image obtained from MRI imaging of phantom volume (B).

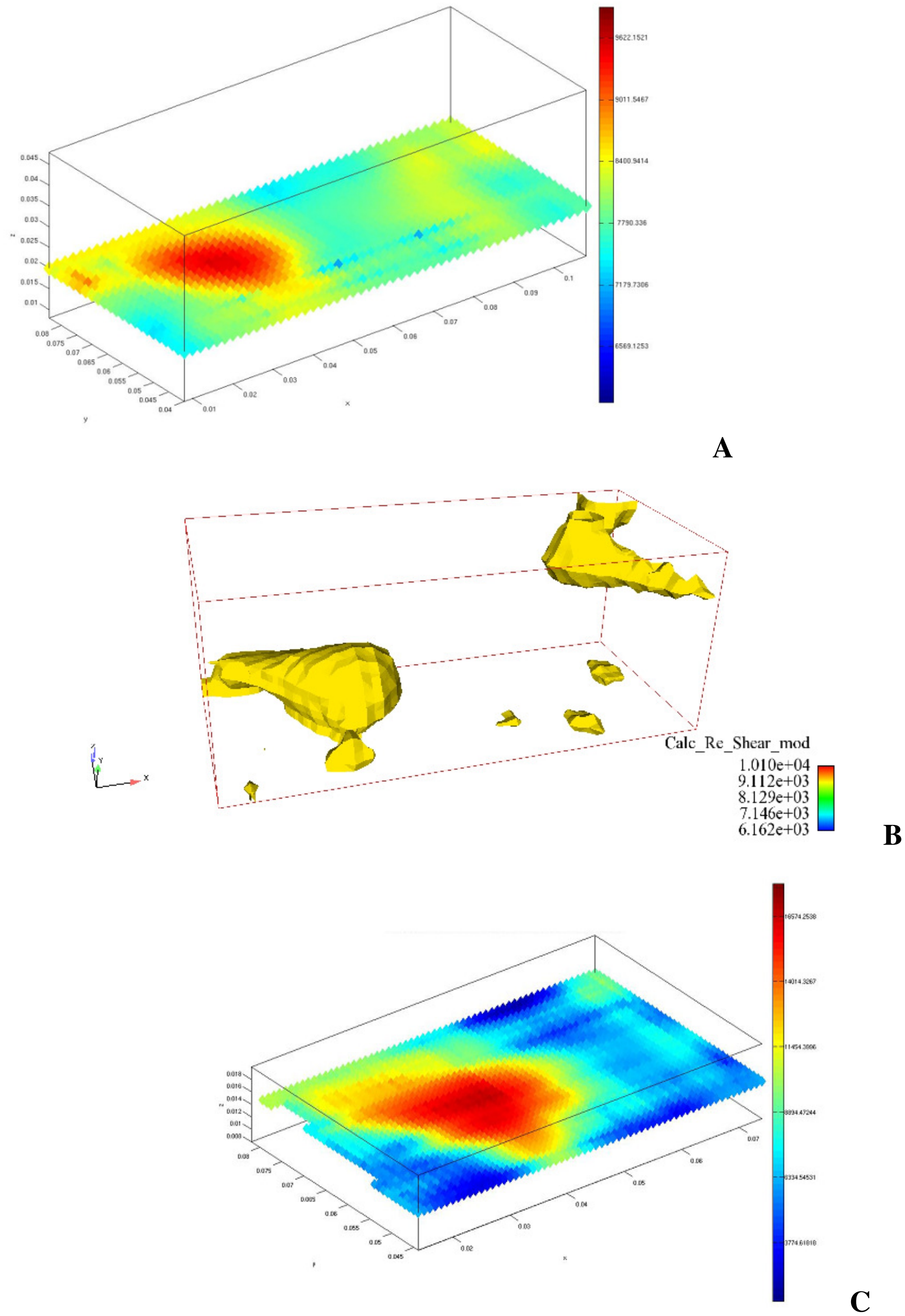

Figure 4- 13 These pictures show three views of the shear modulus reconstruction results for the two cone shaped inclusions isotropic phantom. A satisfactory shear modulus distribution recovery of two cone inclusions with low levels of artifacts in the background with initial guess 10 KPa (A) along with a 3-D view of two cone shaped inclusions (B), and also the shear modulus reconstruction result with initial guess 15 KPa (C) are shown.

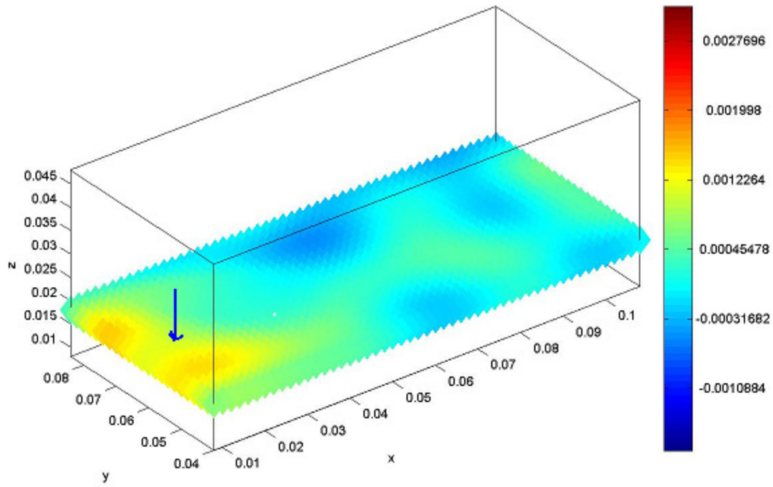

Figure 4- 14 The displacement pattern for the two cone shaped inclusions phantom excited by the Type-B actuation system. An irregular motion pattern around the inclusions illustrates the existence of stiffer inclusions in the medium. The small arrow shows the displacement pattern disturbance around the conical inclusion located at the bottom of the phantom.

4.7.2.3 Reconstruction Results Analysis

A successful shear modulus distribution reconstruction with low levels of artifact in the background of the image is illustrated in Fig. 4.16 for the two conical inclusions phantom excited by the Type-B actuation system. Table 4.2 shows the mean values of the shear modulus reconstructions with two different initial guesses, 10 and15 KPa. Table 4.2 illustrates that the mean value of the shear modulus reconstruction is raised by increasing the initial guess from 10 to 15 KPa.

The Mean Values for Shear Modulus Reconstructions (KPa)		
Initial guess=10	Initial guess=15	Difference
8.0956e+003	10.1700e+003	2.0744e+003

Table 4- 2 The mean values of the shear modulus reconstructions with two different initial guesses, 10 and15 KPa, for the two conical inclusions phantom are represented.

Figures 4.16-A and 4.16-C exhibit that the stiffness contrast between background and the inclusions using initial guess 15 KPa is more improved in comparison with the initial guess 10 KPa. The displacement field image shown in Fig.4.17 with the mean value of 8.3909e-004 μm represents an irregular motion pattern around the inclusions which implies the existence of stiffer inclusions in the medium. This also can mean that the Type-B actuation system allows the phantom to move freely on all sides while is being excited and this might be a reason for the strong perturbation around the conical inclusions. From one glance at the phantom situation in Fig. 4.4 it can be seen that the two conical inclusions phantom is restricted on the actuation tray on only one side (the bottom), and the other five sides are free. This may explain the high motion magnitude level within the phantom and fewer artifacts as the inclusions could be detected in the reconstruction procedure.

4.7.3 Discussion and Conclusion

High-quality elastic property images have always been the objective of MRE, to facilitate differentiation between benign and cancerous lesions. The approach presented here investigates the role of boundary condition as a possible key factor in better property reconstructions with fewer artifacts. The goal was to compare two different actuation systems in order to suggest a realistic design guideline for advanced MRE actuation systems. Phantom experiments with different piezoelectric actuators have been previously performed to demonstrate the artifact caused by constraints applied by the actuation system.

In general, when a shear wave travels through a medium, a part of this wave will be deflected away from any surfaces or boundaries and another part will be scattered especially from the corners of the object. This deflection and scattering of the wave can also occur within the interface of two materials with different stiffness, such as a stiffer inclusion inside a softer background, as well as creating a perturbation around the inclusion. In 2005 Parker and et al. [163] showed that the presence of inhomogeneity, such as the existence of stiffer inclusions in the tissue or phantom, can be indicated by the perturbation in displacement fields [164, 165, 166, 167].

In the MRE image implementation, this wave perturbation and irregularity in the motion pattern will translate as a material properties contrast which happens when the wave faces a different medium or an inclusion inside a phantom in this case. A highly constrained actuation system does not allow sufficient perturbations in the displacement field around the inclusions to facilitate the reconstruction.

This can lead to the existence of artifacts in the boundaries and corners as well, because of the existence of the wave disturbance in those areas. Also, by considering wave energy dissipating on the rigid boundaries [168, 169], a strong motion which is the source of the perturbation in the displacement field cannot be generated. This fact can be seen in the displacement field in the Type-A actuator case which was overly constrained.

In the comparison of two piezoelectric actuators, Type-A and Type-B, with two different boundary conditions, a satisfactory shear modulus reconstruction with fewer artifacts demonstrated with the Type-B actuation system. This investigation has shown that by raising the initial guess in the shear modulus reconstruction, the elasticity contrast between the inclusion and the background is increased. Table 4.3 evaluates the difference between MRI real data reconstruction mean values of two cylindrical and conical inclusion phantoms obtained from the Type-A and the Type-B actuation systems respectively. This evaluation reveals that the conical inclusion phantom excited by Type-B actuator illustrates a higher mean value in the both image reconstruction, shear modulus with two different initial guess and displacement.

The displacement field observed in the Type-B actuation also shows an irregular pattern (Fig. 4.17) while this displacement pattern in the Type-A actuation are regular without any disturbance around the inclusions (Fig. 4.11). While the displacement magnitude level in actuator Type-B is slightly higher than that of actuator Type-A, this cannot be the only reason for the successful image reconstruction in the conical inclusion phantom. The important point is the disturbance level around the inclusions. This can be seen in the Type-B actuation which was able to create enough perturbation around the inclusions and as a result, better elasticity image reconstructions were obtained.

Reconstruction Results Mean Value Differences Using Real MRI Data for Two Conical and Cylindrical Phantoms			
Phantom / Recon.	**Conical Inclusion Type-B**	**Cylindrical Inclusion Type-A**	**Difference**
Shear Modulus with Initial Guess=10 KPa	8.0956e+003	7.1895e+003	0.9061e+003
Shear Modulus with Initial Guess=15 KPa	10.17e+003	9.8511e+003	0.3189 e+003
Displacement	8.3909e-004	8.007e-004	0.3839e-004

Table 4- 3 The difference between MRI real data reconstruction mean values of two cylindrical and conical inclusion phantoms obtained from the Type-A and the Type-B actuation systems are evaluated.

While the results obtained from the real MRI datasets verify that the boundary condition in MRE reconstruction may play an important role in the quality of reconstructed MRE images, more accurate tests are still required to determine the exact cause of the artifacts. This hypothesis can be better clarified by simulation studies in the future.

The discussion is open for more evaluation about other factors which may create the artifacts in MRE actuation systems (i.e. the frequency of the actuation). Questions still remain over parameters which may affect this problem such as reconstruction procedures (i.e. zone size), elasticity properties (i.e. initial guess), data acquisition conditions, and the phantom fabrication process which is being used to manufacture the phantoms.

As shown, regardless of the type of actuator, by increasing the initial guess the elasticity image reconstructions obtained from real MRI and simulated datasets are improved. This indicates that initial guess can be another factor which might play an important role in MRE image reconstructions. The discussion about the initial guess and its influence in elasticity reconstruction results and artifacts will be continued in the following chapters.

"A person, who never made a mistake, never tried anything new".   Albert Einstein

Chapter 5

5.1 Orthotropic Incompressible Phantoms

To evaluate a realistic orthotropic incompressible model, several biological phantoms (with and without gelatin embedding) and a series of non-biological tissue-like gelatin phantoms were developed and tested for this thesis. Choosing the best phantom that mimics an orthotropic material can be very challenging, as there is little quantitative information available in MRE experiments regarding orthotropic phantom fabrication.

This research project is mainly based on the orthotropic incompressible phantom development along with data acquisition and image reconstruction, to describe the orthotropic behavior. Several orthotropic phantoms were designed and manufactured for MRE data acquisition. Orthotropic image reconstruction was then carried out to map orthotropic elasticity properties in 3D using a few MRI datasets which are presented in this chapter, and their results will be discussed in the following chapters. This chapter presents some experiments with tissue-like gelatin phantoms and muscle phantoms which include:

- Orthotropic phantom manufacturing protocols
- Boundary conditions regarding orthotropic materials
- Orthotropic data acquisition
- Protocol analysis and manufacturing remarks

5.2 Biological Orthotropic Phantoms

Recently, *ex vivo* phantom elastography such as muscle phantoms, have been developed for non-invasively measuring the stiffness of biological tissues [159]. As real cancerous tissue is not always available for MRE testing, one focus on this investigation was to design and manufacture a series of muscle phantoms and tissue-like gelatin phantoms that could mimic the tissue and tumors with orthotropic properties.

In this approach, two kinds of biological orthotropic phantoms were developed and made for the orthotropic dataset acquisition. These were muscle phantoms and a pineapple phantom.

5.2.1 Muscle Phantom Experiments

Due to the structural properties and myofibril protein orientations within the muscle, this material can be a good example of orthotropic incompressible behavior. As muscle is known to be highly orthotropic [170], to develop clinically realistic orthotropic phantoms, bovine muscle was chosen and tested. To examine the muscle phantom, two different kinds of phantoms were designed, and then tested with two different types of actuators. These actuators were piezoelectric actuation systems (Type-A and Type-C), and a pneumatic actuator. Phantoms which were fabricated and tested in this category were: a gelatin-muscle phantom and multiple free standing muscle phantoms.

5.2.1 .1 Gelatin-muscle phantom

- **Manufacturing Protocol**

The purpose of making this phantom was to simulate an orthotropic tumor (cubic beef muscle in this test) inside a soft tissue (gelatin). This phantom was fabricated for the Type-A actuation system.

The gelatin-muscle phantom was made from a cubic piece of bovine muscle embedded in unflavored homogenous gelatin (Davis Gelatin, NZ, Ltd). Gelatin is a suitable material for tissue-mimicking phantom manufacturing as it is safe, relatively easy material to work with, and can also be set quickly. Early experiences have shown that an acceptable concentration of gelatin is around 9.9g/100mL [171].

To make this phantom, 25g gelatin was weighed and added to 250 ml hot water and then mixed. A magnetic stirrer was used to help dissolve the gelatin in the water while the mixture was heated on a hotplate to around 70^o C.

The temperature of the mixture was measured by a thermometer which was placed inside the hot water. The mixture was then cooled in a water bath to around 32^o C. The reason that the mixture was cooled to around 32^o C was to prevent over heating the bovine muscle while it was being surrounded by gelatin, as the heat may change the material property of the tissue. Before pouring this liquid inside the phantom box all screw holes of the phantom box were sealed to avoid liquid leaking out.

In the next step, one third of the phantom box was filled by this solution and then the phantom was set overnight in the refrigerator. After the gelatin was set, a cubic bovine muscle was prepared ($7\times7\times5$cm) and located on the top of the gelatin base inside the phantom box. The geometry of the cubic bovine muscle was designed in such a way that was suspended in the gelatin without touching the phantom box faces (Fig. 5.1).

At this stage, the markers (oil capsules) were applied on top of the gelatin base between the cubic muscle and internal phantom faces (Fig. 5.2) in the manner that was explained before in 4.3.1. The phantom and the cubic bovine muscle were then surrounded by $25^o C$ gelatin and then kept in the refrigerator to facilitate setting.

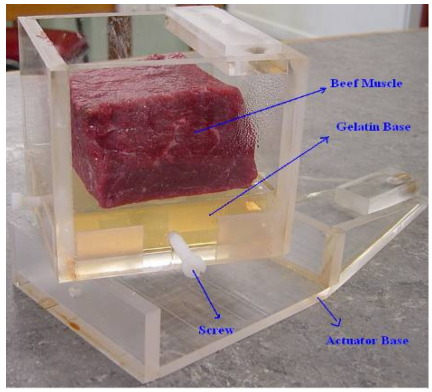

Figure 5- 1 A configuration of the gelatin-muscle phantom. The position of the cubic bovine muscle on top of the gelatin base is shown.

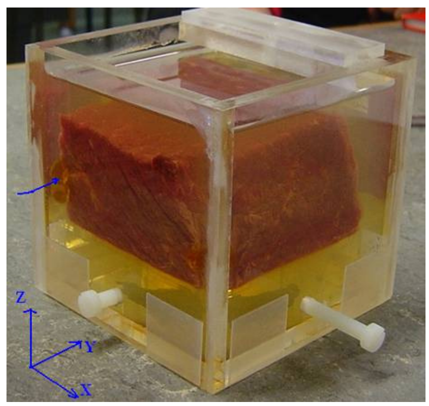

Figure 5- 2 This image depicts the completed gelatin-muscle phantom. The small arrow shows the position of the markers regarding the coordinate system. The cubic bovine is shown suspended inside the gelatin.

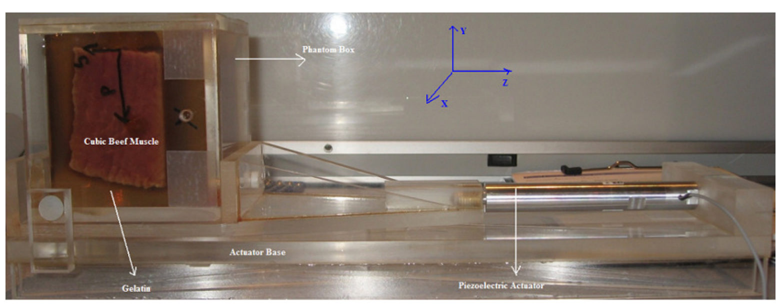

Figure 5- 3 The Type-A actuation system set up is depicted while the phantom box included the gelatin-muscle phantom is coupled with the piezoelectric actuator. The coordinate system shows the phantom alignment inside the phantom box.

- **Orthotropic Data Acquisition**

The gelatin-muscle phantom was tested by the Type-A actuator at a frequency of 100 Hz. The experimental set up arranged for this test included the gelatin muscle phantom located inside the phantom box which was coupled to the piezoelectric actuator. The actuator was then placed into a head coil which was used to receive the MRI motion data. Finally, this system was inserted inside the MR bore (Fig. 5.4).

Figure 5- 4 This picture shows the experimental arrangement for the gelatin muscle phantom. The phantom located inside the actuator Type-A was place inside a head coil. The head coil is shown while it is being inserted inside the MRI bore.

Before phantom scanning, a pre-scan was carried out to check the correct orientation of the scan plane in the magnitude image. The phantom was then scanned in three dimensions to measure the real and imaginary parts of the motion data in the magnitude and phase images format. The slice thickness for this MRE test was 2 cm while considering a cubic voxel ($1 \times 1 \times 1$ mm).

- **Orthotropic Boundary Conditions**

The phantom was scanned in three dimensions by rotating the phantom box 90^o in 3-D.

As mentioned in chapter 3, to obtain enough motion data from an orthotropic material, multiple measurements in 3-D are required. By rotating the phantom box 90^o in 3-D, the phantom could be efficiently actuated in three directions. The schematic of boundary conditions assigned to the phantom box including the muscle gelatin phantom, is depicted in figure 5.5. The phantom was scanned in three stages with one specific excitation frequency of 100 Hz. In each stage, this load condition was assigned to the side of the phantom box which was coupled to the piezoelectric actuator in the excitation direction (Z).

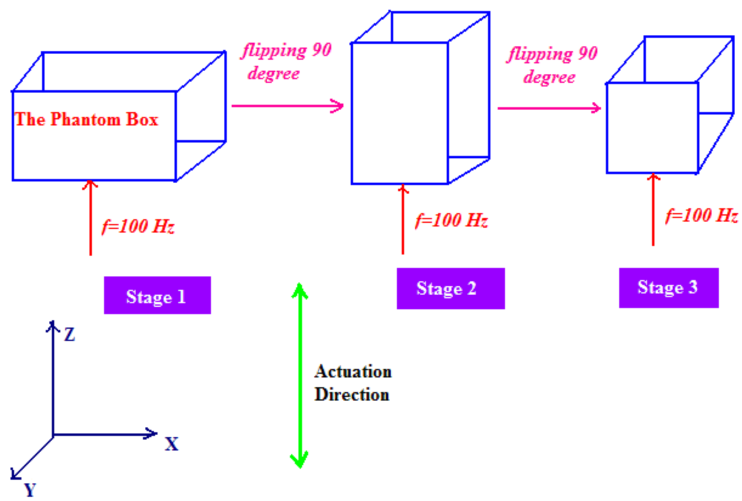

Figure 5- 5 This schematic depicts three stages of the boundary conditions applied to the muscle gelatin phantom located inside the phantom box. This picture illustrates that only one specific frequency of 100Hz was assigned to the phantom in 3D while the phantom is being excited in the Z direction. The phantom box has been flipped 90^o in each stage to capture multiple measurements in 3-D from this orthotropic sample.

- **Protocol Analysis and Manufacturing Remarks**

A view of the $T2^*$ weighted MR magnitude image captured from the gelatin muscle phantom is shown in Fig. 5.6. Unfortunately, the MRI dataset from this phantom did not exhibit sufficient transmission of shear waves to the muscle, thus this phantom was not used for the reconstruction procedure.

To explain this deficiency, a reason could be again that the boundary conditions applied from the five rigid faces of the phantom box to the gelatin-muscle phantom using the Type-A actuation set up which overly constrained the phantom. This reduced the motion magnitude level and the perturbation within the phantom, as discussed in chapter 4.

As initial elasticity image reconstructions obtained from phantoms (silicone gel and gelatin muscle phantoms) tested by the Type-A actuator has not revealed satisfactory results, this actuator is no longer used for the MRE data acquisition owing to its constraints on the phantoms.

Figure 5- 6 A view of the MR magnitude image ($T2^*$ weighted) obtained from the gelatin muscle phantom. The cubic bovine muscle embeded inside the gelatin is visible.

5.2.1.2 Free Standing Muscle phantoms

Research has shown that motion signals obtained from free standing muscle are significantly stronger than gelatin-muscle phantoms [159]. A reason can be that the motion magnitude level may be higher in the free standing muscle phantoms than the muscle embedded in the gelatin. As explained before, the higher the mass in the gelatin-muscle phantom with a constant load condition causes a reduction in the system's acceleration. This does not allow strong waves to be made within the phantom. For this reason, free standing muscle phantom was fabricated, with the muscle actuated directly without any gelatin embedding for the data acquisition.

As experiences have shown, material properties of the tissue (i.e. the stiffness) can be changed by heating. This idea was applied to create an inclusion inside the muscle phantom to simulate an orthotropic tumor inside the tissue.

In this approach, several methods were developed to create an inclusion within the muscle phantom using heating and chemical processes. These techniques took advantage of a laser system and electricity to produce heat in a small area inside the muscle phantom. Using a chemical material such as acetone to change the elastic property of the tissue to simulate an inclusion within the muscle phantom was another approach that was also investigated. These protocols are explained in this section.

5.2.1.2.1 Laser

Laser stands for "*Light Amplification by Stimulated Emission of Radiation*" [172]. It is a device which uses atoms or molecules of a substance and excites them to produce an excited energy during a procedure known as stimulated emission to release coherent light (electromagnetic radiation) of a precise wavelength as a narrow beam (low divergence beam) [172, 173]. The laser emission is transferred by glass or plastic fibers which are used to carry the light along its length. There are two kinds of fiber; single-mode and multi-mode. Multi-mode fibers have a significantly large core diameter (50-1000 μm) in comparison to single-mode (4-10 μm) (Fig. 5.7) [174, 175].

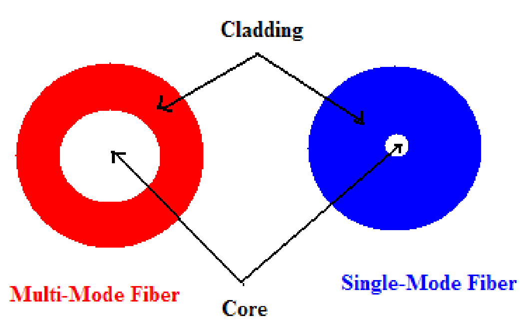

Figure 5- 7 A schematic of the single-mode fiber (right) and the multi-mode fiber (left). The difference between their cores and their claddings are shown.

- **Manufacturing Protocol**

In this research, the laser (Ultrafast Mai Tai® Lasers, Spectra-Physics ®, Mountain View, CA) was used to carry the laser energy to heat a spot inside the tissue (Fig. 5.8). This device can produce a wavelength range between 690-1020 nm. The actual wavelength associated for this test was around 802 nm powered by 1.5 W.

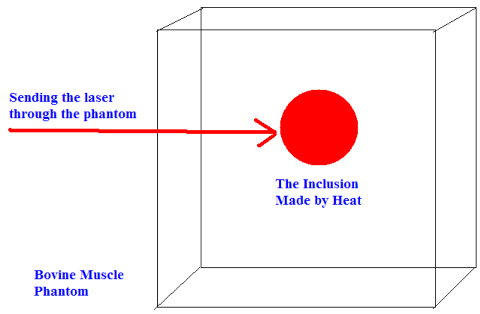

Figure 5- 8 The protocol configuration of making an inclusion by heating a spot within the muscle phantom using the laser is shown.

For the first trial, the single-mode fiber was used. The test was carried out by applying a metal needle (Fig. 5.9) to conduct the single-mode fiber (about 10 μm) to the inclusion location within the phantom. The laser transmission along the fiber (Fig. 5.10) was then carried out for twenty minutes to heat a small area within the muscle phantom and create a stiff inclusion (Fig. 5.11).

Figure 5- 9 The metal needle shown in this picture was used to facilitate locating the single-mode fiber through the muscle phantom.

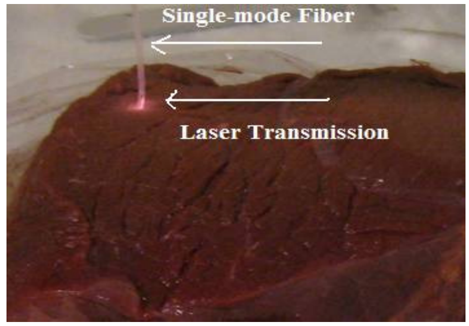

Figure 5- 10 The laser transmission along the single-mode fiber applied to the muscle phantom is shown. This test was carried out for twenty minutes.

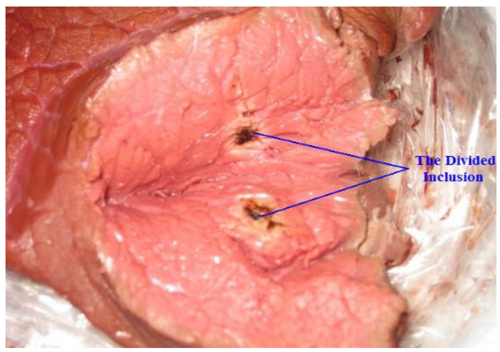

Figure 5- 11 This picture depicts a view of the muscle phantom which was cut to observe the quality of the inclusion after the laser transmission. The small and overheated inclusion is due to a high laser transmission in a small area using the single-mode fiber.

Figure 5.11 shows a view of the muscle phantom which was cut to observe the quality of the inclusion. As the single-mode fiber has a very small light carrying core with a high transmission rate, the inclusion generated by this fiber was small (about 5mm diameter) and overly heated. This muscle phantom was not used for data acquisition as it was assumed that this small inclusion may not be visible in the MRI scan and elasticity reconstructions.

The next laser transmission trial was carried out for twenty minutes in order to make another inclusion inside the muscle phantom using the multi-mode fiber (1mm diameter) (Fig. 5.12).

The same technique which was used to locate the single-mode fiber inside the muscle phantom was utilized for placing the multi-mode fiber within the tissue. As mentioned in Fig. 5.7 the multi-mode fiber has a larger light carrying core and as a result a larger area can be heated by the laser (Fig. 5.13). Figure 5.13 shows a view of the bovine muscle phantom which has been cut to observe the heated area. The material property within the tissue was changed successfully by this technique with a larger inclusion diameter. The changed color area represents the generated inclusion (over 20 mm diameter).

Figure 5- 12 This picture depicts a demonstration of the multi-mode fiber with 1 mm diameter located inside the muscle phantom for twenty minutes in order to heat and create an inclusion using the laser transmission.

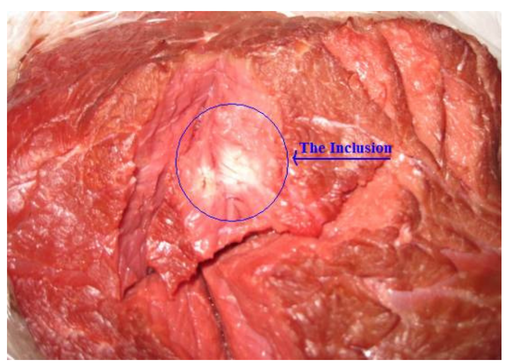

Figure 5- 13 This picture shows a view of the bovine muscle phantom tested with the multi-mode fiber with a larger laser carrying core. The phantom has been cut for better observation of the heated area. The circled spot exhibits the material property changing within the tissue. The changed color area represents the generated inclusion of about 20 mm diameter.

As the previous phantom was cut for the observation, another muscle phantom was fabricated in the same manner as the previous phantom using the multi-mode fiber for the MRI scan. A coordinate system was defined for the phantom using three fiducial markers (MR-SPOTS, Beekley Corporation, USA) as shown in Fig. 5.14.

Figure 5- 14 The performance of the final muscle phantom which was used for the MRI scan. A coordinate system was defined for the phantom using three fiducial markers as shown in this picture.

- **Orthotropic Data Acquisition**

Figure 5.15 shows an experimental set up for the muscle phantom which was located on the contact plate of the Type-C actuation system while a pair of surface coils is coupled from both sides. A large pad is applied to stablize the other side of the plate.

The driven force supplied by two piezoelectric actuators excited the phantom. Two thin rubber mats were used underneath the actuator's legs to prevent shaking the actuation system during the scanning.

As this picture shows the direction of the actuation system is in the X direction of the MRI scan coordinate system. The MRE dataset was collected with fifteen slices and the voxel size was $2\times2\times1.8$ mm including a 0.9 mm slice gap.

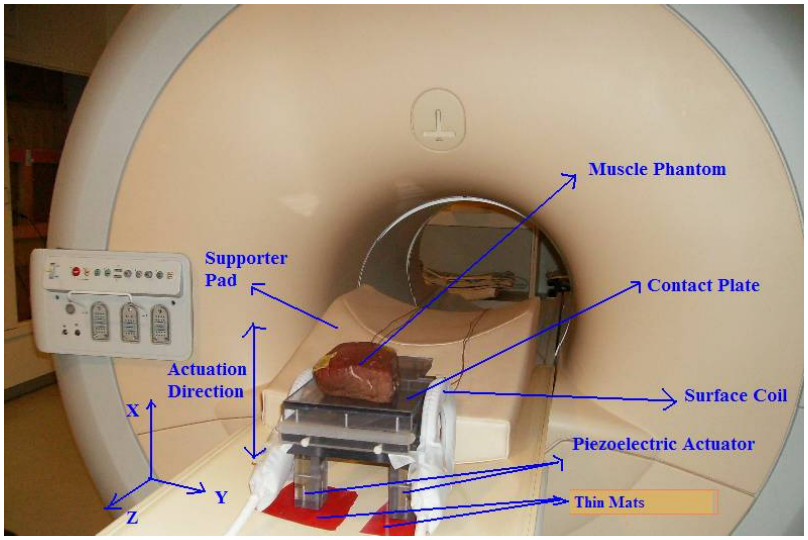

Figure 5- 15 A demonstration of the experimental set up for the muscle phantom which was excited by the Type-C actuation system while a pair of surface coils is attached to both sides. The situation of the large pad, two thin rubber mats, and the actuation direction, are also illustrated.

- **Boundary Conditions**

The muscle phantom was scanned with an excitation frequency of 100 Hz in three directions by rotating the phantom box 90^o in 3-D to capture enough MRI motion data from this orthotropic phantom (Fig. 5.16). By rotating the phantom faces 90^o in 3-D, the phantom could effectively be actuated in three directions. Boundary conditions applied to the muscle phantom show that only one face of the phantom which is located on the contact plate is restricted and the phantom is free on its other five sides.

- **Protocol Analysis and Manufacturing Remarks**

The successful material property transformation using the laser transmission has shown that this method is capable of creating an *ex vivo* inclusion within the muscle phantom (Fig. 5.17) where the real case was not available for the MRE experimental tests.

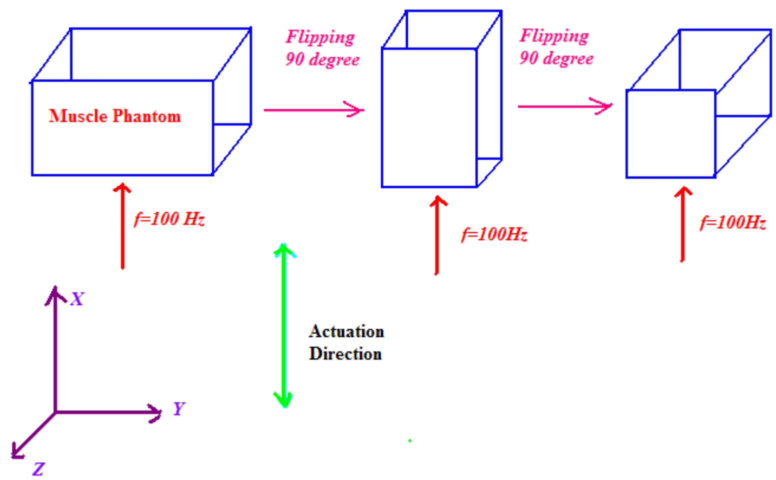

Figure 5- 16 This schematic shows the applied boundary conditions for the muscle phantom with a frequency of 100 Hz in three dimensions along the actuation direction (X). Note that the actuation direction is constant but the phantom faces are rotating 90^o in 3-D.

While the goal of elastic property modification using the laser protocol has been achieved in this experiment, a satisfactory MRI dataset was not captured from this muscle phantom. The muscle phantom set up shown in Fig. 5.15 may express one reason for this inadequacy. The improper adjustment of the surface coils with respect to the phantom can cause the insufficient MRI data collection. As explained in 4.2.3, the best position of the phantom-coil set up is when the coil is near the phantom. This form of the phantom-coil set up would help to detect stronger motion signals by the coil.

On the other hand, the inclusion spot is fairly small in comparison to the muscle phantom size. For these reasons, the recorded MRI datasets from this phantom were not used for the orthotropic reconstruction procedure.

The stiff inclusion construction for tissue-equivalent phantoms using the laser is still an open approach needing more investigation. For future trials, adjusting the procedure of heating for a longer time and using several multi-mode fibers to create the larger spot are suggested.

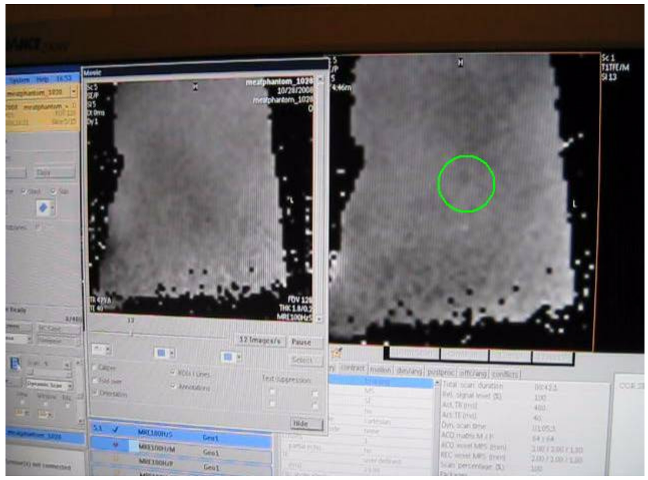

Figure 5- 17 The MRI magnitude image (proton density weighted) obtained from the laser protocol to change the elasticity property of an internal spot within the muscle phantom. The circled area shows the inclusion location.

5.2.1.2.2 Electricity

Direct current (DC) is the constant flow of electrons which is generated by power supply units such as batteries etc. This continuous movement of electrons will flow through a conductor such as a wire from a negative terminal of a power source to a positive end. A DC electricity system in a circuit comprises voltage, current, and resistance. A DC voltage is provided by an electricity generator such as battery [176, 177, 178].

- **Manufacturing Protocol**

An approach to making an *ex vivo* inclusion using DC electricity to produce the heat in order to transform the material property within the muscle phantom is shown in Fig. 5.18. For this purpose, a resistor (5W 3Ω 9J YAGEO DGK, Oxygen Electronics LLC USA) was coupled between two plastic protected wires using a soldering iron. The end of each wire was stripped of plastic and joined to the resistor's wires which had also been stripped (Fig. 5.19).

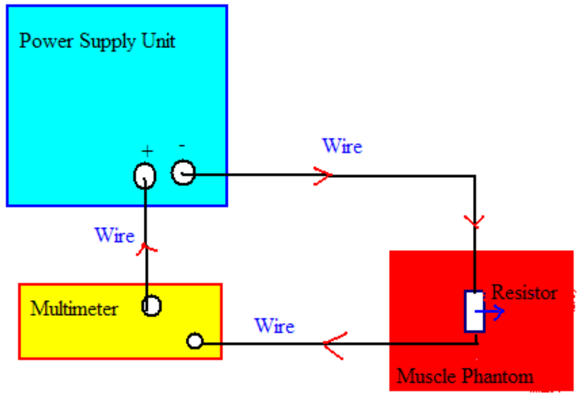

Figure 5- 18 This picture shows a configuration of the DC electricity system which was designed for an *ex vivo* inclusion fabrication within a muscle phantom. This circuit includes a resistor to generate heat inside the muscle phantom, a power supply unit to produce the voltage, and a multimeter for measuring and adjusting the current.

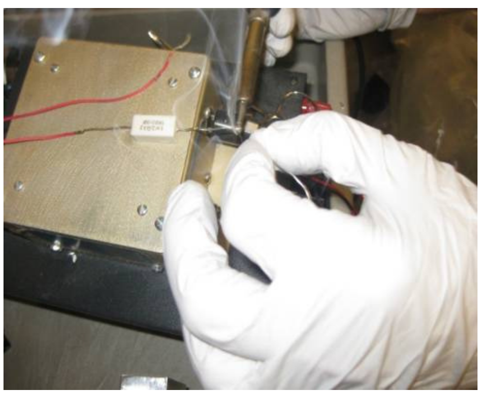

A

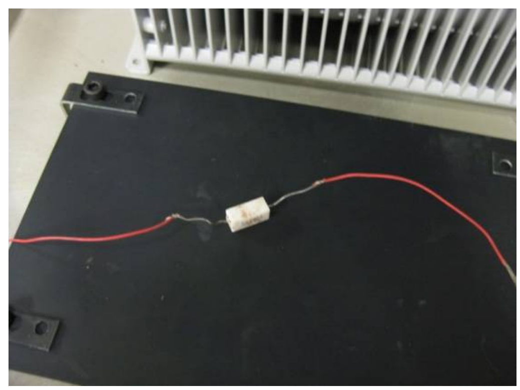

B

Figure 5- 19 In these pictures, the procedure of joining the resistor to a wire using a soldering iron (A) and the resistor coupled between two plastic protected wires (B) are depicted.

The resistor was then placed inside the muscle phantom (Fig. 5.20). Two wires were then attached to the positive and negative terminals of a DC power supply unit (6114 A Precision Power Supply, Test Path Inc, USA) while a digital multimeter (Fluke 77 Multimeter, Optimum Energy Products Ltd, USA) was connected to the power supply unit to complete this system by adjusting the DC current, which was passing through the muscle phantom (Fig. 5.21). The power supply unit could generate voltage in the range between 0-50 V.

Several experiments with the voltage range between 24-35 V and the current range between 0.5-1 A were carried out to fabricate this muscle phantom successfully. For the ultimate test, a voltage of 35V and current of 1 A were applied to heat the muscle phantom sufficiently. The final designed system is shown in Fig. 5.22.

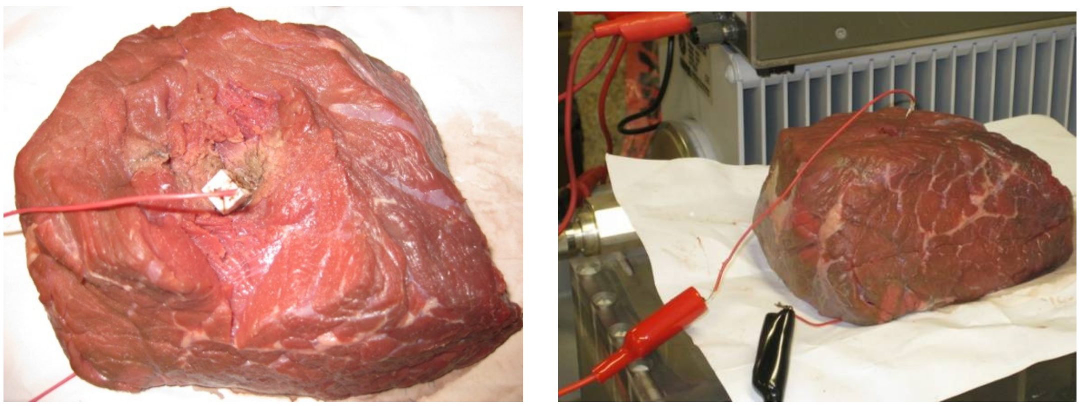

Figure 5- 20 These pictures show two views of the muscle phantom and the locating scenario of the coupled resistor between two wires within the phantom.

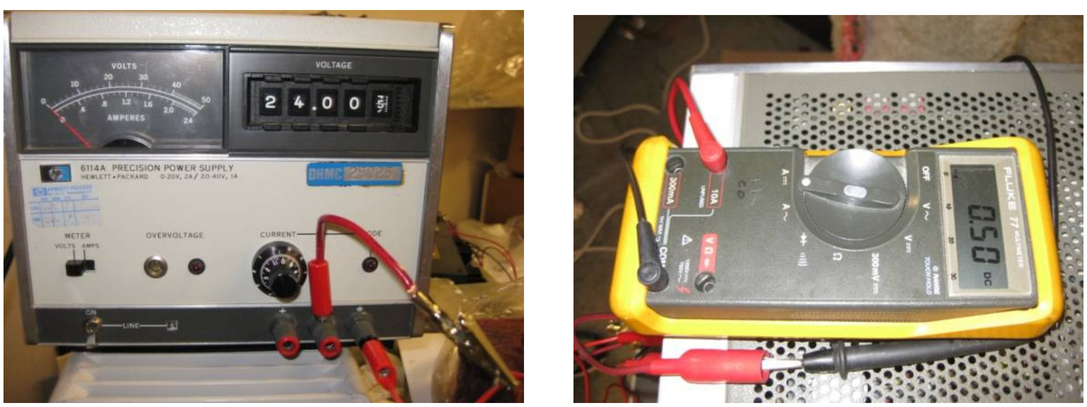

A B

Figure 5- 21 The power supply unit used for this test to provide the voltage (A) and a digital multimeter to measure and adjust the DC current which was passing through the muscle phantom (B), are displayed.

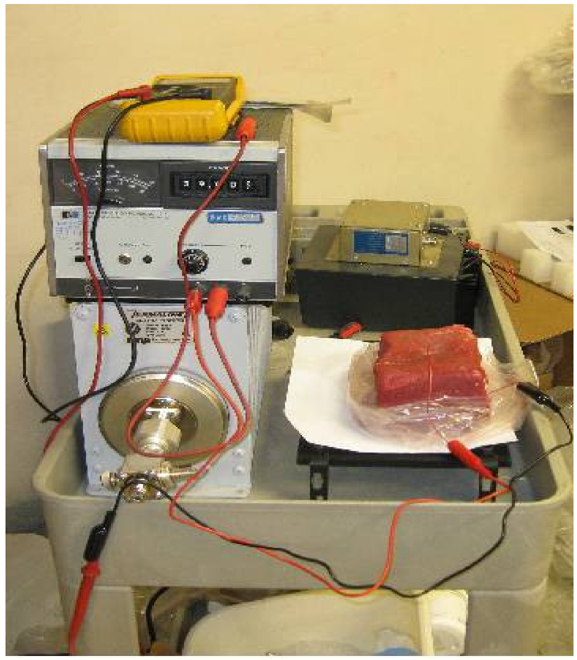

Figure 5- 22 The final designed system to set up the DC circuit to fabricate the muscle phantom included a stiffer inclusion which was created by heat. The resistor located within the muscle phantom is able to convert the electric energy to heat. This heat changes the material property inside the phantom. The DC electricity flow was generated by a power supply unit which was connected to a multimere to adjust the current.

- **Protocol Analysis and Manufacturing Remarks**

Transforming the material properties within the muscle phantom in order to make a stiffer inclusion using the electricity energy to produce heat was successful as well as the laser transmission procedure. This technique has been shown to be a safe and fairly easy method to fabricate *ex vivo* phantoms with stiffer inclusions. However, this approach still needs to be modified. Fig. 5.20 shows that the muscle phantom had to be damaged to locate the large resistor. As a result a large hole was observed after removing the resistor from the muscle phantom (Fig. 5.23) which may affect the quality of the obtained MRI datasets.

Using thin resistors can be helpful for future muscle phantom manufacturing. Also, more investigations are needed to adjust the voltage and the current of the DC electricity for the optimum temperature to make a larger and stiffer inclusion.

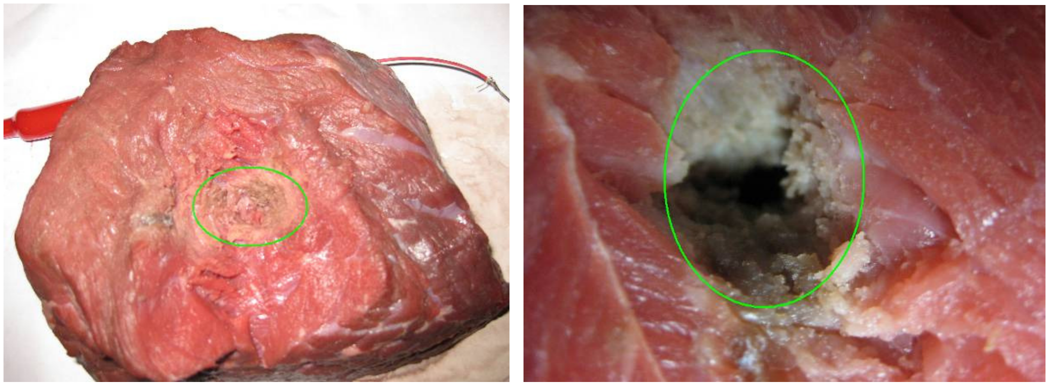

A **B**

Figure 5- 23 These images display two views of the stiffer inclusion within the muscle phantom. The location of the inclusion is circled. The phantom was slightly cut for observation (A). The transformed color inside the muscle phantom means the material property of this area is changed. The closer view (B) shows a fairly large hole within the phantom which was where the resistor was located.

A suggested option to provide the electric energy could be the alternating current (AC), considering the safety issues. This phantom was not taken to the MRI scan as it was assumed that useful MRI datasets would not be captured from the damaged muscle phantom.

5.2.1.2.3 Electrosurgical Device

An electrosurgical device is a surgical instrument which uses high frequency current, usually upwards of 100 KHz, on a particular area of the body for surgical purposes. This device is typically applied to seal off blood vessels and remove unwanted tissue. Some surgical techniques use the electrosurgical device to create a surgical incision on different tissues. The advantage of the electrosurgical device is that it is clean, safe, and more efficient than other similar surgical techniques [179, 180, 181, 182].

- **Manufacturing Protocol**

In this muscle phantom fabricating protocol, the electrosurgical device (Force 2, Valleylab, USA) was used to create the heat inside the phantom in order to make a stiffer inclusion (Fig. 5.24).

The electrosurgical generator produces the voltage for electricity flow as well as converting the AC electricity to high frequency waveforms. For example, an AC with 60 Hz can be transformed to 100,000 Hz which is known as radio frequency (RF). Two different techniques exist for electrical circuit set up: monopolar (monoterminal) and bipolar (biterminal) [183].

In the monopolar method, the electrical flow is sent through the tissue by only one single active electrode (Fig 5.25–A), and it is then received from a return electrode pad (Fig 5.25–B). In the bipolar approach, the active and the return electrodes are placed in one handpiece pencil (forceps), and the return pad is no longer needed as is shown in Fig 5.25–C. A monopolar configuration of an electrosurgery circuit comprises: an electrosurgical generator which supplies the power, a hand-piece known as 'pencil' or active electrode, including one or several electrodes, a return electrode pad, and the tissue as a resistor.

A schematic of this technique is displayed in Fig. 5.26. In electrosurgery, the principle is that the tissue plays the role of a resistor between two electrodes. Since the resistance of the tissue is high, it converts the electric energy to thermal energy and this heat can be used to transform the material property within the muscle phantom.

In this procedure, the RF current produced by the electrosurgical generator was sent through the muscle phantom by an active electrode known as a 'pencil' or 'RF knife' and it was then received from the return electrode pad. The electric current received from the return electrode pad is then sent back to the AC source (electrosurgical generator). On the tip of all electrosurgical pencils there is a removable small contact plate known as a probe which is made from stainless steel and acts as an electrode.

Usually, when the high frequency flow passes through the pencil's electrode, it spreads in a localized region only near the probe tip, inside the tissue. Once this electricity flow faces the tissue's resistance, the heating procedure occurs which raises the tissue temperature. The pencil's functions can be controlled by pushing the yellow and blue buttons which are located on the pencil's hand piece (Fig. 5.25-A).

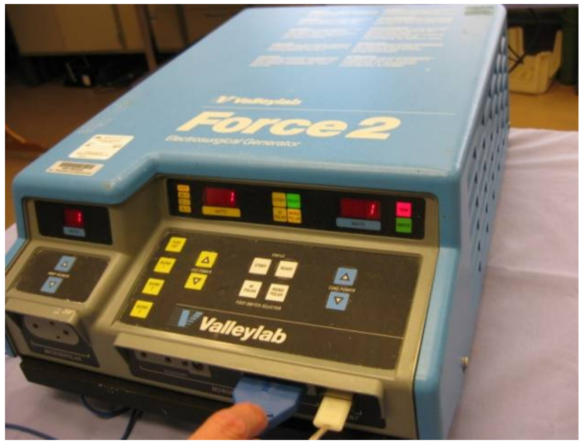

Figure 5- 24 The electrosurgical generator used for the MRE test to create the heat inside the muscle phantom in order to make a stiffer inclusion is shown. This power supply produces the voltage for electricity flow as well as converting the AC electricity to high frequency waveforms.

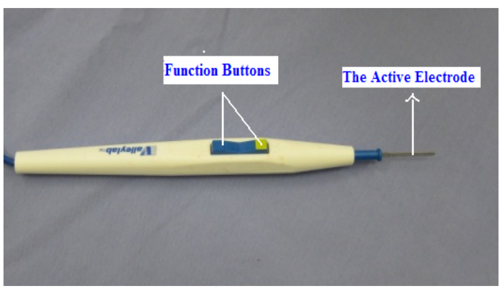

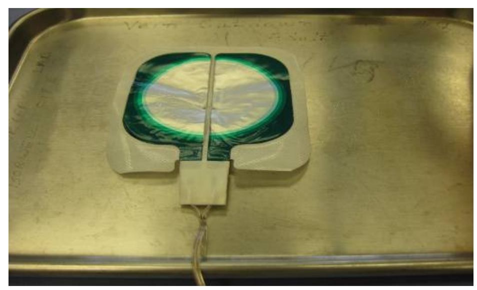

A **B**

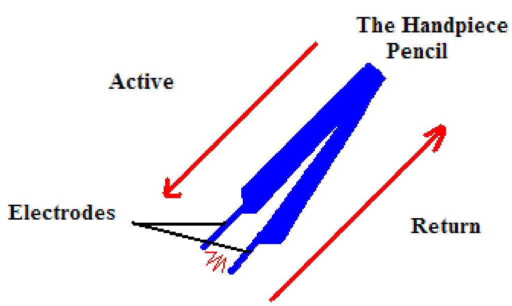

C

Figure 5- 25 Three electrosurgical accessories are displayed in this picture. The active electrode known as the electrosurgical pencil (A) and the return electrode pad (B) which are both used in the monopolar technique are shown. The forceps with two active/return electrodes in one handpiece pencil which is applied in the bipolar method also illustrated (C).

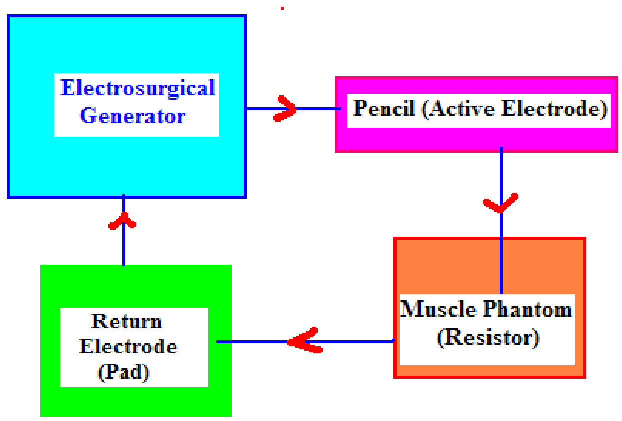

Figure 5- 26 A schematic of electrosurgical accessories. This circuit comprises an electrosurgical generator (power supply), a pencil (active electrode), and a return electrode pad and tissue (muscle phantom) as a resistor.

In this test, the return electrode pad acted as a pathway for the current to be taken back to the electrosurgical generator again. This pad is flexible and usually made from a viscoelastic polymer. This pad also plays an isolator role to prevent the current flowing to the ground (Fig. 5.25-B).

The muscle phantom was placed on the return electrode pad which was connected to the electrosurgical generator. The pencil-like active electrode was then gently inserted through the muscle phantom. The test was carried out for five minutes with 35W of power.

Figure 5.27 illustrates the configuration of the set up which was designed for this experiment. As this picture shows, the pencil's yellow button was held during the test to transfer the RF through the muscle phantom.

- **Protocol Analysis and Manufacturing Remarks**

The muscle phantom was then excised after testing with electrosurgical device to observe the resultant inclusion (Fig. 5.28). The demonstration of the stiffer inclusion represents that this method was capable of changing the material property within the muscle phantom.

The transformed colour of the tissue shows that this technique was successful, safe, and fast to produce enough heat inside the phantom which is necessary for converting the tissue to an inclusion. However, this approach has a disadvantage.

Fig. 5.28 reveals that the monopolar technique with a thin probe is not able to create an inclusion with sufficient thickness. This test was carried out for a longer time on the assumption that maybe by increasing the time more heat can be generated and as a result it could make a larger inclusion. Unfortunately this idea was not helpful as the inclusion became longer but no thicker. A reason could be the small pencil's probe which spreads the RF flow in a localized region only near the electrode's tip.

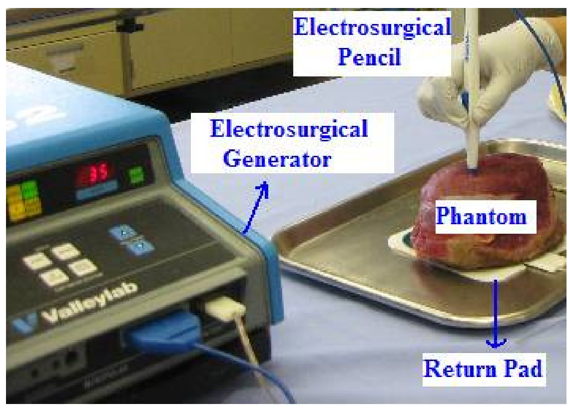

Figure 5- 27 The configuration of the designed set up for the muscle phantom to create a stiffer inclusion using electrosurgical device is depicted in this picture. The muscle phantom was placed on the return electrode pad which was connected to the electrosurgical generator. The pencil was then inserted through the muscle phantom gently. The pencil's yellow button was held continuously during the test to transfer the electrical current through the muscle phantom.

Although this method was sufficiently fast and efficient to transform the material property of the muscle phantom, more modifications are still needed to create a qualified inclusion for future MRE investigations. A suggestion for future MRE muscle phantom tests using the electrosurgical method could be to apply the bipolar pencil rather than a single active electrode pencil (monopolar).

In this technique, a piece of the tissue in the muscle phantom can be trapped between two electrodes of the forceps which may be helpful to create a thicker inclusion as shown in Fig. 5.29. This muscle phantom was not taken for the MRI scan again as it was assumed that the thin inclusion may not be obvious in the MRI scan and the orthotropic reconstructions.

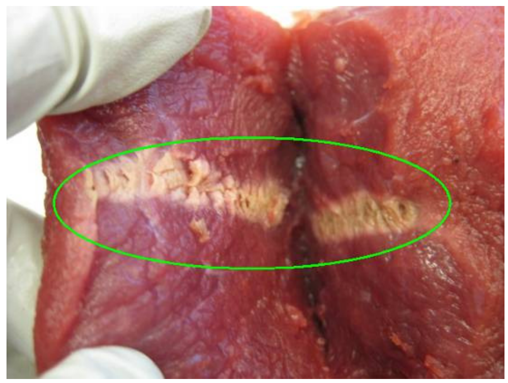

Figure 5- 28 This picture depicts a view of the muscle phantom which was cut for observation after the electrosurgical test. The circled area shows the location of the stiffer inclusion with the small thickness. The transformed color of the tissue reveals that the material property within the muscle phantom has been changed.

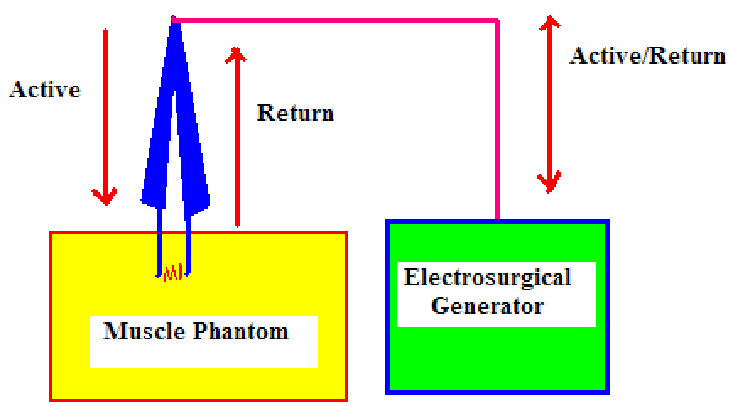

Figure 5- 29 A proposed set up using the bipolar electrosurgical technique is depicted in this schematic. The bipolar forceps is inserted through the muscle phantom while a piece of tissue can be trapped between two active and return electrodes. This may increase the chance of creating a thicker inclusion.

5.2.1.2.3 A Chemical Process for Inclusion Generation

Fixation is a chemical procedure used to stabilize a tissue from degeneration. This method is widely used in histology, pathology and so on to terminate biochemical functions in tissue. Experiences have shown that the fixation process increases the mechanical stiffness and the stability of the tissue. In this technique the tissue can be preserved by different chemical agents known as fixatives such as acetone and formalin (formaldehyde) [184, 185].

In this experiment, acetone was used to make a stiff inclusion inside a muscle phantom by taking advantage of the effects of this chemical agent the mechanical property of the tissue.

- **Manufacturing Protocol**

Acetone is an alcoholic precipitating fixative with the formula OC $(CH_3)_2$, which, by diminishing the solubility of protein molecules and destroying the hydrophobic functions, changes the nature of the material structure within the tissue. Acetone is a colorless, flammable and mobile liquid which is known to cause considerable shrinkage and hardening of the tissue during fixation [186, 187, 188]. In this test, 2 ml acetone (A18-4, Fisher Scientific, Inc, USA) (Fig. 5.30-A) was injected inside the muscle phantom with a small syringe (2 ml) (Fig. 5.30-B). From a central point of penetration, several injections were made at different angles to spread the acetone evenly throughout the muscle phantom.

This technique of injection was carried out to fabricate a three dimensional inclusion with sufficient thickness within the phantom. A schematic of the injection technique with different angles to make a 3D inclusion within the muscle phantom is illustrated in Fig. 5.31. After acetone injection, the muscle phantom was cut for observation (Fig. 5.32). The color conversion of the injected area can be interpreted to mean that material properties of this region have changed. In fact, a stiffer inclusion was created because of the tissue hardening effect of the acetone fixation process. Another muscle phantom with a stiffer inclusion was fabricated using the acetone injection technique, in the same manner as the previous muscle phantom for the MRI scan.

A **B**

Figure 5- 30 Acetone was used as an alcoholic fixative to fabricate the muscle phantom with a stiffer inclusion as this chemical agent can cause shrinkage and hardening of the tissue during fixation (A). A 2 ml syringe was applied to inject the Acetone inside the muscle phantom as shown in B.

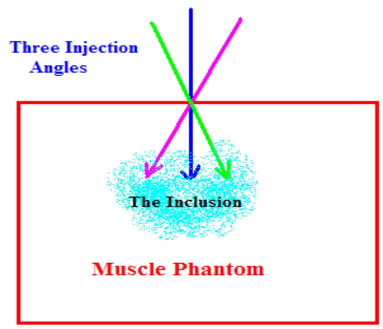

Figure 5- 31 This schematic shows the technique of injection with different angles which was carried out to create the stiffer inclusion in 3D within the muscle phantom. From a central point of penetration, several injections were made at different angles to spread the acetone evenly throughout the phantom.

Figure 5- 32 The circled area displays the transformed color of the inclusion after the injection process which indicates that the material property of this volume has been changed by acetone.

- **Orthotropic Data Acquisition**

Figure 5.33 demonstrates an experimental set up for the muscle phantom which was located on the membrane of the pneumatic actuation system while a pair of surface coils is coupled from both sides. The system was supported by two sand bags to prevent undesirable movement of the system during the excitation. The actuation system had to be covered by a cloth because the phantom was leaking blood during the test.

As this picture shows the direction of the actuation system is in the X direction of the MRI scan coordinate system. The MRE dataset was recorded with fifteen slices and the voxel size was $2 \times 2 \times 1.8$ mm including a 0.9 mm slice gap.

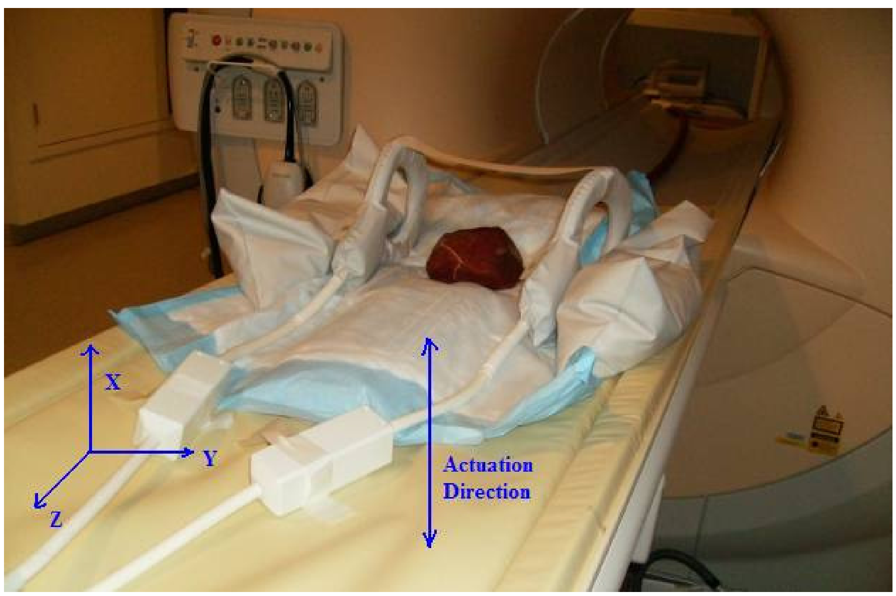

Figure 5- 33 The set up for the free stand muscle phantom with an inclusion made by acetone. The pneumatic actuation system was used for exciting the phantom in the X direction with a frequency of 100 Hz. The actuator had to be covered because of the phantom blood leakage. The phantom was located on the top of the actuator membrane. The position of the surface coils and the sand bags are also shown. Note that the actuation direction is constant but the phantom faces are rotated 90^o in 3-D.

- **Boundary Conditions**

The free standing muscle phantom was scanned with a specific excitation frequency of 100 Hz in three dimensions by rotating the phantom box 90^o in 3-D in three phases to collect sufficient motion data from this orthotropic phantom similar to the previous MRI data collection which is illustrated in Fig. 5.16. By rotating the phantom faces 90^o in 3-D, the phantom could be actuated in three dimensions. Boundary conditions applied to the muscle phantom allowed that only one face of the phantom which is located on the membrane of the pneumatic actuator is constrained. As a result, the phantom was free to move on its other five sides.

- **Protocol Analysis and Manufacturing Remarks**

Although the acetone injection method was successful in changing the tissue hardening and creating a stiffer inclusion, the inclusion was not detected in the MRI datasets (Fig. 5.34). More investigations about this technique and alcoholic fixatives revealed that the tissue hardening influence due to acetone is temporary and after a short time (about 20 minutes), acetone evaporates or dissolves in the water medium of the tissue. This causes the tissue to lose its hardness and return to its original form. This technique can be modified in future trials by paraffin embedding as the paraffin stabilized the acetone and prevents its evaporation and its solubility in the tissue water.

Another alternative for future MRE testing to manufacture a muscle phantom with a stiffer inclusion using chemical materials is applying other fixatives such as formaldehyde (formalin). Formaldehyde exists as a gas form while formalin, with the formula CH_2O, is formaldehyde dissolved in water which is often used as 10% Neutral Buffered Formalin (NBF) [189, 190]. This material is a cross-linking fixative which generates the covalent bonds between proteins within the tissue. Although formalin is able to make a stiffer inclusion by creating long term tissue rigidity, this material is reasonably carcinogenic and considering safety issues during the test is strongly recommended.

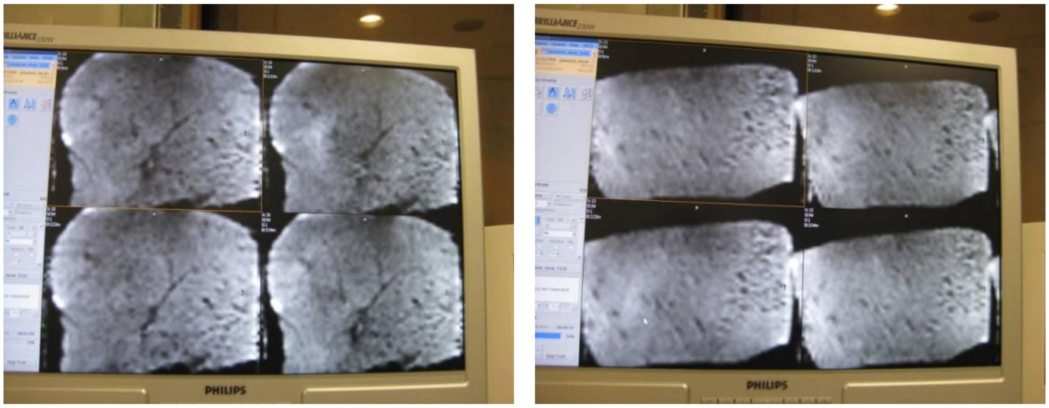

Figure 5- 34 Two views of the MRI $T2^*$ weighted magnitude image, captured from the muscle phantom after injecting the acetone. The stiffer inclusion was not seen in this MRI data collection as the tissue lost its hardness owing to acetone's solubility in the water.

Wearing clothing made with special materials such as cotton, nylon, and so on, along with a mask and gloves, is important to prevent exposure to this chemical compound. As formalin evaporates quickly, working under a hood with ventilation, opening doors and windows are other important precautions that should be pointed out [191, 192].

Freezing the tissue with some special fixatives or chemical material such as liquid nitrogen could also be another suggestion to fabricate a muscle phantom with a degenerated inclusion.

5.3 Orthotropic Gelatin Phantom Experiments

Following muscle phantom fabrication, tissue-equivalent gelatin phantoms were developed to evaluate the orthotropic incompressible model *in vitro*. Several orthotropic gelatin phantoms were designed and manufactured for the MRE data acquisition, to reconstruct orthotropic elastic properties in three dimensions.

These tissue-like gelatin phantoms are classified into two categories: biological and non-biological.

For the biological gelatin phantom, a piece of pineapple was chosen as an orthotropic inclusion to simulate a tumor with a gelatin background as the benign tissue. For the non-biological gelatin phantoms, some bristles were applied inside a gelatin base. These phantoms were excited by a pneumatic actuation system. In this section, fabricating of these orthotropic gelatin phantoms along with the MRE data acquisition procedures, and applied boundary conditions are discussed.

5.3.1 Biological Tissue-like Gelatin Phantom

Fabricating a biological gelatin phantom using fruit for MRE *in vitro* testing is a novel technique which was developed for this research. This method is simple and inexpensive, and can be used when there is no cancerous tissue available for *in vivo* MRE testing. For this purpose, a piece of pineapple was chosen to fabricate an orthotropic gelatin phantom. In this experiment, the ability of the pineapple to mimic tissue with orthotropic properties is investigated.

5.3.1.1 Pineapple Phantom

While there is little information available in literature regarding the mechanical properties of the pineapple, this natural fibril reinforced bio-composite material can be considered to be a highly orthotropic material owing to its structural properties and different fibril orientations, which incorporate a variety of fibril lengths and thicknesses within the pineapple's matrix [193, 194].

- **Manufacturing Protocol**

The protocol utilized to fabricate the gelatin phantoms' background in this section is different from the method described in 5.2.1.1. The background of all orthotropic gelatin phantoms manufactured in this section followed a similar fashion which is explained.

The porcine skin gelatin (Type A, Sigma, Life Science Inc, USA) was used to make the phantom base (Fig. 5.35). A large glass beaker (1000 ml) was used to combine 100 g scaled gelatin with 900 ml distilled water. To improve the solution of the gelatin into the water, the mixture was heated by placing it in a microwave oven for 20 seconds (Fig. 5.36). The beaker was then removed from the microwave and placed on the hotplate to cool down gradually to around 30^{o} C, while a magnetic stirrer was agitating the mixture. This helped to remove air bubbles and obtain a homogenous gelatin solution (Fig. 5.37). The temperature was monitored by a digital thermometer.

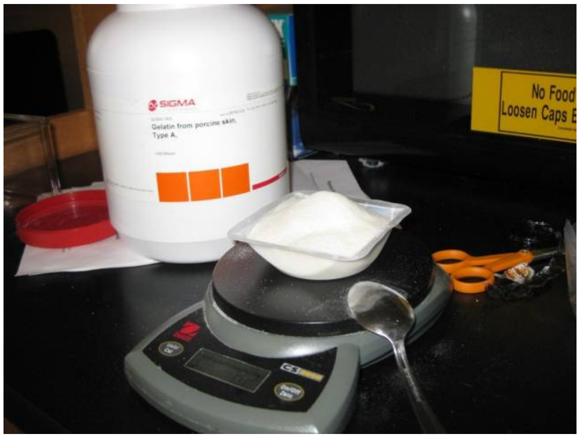

Figure 5- 35 The material (the gelatin from porcine skin) and the scale used to make the background of the pineapple gelatin phantom are shown.

Figure 5- 36 The mixture of gelatin and water was placed inside a microwave oven and heated up for 20 seconds to help dissolve the gelatin into the water.

The first layer of gelatin was poured into a small plastic container (13×13×7 cm) filling one third of the container, which was greased by petroleum jelly beforehand to facilitate removing the phantom from the plastic container. The mixture was kept in the refrigerator to let the gelatin solidify for one hour.

Figure 5- 37 The beaker was placed on the hot plate after removing from the microwave oven to cool down gradually to around 30^{o} C, while a magnetic stirrer was agitating the mixture. This was helpful to remove air bubbles from the gelatin background and obtain a homogenous mixture.

After the first layer of the gelatin was set, a circular slice of pineapple (Dole Food Company, Inc, USA) (Fig. 5.38) was placed on top of the bottom layer of background and the rest of the background gelatin was poured very slowly to prevent air bubble forming.

The gelatin phantom was again refrigerated overnight to facilitate setting and also to provide the phantom an optimum condition before MRI scan. Usually the sample should be kept at room temperature two hours before MRE imaging.

The coordinate system was defined for the sample by locating three fiducial markers on the phantom (Fig. 5.39).

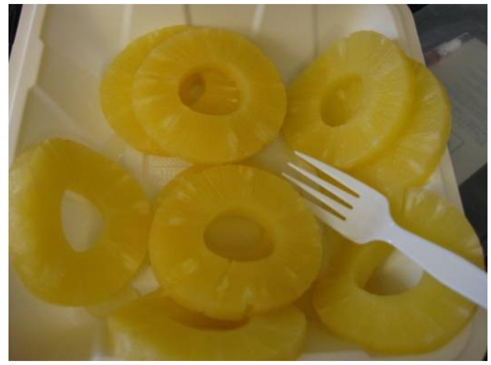

Figure 5- 38 A circular slice of pineapple provided from a cane was used to fabricate the pineapple gelatine phantom for the orthotropic MRE testing. Different fibre orientation with different length in the pineapple can be observed.

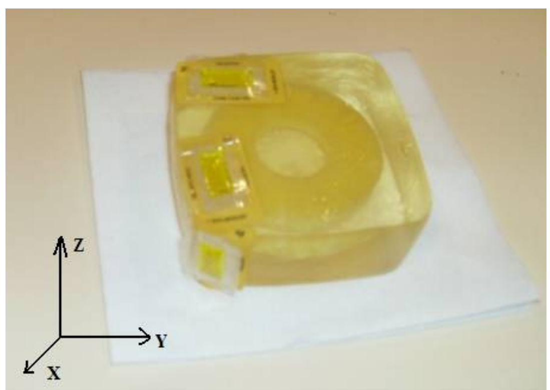

Figure 5- 39 The completed pineapple tissue-like gelatin phantom with a coordinate system defined three fiducial markers.

- **Orthotropic Data Acquisition**

Two views of the experimental set up for the orthotropic MRE imaging are demonstrated in figures 5.40 and 5.41. The pineapple gelatin phantom was located on the membrane of the pneumatic actuation system while two surface coils are attached to the pineapple sample. To avoid undesirable shaking of the actuation mechanism during the excitation, the system was supported by two sand bags.

The excitation direction of the actuation system was in the X direction of the MRI scan coordinate system. The MRE dataset was captured with twelve slices while the voxel size was $2 \times 2 \times 1.8$ mm. The slice gap of 0.9 mm was chosen along with the slice thickness of 18 mm.

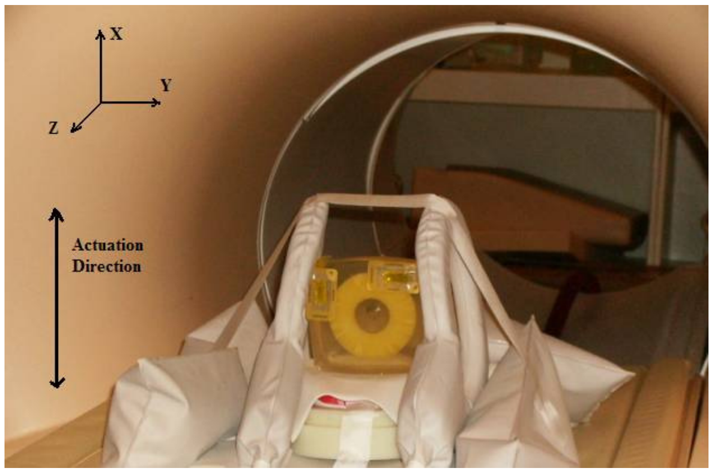

Figure 5- 40 The apparatus of the experimental set up for the pineapple gelatin phantom with three fiducial markers to indicate the phantom's coordinate system while it is being imaged. The position of the phantom standing on the membrane of the pneumatic actuator with the excitation in X direction is shown. Note that the surface coils are attached to the phantom to receive the motion data. The system was also stabilized with three sand bags and secured by wrapping adhesive strapping around the coils and sand bags.

Figure 5- 41 Another view of the same experimental set up for the pineapple gelatin phantom while it has been flipped 90^o to capture multiple measurements in 3-D from this orthotropic sample.

- **Orthotropic Boundary Conditions**

To obtain enough motion data from this orthotropic sample, the pineapple gelatin phantom was scanned in three stages with three different excitation frequencies; 85 Hz, 100 Hz and 125 Hz. In each stage, all these three frequencies were applied on the side of the phantom which was resting on the actuator membrane and in the excitation direction (X). As a result, boundary conditions were applied only on one face of the phantom which was located on the membrane and the phantom was free on its other five sides (Fig. 5.42).

As for an orthotropic material, multiple independent measurements in 3-D are required. By rotating the phantom 90^o in 3-D and repeating this procedure, the phantom could be actuated in three independent dimensions to record sufficient MRE datasets. These imaging datasets measured the real and imaginary components of the motion in the magnitude and phase images which are presented in Table 5.1.

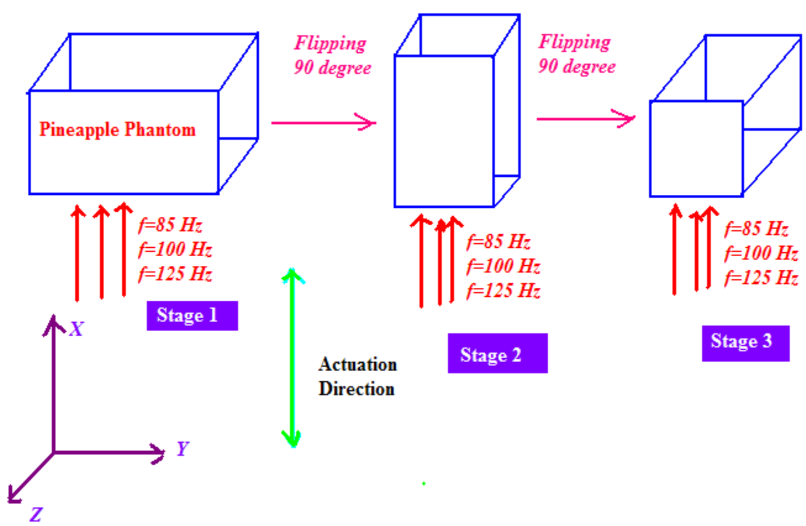

Figure 5- 42 This schematic illustrates boundary conditions applied to the pineapple gelatin phantom in three stages. By rotating the phantom 90^o it could be excited in 3D with three different excitation frequencies: 85 Hz, 100 Hz and 125 Hz are shown. In each stage, all these three frequencies were applied only on the side of the phantom which was located on the actuator membrane with excitation at X direction.

- **Protocol Analysis and Manufacturing Remarks**

This phantom was more successful than previous phantom experiments, not only in the phantom fabricating protocol but also in the procedure of the correct phantom set up and MRE scanning process to capture better images with fewer artifacts.

Successful pineapple gelatin phantom fabrication with no significant air bubbles in the background has indicated that the protocol of phantom manufacturing described in 5.2.2 is suitable as a guide line for making tissue-like gelatin phantoms with a homogenous base. The recorded orthotropic MRE datasets within the frequency range (85-125 Hz) were satisfactory for the pineapple gelatin phantom. The position of phantom-coil with a proper adjustment shown in Fig. 5.40 allowed the collection of sufficient and strong MRI motion data. On the other hand, several independent boundary conditions can be derived from the complete boundary conditions applied to the pineapple gelatin phantom shown in Fig. 5.42. These different boundary conditions can be used individually in the MRE image reconstruction process depending on the problem's circumstances and reconstruction's requirements which are displayed in figures 5.43, 5.44 and 5.45.

According to these schematics the boundary conditions can be assigned as one specific frequency in 3D (i.e. 100Hz), three different frequencies (i.e. 85 Hz, 100 Hz and 125 Hz) in 1D and three different frequencies in 3D with respect to the phantom such that each frequency is assigned to one side of the phantom. Applying boundary load conditions to this phantom as three independent frequencies in three independent dimensions (Fig. 5.42) could provide more information which is needed to capture all mechanical properties of this orthotropic phantom in 3D during the image reconstruction procedure.

Selecting a suitable inclusion regarding the material type and its geometry for the orthotropic tissue-equivalent phantoms is still an open question which needs more investigation. Experience has shown that using an inclusion with symmetrical geometry such as circular pineapple can cause ambiguity in the shear modulus reconstructions as for example by assuming an circle as X-Y plane, the shear modulus obtain from X direction image reconstruction may be very similar to the shear modulus in Y direction because of symmetry.

Mode / Frequency (Hz)	Magnitude Image	Real Image	Phase Image
85	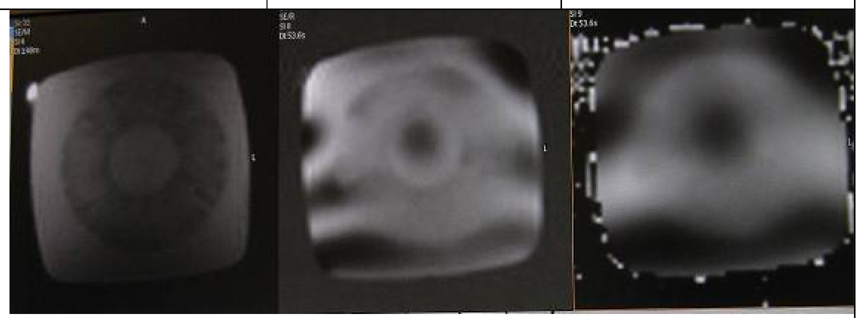		
100	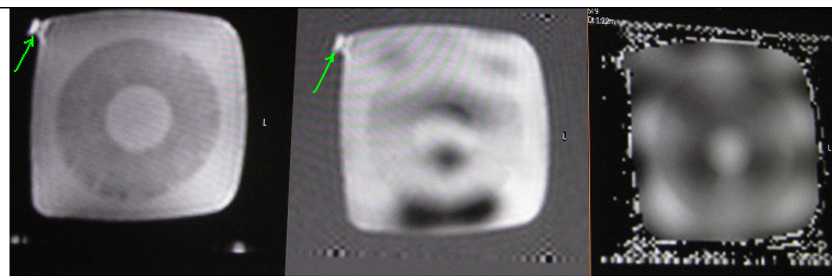		
125	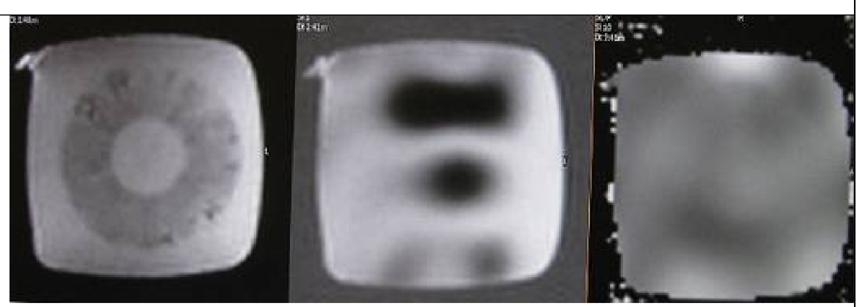		

Table 5- 1 The orthotropic MR imaging recorded within the frequency range (85-125 Hz) for the pineapple gelatin phantom is depicted in this Table. From left to right, the $T2^*$ weighted magnitude image, the real part of the image with smooth waves and the phase pattern with a low level of artifact and high perturbation in the motion pattern are shown. Small arrows illustrate the position of one fiducial marker.

One suggestion to solve this problem can be using an asymmetrical inclusion such as a quadratic pineapple. In this research, the three dimensional MRE dataset captured from this developed pineapple gelatin phantom was used for the image reconstructions. Results obtained from shear modulus and displacement reconstructions are presented in the next chapter.

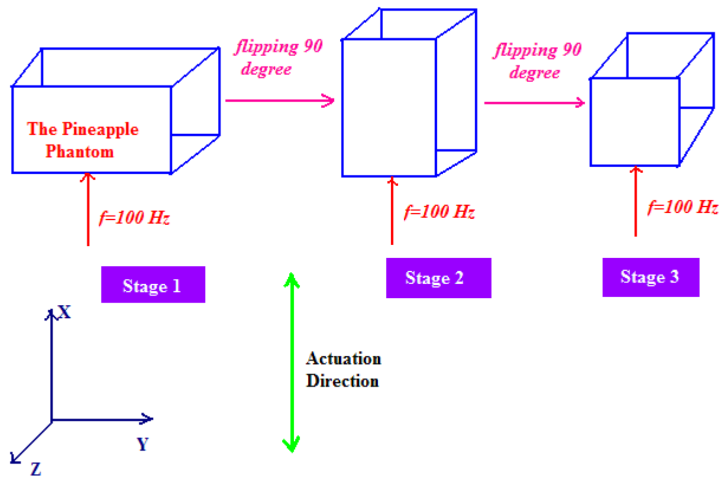

Figure 5- 43 This schematic depicts three stages of the boundary conditions derived from Fig. 5.40. This picture illustrates one specific frequency (i.e. 100Hz) assigned on the pineapple gelatin phantom in 3D while the phantom is being excited in the X direction. This specific frequency can also be changed to 85 Hz and 125 Hz.

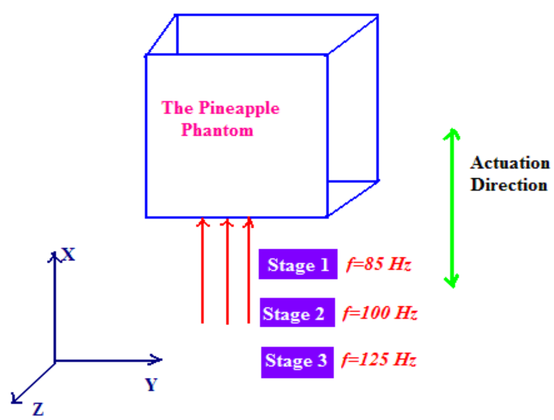

Figure 5- 44 This schematic displays another three stages of the boundary conditions derived from Fig. 5.40. This picture shows three frequencies (85 Hz, 100Hz and 125 Hz) applied on the pineapple gelatin phantom in 1D while the phantom is being excited in the X direction.

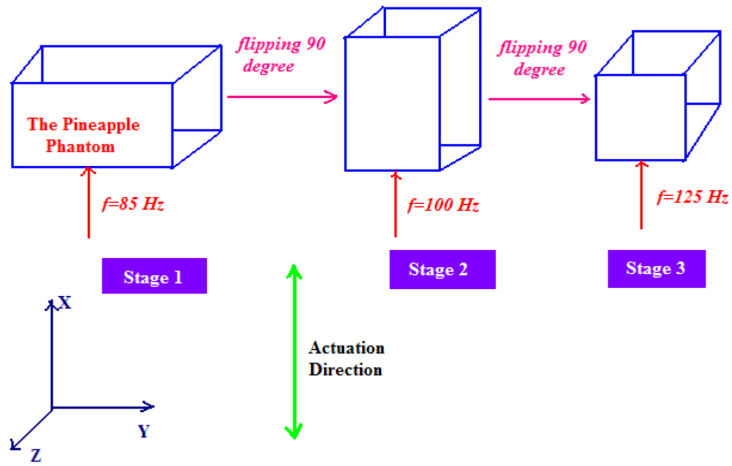

Figure 5- 45 This schematic shows the last three stages demonstration of the boundary conditions obtained from Fig. 5.40. This picture indicates three different frequencies (85 Hz, 100Hz and 125 Hz) assigned on the pineapple gelatin phantom in 3D while the phantom is being excited in the X direction.

5.4 Non-Biological Tissue-like Gelatin Phantoms

Fabricating non-biological composite-like gelatin phantoms using some bristles for *in vitro* MRE testing were other approaches which were developed for this research. These phantoms were designed and manufactured to simulate tissue as a bio-composite material and validate other biological phantoms which were made during this investigation. This attempt was also taken to evaluate the ability of non-biological tissue-equivalent gelatin phantoms to mimic the orthotropic behavior.

5.4.1 Bristles Phantoms

By definition, a composite material is a matrix reinforced by fibers where the mechanical properties of these two materials are significantly different. These fibers can be aligned within the matrix with different orientations. Composites demonstrate significant directional elasticity properties, when they are reinforced with continuous fibers [195, 196, 197, 198, 199].

By considering the tissue as a bio-orthotropic composite, two non-biological tissue-like gelatin phantoms were developed with bristle fiber inclusions to investigate the orthotropic behavior of a non-biological composite in vitro. In this study, these two non-biological tissue-like gelatin phantoms are described as vertical and circular bristle gelatin phantoms. Both phantoms were made from natural fiber Palmyra bristles (Carlisle Sanitary Maintenance Products, USA) and the gelatin from porcine skin (Type A, Sigma, Life Science Inc, USA).

5.4.1.1 Vertical Bristle Gelatin Phantom

The vertical bristle gelatin phantom in this study includes bristle fibers which are suspended in the vertical position inside the gelatin phantoms and a bunch of them are considered as a stiffer inclusion. The vertical bristles gelatin phantom simulates the tissue as an orthotropic bio-composite material that is reinforced by micro fibers and filaments and causes the difference in mechanical properties. The fiber orientation in the vertical bristle gelatin phantom shown in Fig. 5.50 displays the path of each fiber which is straight and fairly well aligned in parallel with other fibers.

- **Manufacturing Protocol**

The fabrication protocol to make the background of the vertical bristle gelatin phantom followed the same fashion as pineapple gelatin phantom base. The homogenous gelatin solution was prepared in the same manner as explained above and was then poured in the large greased plastic container ($14\times21\times8$ cm) to make a gelatin base for the phantom (Fig. 5.47-A). Four fish oil capsules (Ultra Omega DHA/EPA, Country Life, USA) were chosen as markers (Fig. 5.46-A) and then placed inside of the plastic phantom box corners on the gelatin base top (Fig. 5.46-B). This coordinate system and the location of fish oil capsules are shown in Fig. 5.46-B. Two of these markers were stuck on each other to represent direction Z. One marker was located in one corner of the phantom box to illustrate the X direction and the other one was arranged in the middle of one side to show direction Y.

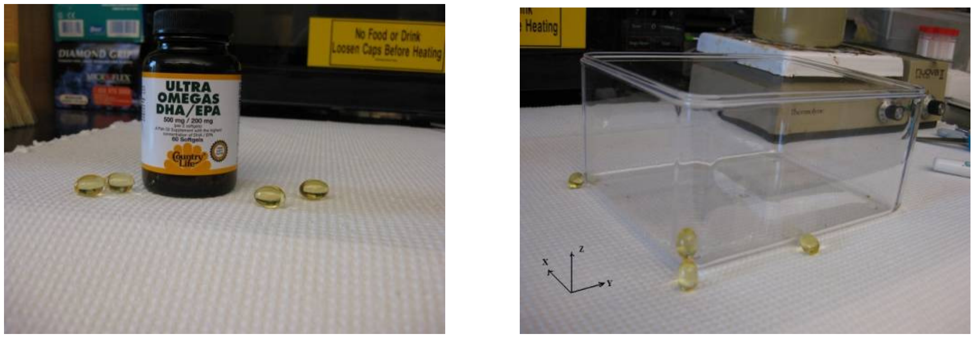

A **B**

Figure 5- 46 The coordinate system was determined for the vertical gelatin phantom by using four fish oil capsules which were chosen as phantom coordinate system markers (A). The demonstration of this coordinate system before locating the fish oil capsules inside the plastic container is depicted (B). Two of these markers were stuck on each other to represent direction Z. One marker was located in one corner of the phantom box to illustrate the X direction and the other one was placed in the middle of one side to show direction Y.

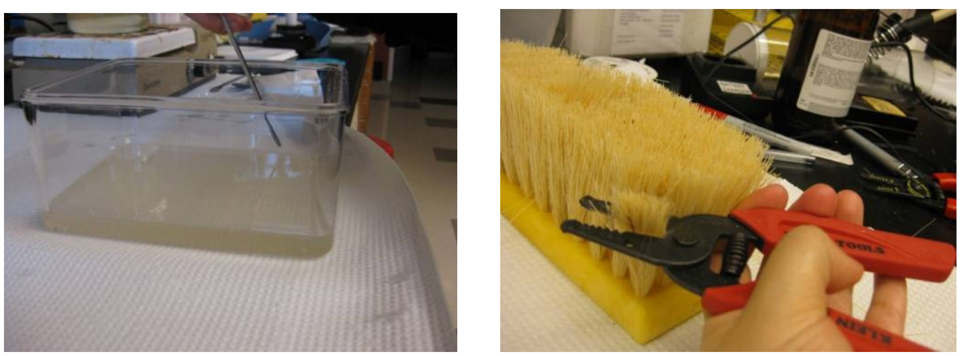

A **B**

Figure 5- 47 The first layer of gelatin phantom base (around 2 cm) which is partially set (A) and the bristles being cut by a wire-cutter (around 3 cm in height) (B) are displayed.

This was to identify the phantom orientation while it is being imaged as these markers can be seen as three bright spots during the MRI scanning. After the first layer of gelatin was partially set, bristles were cut by a wire-cutter with a height around 3 cm (Fig. 5.47-B) and planted on the gelatin base top (Fig5.48-A).

The coordinate system was determined for the vertical gelatin phantom in the same manner as discussed in the 4.3.1. To avoid air bubbles forming, the gelatin mixture was poured from a corner of the plastic container gently (Fig. 5.49). Vertical bristles were surrounded by the gelatin solution which was poured very slowly again from a corner of the container to prevent air bubble forming. This phantom was again refrigerated overnight to facilitate setting and to provide a suitable environment for the phantom before MRI scan. The vertical bristle gelatin sample was kept in room temperature two hours before imaging (Fig. 5.50).

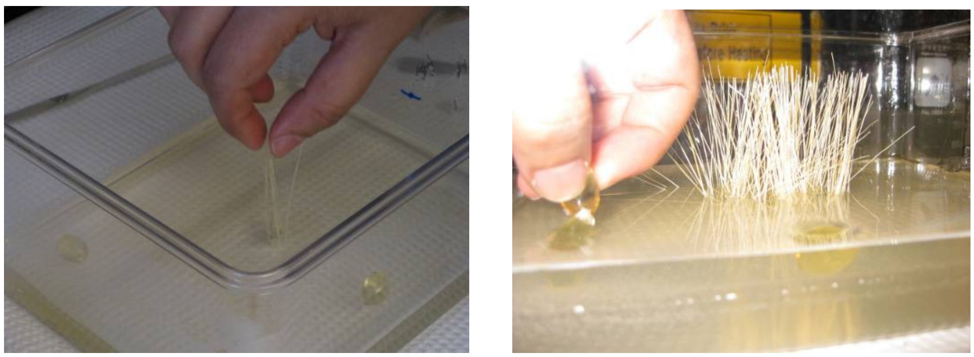

A **B**

Figure 5- 48 These images depict planting the bristles on the gelatin phantom base top vertically (A) and also inserting the fish oil capsules inside the gelatin base to determine a coordinate system for the phantom (B).

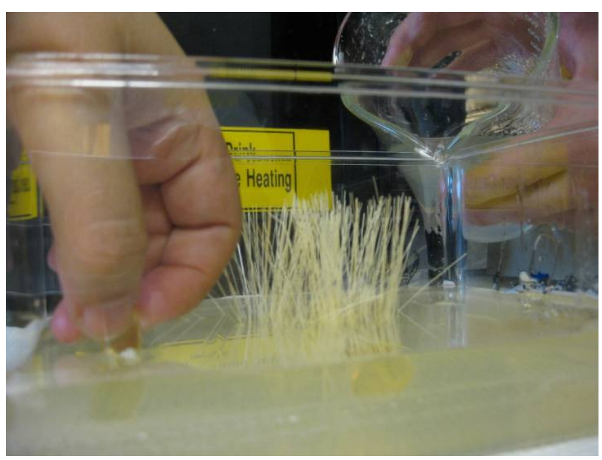

Figure 5- 49 This image shows the correct method of pouring the gelatin inside the phantom box to prevent air bubbles forming. As this picture depicts, the gelatin solution should be poured from a corner of the plastic container gently so that the solution would be in contact with the box’s wall.

- **Orthotropic Data Acquisition**

Figures 5.51 and 5.52 are displayed two views of the experimental set up for the composite-like vertical gelatin phantom. The orthotropic vertical bristle gelatin phantom was placed on the membrane top of the pneumatic actuation system in the presence of two surface coils for MRE imaging. The phantom-coil system was secured by sand bags to prevent undesirable movement of the actuation system during the excitation.

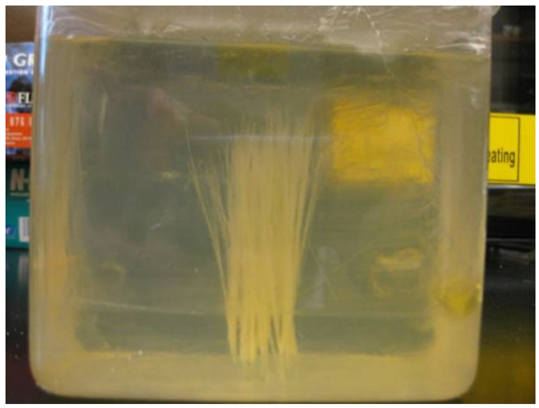

Figure 5- 50 This image illustrates the completed vertical bristles gelatin phantom with suspended bristle fibers as a stiffer inclusion aligned in one vertical direction.

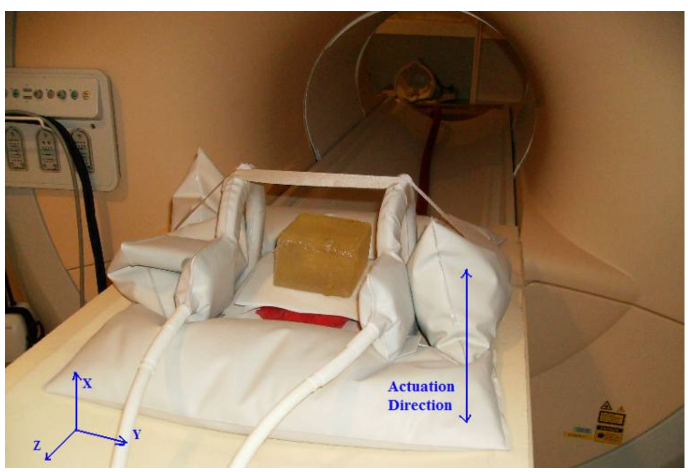

Figure 5- 51 The experimental set up for the vertical bristle gelatin phantom while sitting on the membrane of the pneumatic actuator with the excitation in X direction. The position of the surface coils and sand bags while they are supported by wrapping adhesive strapping around the coils and sand bags is shown.

Figure 5- 52 Another view of the same experimental set up for the vertical bristle gelatin phantom while it has been flipped 90^o to obtain multiple measurements in 3-D from this orthotropic composite-like sample.

As figure 5.51 shows the phantom was excited in the X direction. The MRE dataset was collected with fifteen slices while the voxel size was $2\times2\times1.8$ mm including a 0.9 mm slice gap and with the slice thickness of 18 mm. Figure 5.52 illustrates another view of the vertical gelatin phantom set up while the phantom has been flipped 90^o.

- **Orthotropic Boundary Conditions**

Figure 5.53 depicts a schematic of boundary conditions applied to the vertical bristle gelatin phantom to record sufficient motion data from this orthotropic composite-like sample in 3D. The phantom was scanned in three stages with one excitation frequency of 100 Hz. In each stage, this load condition was assigned on the side of the phantom which resting on the actuator membrane and in the excitation direction (X). This boundary condition allows the phantom move free on its other five sides. By rotating the phantom 90^o in 3-D and applying the frequency for this orthotropic composite phantom, multiple independent measurements in 3-D could be obtained.

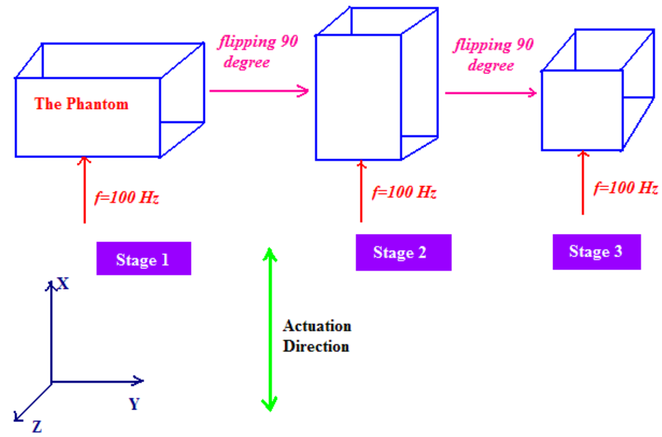

Figure 5- 53 This schematic shows three stages of the boundary conditions applied to the vertical bristle gelatin phantom. This picture depicts that only one specific frequency of 100Hz was assigned on the phantom in 3D while the phantom is being excited in the X direction. The phantom has been flipped 90^o in each stage to capture multiple measurements in 3-D from this orthotropic composite-like sample.

- **Protocol Analysis and Manufacturing Remarks**

Figure 5.54 demonstrates the MR magnitude image recorded from the vertical bristle gelatin phantom in 3D. While the stiffer bristles inclusion could be captured in the MR image, bristle fibers are not significantly visible especially in the X-Y plane because of their very small thickness and one directional orientation. Early shear modulus image reconstructions of the vertical bristle phantom have not also shown the bristles inclusion significantly within the gelatin phantom. This idea may be modified by using thicker fibers in different fiber orientations.

5.4.1.2 Circular Bristle Gelatin Phantom

The laminated circular bristles inclusion was constructed from three stiffer fiber layers embedded in the soft gelatin base. Short straight fibers were aligned radially in a circular shape in the centre of the phantom. The circular fiber layer with different orientation around of a circle determines an orthotropic plane with respect to the rectangular axes.

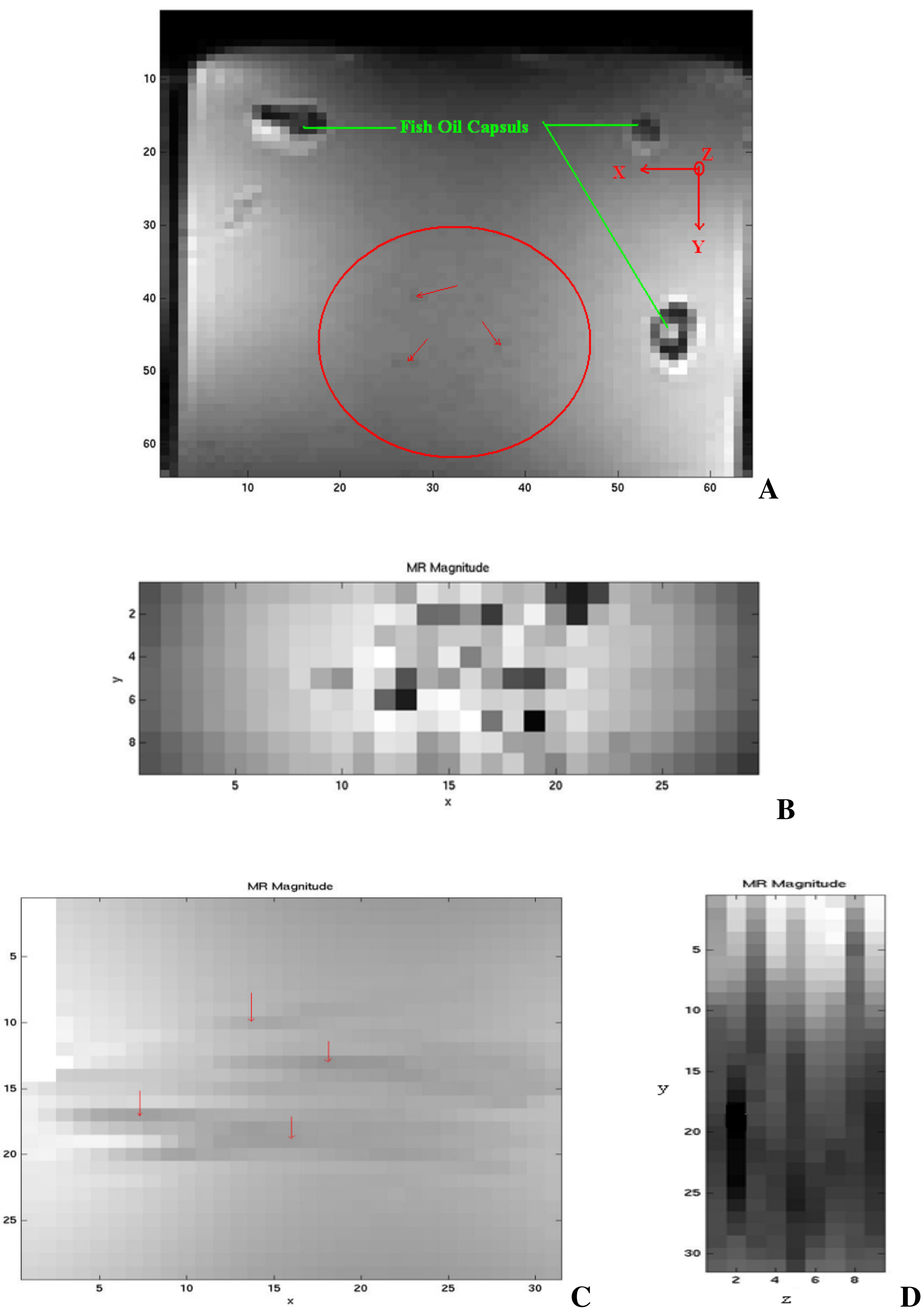

Figure 5- 54 This picture depicts four views of the MR magnitude image (T^{2*} weighted) recorded from the vertical bristle gelatin phantom. Fish oil capsules positions which indicate the phantom coordinate system in the MR image and the bristle fibers cross sectional inside the circle shown by some arrays (A) another view of the bristle fibers cross section in the x-y plane (B) the x-z plane view of fibers illustrated by some arrays (C) bristle fibers in the y-z plane are displayed.

The non-biological circular gelatin phantom was made to simulate and validate the biological pineapple gelatin phantom for the *in vitro* MRE testing. This phantom included three circular bristle layers which were suspended inside the homogenous gelatin background.

- **Manufacturing Protocol**

The same fabrication method with the same materials (bristles and gelatin) as vertical bristle gelatin phantom was used to manufacture the gelatin base of the circular gelatin phantom. Bristles were again cut by a wire-cutter with a height around 3 cm and arranged in the middle size greased plastic container ($9.5\times15.5\times6.5$ cm) on the gelatin base top which was already set to make the first circular bristles layer.

The coordinate system was determined for the circular gelatin phantom by fish oil capsules as well as vertical gelatin phantom with the same fashion but with one difference. To determine the Y direction of the coordinate system, the fish oil capsule was located in another corner of the plastic phantom box instead of the middle container side as was used for the vertical bristle phantom (Fig. 5.55).

The second layer of homogenous gelatin solution was gently poured from the corner of the plastic container on the arranged circular bristles to cover them completely by gelatin. After the second gelatin layer was set, the third circular bristles layer was made with same manner as above and was surrounded by gelatin solution again. The phantom was then kept in the refrigerator overnight to facilitate the final setting.

- **Orthotropic Data Acquisition**

The circular bristle gelatin phantom was scanned by the MRI system in the same fashion as vertical bristle phantom. The sample was brought to room temperature two hours before MR imaging. Figure 5.57 illustrates the experimental set up for the composite-like circular gelatin phantom.

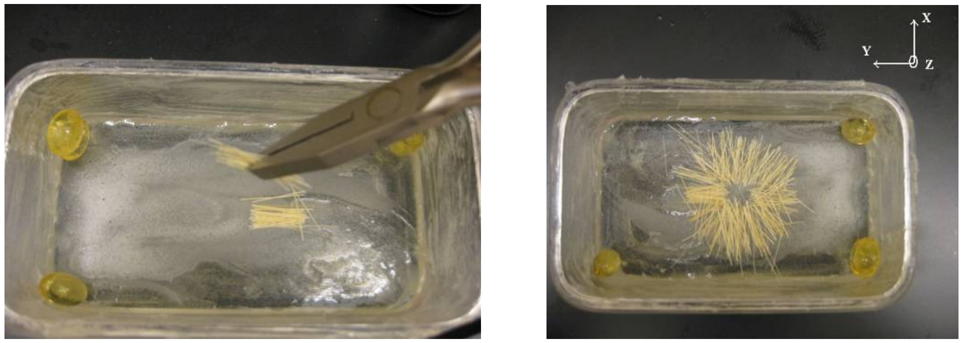

A B

Figure 5- 55 This image depicts the arrangement of the first bristle layer of the circular bristle phantom (A) along with fish oil capsules in three corners of the greased plastic phantom box which determine the phantom coordinate system (B). These fish oil capsules can be illuminated in the MR image as three bright spots. The completed first bristle layer of the circular bristle phantom is also shown in B.

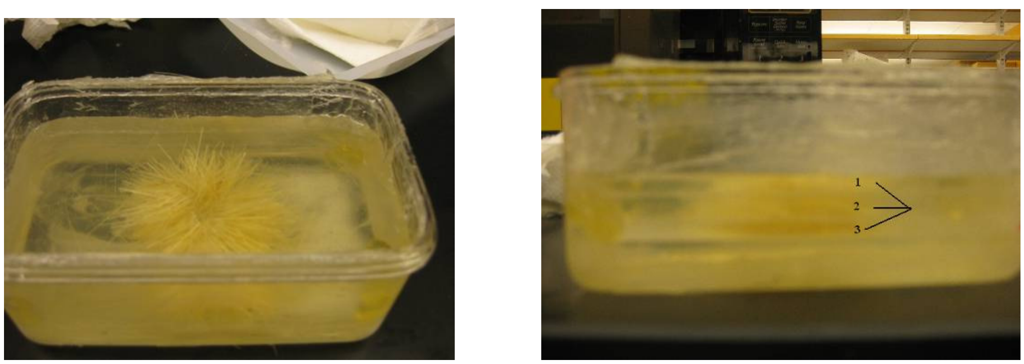

A B

Figure 5- 56 These images display two views of the completed circular bristle gelatin phantom with a circular stiff laminated inclusion made from three bristle layers (A). Three circular bristle layers of stiffer inclusion are shown in B.

The orthotropic circular bristle gelatin phantom was placed on the membrane top of the pneumatic actuation system while two surface coils were located on the both sides of the phantom for MR imaging. The phantom-coil system was again secured by sand bags to avoid undesirable shaking of the actuation system during the excitation. The phantom was excited with the frequency of 100 Hz in the X direction.

The MRE dataset was captured with fifteen slices while the voxel size was $2\times2\times1.8$ mm including a 0.9 mm slice gap and with the slice thickness 1.8 cm.

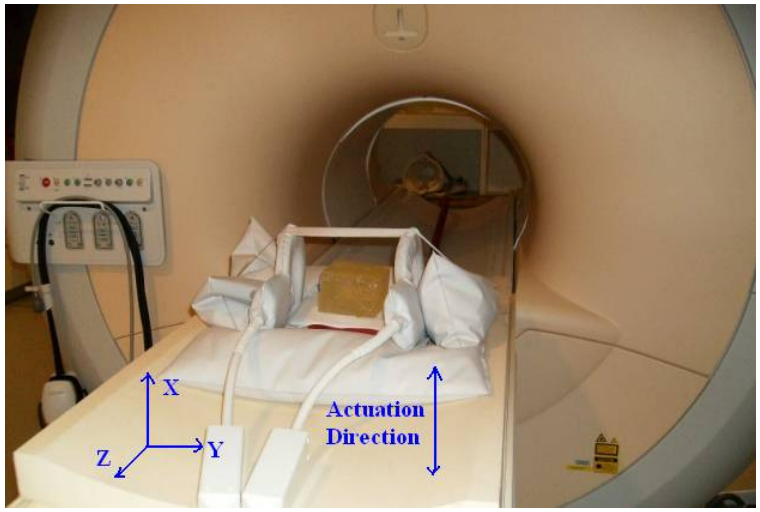

Figure 5- 57 This image depicts the test condition for the circular bristle gelatin phantom. This picture displays the phantom-coil experimental set up before the system is inserted inside the MR bore. The phantom is resting on the membrane of the pneumatic actuator with the excitation frequency of 100 Hz in the X direction. The position of the surface coils and sand bags while they are supported by wrapping adhesive strapping around the coils and sand bags is also shown.

- **Orthotropic Boundary Conditions**

The schematic of boundary conditions assigned to the circular bristle gelatin phantom is depicted in figure 5.58. The phantom was scanned in three stages with one excitation frequency of 100 Hz. In each stage, this load condition was assigned on the side of the phantom which was resting on the actuator membrane and in the excitation direction (X). By this method of boundary load condition, the motion data can be collected sufficiently from this orthotropic composite-like sample in 3D. This boundary condition allows the phantom to move freely on its other five sides while it is only constrained on one side. By rotating the phantom 90^o in 3-D and applying the frequency for this phantom, multiple independent measurements in 3-D could be obtained.

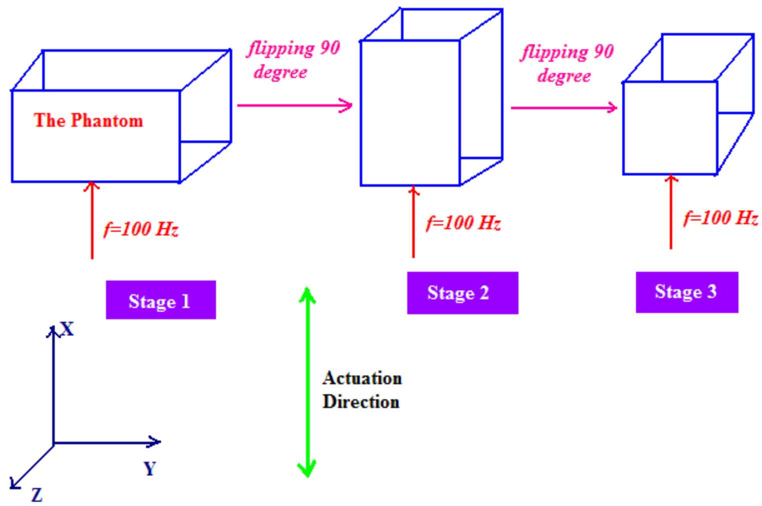

Figure 5- 58 This schematic depicts three stages of the boundary conditions applied to the circular bristle gelatin phantom. This picture illustrates that only one specific frequency of 100Hz was assigned on the phantom in 3D while the phantom is being excited in the X direction. The phantom has been flipped 90^o in each stage to capture multiple measurements in 3-D from this orthotropic composite-like sample.

- **Protocol Analysis and Manufacturing Remarks**

The orthotropic circular bristle gelatin phantom with stiffer laminated inclusion was fabricated for this MRE testing with no significant air bubbles in the gelatin background. The satisfactory orthotropic MRI dataset was captured with the frequency of 100 Hz from circular bristles gelatin with a visible stiffer inclusion with circular fiber orientations (Table 5.2). Three independent boundary conditions stages with one specific frequency in 3D could provide more information which is needed to capture all the mechanical properties of this orthotropic phantom in 3D during the image reconstruction procedure.

While the laminated inclusion with three circular bristle layers spread in X-Y plane of the phantom was more visible in the MRI imaging in comparison with the one directional vertical bristle phantom, there is still an issue regarding the fairly symmetrical geometry of the circular bristles inclusion.

Mode / Frequency (Hz)	Magnitude Image	Real Image	Phase Image
100	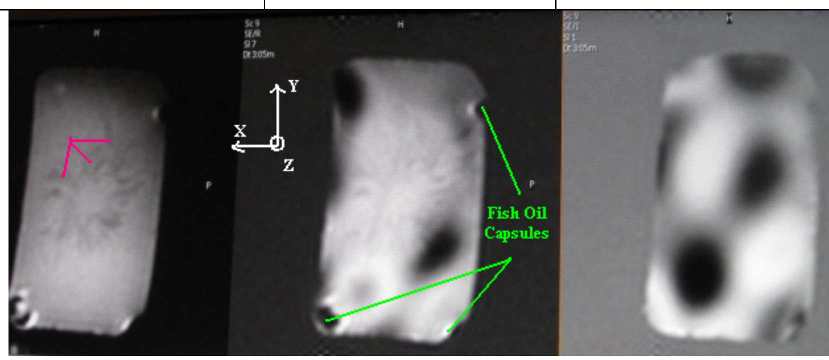		

Table 5- 2 This table depicts the orthotropic MR imaging ($T2^*$ weighted) of the circular bristle gelatin phantom with the excitation frequency of 100 Hz. From left to right, the magnitude image, the real part of the image with smooth waves and the phase pattern with a low level of artifact and high perturbation in the motion pattern are displayed. Different circular fiber orientations of the stiffer inclusion are shown in the magnitude image (left). Fish oil capsules are visible which also indicate the phantom's orthogonal coordinate system.

The problem with a symmetrical inclusion (i.e. in the X-Y plane) is that in the orthotropic elasticity image reconstruction, different shear modulus may not be distinguished from two different directions and the shear modulus obtained from the X direction would be the same as the Y direction.

One potential major issue is that the rectangular phantom box is not proportional with the circular inclusion and this caused a reduction in the gelatin matrix around the inclusion on the longer side. This point is important as artifacts are often generated around the phantom boundaries. As a result, when the distance between inclusion and the phantom boundaries is small, this artifact may overlap with the inclusion in the elasticity image reconstruction.

In the phantom fabrication, the ratio between phantom matrix and the inclusion should be considered so that sufficient gelatin matrix surrounds the inclusion to keep the inclusion far from the phantom boundaries.

Initial orthotropic shear modulus image reconstructions of the circular bristles phantom have shown a poor visibility of the bristles inclusion within the background. This indicates that the bristle fibers' thickness was rather thin for this inclusion. One approach to improve bristle inclusion would be using thicker fibers by attaching a large number of bristles together.

5.2 Orthotropic Incompressible Phantom Developments Applied to MRE

The heart of each MRE testing beats with a high quality MRI dataset with a low level of artifacts. It is important to consider the factors which affect reaching this point, as they can cause the failing of the whole elastography procedure.

In MRE phantom studies, the elimination of artifacts from each step, such as phantom fabrication and data acquisition procedures, is essential as each of these stages plays a key role in obtaining high image quality, and limiting chances of the misrepresentation of artifacts which may give confusing or erroneous results.

In this research, the main focus was on developing a variety of orthotropic phantoms and fabricating them for MRE testing using a robust manufacturing protocol to evaluate a realistic orthotropic, incompressible model.

Along with phantom fabrication, several modifications were made to the phantom-coil set up by considering three dimensional boundary conditions to improve the MRE data acquisition procedure suitable for orthotropic incompressible materials that can be a guide line for future MRE clinical applications.

Three orthotropic incompressible MRE datasets were successfully developed from biological and non-biological gelatin phantoms using the manufacturing protocols, mentioned in this chapter for the next MRE procedure; the orthotropic elasticity image reconstruction.

Fabricating biological gelatin phantoms using fruit for MRE orthotropic *in vitro* testing is a novel technique which was developed for this research. The pineapple was chosen to manufacture the biological gelatin phantom as this natural fibril reinforced bio-composite material can be considered to be a highly orthotropic material owing to its structural properties and different fibril orientations. This method was a simple, inexpensive, and efficient way to generate the orthotropic MRE datasets of a biological material *in vitro*.

The successful fabrication of a pineapple a gelatin phantom has indicated that the manufacturing protocol for this phantom is capable of producing tissue-like gelatin phantoms with no significant air bubbles in the background. Reducing air bubbles in MRE phantoms is a major issue as no MR signal can be generated from air bubbles, and in the resulting image they are seen as null spots, which can lead to artifacts and significantly affect the image reconstruction results.

The satisfactory improvement of the orthotropic data acquisition from one specific frequency to three different frequencies collected in one set of data and in three different actuation directions relative to the phantom, where all of these frequencies were applied to one side in each actuation procedure, was another approach which was developed for this research.

Multiple measurements from the pineapple gelatin phantom were made by applying several independent boundary conditions within the frequency range (85-125 Hz) in three orthogonal dimensions, could provide a complete record of MRE information which is needed to capture all mechanical properties of this orthotropic phantom in 3D during the image reconstruction procedure. This completed MRE dataset can cover three individual load conditions: one specific frequency (i.e. 100Hz) in 3D relative to the phantom, three different frequencies (i.e. 85 Hz, 100 Hz and 125 Hz) in 1D, and three different frequencies in 3D with respect to the phantom in that each frequency is assigned to one side of the phantom.

Experience from initial elasticity image reconstruction has shown that using an inclusion with symmetrical geometry such as circular pineapple can cause ambiguity in the shear modulus reconstructions, as for example by considering circle in the X-Y plane, the reconstructed shear modulus obtain from the X direction may be very similar to the shear modulus in the Y direction due to symmetry. For future phantom fabrication, using an asymmetrical inclusion shape is suggested.

The ability of the pineapple gelatin phantom to mimic tissue with orthotropic properties is more validated by evaluating the results obtained from elasticity image reconstructions, which will be discussed in the following chapters.

Bristle gelatin phantoms with vertical and circular inclusions were also successfully developed to manufacture non-biological composite-like phantoms *in vitro*, with one specific frequency applied in three stages for recording the orthotropic MRE datasets in 3D. While the stiffer bristles inclusion could be captured in the MR image, early shear modulus image reconstructions of the vertical bristle phantom have not shown the bristle inclusion significantly within the gelatin phantom.

While the laminated inclusion of the circular bristle gelatin phantom with three circular bristle layers was more visible in the MRI imaging in comparison to the one directional vertical bristle phantom, there is still an issue regarding the fairly symmetrical geometry of the circular bristles inclusion, as mentioned above.

One potential major issue of the circular bristle gelatin phantom was that the size and geometry of the circular inclusion were not proportional with the rectangular phantom box. This reduced the distance between the inclusion and the phantom boundaries, which potentially can cause the artifacts around the phantom boundaries in the image reconstruction procedure. This leads to an important point in the phantom fabrication process. The ratio between the phantom matrix and the inclusion should be considered given that sufficient gelatin matrix is surrounding the inclusion, to keep the inclusion far away from the phantom boundaries.

Initial orthotropic shear modulus image reconstructions of the circular bristles phantom have shown fairly poor visibility of the bristles within the background. This indicates that the bristle fibers' thickness was rather thin for this inclusion. One approach to improve bristle inclusion would be using thicker fibers by attaching a large number of bristles together.

In the developing of muscle phantoms, the satisfactory material property transformation using several techniques such as the laser transmission, electricity, electrosurgery device, and chemical components, has shown that these methods are capable of creating a stiffer *ex vivo* inclusion within the muscle phantom.

However, muscle phantoms and tissue-like gelatin phantoms have a limited lifetime and they need to be discarded after use. Preferably, they should make one day before MRI scan as the accuracy of the test will be reduced by repeating the experiment on the same phantom.

While the goal of elasticity property transformation using these techniques has been achieved, more modifications are still needed to create a well formed inclusion within the muscle phantom, and to capture a high quality MRI dataset. Questions still remain over the development of the inclusion fabrication techniques for the ex vivo muscle phantoms which will require more complete testing to prepare a suitable *ex vivo* muscle phantom with a stiffer inclusion for orthotropic elastography experiments.

For future MRE muscle phantom tests, replacing the bovine muscle phantom with other animal muscle such as chicken muscle can be another alternative used to make a harder inclusion using heat, as it may have a better thermal conductivity to create a suitable inclusion within the phantom.

Selecting a suitable inclusion regarding the material type and its geometry for the *in vitro* orthotropic gelatin phantoms, whether biological or non-biological, which can mimic the real tissue behavior is still an open question needing more investigation.

"All that we are is the result of what we have thought".

Buddha

Chapter 6

6.1 Orthotropic Incompressible Reconstructive Imaging

The elasticity property results obtained from three dimensional reconstructive imaging presented in this chapter used a robust algorithm which was specifically developed for non-linear 3-D orthotropic incompressible materials. This investigation into the distributed orthotropic incompressible parameter reconstruction was performed to indicate how well this novel material property reconstruction algorithm will be able to detect differences in orthotropic incompressible shear stiffness parameters in three dimensions.

The ability of the pineapple gelatin phantom to mimic the tissue with orthotropic properties is validated by evaluating the results obtained from orthotropic and isotropic elasticity image reconstructions which will be discussed in the followings sections. As early reconstruction tests set orthotropic phantoms fabricated for this research, the pineapple gelatin phantom indicated better results, therefore, the MRE information recorded from this phantom was chosen for orthotropic incompressible image reconstructions.

In this investigation, the results of orthotropic elasticity reconstructions from real MRI datasets captured from the pineapple gelatin phantom are evaluated. The resultant orthotropic shear moduli distributions in 3-D obtained from different initial guesses, along with displacement patterns are discussed.

For the orthotropic pineapple gelatin phantom, several isotropic image reconstructions with the same initial guesses as orthotropic reconstructions were attempted.

Isotropic image reconstructions used the incompressible linear elasticity algorithm to evaluate the correlation between two orthotropic and isotropic reconstructions in three directions.

6.2 Pineapple Phantom Image Reconstructions

As mentioned in 5.2.2, the problem with the symmetric pineapple inclusion was that in the orthotropic elasticity image reconstruction, different shear moduli may not be distinguished from two different directions (the symmetrical plane) and this can cause ambiguity in the reconstructed shear modulus analysis. To remove this problem, an arc shaped quarter section of the circular inclusion pineapple phantom was considered for the orthotropic finite element implementation to reduce this problem as much as possible. The elasticity image reconstruction analysis with orthotropic incompressible algorithm has shown that the procedure of the orthotropic inverse reconstruction is prohibitively slow. For example, only a few iterations were taking weeks to generate reconstructed image results.

Considering a quarter of the full MRE dataset collected from the pineapple gelatin phantom was also a way to reduce the number of nodes and elements in the FE model and consequently increased the calculation speed.

6.3 Orthotropic Reconstructions Using Real MRI Datasets

Orthotropic elasticity image reconstructions were carried out to map orthotropic elasticity properties (shear moduli) in 3-D based on MR detected motion datasets captured from the pineapple gelatin phantom.

The capability of the orthotropic reconstruction program to generate accurate results using the real MRE data is demonstrated through these reconstructions of a tissue-mimicking pineapple gelatin phantom.

The full MRE datasets collected from the pineapple gelatin phantom comprised three different actuation directions with respect to the phantom in which each direction included three different frequencies, 85 Hz, 100, Hz and 125 Hz. From the three actuation directions in the frequency range 85-125 Hz, the MRE motion datasets actuated with the frequency of 85 Hz in the global dimension X was chosen for this specific study to produce the orthotropic FE model, and then for image reconstructions.

The FE model used the 27 node quadratic hexahedral element to implement the geometry of the model with 523 elements and 5285 nodes from the real MRE datasets with an arc shaped pineapple inclusion. The cubic subzone geometry with a zone overlap of 15% and a zone size ratio of 3, 2 and 1 in X, Y and Z, respectively was considered. The subzone based orthotropic incompressible reconstruction algorithm was based on the nonlinear CG optimization method to gain computational efficiency, and also used TV regularization techniques with a weighting regularization parameter of 1.d-5 to constrain the solution process by controlling the relative abnormal irregularities of the parameter solution in the optimization problem.

The adjoint-residual approach was also utilized to improve the efficiency of the gradient descent based algorithm. The global iteration limit was 100 for CG and 1 per zone to facilitate the material property solution approaching convergence. As this was the first time that the algorithm was tested for orthotropic incompressible reconstructions, a variety of settings for the various options in the program were arranged to find the optimal configuration. The initial guess for the material property is one of these parameters, which seems to affect the reconstruction results. This initial guess can be an initial value of a quantity which needs to be minimized (i.e. shear modulus). A good choice of initial guess can help the algorithm converge to the actual solution.

The strategy is that the iterative optimization algorithm begins with an initial guess of the parameter to be reconstructed and builds up in a sequence of updated estimates until they meet the solution. In this improving sequence, the technique is to move from one iterate to the next.

In this investigation, one goal is to show the sensitivity of the algorithm to the initial guess as well as finding an optimum initial guess for our orthotropic elasticity image reconstructions, which directs the procedure to the actual solution as much as possible.

For this iterative approach, different initial guesses for the real shear modulus within the value range of 1-20 KPa were taken to reach a successive approximation for a correct solution for each set of reconstruction procedures. Initial guesses used for this study were, 1 KPa, 2 KPa, 3 KPa, 4 KPa, 5 KPa, 10 KPa, and 20 KPa. Usually sufficient information cannot be detected from the first and last slice of a full dataset, thus in this study, from the twelve slices that were obtained from MRE data acquisition, only nine slices were chosen for image reconstructions, the first two, and the last slice were discarded.

6.3.1 Orthotropic Reconstruction Analysis in Three Dimension

In this section, the orthotropic image reconstruction results from the pineapple gelatin phantom, with an arc shaped inclusion captured from orthotropic real MRI datasets are presented. A global coordinate system shown in upper case 'X', 'Y', and 'Z' was used as a reference to display the orthotropic results in three global directions. The displacement components in three directions were illustrated as u^X, u^Y, and u^Z. The orthotropic shear moduli results at each node were also shown as $\mu_{XY,}$ $\mu_{ZY,}$ $\mu_{ZX,}$.

The results in this section comprise the $T2^*$ MRI magnitude images distributed within nine slices (Fig. 6.1), presented individually in one single slice (slice 7) (Fig. 6.2), the orthotropic measured displacement patterns in three directions (Fig. 6.3), and the distribution of the orthotropic shear moduli in 3-D (Fig. 6.4). These results also represent the correlation between the $T2^*$ MR magnitude image of the arc shaped pineapple inclusion in three different positions with respect to a global 3-D reference frame. The $T2^*$ MR magnitude image, orthotropic magnitude shear modulus, and calculated orthotropic shear moduli, are correlated by default in the geometry and orientation in which they were either measured or calculated, as they are in the same orientation and geometry.

The orthotropic magnitude real shear modulus presented here is calculated by the equation (6.1). The orthotropic magnitude shear modulus at each node, μ_{mag}, is a scalar considered as a summation of squared orthotropic real shear moduli components $\mu_{XY,}\ \mu_{ZY,}\ \mu_{ZX,}$, reconstructed in three dimensions given as:

$$\mu_{mag} = \sqrt{\mathrm{Re}\left\{ (\mu_{XY})^2 + (\mu_{ZY})^2 + (\mu_{ZX})^2 \right\}} \qquad (6.1)$$

This equation shows that each calculated orthotropic shear modulus component has an allocation to build the orthotropic magnitude shear modulus. It should be pointed out that μ_{mag} is only a scalar without physical meaning and it is calculated only for comparison purposes in this research.

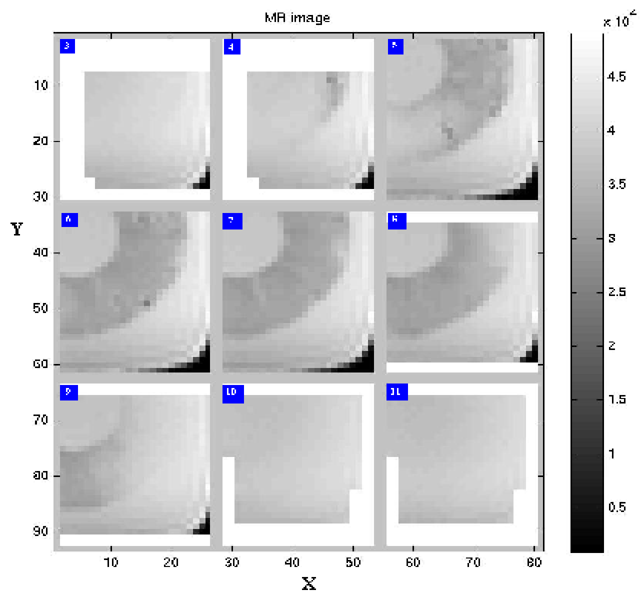

Figure 6- 1 This picture shows the $T2^*$ MRI magnitude images distributed within nine slices captured from the pineapple gelatin phantom with an arc shaped inclusion. The number labeled on the slices shows that only nine slices from slice number 3 to 11 were chosen and slices 1, 2, and 12 have been ignored as sufficient information could not be detected from these slices.

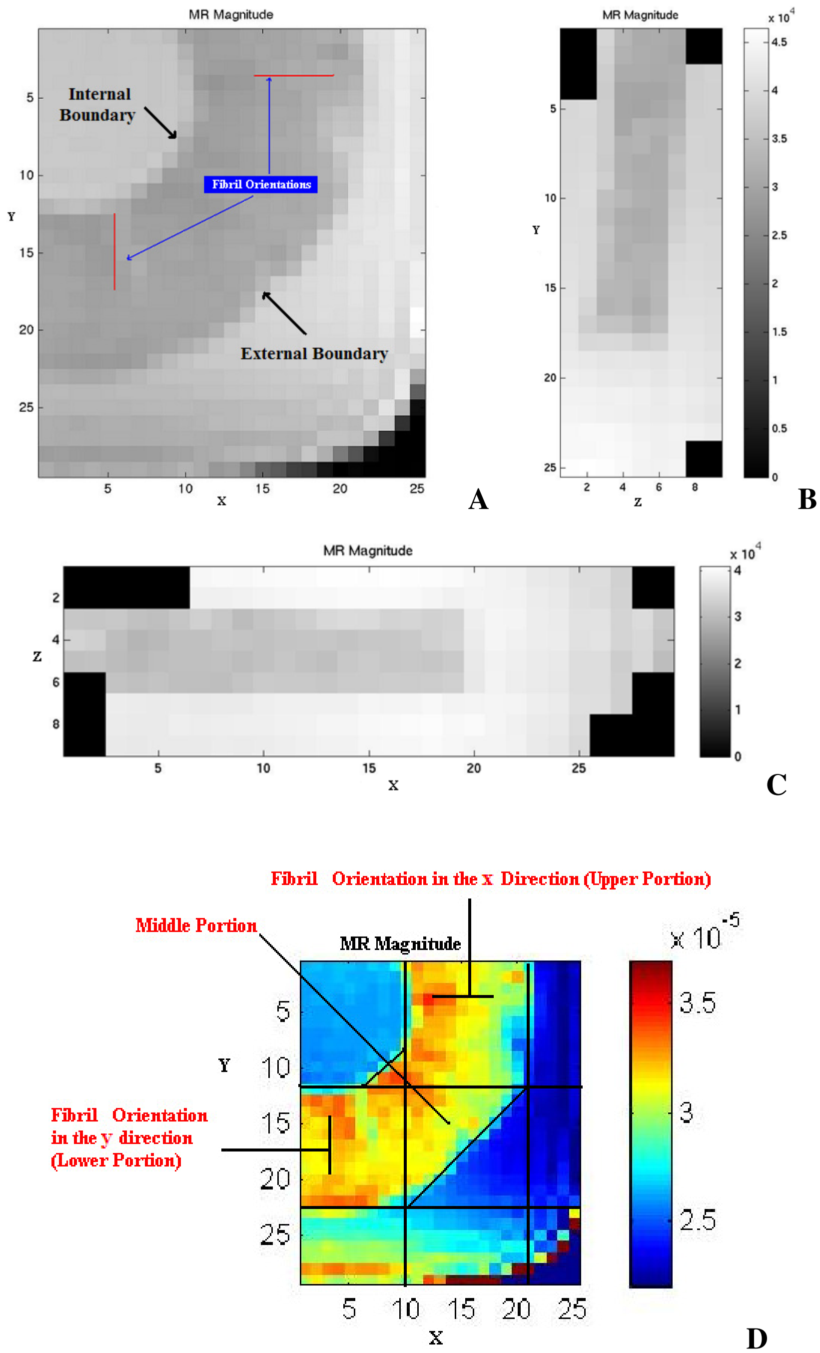

Figure 6- 2 The $T2^*$ MR magnitude images obtained from slice 7 of the pineapple gelatin phantom with an arc shaped inclusion. The inclusion's internal and external boundaries along with the fibril orientation in different directions are shown. The A, B, and C images show three views of the inclusion in three positions in a global coordinate system, X-Y frame (A and D), Z-Y frame (B), and Z-X frame (C). Upper, lower, and middle portions of the inclusion are also illustrated in (D).

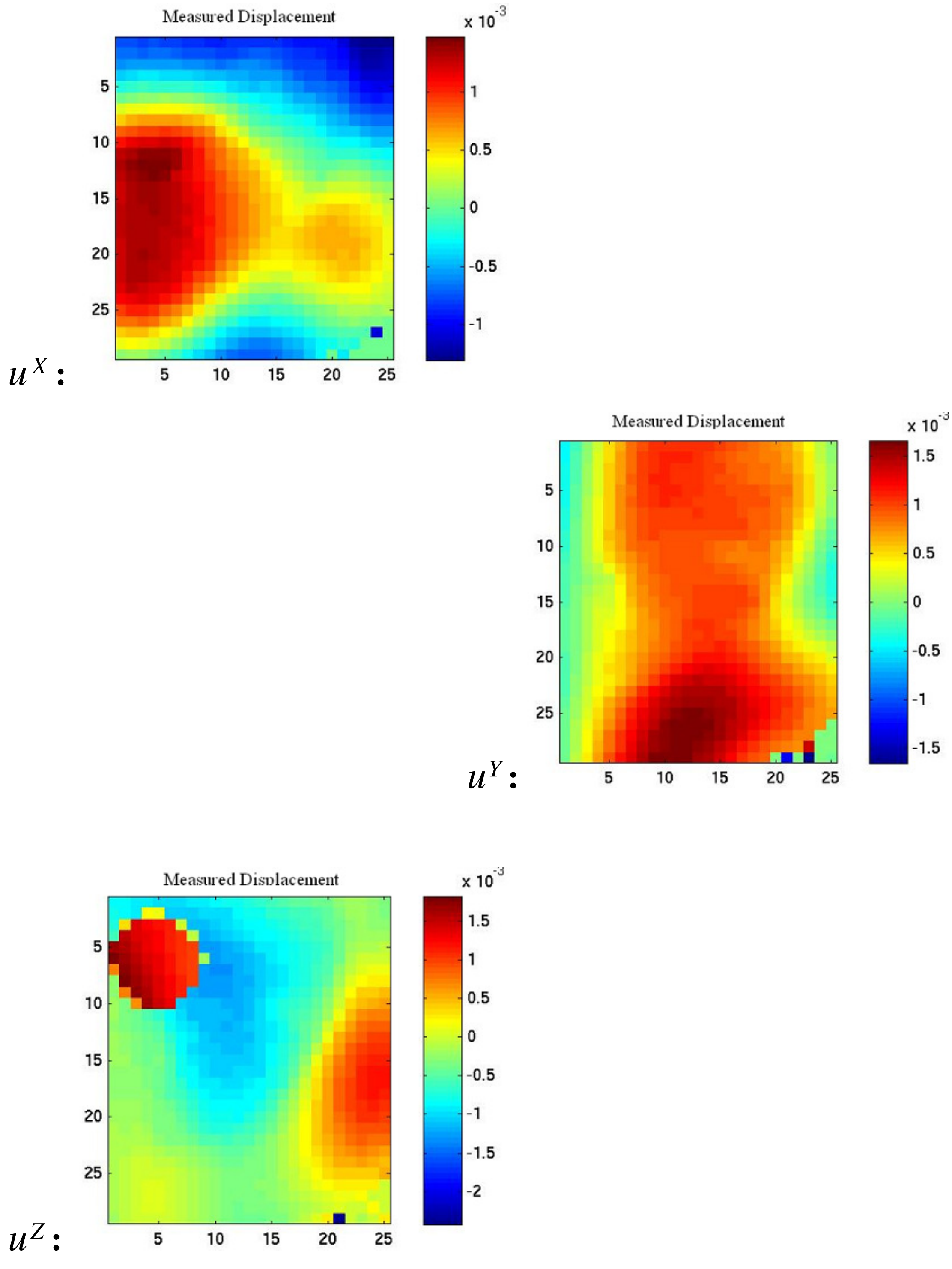

Figure 6- 3 The measured orthotropic displacement components in three orthogonal directions for slice 7 of the pineapple gelatin phantom with an arc shaped inclusion. Three different irregular motion patterns in the measured displacement field are displayed.

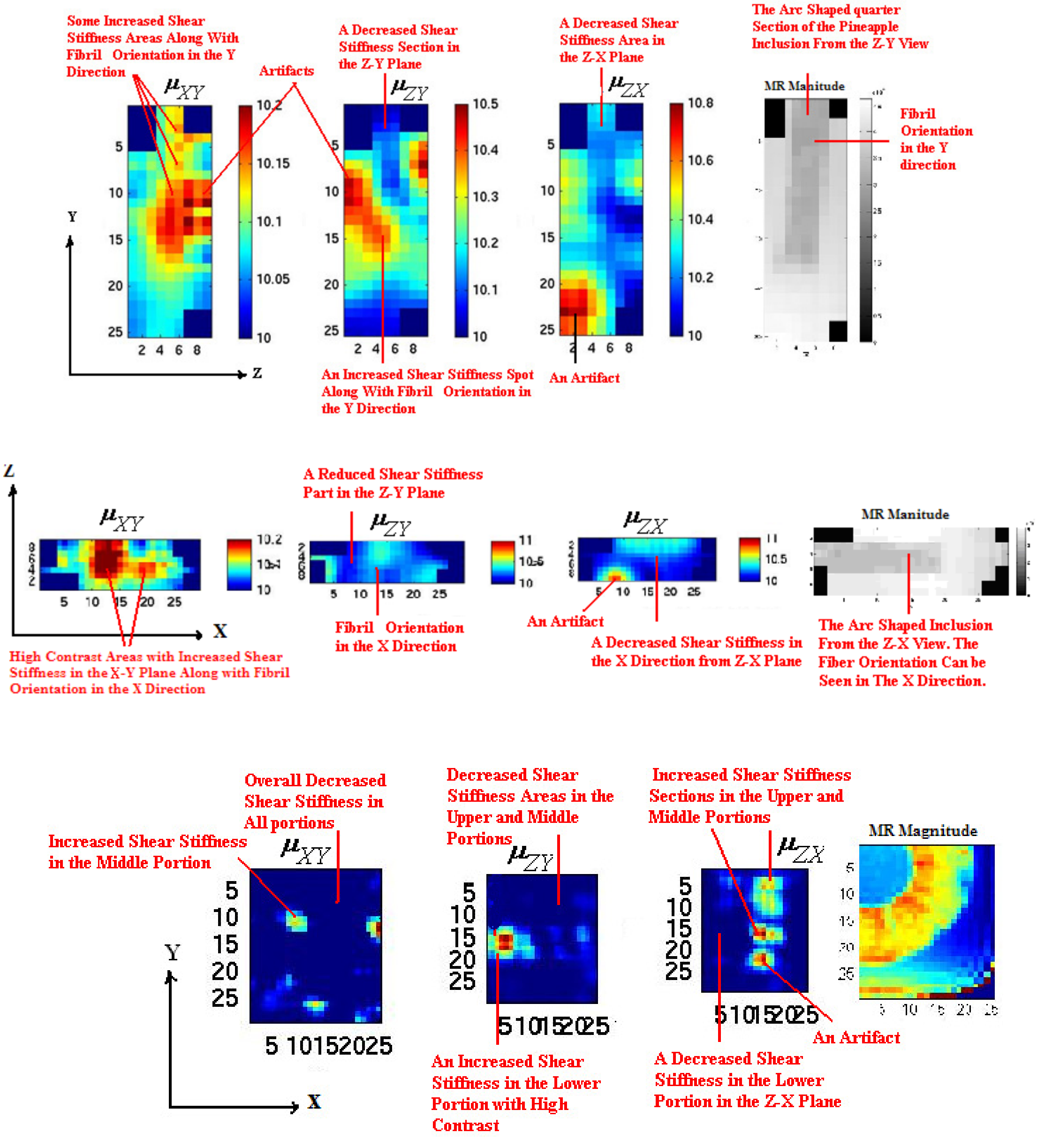

Figure 6- 4 The correlation between the $T2^*$ MR magnitude image and the reconstructed orthotropic real shear moduli distribution results from early iterations. These results obtained from slice 7 of the pineapple gelatin phantom with an arc shaped inclusion after three iterations when the initial guess was 10 KPa. The reconstructed orthotropic shear moduli components are shown with respect to the 3-D global coordinate system (X, Y, and Z). In each global coordinate system frame, the distributions of the shear moduli components at each node μ_{XY}, μ_{ZY}, μ_{ZX}, are depicted. The elevated shear stiffness obtained from the calculated shear moduli results is also displayed.

6.3.2 Orthotropic Correlation Reconstruction Results

The correlation results between the collected motion data known as "measured displacements" and displacements obtained from elastographic image reconstructions which are called "calculated displacements", are presented in this section. The correlation between the $T2^{*}$ MR magnitude image and the calculated orthotropic shear moduli results in three dimensions from slice 7 of the pineapple gelatin phantom with an arc shaped quarter inclusion also investigated.

Although in this research, all orthotropic image reconstructions were set for 100 iterations, this aim could not be reached in practice as the iterative sequence improvement of the orthotropic inverse optimization procedure was prohibitively slow.

The maximum iteration for these tests was 17 iterations which belonged to the orthotropic image reconstruction with an initial guess of 10 KPa using a runtime of nearly two months on the high performance super computer (HPC), accessed by 32 processors and 64 GB of memory for 400 hours. All orthotropic image reconstruction results presented in this section are from the highest available iteration for all of their higher iteration counts.

In this investigation, it was more convenient to choose the X-Y frame as a correlation reference to plot the correlation of the $T2^{*}$ MR magnitude image and the calculated orthotropic shear moduli solutions in three directions, as this frame corresponded to the original slice direction of the data. In fact, the resulting images were produced in the "slice plane", which is the plane that the slices were taken from using the original data.

Although the images are plotted only for one frame (X-Y), the correlation calculation takes into account all three dimensions of the data as correlation values are calculated for the full image volume (every voxel) in the reconstructed volume, and the plotted correlation image in one plane is only for reference purposes.

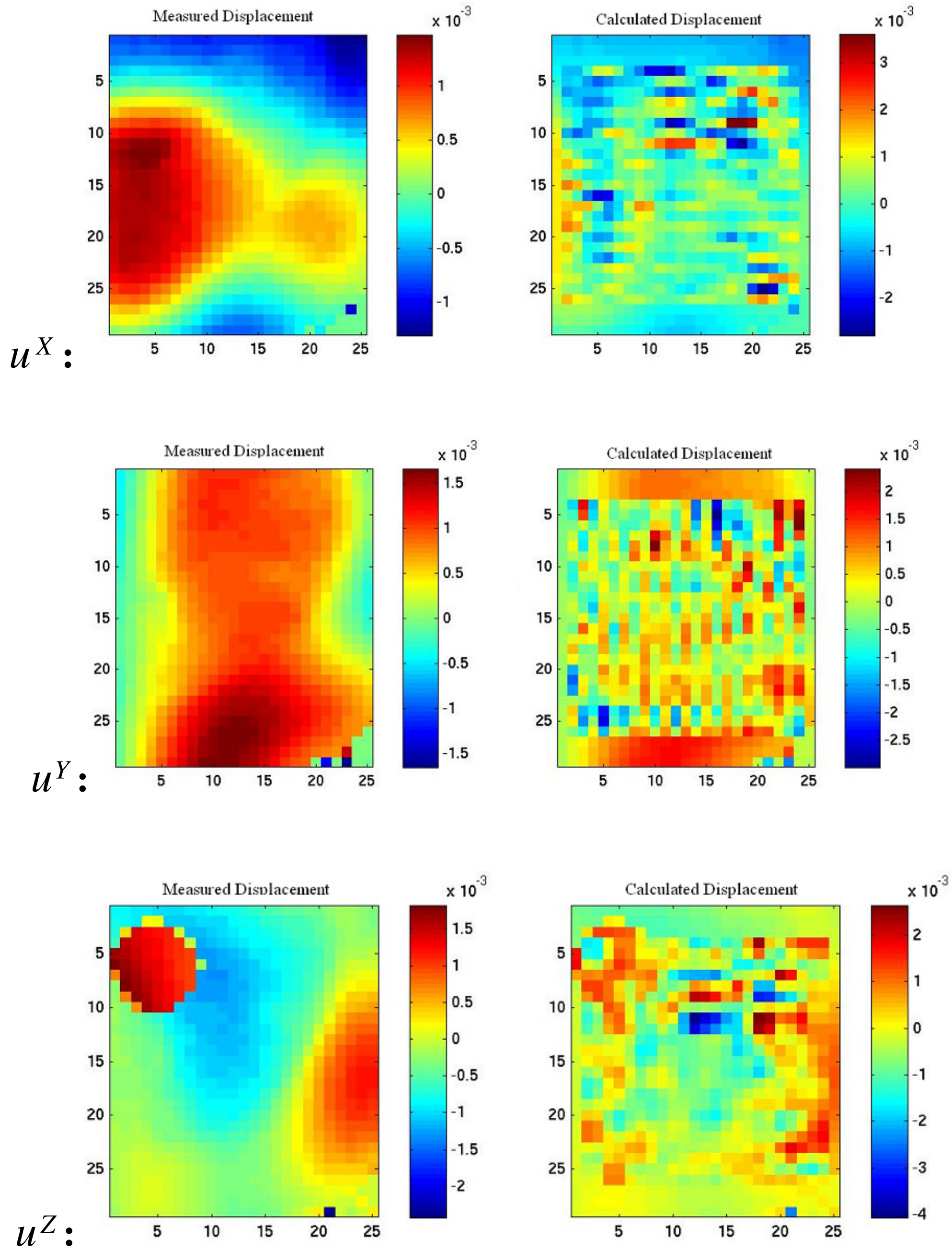

Figure 6- 5 The association between the measured and the calculated orthotropic displacement patterns in three different dimensions are displayed for slice 7 of the pineapple gelatin phantom with an arc shaped inclusion. The calculated orthotropic displacements in 3-D were obtained from the image reconstructions with an initial guess of 1 KPa. The irregular motion pattern is visible in the measured displacement field while a high level of artifact with a poor correlation can be seen in all calculated displacement images.

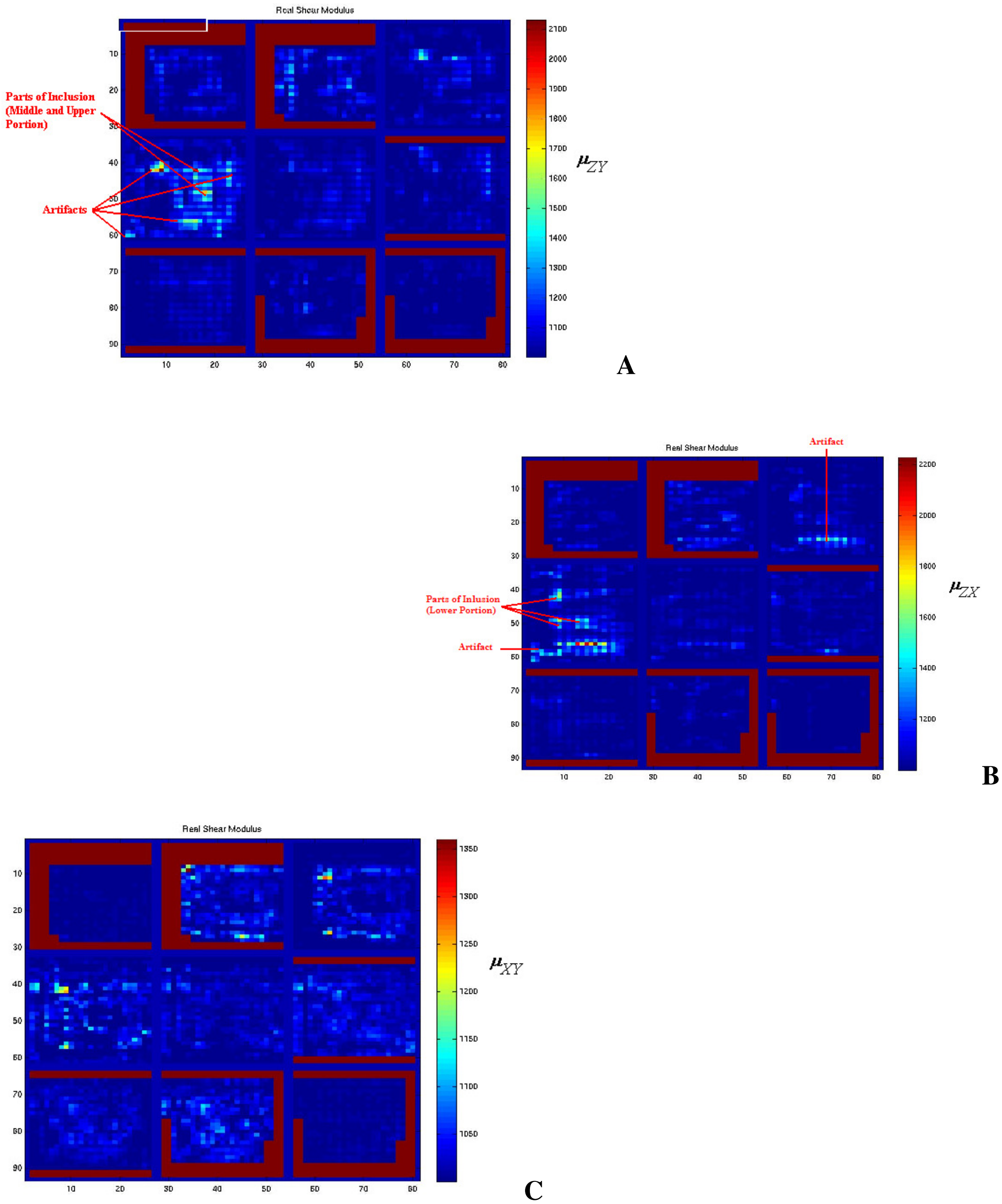

Figure 6- 6 Resulting reconstruction with an initial guess of 1KPa of the orthotropic real shear moduli distribution obtained from the nine slices of the pineapple gelatin phantom with an arc shaped inclusion are displayed. The reconstructed orthotropic shear moduli components μ_{XY}, μ_{ZX}, μ_{ZY} are depicted. A few spots of the inclusion have been recovered mostly in the (A) and (B), which show a poor elasticity reconstruction.

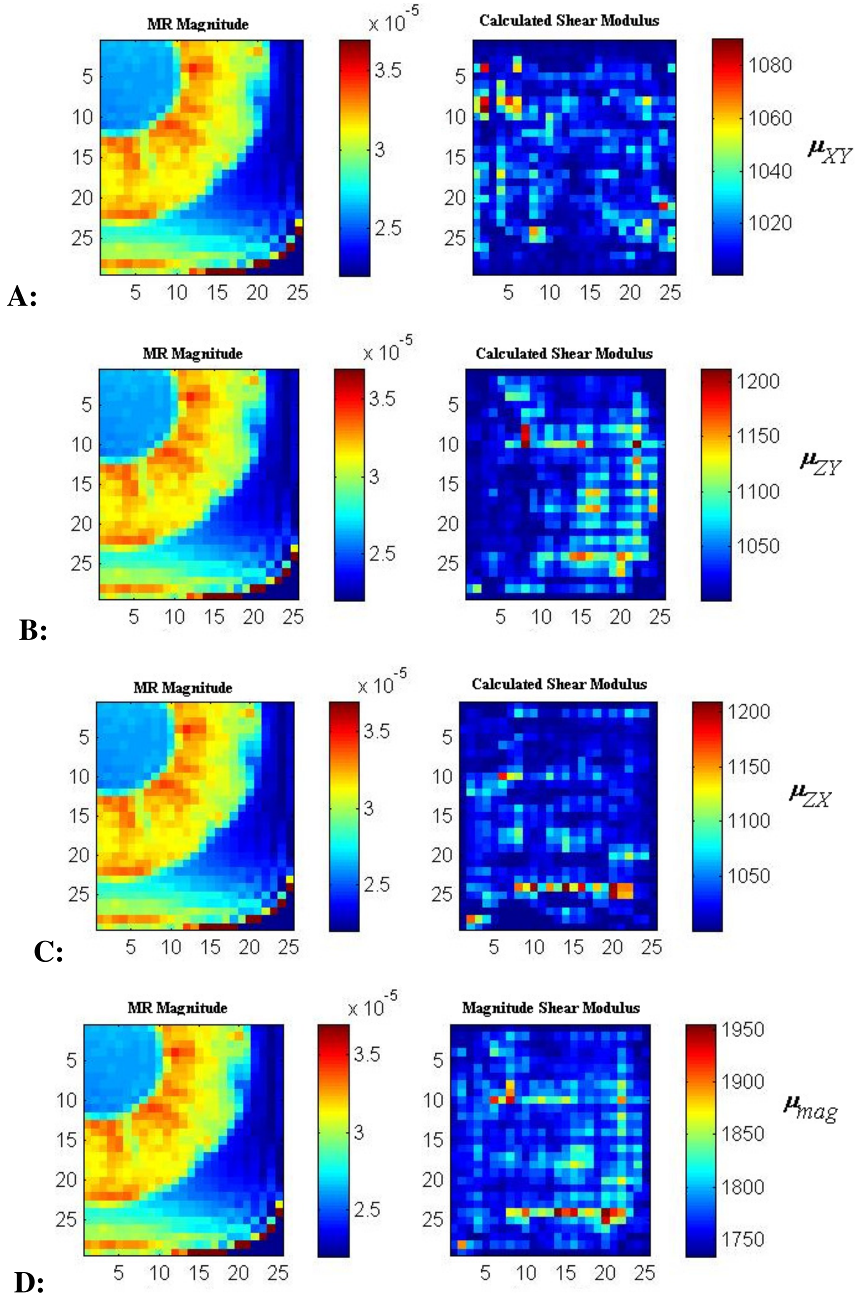

Figure 6- 7 Reconstruction results after six iterations with an initial guess of 1KPa are displayed for the orthotropic real shear moduli distribution obtained from slice 7 of the pineapple gelatin phantom with an arc shaped quarter inclusion. The correlation between the $T2^*$ MR magnitude image with the magnitude shear modulus and reconstructed orthotropic shear moduli components are depicted. A few spots of the inclusion have been recovered for all shear moduli components which overall show a poor elasticity reconstruction. Pictures also show a fairly high level of artifacts in the background while the whole inclusion is barely visible.

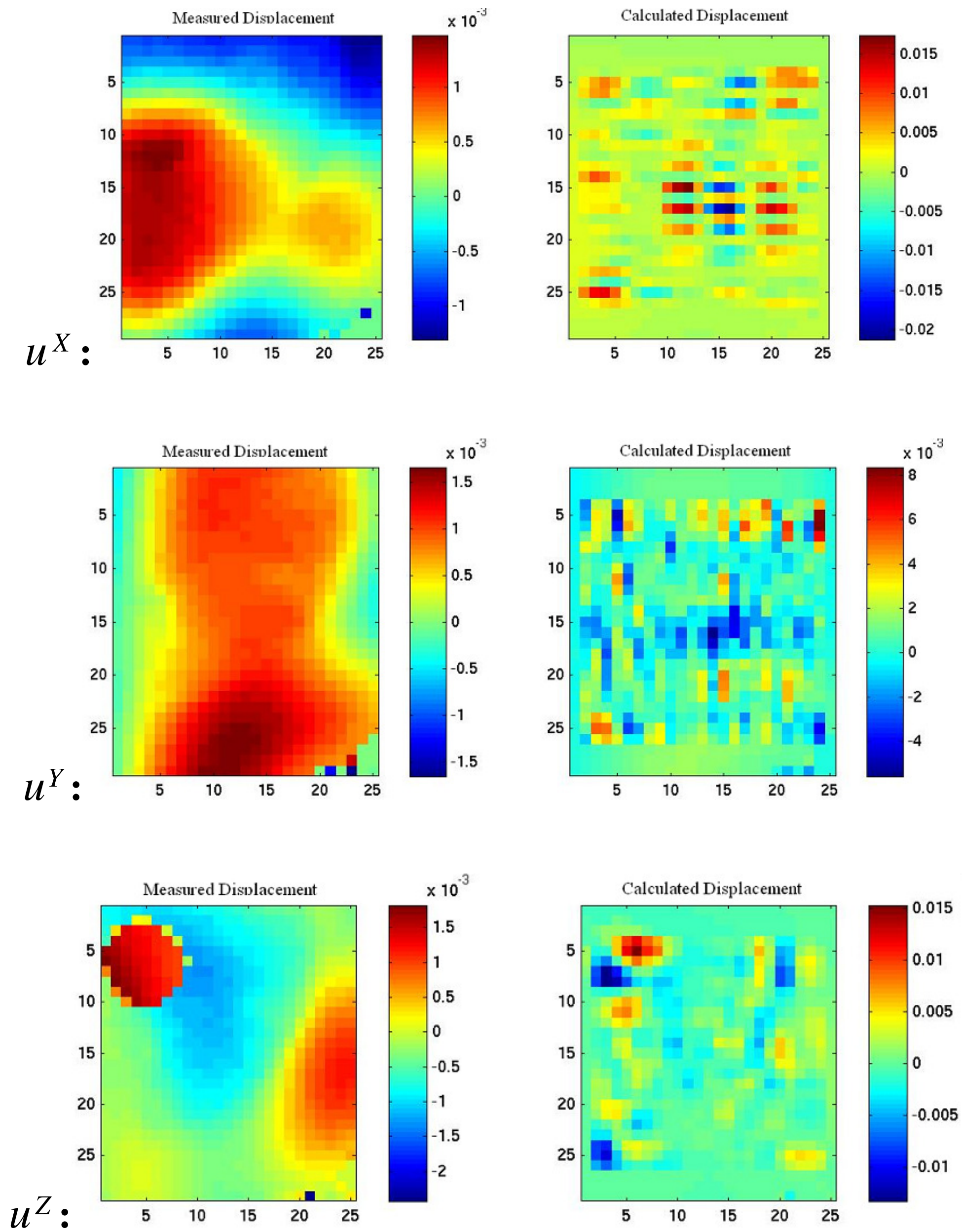

Figure 6- 8 These elastographic images show the correlation between the orthotropic measured and the calculated displacements field obtained from slice 7 of the pineapple gelatin phantom with an arc shaped inclusion with an initial guess of 2 KPa in three different dimensions. The orthotropic displacement reconstructions in 3-D show a poor motion pattern with a high level of artifact which can be observed in almost all calculated displacement images.

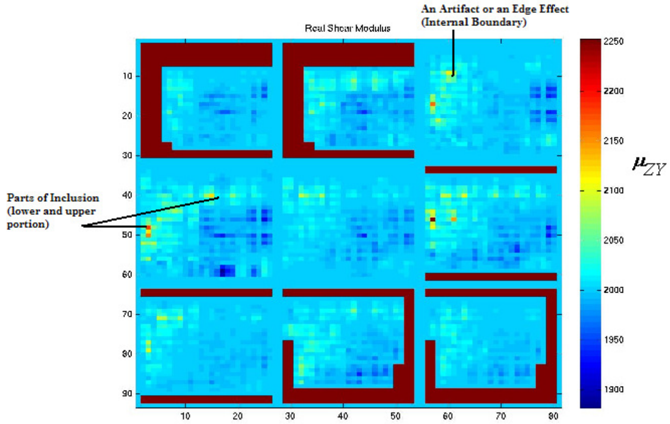

A

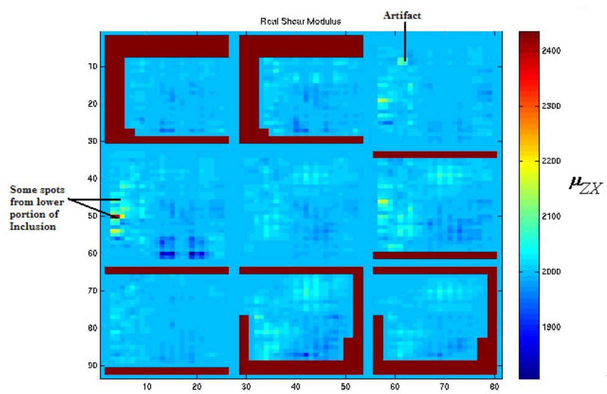

B

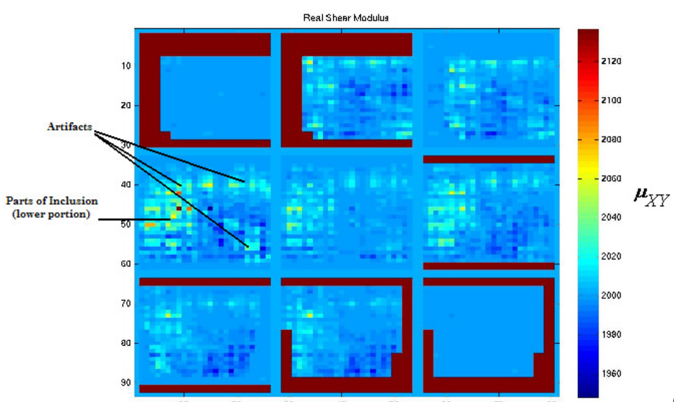

C

Figure 6- 9 These pictures show nine slices of reconstruction results with an initial guess of 2 KPa from the orthotropic real shear moduli distribution obtained from the pineapple gelatin phantom with an arc shaped inclusion. The orthotropic reconstructed shear moduli components μ_{XY}, μ_{ZY}, μ_{ZX}, are also depicted. Parts of inclusion from the lower portion of the pineapple are illustrated in all pictures. Artifacts can be seen in the background along with a few spots of the inclusion which reveal a poor elasticity reconstruction.

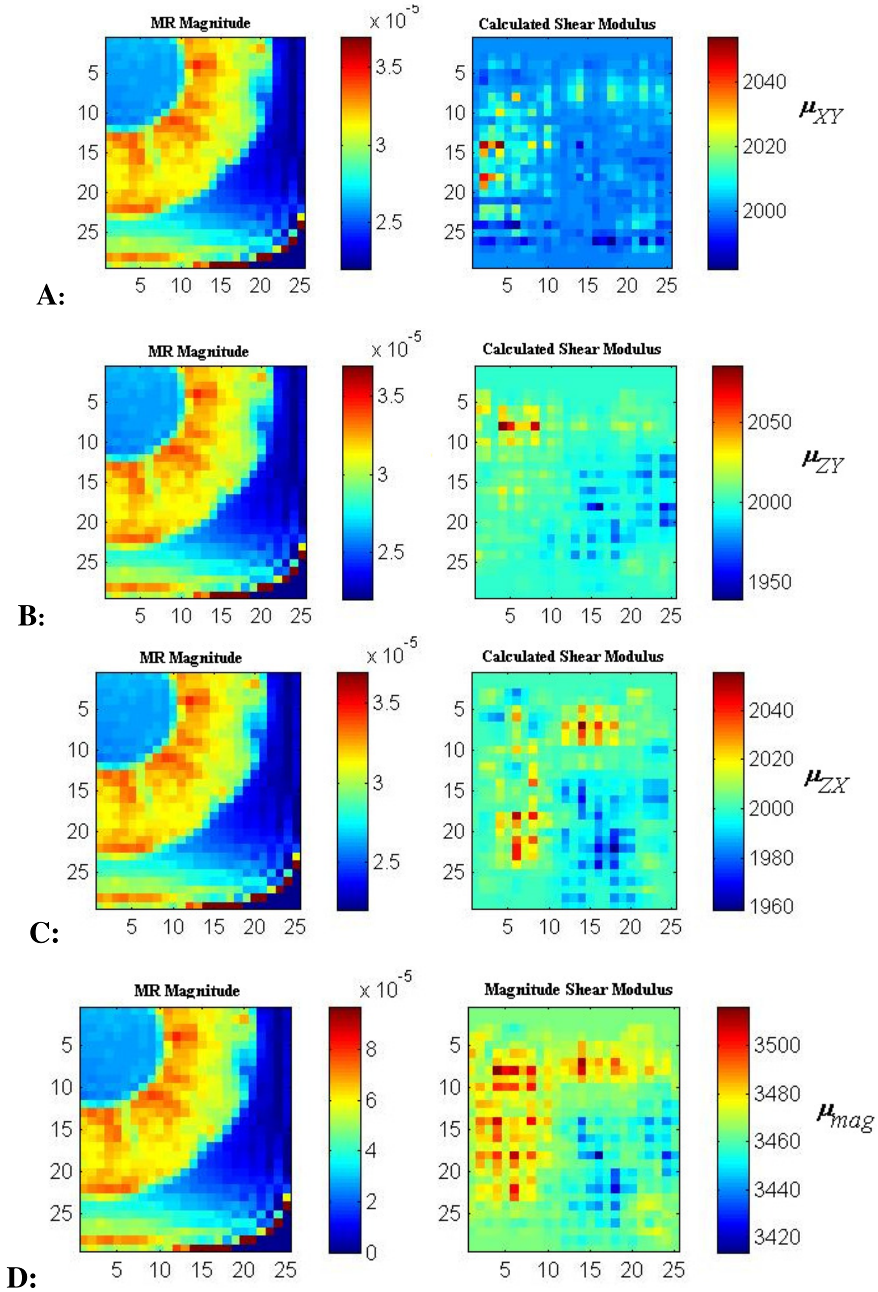

Figure 6- 10 These pictures show reconstruction results from slice 7 after one iteration with an initial guess of 2 KPa from the orthotropic real shear moduli distribution obtained from the pineapple gelatin phantom with an arc shaped inclusion. The orthotropic magnitude shear modulus and the reconstructed shear moduli components are depicted in correlation with the $T2^*$ MR magnitude image. Parts of the inclusion from the lower and upper portions of pineapple are illustrated mostly in (C) and also the lower portion in (A). A few artifacts are visible in the background and one significant artifact can be seen towards the centre.

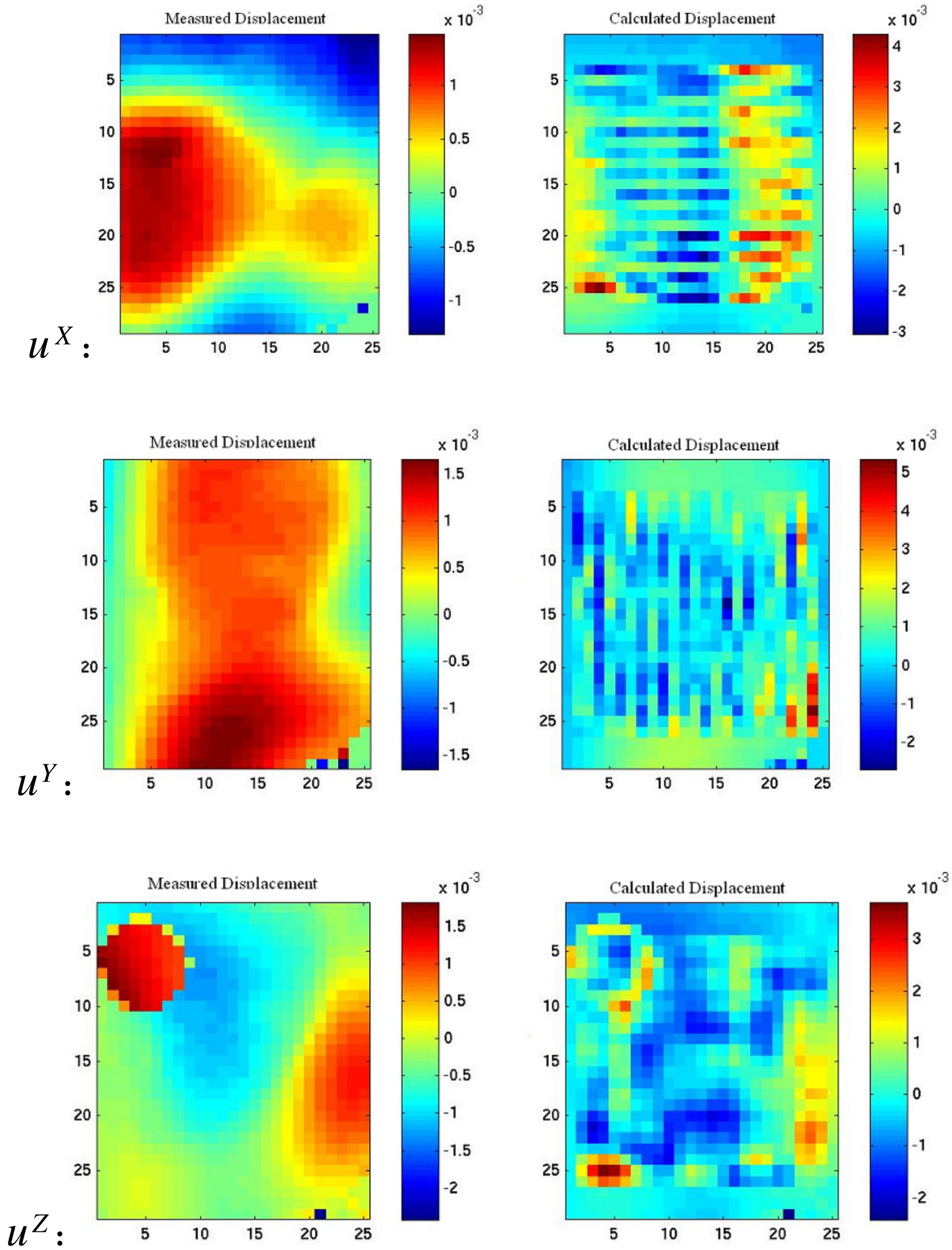

Figure 6- 11 The orthotropic real measured and calculated displacement patterns in three different dimensions for slice 7 of the pineapple gelatin phantom with an arc shaped inclusion are demonstrated. The orthotropic calculated displacements in 3-D were captured from the image reconstructions with an initial guess of 3 KPa. The motion direction, irregular pattern, a high level of artifacts, and a low level of correlation, are visible in all calculated displacements in three dimensions.

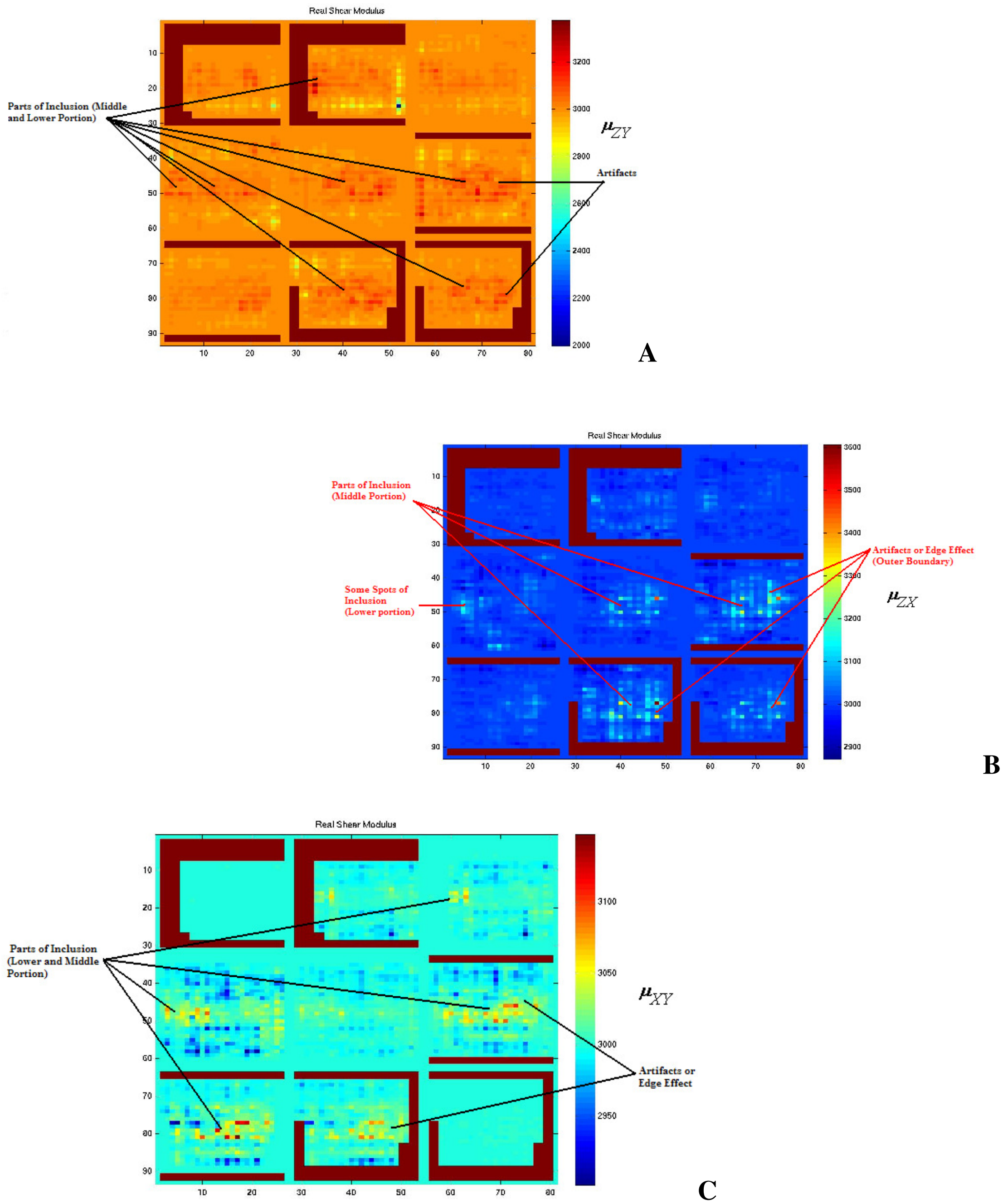

Figure 6- 12 The results from the pineapple gelatin phantom with an arc shaped inclusion reconstructed with an initial guess of 3 KPa. The orthotropic real shear moduli distribution are illustrated as μ_{XY}, μ_{ZY}, μ_{ZX}. Parts of the inclusion in the lower and middle portions are observable as shown. A few artifacts can be seen in the background around the outer boundary which may be an edge effect in (B).

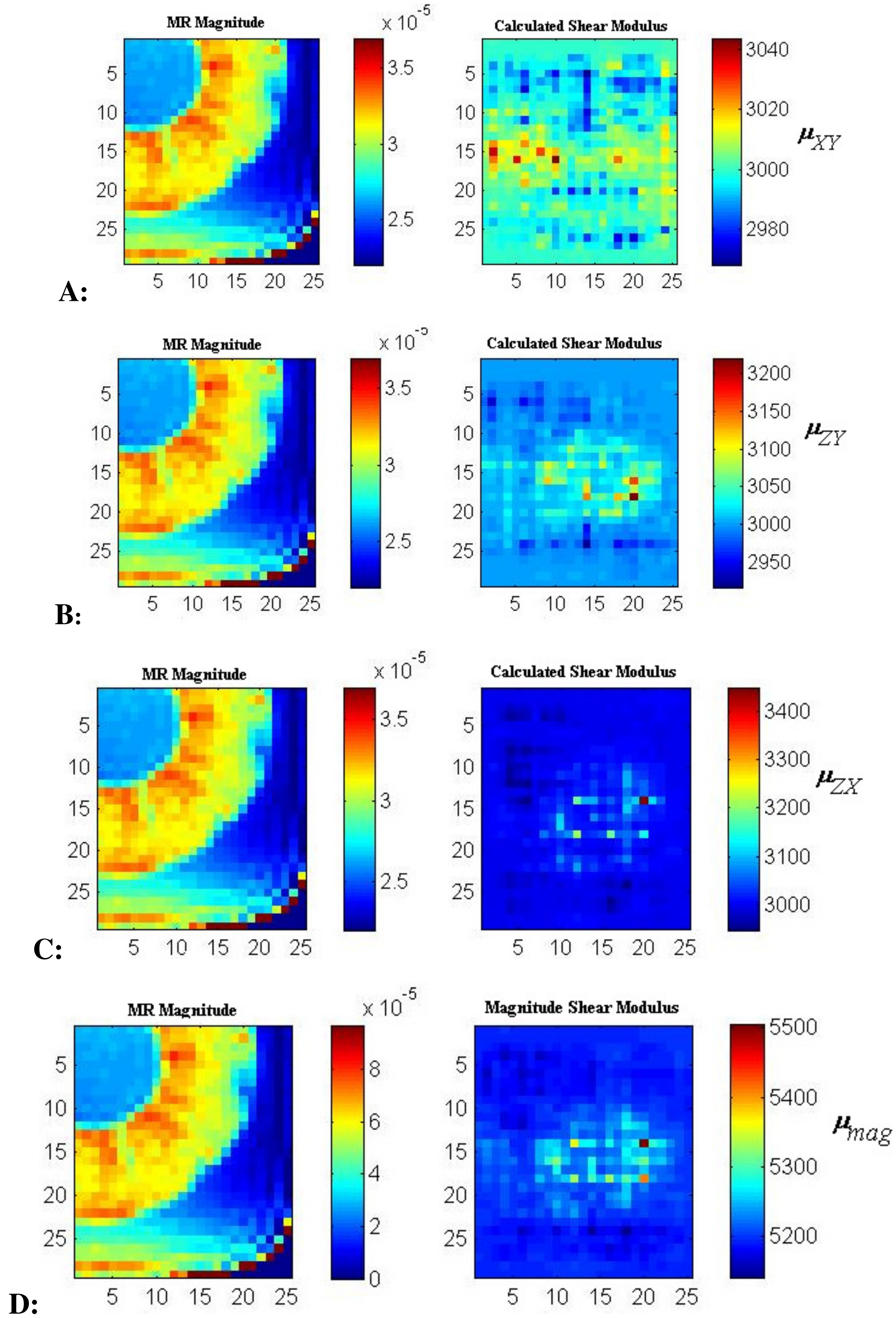

Figure 6- 13 The correlation results for the $T2^*$ MR image and the magnitude shear modulus with its components in 3-D after three iterations are illustrated. These results are from the pineapple gelatin phantom with an arc shaped inclusion reconstructed with an initial guess of 3 KPa. Parts of the inclusion in the lower and middle portion of the pineapple are reconstructed in (A) and (B) as shown. A few artifacts can be seen around the outer boundary which might be an edge effect in that region.

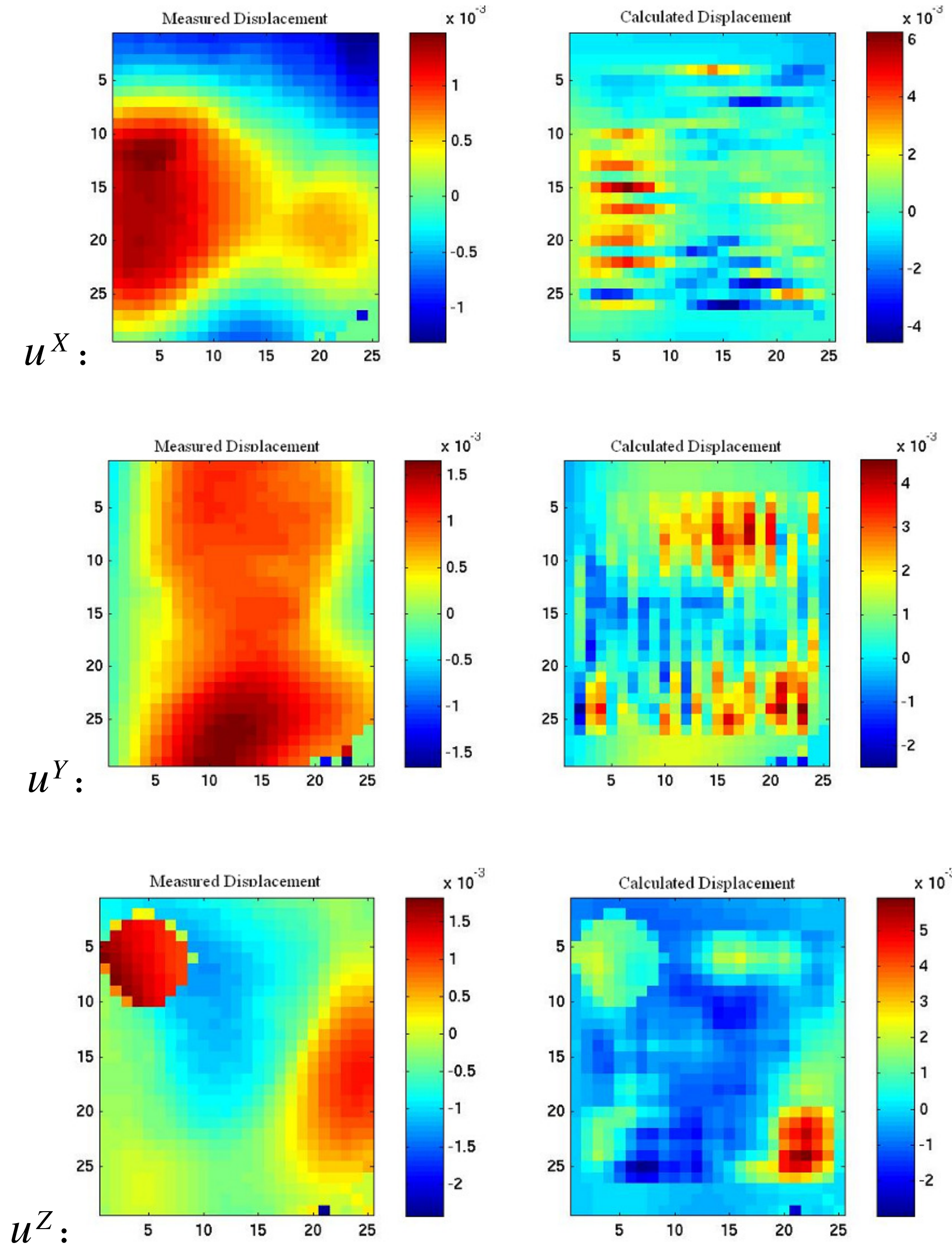

Figure 6- 14 The orthotropic correlation between measured and the calculated displacement components in three directions obtained from slice 7 of the arc shaped inclusion in the pineapple gelatin phantom, and with an initial guess of 4 KPa are illustrated. Poor correlation is shown in all directions along with an irregular displacement pattern and a few artifacts.

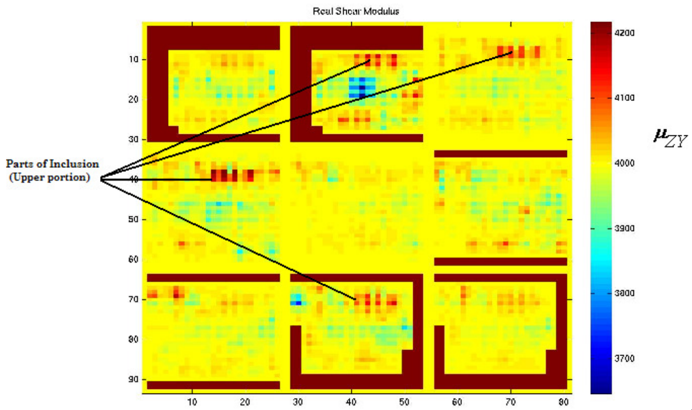

A

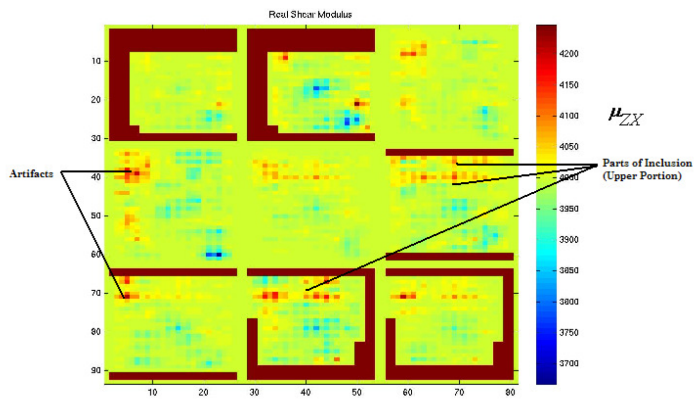

B

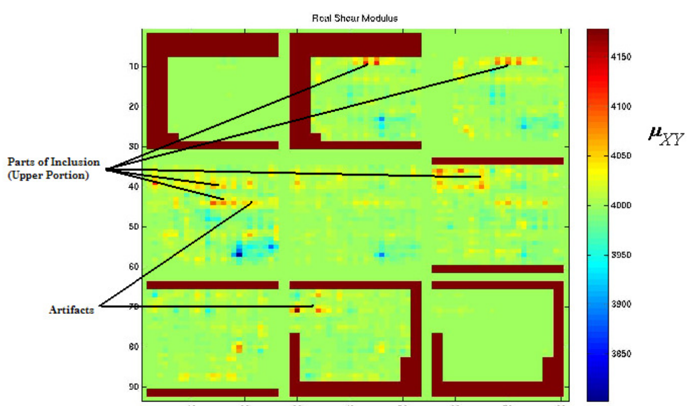

C

Figure 6- 15 These pictures show nine slices of the orthotropic real shear moduli reconstruction results with an initial guess of 4 KPa captured from the pineapple gelatin phantom with an arc shaped inclusion. The orthotropic reconstructed shear moduli distributions in 3-D are depicted. Small parts of the inclusion (upper portion) have been recovered along with some artifacts in the background.

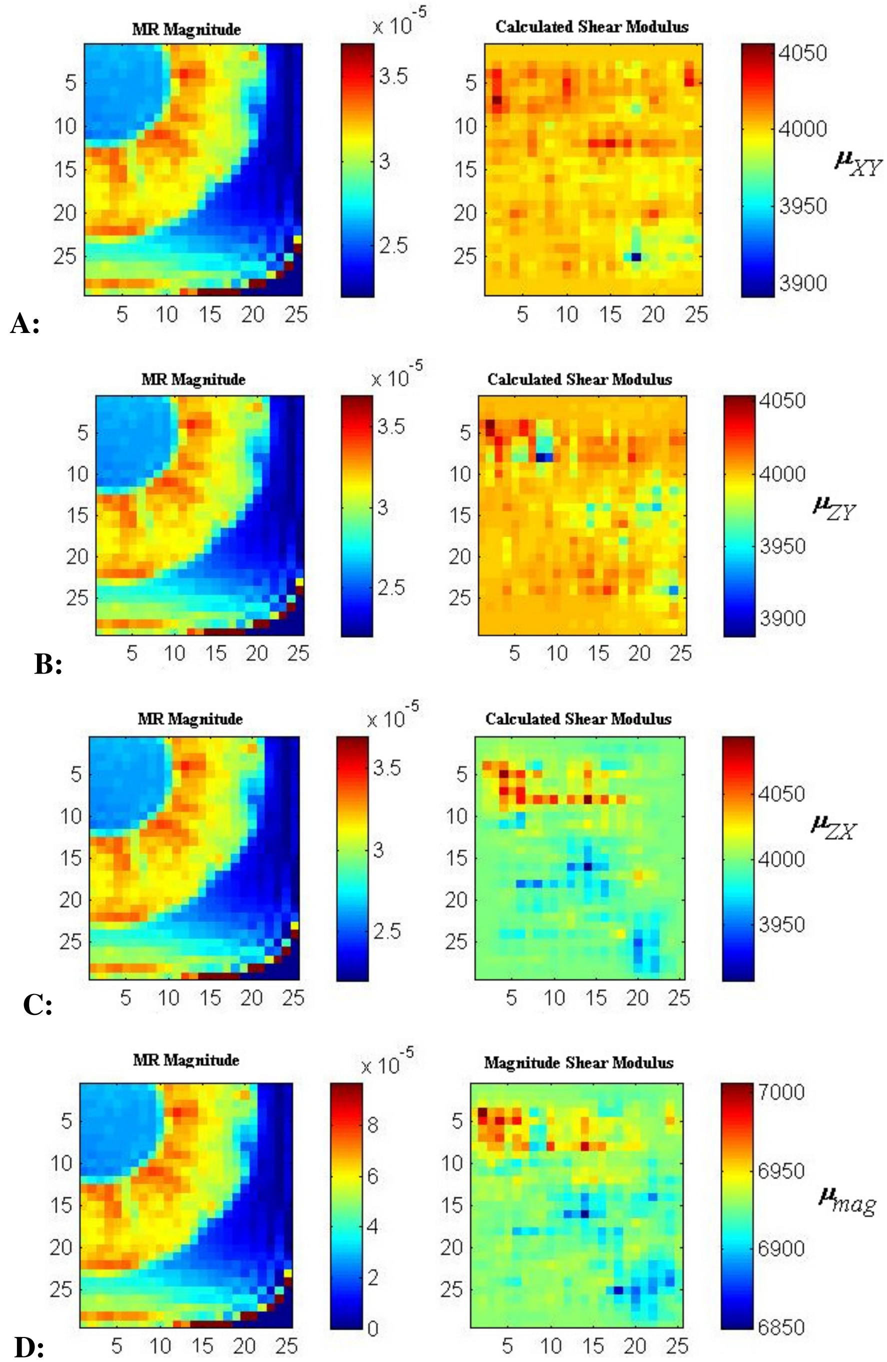

Figure 6- 16 These pictures show the orthotropic correlation results between the $T2^*$ MR image and the magnitude shear modulus image with its reconstructed components in 3-D recorded from the pineapple gelatin phantom with an arc shaped inclusion. These reconstructions were carried out with an initial guess of 4 KPa and the results are presented after three iterations. Small regions of the inclusion (upper portion) have been recovered along with some artifacts in the background.

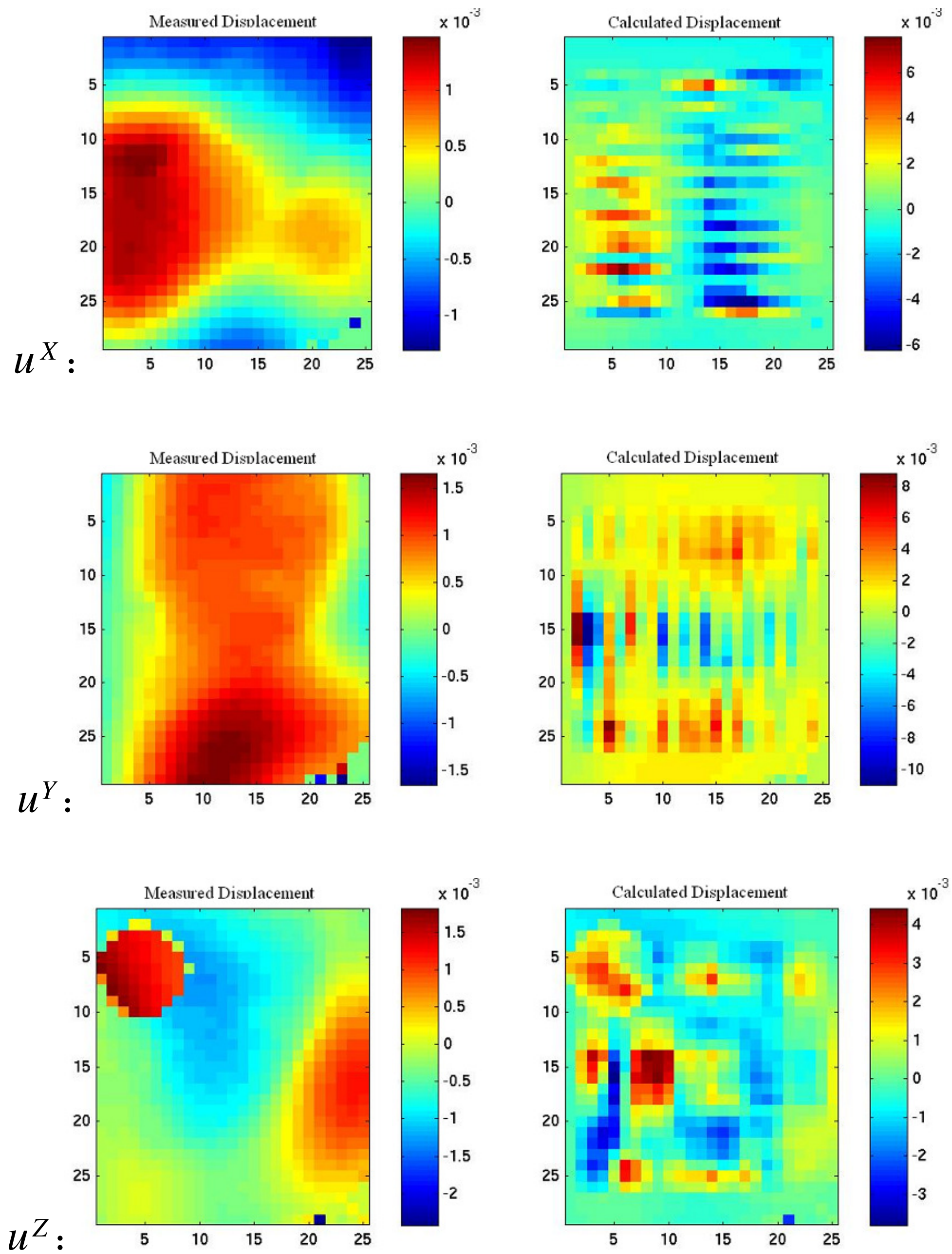

Figure 6- 17 The orthotropic measured and the calculated displacement patterns in three different dimensions are displayed for slice 7 of the pineapple gelatin phantom with an arc shaped inclusion. The orthotropic calculated displacements in 3-D were obtained from the image reconstructions with an initial guess of 5 KPa. The direction of the irregular motion pattern is visible. A poor correlation between measured and calculated displacement fields with a high level of artifacts can still be seen.

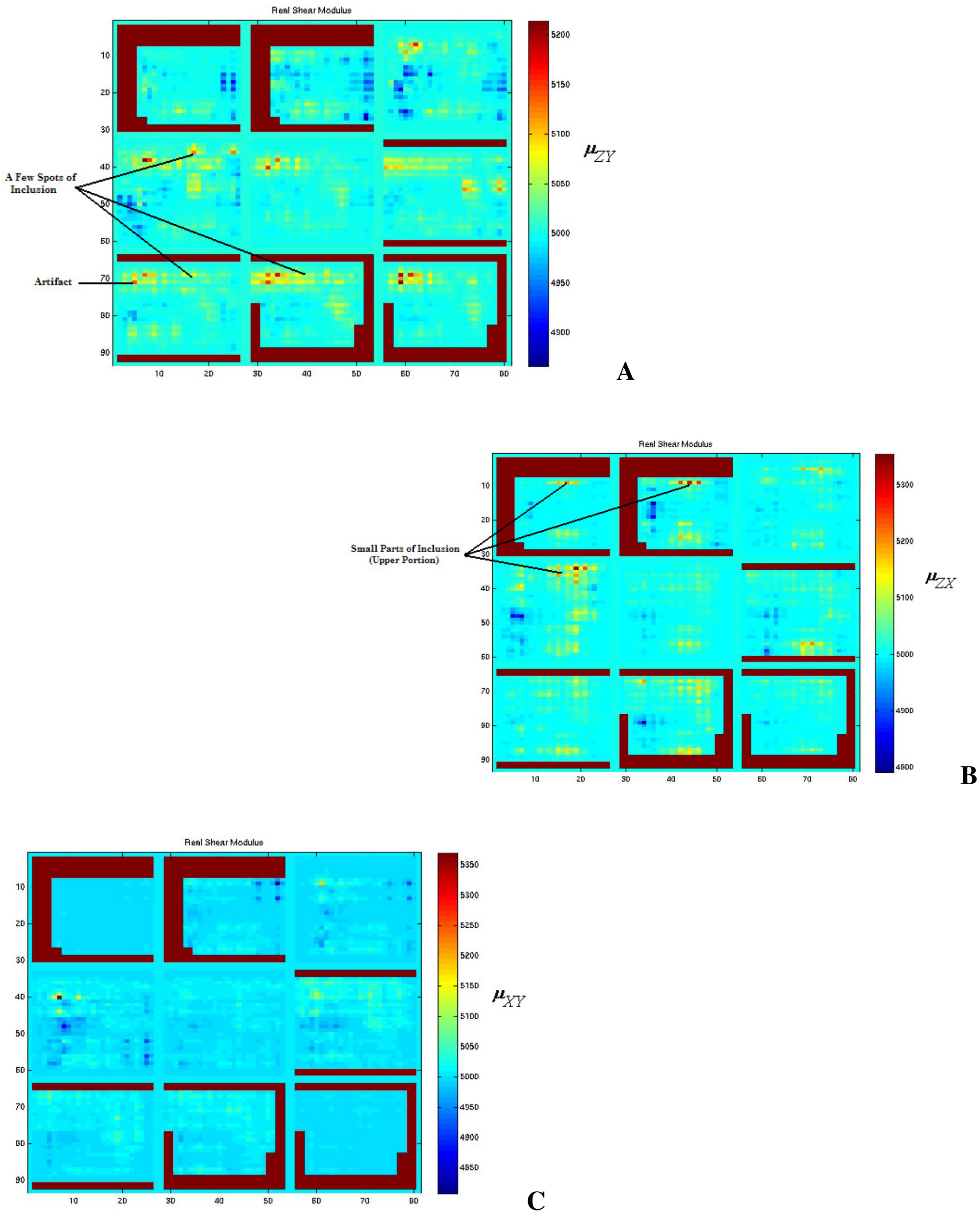

Figure 6- 18 Resulting orthotropic shear moduli componenets with an initial guess of 5 KPa distributed in nine slices obtained from the pineapple phantom with an arc shaped inclusion. A few parts of the inclusion were recovered which are shown in (A) and (B) along with some artifact spots in the background which shows a poor elasticity reconstruction.

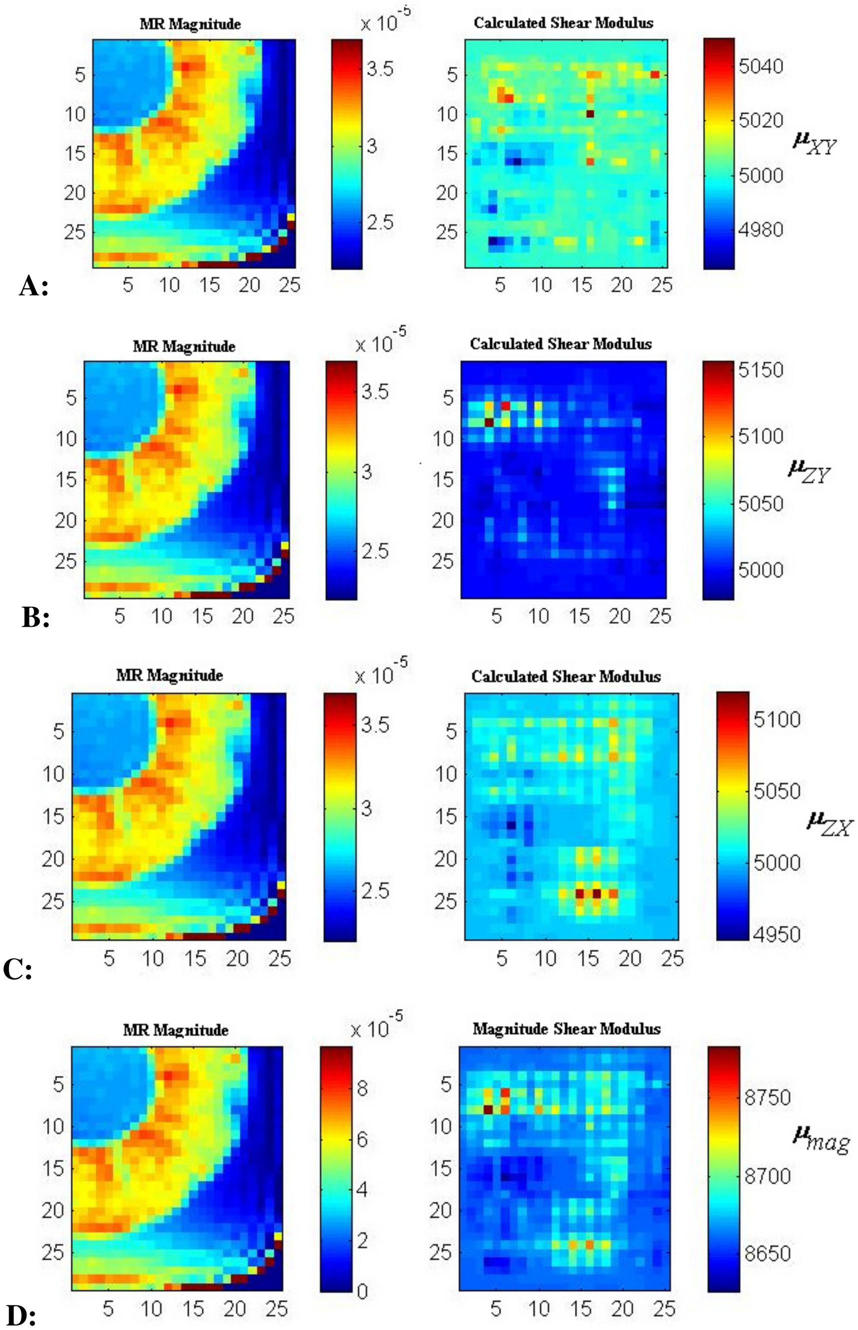

Figure 6- 19 Resulting reconstructions after one iteration with an initial guess of 5 KPa of the orthotropic real shear moduli distribution captured from slice 7 of the pineapple gelatin phantom with an arc shaped inclusion are displayed. The correlation between the $T2^*$ MR magnitude image with the magnitude shear modulus and reconstructed orthotropic shear moduli components in 3-D are depicted. A few spots of the inclusion have been recovered (mostly in the upper portion) which shows a poor elasticity reconstruction. Pictures show some significant artifacts in the background.

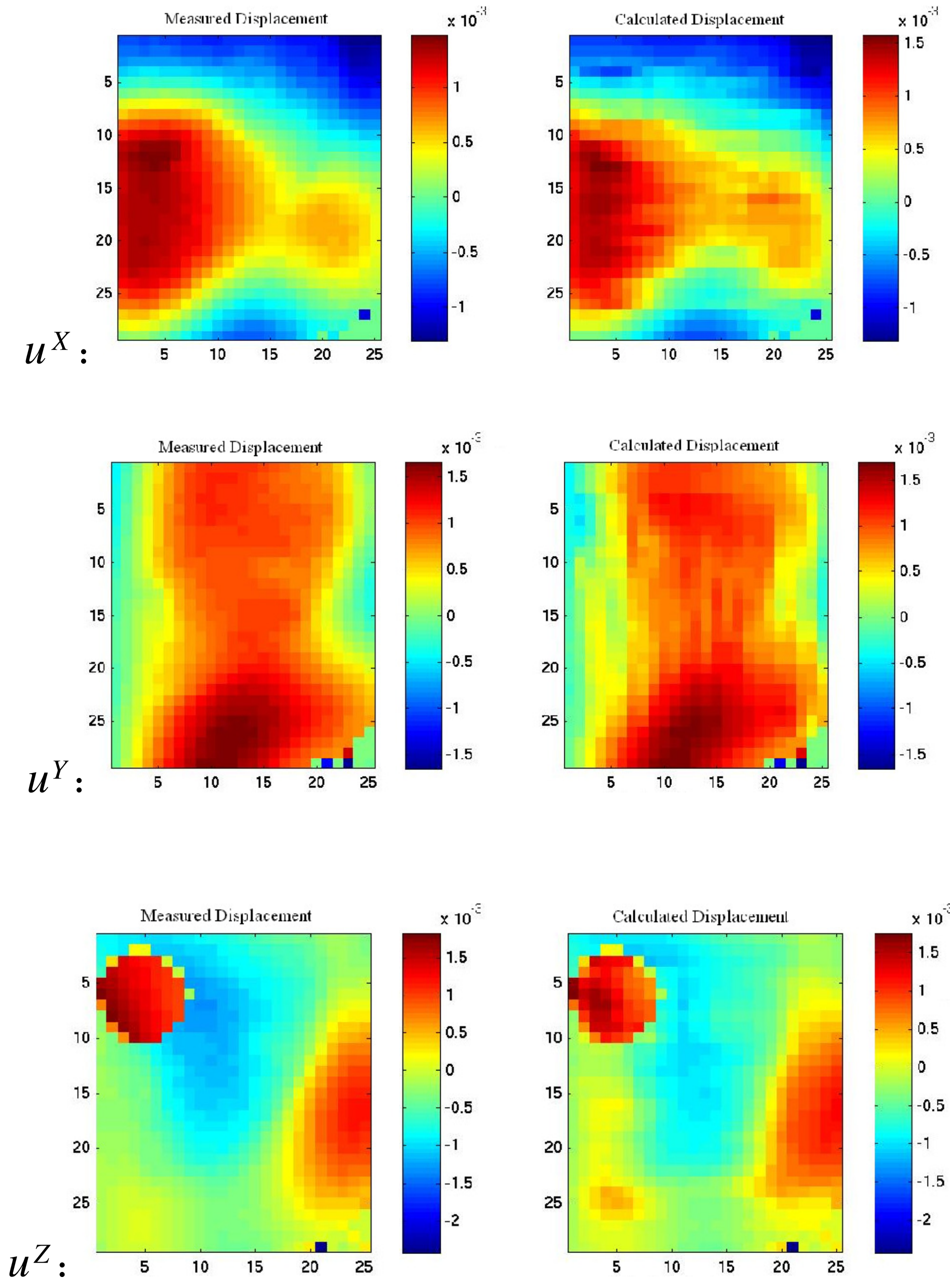

Figure 6- 20 Here the correlation between orthotropic measured and calculated displacement patterns in three directions, obtained from slice 7 of the arc shaped pineapple inclusion, with an initial guess of 10 KPa is illustrated. The irregular pattern of displacement with a high level of correlation and low level of artifact are shown.

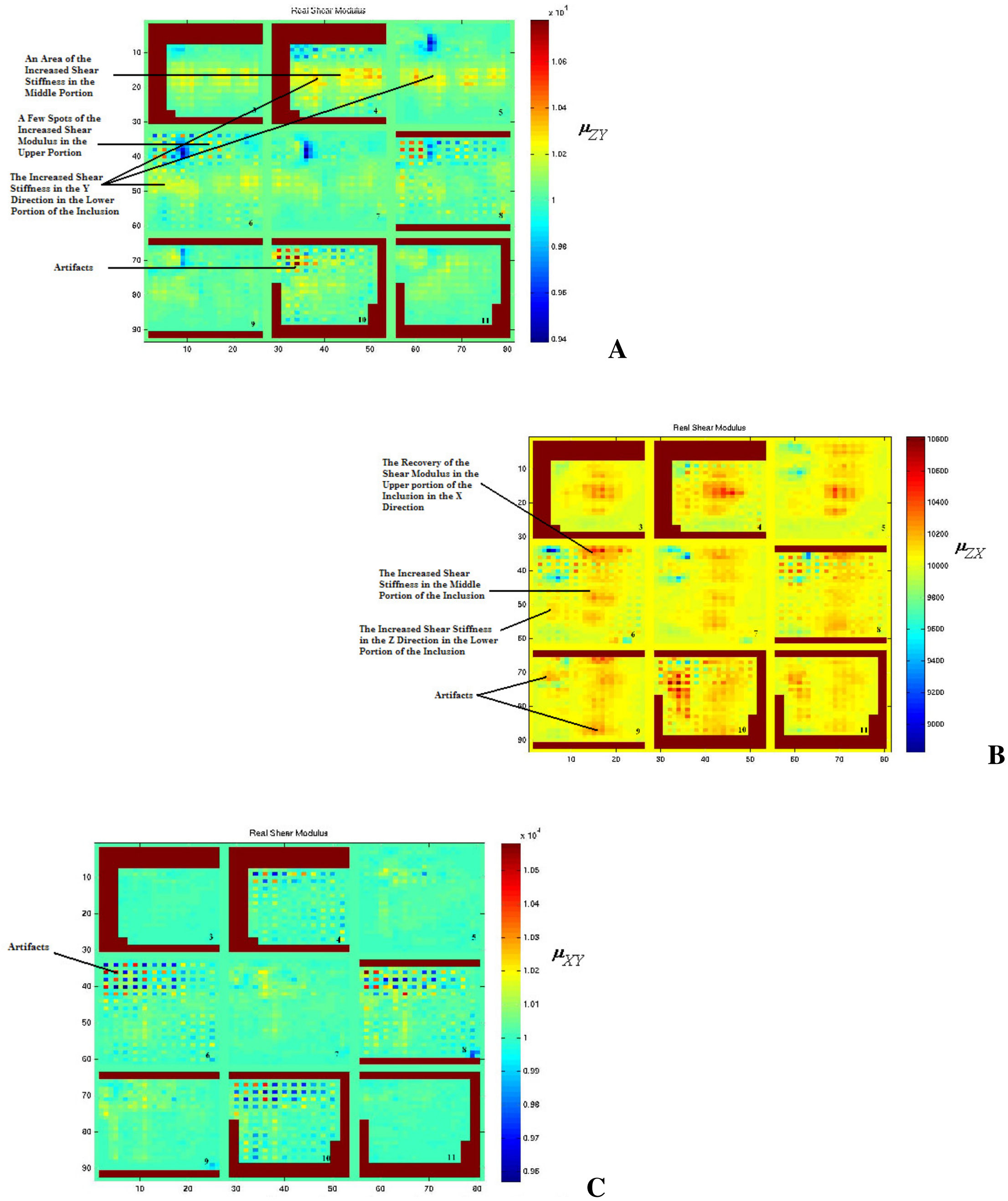

Figure 6- 21 The reconstruction results with an initial guess of 10 KPa from the orthotropic real shear moduli distribution are captured from the pineapple gelatin phantom with an arc shaped inclusion. Resulting orthotropic shear moduli componenets within nine slices are demonstrated. Almost three parts of the inclusion (upper, middle and lower) were recovered which are shown in (A) and (B) along with some artifact spots in the background.

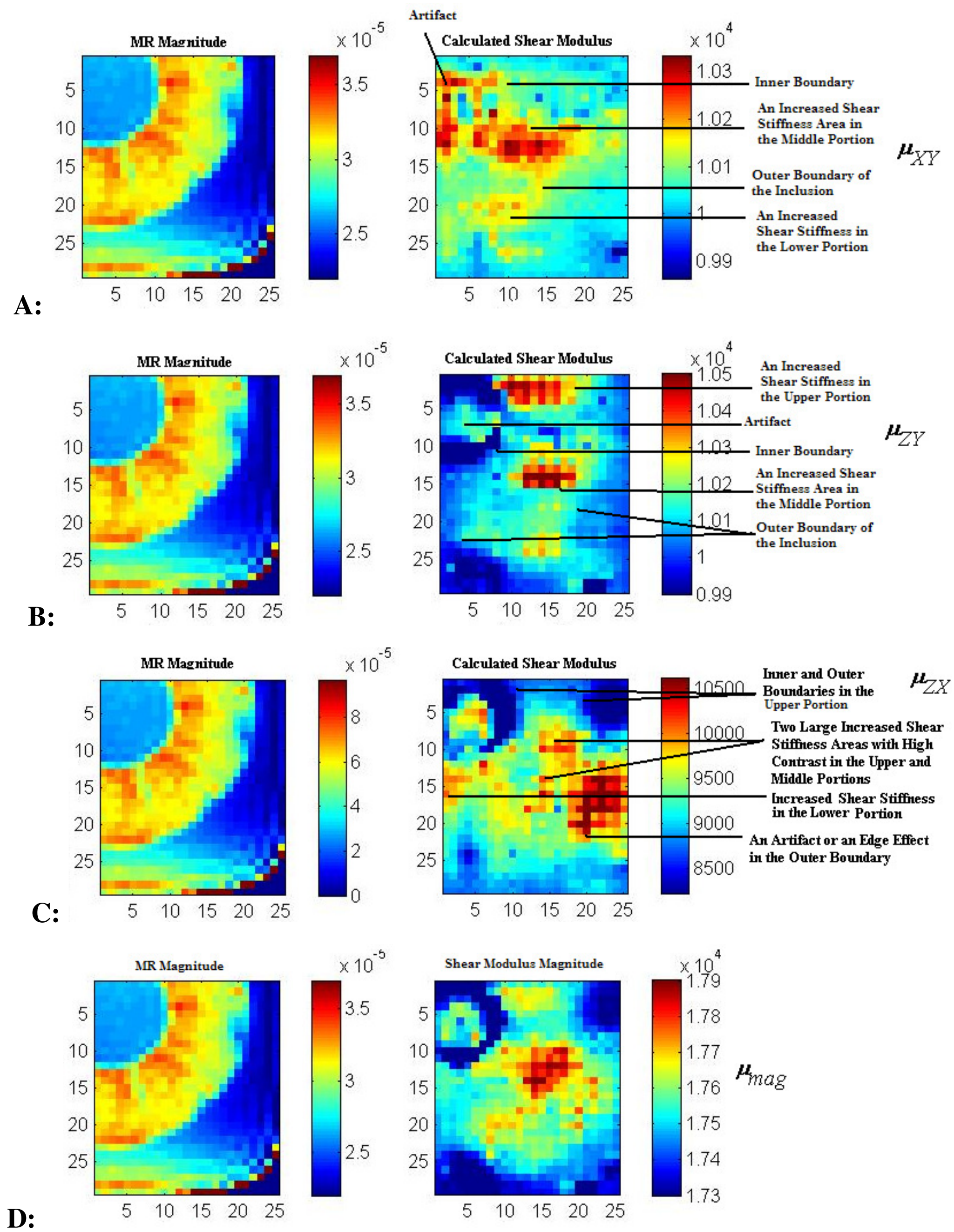

Figure 6- 22 The correlation results between the $T2^*$ MR image and the magnitude shear modulus with its components reconstructed with an initial guess of 10 KPa and after 17 iterations are illustrated. Almost three portions of the inclusion were reconstructed as shown. Artifacts can be seen in the center and the background around the outer and the inner boundaries which may be edge effects.

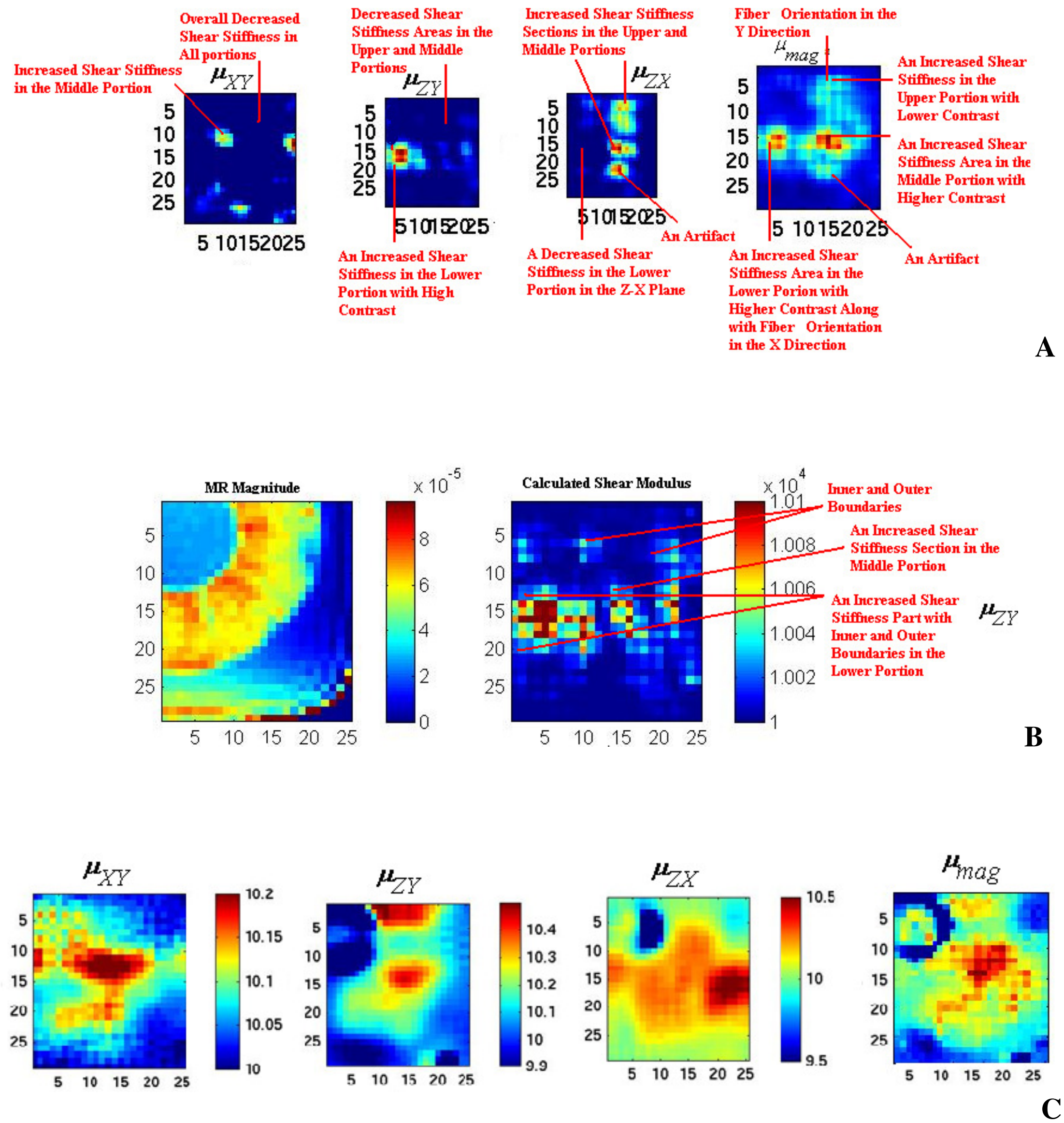

Figure 6- 23 These pictures show the successive improvement in results after 3 iterations (A), and after 17 iterations (B) of the orthotropic elastography image reconstructions with an initial guess of 10 KPa from the pineapple gelatin phantom with an arc shaped inclusion. The correlations between the magnitude shear modulus and its shear moduli components after three iterations (A), the $T2^*$ MR image and one calculated shear modulus component (B), and the magnitude shear modulus and its shear moduli components after 17 iterations (C) are demonstrated. Almost three portions of the inclusion were successfully reconstructed. Some artifacts are visible (C) in the centre and the background, around the outer and inner boundaries which may be edge effects.

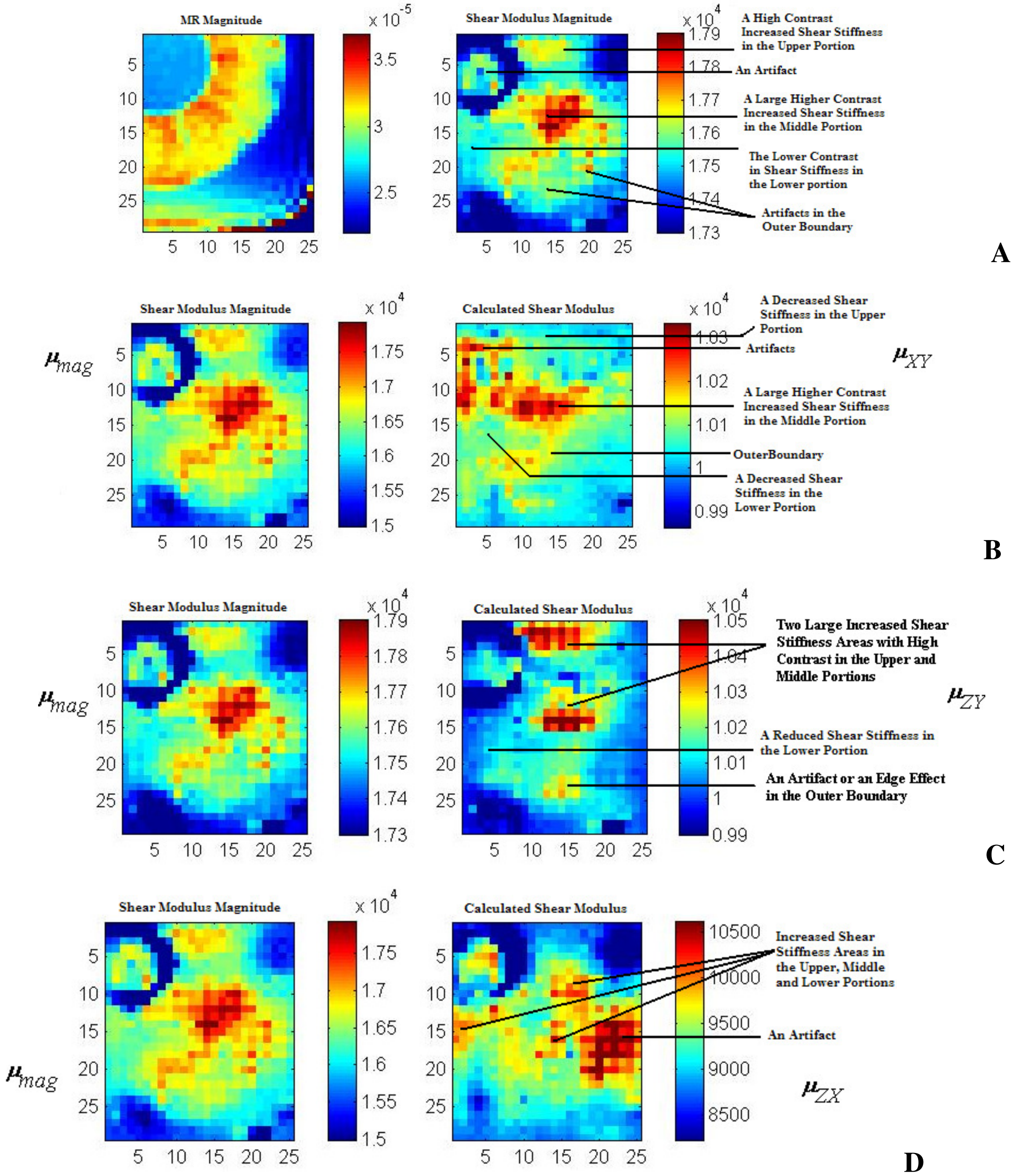

Figure 6- 24 The correlation between the $T2^*$ MR image and the magnitude shear modulus (A), and each calculated orthotropic shear moduli components with the magnitude orthotropic shear modulus after 17 iterations, are shown (B, C, D). These results obtained from the pineapple gelatin phantom with an arc shaped inclusion were reconstructed with an initial guess of 10 KPa. In the shear moduli reconstruction, some parts of the inclusion in three portions are reconstructed with high contrast. The increased and decreased shear stiffness regions with different contrasts reveal the orthotropic elasticity response of the pineapple fibrils to the shear motion in different orientations.

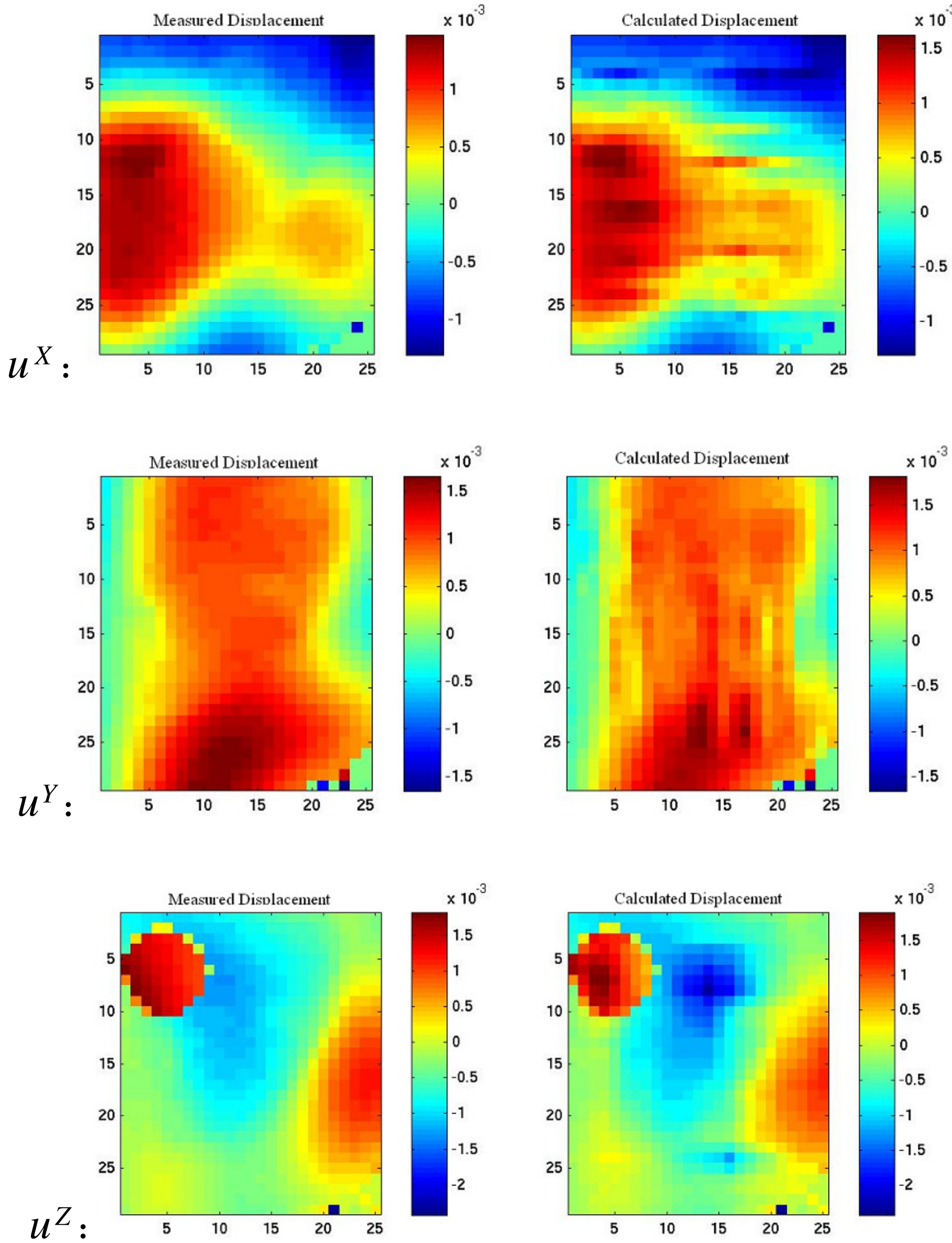

Figure 6- 25 The orthotropic measured and the calculated displacement patterns in three different dimensions are displayed for slice 7 of the pineapple gelatin phantom with an arc shaped inclusion. The orthotropic calculated displacements in 3-D were obtained from the image reconstructions with an initial guess of 20 KPa. The irregular motion pattern and the direction of the shear waves with a high level of correlation and a low level of artifact are visible.

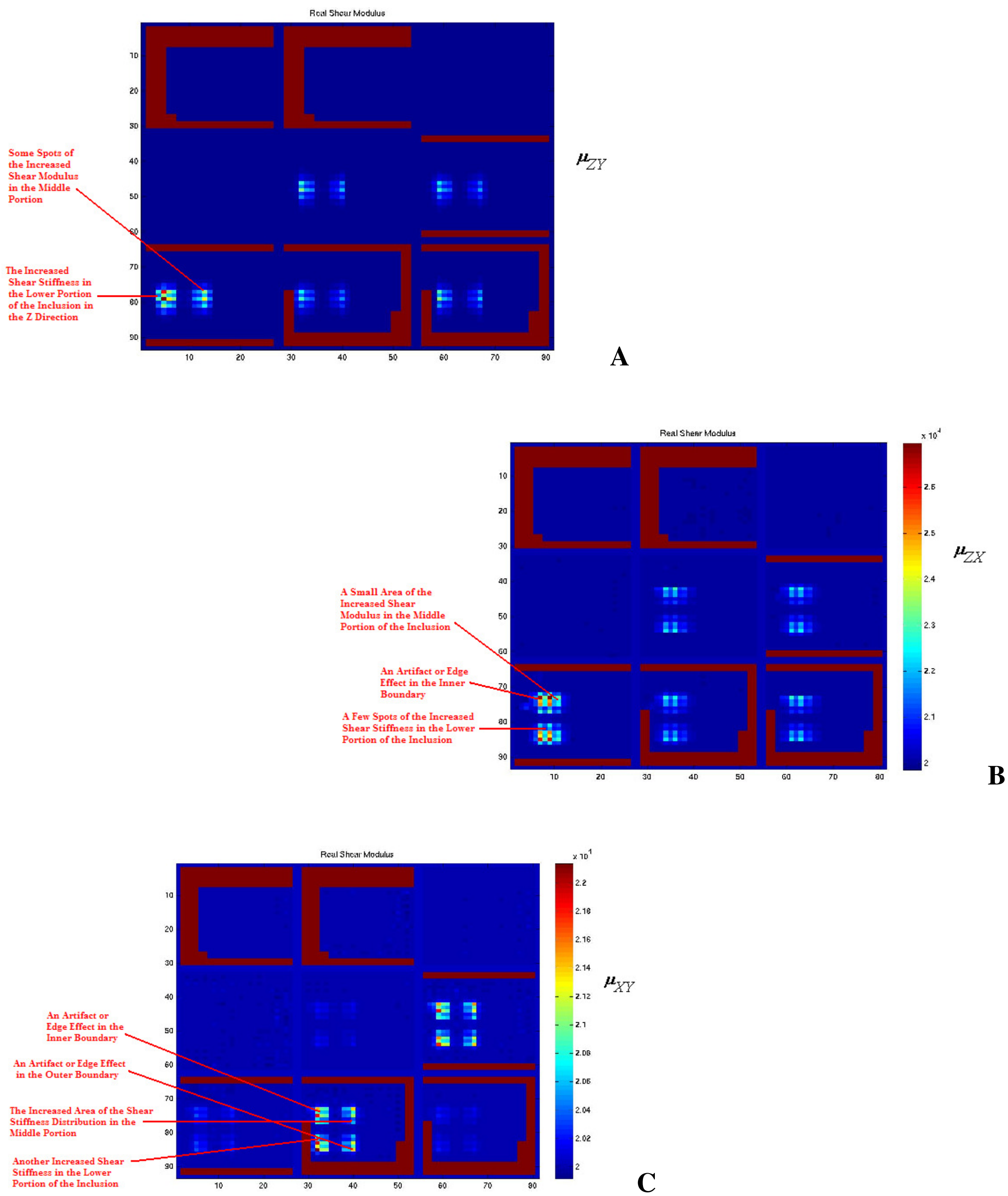

Figure 6- 26 Reconstruction results with an initial guess of 20 KPa of the orthotropic real shear moduli distribution captured from the pineapple gelatin phantom with an arc shaped inclusion shown within nine slices are shown. The orthotropic reconstructed shear moduli components μ_{XY}, μ_{ZY}, μ_{ZX}, are demonstrated. The lower portion of the inclusion with a low level of artifacts in the background can be seen. Other parts of the inclusion (middle and upper portions) cannot be seen.

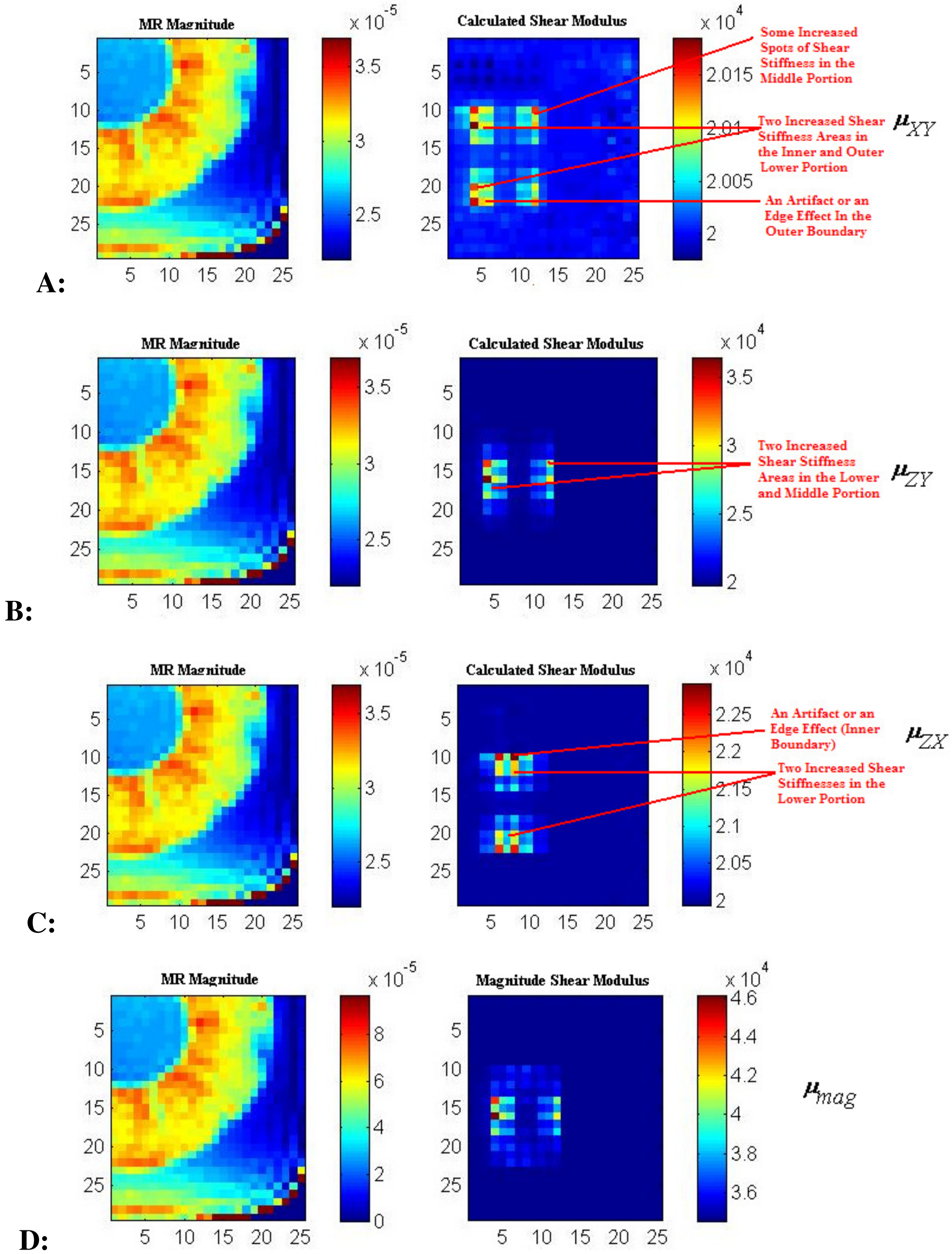

Figure 6- 27 Reconstruction results with an initial guess of 20 KPa of the orthotropic real shear moduli distribution obtained from slice 7 of the pineapple gelatin phantom with an arc shaped quarter inclusion, and after two iterations, are displayed. The correlation between the $T2^*$ MR magnitude image with magnitude shear modulus and reconstructed orthotropic shear moduli components are depicted. The lower portion of the inclusion has been recovered as shown whilethe middle and lower portions of the inclusion are not visible.

6.4 Isotropic Reconstructions Using Real MRI Datasets

Along with orthotropic elastography reconstructions, isotropic elasticity image reconstructions were also carried out to map isotropic shear modulus distribution. These were based on MRE motion datasets captured from the tissue-equivalent pineapple gelatin phantom. In this investigation, the results obtained from orthotropic elastography were compared to isotropic cases in equal conditions to evaluate the capability of these methods to produce more accurate results.

The same FE mesh model which was made for the orthotropic elastographic reconstruction from the pineapple gelatin phantom with an arc shaped quarter inclusion was used for isotropic image reconstructions using the exact same conditions, such as the element type, number of elements, nodes etc. Again, the MRE motion datasets excited with the frequency of 85 Hz in the global dimension X were chosen to generate this isotropic FE model.

The nonlinear CG optimization technique along with the TV regularization method with the weighting regularization parameter of 1.d-5, were used to minimize the objective function. Also, the subzone implementation approach with a zone overlap of 15% and the zone size ratio of 3, 2, and 1 in X, Y, and Z respectively, were applied to reduce the global inversion process by dividing the problem into multiple local inversion problems.

The adjoint-residual approach was also utilized to improve the efficiency of the gradient descent based algorithm. The global iteration limit was 100 for CG and 1 per zone to facilitate the material property solution approaching convergence.

As this isotropic iterative approach was carried out for comparison with the orthotropic case, the conditions were kept the same as much as possible. Different initial guesses for the real shear modulus in the value range of 1-20 KPa were also taken to reach a successive approximation for the actual solution at each set of reconstruction procedures. Initial guesses taken for this isotropic study were the same as the orthotropic cases, 1 KPa, 2 KPa, 3 KPa, 4 KPa, 5 KPa, 10 KPa, and 20 KPa.

6.4.1 Isotropic Reconstruction Results

The isotropic elasticity image reconstruction results from the pineapple gelatin phantom with an arc shaped inclusion are presented in this section.

These results comprise the isotropic correlation between measured and calculated displacement patterns from slice 7 in three directions (Fig. 6.28), the correlation between the $T2^*$ MR image and the isotropic shear modulus from slice 7 for all initial guesses (Fig. 6.29) and (Fig. 6.30), and the isotropic shear modulus distributed in nine slices (Fig. 6.31).

As the correlation images between measured displacements and calculated displacements obtained from isotropic elastographic image reconstructions for all initial guesses were similar, only the correlations between measured displacements and calculated displacements captured from isotropic reconstruction with the initial guess of 10 KPa are displayed here.

It should be pointed out that the correlation between the $T2^*$ MR image and the isotropic shear modulus from the initial guesses 1-5 KPa are presented after 100 iterations, while the results for the initial guesses of 10 KPa and 20 KPa are shown after 16 and 5 iterations respectively, to make a comparison with the orthotropic results.

The displacement components in three directions were also illustrated as u^X, u^Y and u^Z.

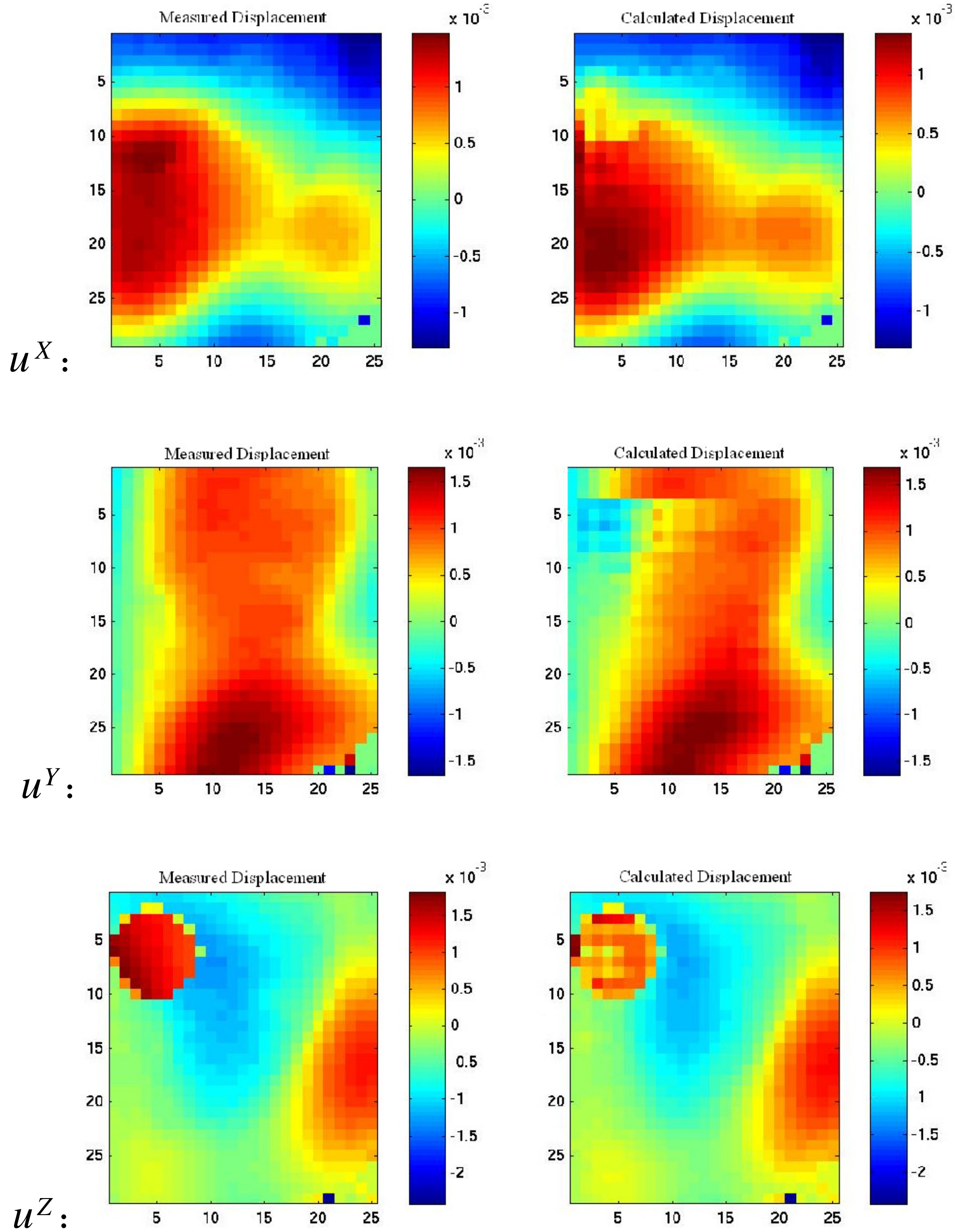

Figure 6- 28 The isotropic correlation between measured and calculated displacement fields in three directions, obtained from slice 7 of the pineapple gelatin phantom with an arc shaped inclusion, are displayed. The irregular pattern of displacement with a fairly low level of artifact is demonstrated.

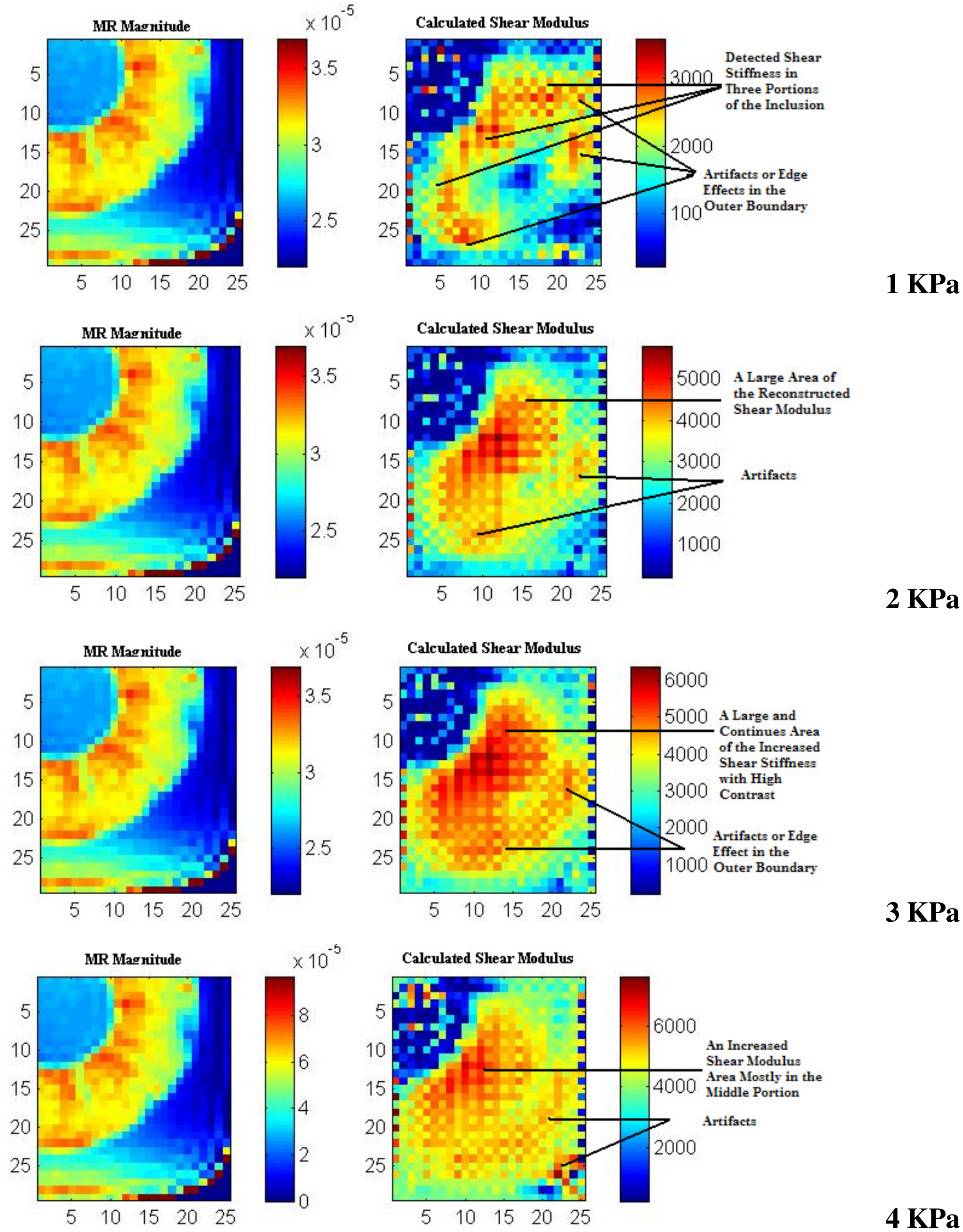

Figure 6- 29 Isotropic real shear modulus reconstruction results with initial guesses of 1KPa, 2KPa, 3KPa, and 4KPa obtained from slice 7 of the pineapple gelatin phantom with an arc shaped inclusion. The correlation between the $T2^*$ MR magnitude image and the reconstructed isotropic shear modulus after 100 iterations are depicted. A fairly homogenous region of the inclusion has been recovered in nearly all images. A high level of artifacts can be seen in the background around the inner boundary towards the centre, and also the outer boundary.

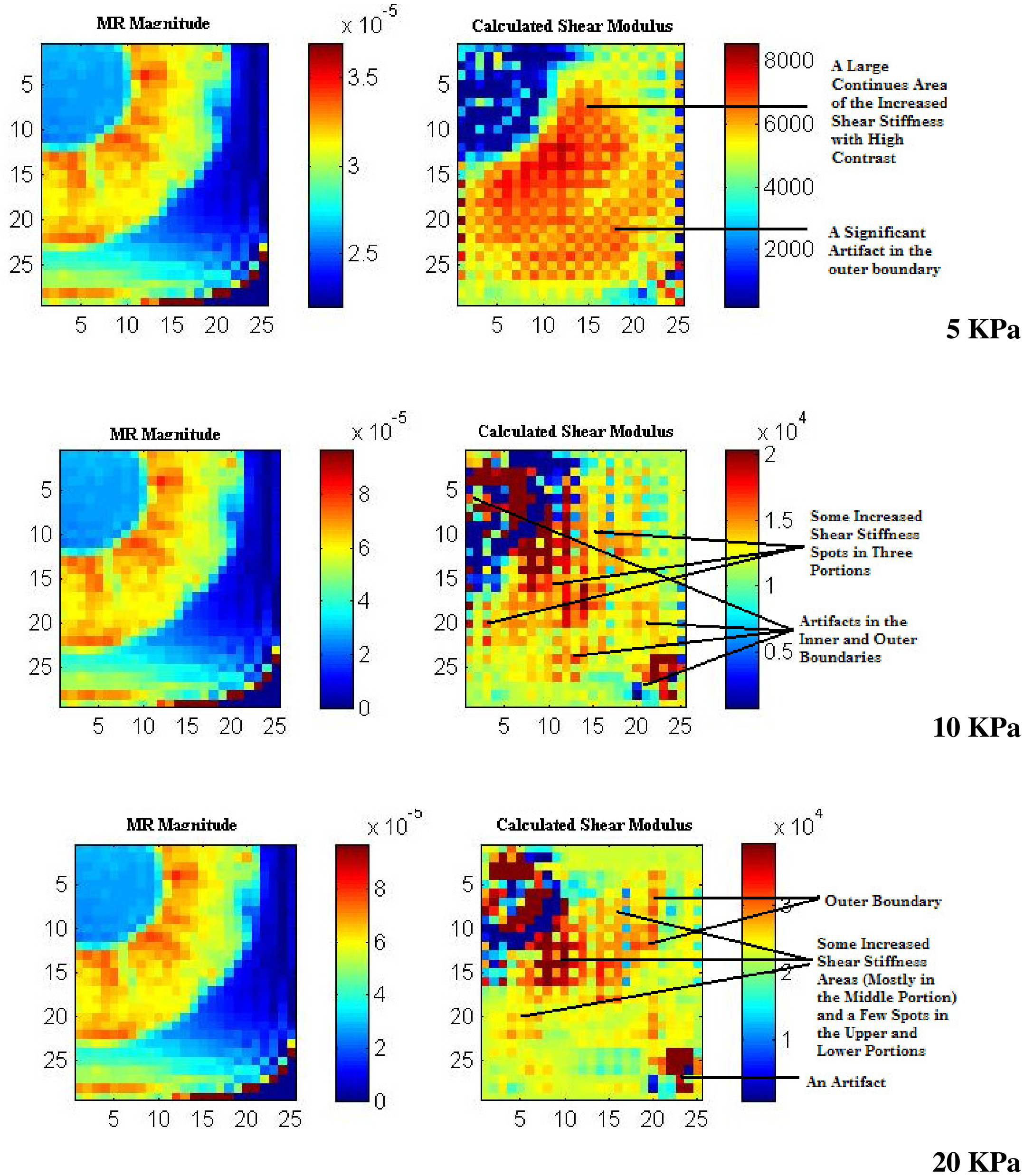

Figure 6- 30 The isotropic correlation results from the pineapple gelatin phantom with an arc shaped inclusion reconstructed with initial guesses of 5 KPa, 10 KPa, 20 KPa, and after 100, 16, and 5 iterations. The $T2^*$ MR image and reconstructed shear modulus are illustrated. Large area of the inclusion in all reconstructions, along with some artifacts can be seen in the outer and inner boundaries, the centre and the background.

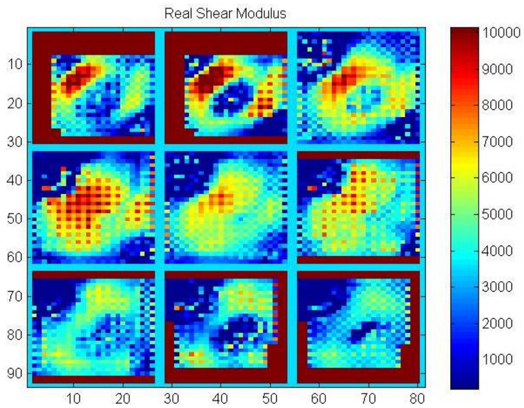

2 KPa

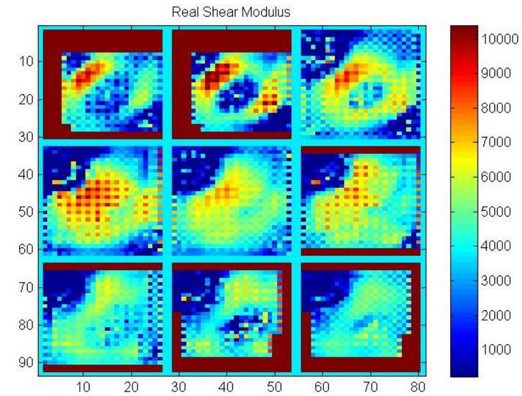

3 KPa

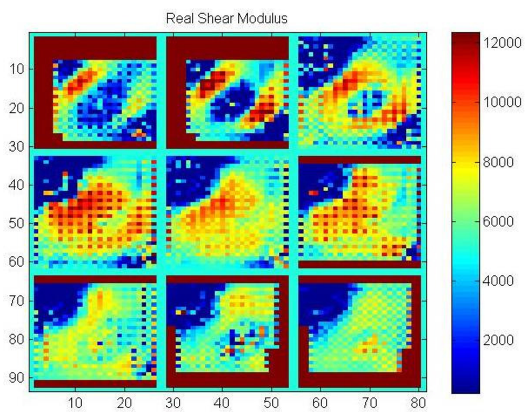

5 KPa

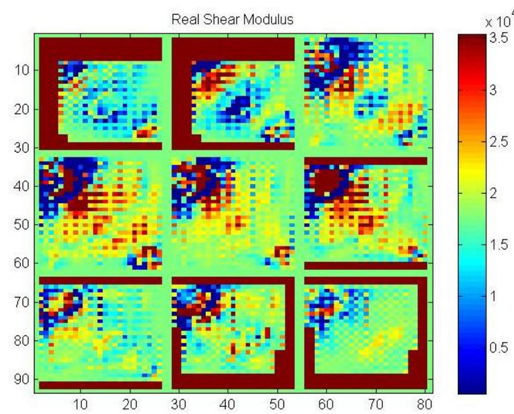

10 KPa

Figure 6- 31 These pictures show nine slices of isotropic reconstruction results with initial guesses of 2 KPa, 3 KPa, 5 KPa, and 10 KPa of the isotropic real shear modulus distribution, obtained from the pineapple gelatin phantom with an arc shaped inclusion. Large increased shear stiffness areas can be seen mostly in the middle portion of the inclusion, along with high levels of artifacts which are visible in the background, the inner and outer boundaries.

6.5 Comparison Analysis between Orthotropic and Isotropic Reconstructions

Tables 6.1 and 6.2 represent mean values and standard deviations (STD) of the orthotropic magnitude shear modulus and its shear moduli components, at each node in 3-D in comparison with each other, and also in comparison with isotropic shear modulus distribution with seven different initial guesses (I.G.), from 1-5 KPa, 10 KPa, and 20 KPa, for the pineapple gelatin phantom with an arc shaped inclusion. In these two tables the mean values and STDs of the highest available iteration with higher iteration counts for all tests are presented. As Table 6.1 shows, the mean value of the shear modulus reconstruction is raised by increasing the initial guess from 1 KPa to 20 KPa for all tests in both orthotropic and isotropic cases.

Mean Values / I.G. (KPa)	Orthotropic Shear Moduli (KPa) (Highest Available Iteration)				Isotropic Shear Modulus (KPa)
	μ_{XY}	μ_{ZY}	μ_{ZX}	Magnitude	
1	1.0158	1.0386	1.0318	1.0287	1.6951
2	2.0014	2.0023	2.0011	2.0016	2.8347
3	3.0009	3.0037	3.0074	3.0040	3.4598
4	4.0017	3.9965	3.9973	3.9985	4.1250
5	5.0024	5.0056	5.0096	5.0059	4.7654
10	10.086	10.161	10.140	10.129	9.9088
20	20.024	20.282	20.086	20.131	20.020

Table 6- 1 The mean values of the orthotropic magnitude shear modulus and its shear moduli components at each node in comparison with each other, and also in comparison with isotropic shear modulus reconstructions of the pineapple gelatin phantom with an arc shaped inclusion are presented. These results obtained from different initial guesses (I.G.) from 1-5 KPa, 10 KPa, and 20 KPa. In this table, the highest available iteration for all tests with higher iteration counts is considered.

From the initial guess of 1KPa to 4 KPa, a higher mean value can be detected from the isotropic shear modulus reconstruction, while increasing the value of the initial guess from 4 KPa to 20 KPa, the orthotropic magnitude shear modulus reconstruction illustrates a higher mean value in comparison with an isotropic case with the same initial guess.

One result from Table 6.1 shows that by changing the initial guess, the direction of the shear modulus plane with maximum mean value is varied. For example, μ_{ZY} demonstrates the highest mean value in initial guesses of 1 KPa, 2 KPa, 10 KPa, and 20 KPa, while μ_{ZX} shows its maximum mean values in initial guesses of 3 KPa and 5 KPa, and finally μ_{XY} shows its highest mean value in the initial guess of 4 KPa. Table 6.1 also indicates that regardless of the value of the initial guess, in each orthotropic shear moduli reconstruction, different values could be detected from different shear moduli components μ_{XY}, μ_{ZY}, μ_{ZX}, in three dimensions, which is in agreement with the orthotropic behavior of the material.

STD / I.G. (KPa)	Orthotropic Shear Moduli % (Highest Available Iteration)				Isotropic Shear Modulus
	μ_{XY}	μ_{ZY}	μ_{ZX}	Magnitude	
1	2.1111	6.2014	6.1544	3.6670	1.0998
2	0.4059	0.7545	0.8570	0.5230	1.4515
3	0.4825	1.1039	0.9752	0.6168	1.6136
4	0.3208	0.7188	0.6666	0.3947	1.7387
5	0.2616	0.3893	0.5118	0.2785	2.1133
10	1.1435	2.5572	2.6693	1.4703	2.2371
20	0.6254	7.3698	1.9983	2.6678	3.6021

Table 6- 2 This table shows standard deviations (STD) of the orthotropic magnitude shear modulus and its shear moduli components at each node in comparison with each other, and also in comparison to isotropic shear modulus reconstructions when different initial guesses (I.G.) from 1-5 KPa, 10 KPa, and 20 KPa were applied. These results were obtained from the highest achieved iteration for all tests of the pineapple gelatin phantom with an arc shaped inclusion.

Table 6.2 indicates that the orthotropic magnitude shear modulus reconstructions show lower STD values in comparison with isotropic elasticity reconstruction for all initial guesses except the initial guess of 1 KPa. In general, Table 6.2 illustrates the low value of STDs, which implies that the variation from the mean values (average) is small.

Tables 6.3 and 6.4 show the mean values and STDs of the orthotropic magnitude shear modulus and its shear moduli components at each node in three dimensions in comparison with each other, and also in comparison with isotropic shear modulus distribution.

These results were obtained from seven different initial guesses (I.G.), from 1-5 KPa, 10 KPa, and 20 KPa, for the pineapple gelatin phantom with an arc shaped inclusion. These tables represent mean values and STDs of the same iteration for all tests with the same iteration counts.

Mean / I.G. (KPa)	Orthotropic Shear Moduli (KPa) (The Same Iteration)				Isotropic Shear Modulus (KPa)
	μ_{XY}	μ_{ZY}	μ_{ZX}	Magnitude	
1	1.0032	1.0047	1.0041	1.0040	1.0082
2	2.0014	2.0023	2.0011	2.0016	2.0707
3	3.0005	3.0037	3.0041	3.0027	3.0668
4	4.0020	4.0012	4.0018	4.0017	4.0569
5	5.0024	5.0056	5.0096	5.0059	5.0190
10	10.005	10.019	10.023	10.015	9.9946
20	20.024	20.282	20.086	20.130	20.028

Table 6- 3 The comparisons of mean values between the orthotropic magnitude shear modulus and its shear moduli components at each node in 3-D are shown. Also the comparisons between the orthotropic magnitude shear modulus and the isotropic shear modulus in each initial guess reconstruction from 1 KPa to 5 KPa, 10 KPa, and 20 KPa, for the pineapple gelatin phantom with an arc shaped inclusion, are presented. All presented results are from the same iteration (iteration 1) for all tests.

Table 6.3 indicates that by raising the initial guess from 1 KPa to 20 KPa, the mean value of the shear modulus reconstruction whether orthotropic or isotropic is increased. From the initial guess of 1KPa to 5 KPa, higher mean values can be found for the isotropic shear modulus reconstruction, while increasing the value of the initial guess from 5 KPa to 20 KPa, the orthotropic magnitude shear modulus illustrates a higher mean value in comparison with an isotropic case with the same initial guess.

Results from Table 6.3 also demonstrate that the direction of the shear modulus plane with a maximum mean value varies by changing the initial guess. μ_{ZY} , illustrates its highest mean value for initial guesses of 1 KPa, 2 KPa, and 20 KPa while μ_{ZX} indicates its maximum mean value for initial guesses of 3 KPa, 5 KPa and 10 KPa, and finally μ_{XY} shows its highest mean value for the initial guess of 4 KPa.

STD / I.G. (KPa)	Orthotropic Shear Moduli % (The Same Iteration)				Isotropic Shear Modulus
	μ_{XY}	μ_{ZY}	μ_{ZX}	Magnitude	
1	0.6805	1.1249	1.0763	0.6928	0.0277
2	0.4059	0.7545	0.8570	0.5230	0.1448
3	0.4691	1.1312	1.0023	0.6472	0.3650
4	0.2630	0.4902	0.4207	0.2667	0.5591
5	0.2616	0.3893	0.5118	0.2785	0.6409
10	0.1105	0.4579	0.5466	0.2699	1.5208
20	0.6716	7.6003	2.0743	2.7535	3.3193

Table 6- 4 This table represents standard deviations (STD) of the orthotropic magnitude shear modulus and its shear moduli components at each node in comparison with each other, and also in comparison with the isotropic shear modulus reconstructions with different initial guesses (I.G.) from 1-5 KPa, 10 KPa and 20 KPa, for the pineapple gelatin phantom with an arc shaped inclusion. Results presented in this table were obtained from the same iteration (iteration 1) for all tests.

Table 6.3 also reveals that in each orthotropic shear moduli reconstruction, different mean values could be detected, but this fact is not relevant to the value of the initial guess. This clarifies that Tables 6.1 and 6.3 reveal the exact same conclusions to highlight the property of the pineapple as an orthotropic material.

Table 6.4 in general represents low values of STDs for all tests which indicate a small variation from the mean values. This table also shows that the orthotropic reconstructions still show lower STD values in comparison with the isotropic elasticity reconstruction for all initial guesses except the initial guess of 1 KPa.

Table 6.5 compares the shear moduli correlation coefficients (COR. CO.) between the orthotropic and the isotropic image elastography reconstructions obtained from slice 7 of the pineapple gelatin phantom with an arc shaped inclusion.

The correlation coefficient (COR. CO.) is defined as a relationship between two or more variables in which these parameters are relevant or associated together, and it is usually found between zero and one. Two variables are perfectly associated when the correlation coefficient is one and they are not relevant when the correlation coefficient is zero. In this study, all correlation coefficients are obtained in association with the $T2^*$ MR magnitude image as a basic reference.

These comparisons are made between orthotropic shear modului components in 3-D, and also between the orthotropic magnitude shear modulus and the isotropic shear modulus distribution for different initial guesses (I.G.), from 1-5 KPa, 10 KPa, and 20 KPa.

As Table 6.5 shows, the orthotropic magnitude shear modulus indicates a higher COR. CO. in comparison with the isotropic shear modulus for all initial guess tests. For μ_{XY}, the initial guess of 10 KPa illustrates the highest COR. CO. among all other initial guesses, while the initial guesses of 2 KPa and 20 KPa demonstrate their maximum COR. CO. for μ_{ZY} and μ_{ZX}, respectively.

COR. CO. / I.G. (KPa)	Orthotropic Shear Moduli				Isotropic Shear Modulus
	μ_{XY}	μ_{ZY}	μ_{ZX}	Magnitude	
1	0.89929	0.89100	0.89336	0.89732	0.51405
2	0.9002	0.90055	0.90024	0.90038	0.60749
3	0.89955	0.89941	0.89939	0.89955	0.63446
4	0.89983	0.89999	0.89978	0.89991	0.65906
5	0.89965	0.89969	0.89965	0.89968	0.63974
10	0.90015	0.89976	0.89981	0.89962	0.8018
20	0.89996	0.89250	0.90027	0.90011	0.83429

Table 6- 5 In this table the shear moduli correlation coefficient (COR. CO.) comparisons between the orthotropic and isotropic image elastography reconstructions obtained from slice 7 of the pineapple gelatin phantom with an arc shaped inclusion, are presented. These comparisons are made for orthotropic shear modului components in three dimensions, and also between the orthotropic magnitude shear modulus and the isotropic shear modulus for different initial guesses (I.G.) from 1-5 KPa, 10 KPa, and 20 KPa.

The initial guess of 2 KPa also indicates the highest orthotropic magnitude shear modulus COR. CO. among other initial guesses, while the initial guess of 1 KPa illustrates the lowest shear modulus COR. CO. in all orthotropic directions. In the isotropic reconstructions the maximum and the minimum shear modulus COR. CO are indicated for the initial guesses of 20 KPa and 1 KPa respectively.

Table 6.6 compares the displacement COR. CO. between orthotropic and isotropic cases in three dimensions obtained from image elastography reconstructions. Results are presented for slice 7 of the pineapple gelatin phantom with an arc shaped inclusion. This COR. CO. evaluation has also been carried out for different initial guesses (I.G.) from 1-5 KPa, 10 KPa and 20 KPa. Results obtained from Table 6.6 show that the highest orthotropic displacement COR. CO. in all directions belongs to the initial guess of 10 KPa.

COR. CO. / I.G. (KPa)	Orthotropic Displacements			Isotropic Displacements		
	u^X	u^Y	u^Z	u^X	u^Y	u^Z
1	0.45121	0.34661	0.36818	0.97790	0.96082	0.97105
2	0.26279	0.31052	0.16772	0.97814	0.95963	0.97177
3	0.43523	0.43302	0.44636	0.97788	0.95923	0.97242
4	0.63795	0.55454	0.39498	0.97689	0.95835	0.97262
5	0.44093	0.26062	0.28084	0.97658	0.95717	0.97300
10	0.9808	0.97930	0.93771	0.96976	0.93556	0.96826
20	0.96960	0.97524	0.89211	0.97806	0.96337	0.96246

Table 6- 6 Correlation coefficient (COR. CO.) comparison results between orthotropic and isotropic displacements in 3-D captured from elastography image reconstructions are presented. These comparisons are between orthotropic and isotropic displacements in three dimensions from slice 7 of the pineapple gelatin phantom with an arc shaped inclusion, and for different initial guesses (I.G.) from 1-5 KPa, 10 KPa and 20 KPa.

This means that the calculated displacements in 3-D captured from the initial guess of 10 KPa are more correlated with measured displacements. The evaluation of these results also reveals that the initial guesses of 1 KPa, 4 KPa, 5 KPa, and 10 KPa indicate their highest displacement COR. CO. in the X direction, while this direction is turned to the Y direction by changing the initial guesses to 2 KPa and 20 KPa, and finally it turns to the Z direction by applying the initial guess of 3 KPa. By evaluating isotropic reconstruction results it was found that the maximum and the minimum COR. CO. displacement results are in the X and Y directions respectively, for all initial guesses.

In the X and Y directions, from initial guesses of 1 KPa to 5 KPa, isotropic reconstructions illustrate a higher displacement COR. CO in comparison with orthotropic reconstructions.
While this trend is reversed from the initial guesses of 5 KPa to 20 KPa in the Z direction, isotropic reconstructions indicate a higher displacement COR. CO in comparison with orthotropic reconstructions for all initial guesses.

Table 6.7 illustrates the relative error between measured and calculated displacements in both orthotropic and isotropic image reconstructions. As Table 6.7 shows, regardless of the value of the initial guess, in general orthotropic reconstructions illustrate the greater relative error with a high level of variation in comparison with isotropic cases. From all initial guesses in orthotropic reconstructions, the initial guess of 10 KPa revealed the lowest relative error while the initial guess of 2 KPa displayed the highest displacement mismatch error. In isotropic cases, the initial guess of 3 KPa had the lowest error among other initial guesses.

Rel. Error / I.G. (KPa)	Orthotropic Displacements Mismatch %	Isotropic Displacements Mismatch %
1	86.7845	11.5124
2	243.5108	11.0576
3	80.4247	11.0113
4	84.6689	11.0743
5	136.1876	11.1212
10	20.3031	11.9551
20	22.2715	11.8692

Table 6- 7 This table demonstrates the relative error between measured and calculated displacements in both orthotropic and isotropic cases. In comparison of orthotropic and isotropic cases, the greater relative error with a high level of variation can be seen in orthotropic reconstructions.

The value of the relative error percentage can be calculated through the equation 6.2 as:

$$Rl.\ Err. = \sqrt{\frac{(u^m - u^c)^2}{(u^m)^2}} \times 100 \qquad (6.2)$$

where the $Rl.\ Err.$ is the relative mismatch error between measured displacement, u^m, and calculated displacement, u^c.

6.7 Discussion

The results investigated in this study are classified into two categories; significant points of the orthotropic elastography in a general view, and the orthotropic initial guess study. These are discussed in the following sections.

6.7.1 Orthotropic Elastography Significant Comments

In this research, orthotropic elasticity reconstruction results from real MRI datasets obtained from the pineapple gelatin phantom are evaluated. As mentioned, the shear moduli distribution results obtained from the three dimensional orthotropic reconstructive imaging presented in this chapter used an algorithm which was specifically developed for non-linear 3-D orthotropic incompressible materials.

One goal of this investigation was to indicate the ability of this novel material property reconstruction algorithm to differentiate orthotropic incompressible shear moduli components in three dimensions with reasonable accuracy, and to compare them with isotropic results.

Figures 6.4, 6.22, 6.23, and 6.24 show some evidence that the orthotropic reconstruction algorithm could detect parts of the structure of the pineapple inclusion in three dimensions. The inner, and parts of the outer boundaries, could be captured in the magnitude shear modulus and the calculated shear moduli images, although two significant artifacts are visible in both internal and external boundaries in all pictures.

Figures mentioned above illustrate the different orthotropic elasticity response of pineapple fibrils to the shear motion in different orientations. For example, Figure 6.4 depicts that in the X-Y frame, the shear wave components correspond to different material properties where effected.

For the shear strain in the X direction, the pineapple fibrils, which were in the upper and middle portions of the inclusion, demonstrated higher shear stiffness and for the shear strain in the Y direction, the shear stiffness was incresed in the lower portion of the inclusion which shows the pineapple fibrils had more resisttance against the shear strain in this region.

By focusing on slices 3-9 in Figure 6.21-B, the regions of the elevated shear stiffness roughly correspond to the upper and middle portions of the pineapple inclusion, while on slice 9 in Figure 6.26-A, the area of the raised shear stiffness is mostly related to the lower section of the inclusion.

Also, Tables 6.1 and 6.3 indicate different orthotropic mean values in three different orthogonal directions for all shear moduli components regardless of the value of the initial guess.

This can also be seen in Table 6.5, where the different correlation coefficients are found from orthotropic shear moduli reconstructions in 3-D. This clarifies that the pineapple displays orthotropic behavior as the shear moduli calculated from elastographic image reconstructions are directionally dependent.

Overall, the low value of STDs obtained from Tables 6.2 and 6.4 reveal that the variation from the mean values (average) is small. This fact increases the level of confidence in support of the pineapple as: an orthotropic material, the reliability of the MRE dataset and the capability of the orthotropic algorithm to distinguish three different shear moduli in three directions.

In general, by viewing Table 6.5, it is found that orthotropic reconstructions exhibit a higher shear modulus COR. CO. in comparison with isotropic cases. The evaluation of this table implies that in an optimum initial guess, the orthotropic algorithm was more successful in detecting the inclusion location with respect to a reference compared to the isotropic case. This leads to the higher accuracy of the orthotropic incompressible algorithm to distinguish the orthotropic elasticity parameter within an orthotropic phantom in comparison with the linear elasticity isotropic algorithm.

6.7.2 Orthotropic Initial Guess Study

6.7.2.1 Orthotropic Results Analysis

It is hard to make a judjment regarding the orthotropic results which are mostly from early iterations. Image results from almost all initial guesses appeared that the shear moduli reconstructions could not converge to the actual solution and as a result a good approximation has not achieved from the elasticity property distribution. Although this could be the reason for overall poor reconstructions with high levels of artifacts in most elastographic image reconstructions, there is still some evidence which is promising, and this is disscussed in this section.

In the orthotropic initial guess study, by evaluating the result improvements from initial guesses of 1-20 KPa, the initial guess of 10 KPa has shown successful elasticity image reconstructions with better results compared to other initial guesses in most cases. It seems that the orthotropic shear moduli reconstruction from the initial guess of 10 KPa, could detect three portions of the pineapple inclusion structure in three directions, after three iterations, as shown in Figure 6.4.

Meanwhile results obtained from the initial guess of 1 KPa shown in Figures 6.5, 6.6, and 6.7, demonstrate inconclusive elasticity reconstruction, even after six iterations. Results from other initial guesses illustrate fairly poor elasticity reconstruction to recover the whole structure, and most of them displayed incomplete portions (Fig. 6.10) and (Fig. 6.27), or only a few spots of the inclusion (Fig. 6.13), (Fig. 6.16), and (Fig. 6.19).

Orthotropic elastography reconstructions also exhibited poor calculated displacement results with high levels of artifacts found from initial guesses of 1-5 KPa (Figures 6.5, 6.8, 6.11, 6.14, and 6.17), while this trend was improved from initial guesses of 10-20 KPa (Figures 6.20 and 6.25), as the correlation between measured and calculated displacements was raised to a higher level.

Both Table 6.6 and Figure 6.20 represent that calculated displacements captured from the initial guess of 10 KPa has shown higher COR. CO. compared to other initial guesses in the three directional orthotropic image reconstructions.

In addition, focusing on the COR. CO. between the magnitude shear modulus and its calculated shear moduli components μ_{XY}, μ_{ZY} , and μ_{ZX} captured from the initial guess of 10 KPa after 17 iterations, the values of 0.99939, 0.99922, and 0.99916 were found, respectively, which shows a reasonable association between the magnitude shear modulus image and each calculated shear modulus component.

A consequence of the orthotropic initial guess study was that by changing the initial guess, the maximum mean value is varied for the shear moduli components. For example, μ_{ZY} demonstrates the highest mean values for initial guesses of 1 KPa, 2 KPa, 10 KPa and 20 KPa, while μ_{ZX} shows its maximum mean values for initial guesses of 3 KPa and 5 KPa, and finally μ_{XY} illustrates its highest mean value for the initial guess of 4 KPa.

This trend was also observed in the orthotropic displacements in three dimensions. For instance, initial guesses of 1 KPa, 4 KPa, 5 KPa, and 10 KPa displayed the highest COR. CO. in the X direction while the initial guesses of 2 KPa and 20 KPa have indicated their maximum COR. CO. in the Y direction, and finally the initial guess of 3 KPa has shown its highest COR. CO. in the Z direction.

These result controversies in orthotropic shear moduli and displacements show the orthotropic algorithm sensitivity to the initial guess. This problem could have been caused by the use of only one subset of MRE displacement data which included only one single frequency (85 Hz) where the excitation was in the X direction with respect to the phantom.

Results obtained from this research in both orthotropic and isotropic cases could be that the initial guess can play an important role in elastographic image reconstructions, and a good choice of initial guess can be a key factor to improve the optimization procedure resulting in a better outcome.

6.7.2.2 Orthotropic Image Reconstructions in Comparison with Isotropic Cases

Imaging results shown in Figures 6.29 and 6.30, display that the isotropic elasticity reconstruction could distinguish almost the whole structure of the arc shaped inclusion in most cases. The inner boundary of the pineapple inclusion could be detected along with fairly homogeneous results obtained from initial guesses of 2-5 KPa. However, significant artifacts can be seen in the outer boundary and also in the inner boundary, towards the center. Another artifact is also visible in the center, which appears slightly stiffer.

Table 6.5 indicates that for all initial guesses the orthotropic tests demonstrate a higher shear modulus COR. CO. with a significant difference in comparison to isotropic cases. This clarifies that the orthotropic reconstruction algorithm was able to generate more accurate image results from a material with an anisotropic nature, as well as distinguishing the inclusion location better related to the reality of the pineapple phantom.

Tables 6.1 and 6.3 indicate that from initial guesses of 1KPa to 5 KPa, higher mean values can be detected for the isotropic shear modulus reconstruction, while increasing the value of the initial guess from 5 KPa to 20 KPa, the orthotropic magnitude shear modulus reconstruction illustrates higher mean values in comparison to isotropic cases with the same initial guess. This implies that in the same conditions the optimum initial guess for an isotropic reconstruction can be different from an orthotropic case.

In the evaluation between isotropic and orthotropic reconstructions with almost equal conditions such as similar global iteration, (i.e. 16 for the isotropic and 17 for the orthotropic in this research), and with the same initial guess (i.e. 10 KPa), the orthotropic reconstruction shows better results.

From a glance at the results obtained in Table 6.1 and 6.5, the orthotropic reconstruction with the initial guess of 10 KPa exhibits a higher mean value, a higher shear modulus COR. CO., and a lower STD, in comparison to the isotropic reconstructions.

In a three dimensional assessment of the isotropic reconstructions, the maximum COR. CO. between measured and calculated displacements was always in the X direction, and the minimum COR. CO. was found in the Y direction for all initial guesses. By evaluating Table 6.1 it can be found that the final isotropic solution varies based on the initial guess. This implies that the isotropic process is dependent on the initial guess.

Table 6.6 indicates that with the initial guess of 10 KPa, the higher displacement COR. CO. could be detected in the X and Y directions for the orthotropic reconstruction, while in the Z direction the isotropic case shows the maximum displacement COR. CO.

In comparing the orthotropic and isotropic elastographic results, the orthotropic image reconstruction with a suitable choice of initial guess, was more successful in determining the structure of the pineapple inclusion, and recognizing the inner and outer boundaries correlated with the $T2^*$ MR magnitude image.

6.8 Conclusion and Remarks Applied to the MRE

In this research, orthotropic and isotropic elasticity reconstructions results from real MRI datasets obtained from the pineapple gelatin phantom were evaluated. An aim of this experiment was to investigate the proficiency of a novel orthotropic algorithm which was developed for the non-linear 3-D orthotropic incompressible material, to differentiate three real orthotropic shear moduli distribution in three dimensions.

The ability of this program to produce accurate results using the orthotropic real MRE dataset was also demonstrated throughout the initial guess study and in comparison with a linear elasticity isotropic algorithm.

Although mean value results captured from three dimensional orthotropic reconstructive imaging presented in this chapter have quantitatively shown that regardless of the value of the initial guess, the orthotropic algorithm was able to detect three different shear moduli (Tables 6.1 and 6.3), unfortunately most orthotropic elasticity image results are poor.

The consequence of detecting three shear stiffnesses in 3-D along with low STD values (Tables 6.2 and 6.4) can provide enough evidence to validate the pineapple as an orthotropic material. This qualifies the eligibility of the pineapple phantom: to mimic the tissue behavior in the tissue-equivalent gelatin phantoms for future MRE tests, the reliability of the MRE dataset captured from this phantom, and the capability of the orthotropic algorithm to distinguish the orthotropic behavior.

Orthotropic reconstruction results also demonstrated a higher shear modulus COR. CO. in comparison with isotropic cases (Table 6.5). This clarifies the precision of the orthotropic incompressible algorithm in comparison with the isotropic program to detect the orthotropic elasticity parameter, and the inclusion location within an orthotropic phantom correlated with an image reference ($T2^*$ MR magnitude image).

Although the algorithm was successful in recovering the shear moduli of the pineapple phantom as it could regain almost three portions of the pineapple inclusion in the initial guess of 10 KPa, as well as recognizing parts of the inner and outer boundary, high quality images could not be achieved from this algorithm. These resulting images illustrated a poor elasticity reconstruction with a high level of artifacts. There are several reasons which may explain the orthotropic elasticity image reconstruction deficiency in this experiment. These are:

- Using one set of MRE displacement data; for this orthotropic investigation, only one displacement dataset that was applied to excite the phantom used one single frequency (85 Hz) in the X direction. As mentioned, in an orthotropic case, it is hard to determine the elastic parameters uniquely in 3-D by using only one set of Drichilet boundary conditions, and this may cause the non-uniqueness problems. This can also be a reason for the algorithm sensitivity to the initial guess as shown in the initial guess study.

- Although in this study a high relative error for orthotropic displacement mismatches were found in comparison to isotropic cases shown in Table 6.7, it is still difficult to make an assessment.

Table 6.9 will clarify that this particular dataset (frequency of 85 Hz in one excitation dimension X) which was randomly selected for this investigation shows the highest relative error in comparison with other frequencies in other dimensions. Maybe choosing another displacement dataset from the full MRE dataset will yield more successful results with a lower error.

- ❖ In this research, the orthotropic incompressible program applied for elastography image reconstruction used the nonlinear CG as the optimization technique. As mentioned in 2.4.2.6, the CG algorithm in the nonlinear case became more complicated in terms of calculating α_k and the gradient of the objective function. As the orthotropic elastography inverse problem is a non-linear procedure, the search directions may lose their conjugacy as the iterations progress. Another problem in nonlinear CG is that a general function may have many local minima and in this case CG cannot guarantee to converge to the global minimum.

- ❖ The Secant line search technique was a useful method which was applied to calculate α_k in nonlinear CG, however this approach is not usually able to recognize minima from maxima, and it is also sensitive to the initial guess. This may also explain another reason for the algorithm sensitivity to the initial guess as this method needs a good choice of initial guess close to the actual solution to converge to the minima point successfully.

- ❖ Another problem which could be highlighted more is the ratio between the phantom matrix and the inclusion. As can be seen from images, the inclusion was very close or even attached to the boundaries. As explained in the previous chapters, this might elevate the artifacts, especially around the boundaries and edges.

- ❖ And the last important point was that these orthotropic reconstruction results have not had enough chances to improve the higher iteration to converge towards the actual solution, and most of them were from early iterations.

This perhaps was a reason for increasing the level of artifacts and reducing the accuracy of the orthotropic image reconstructions.

The initial guess study revealed that there is a correlation between a good choice of initial guess and the outcome of an elasticity image reconstruction with fewer artifacts. For this investigation, seven initial guesses were tested for both orthotropic and isotropic cases.

In the orthotropic initial guess study, by evaluating the result improvements from the initial guesses of 1-20 KPa, the initial guess of 10 KPa has shown fairly satisfactory elasticity image reconstruction results, even after three iterations. These image outputs are in terms of qualitative recovery such as the geometry of the inclusion (three portions) with the inner and some parts of outer boundaries, and also most quantitative parameters such as higher displacement COR. CO.

In comparing orthotropic with isotropic cases, orthotropic reconstruction results revealed a higher shear modulus COR. CO. This means that the orthotropic incompressible algorithm has shown more accuracy in comparison with the isotropic program, to distinguish the shear stiffness associated with the inclusion location in three dimensions.

As shown, changing the initial guess directly affects the elasticity image reconstruction improvement. While these results verify that the initial guess in MRE reconstruction may play an important role in the quality of reconstructed MRE images, more accurate tests are still required to determine the exact cause of the artifacts.

To make a fair judgment on the functionality of the orthotropic algorithm and to validate the orthotropic elastographic results obtained from the real MRE dataset, simulation studies with equal conditions should be undertaken in the future.

This discussion is open for more evaluation regarding other factors which may create the artifacts in MRE actuation systems (i.e. frequency, zone size etc).

Questions still remain concerning an optimum initial guess and other parameters which may affect the orthotropic image reconstructions such as: the type of optimization procedure, the regularization parameter, orthotropic data acquisition conditions, and the phantom fabrication process which was used to manufacture the orthotropic phantoms.

The results presented in this research can be used for orthotropic algorithm modification in the future to improve this exsisting robust program, to recover other orthotropic parameters for advanced MRE images.

6.9 Evaluating of Orthotropic MRE Multiple Measurement Using Rayleigh Damping Algorithm

In order to find a perspective for the optimum frequency and dimension from the current full MRE dataset, and also for future MRE data recording, an investigation was attempted using the incompressible Rayleigh damping algorithm [58]. This study was carried out outside the scope of this project using an isotropic shear modulus reconstruction program, to determine the accuracy of these sub-datasets to recover the reconstructed shear stiffness from the orthotropic pineapple phantom with the donut shaped inclusion.

This incompressible viscoelastic algorithm was specifically developed in our MRE group and its capability to recover the elasticity parameters was successfully tested with different phantoms. The Rayleigh damping algorithm is related to both elastic and inertial forces, and under time-harmonic conditions, the model is associated with complex shear modulus and density [204,205]. This model comprises a viscoelastic material implemented through a complex shear modulus, where the level of damping is related only to the elastic forces in the material [206,207]. The initial guess of 15 KPa was chosen for the subzone based CG optimization procedure, with a TV regularization parameter of 1.d-5 to reconstruct the shear modulus. The global iteration was set for 100 while other parameters such as zone size and density were equal to other previous reconstructions in this thesis.

6.9.1 Rayleigh Damping Results for the Full Real MRE Dataset

In this section, the Rayleigh damping image reconstruction results from the pineapple gelatin phantom with a donut shaped inclusion, captured from the full real MRI datasets, are presented. The excitation directions are presented in the global coordinate system as X, Y and Z. The displacement components in three directions are shown as u^X , u^Y and u^Z .

The results in this section comprise the $T2^*$ MRI magnitude image distributed within nine slices (Fig. 6.32), the shear modulus distribution from three frequencies in three dimensions (Figures 6.33-6.35), and the correlations between measured and calculated displacement patterns in three directions, obtained from three frequencies and three global dimensions (Figures 6.36-6.44).

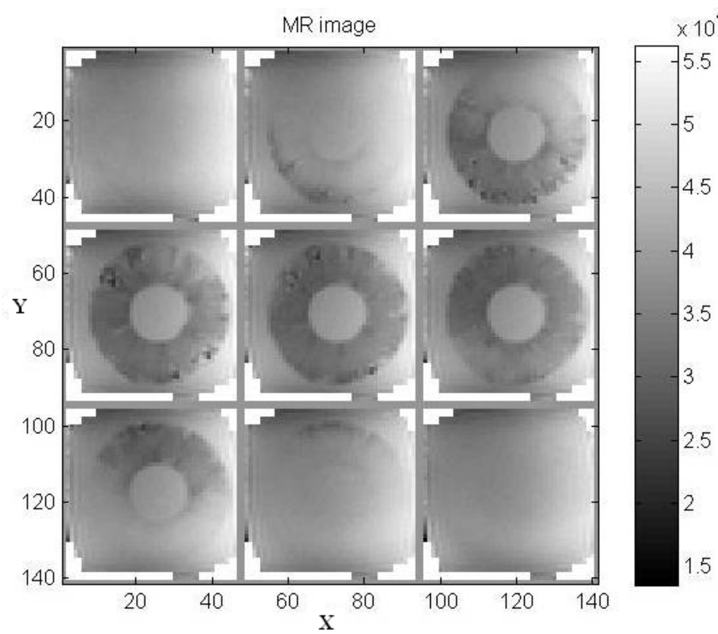

Figure 6- 32 This picture shows the $T2^*$ MRI magnitude images distributed within nine slices (3-11) captured from the pineapple gelatin phantom with a donut shaped inclusion. This picture has obtained from the X-Y plane of the global coordinate system.

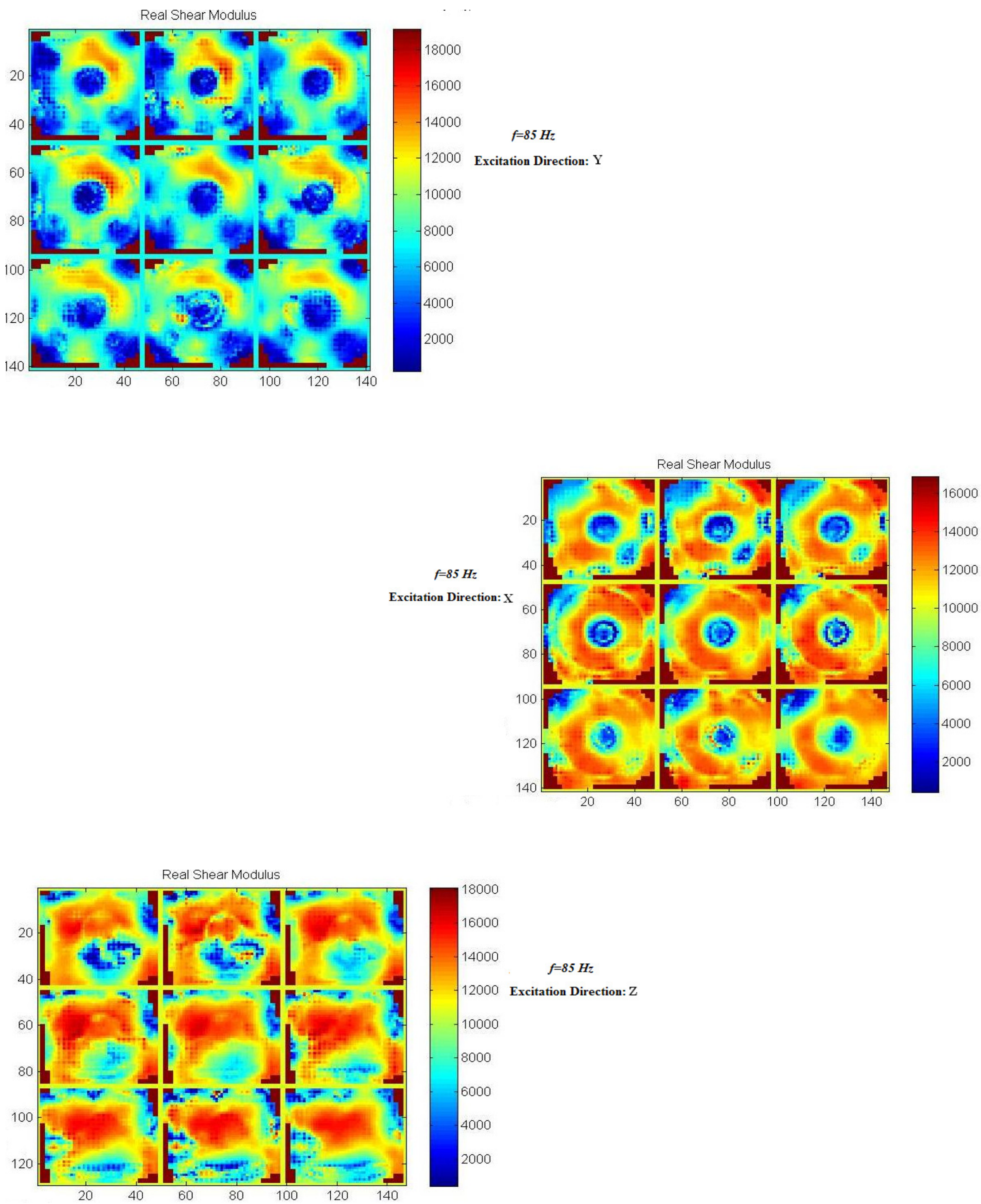

Figure 6- 33 The shear modulus reconstruction results obtained from the Rayleigh damping algorithm with a frequency of 85 Hz from the full MRE dataset. These results captured from the pineapple gelatin phantom with a circular shaped inclusion in three excitation directions (X, Y and Z) with respect to the phantom, distributed in nine slices. Almost all of the inclusion was recovered when the excitation operated in the X direction. While a high level of artifact can be seen when the actuation was in the Z direction.

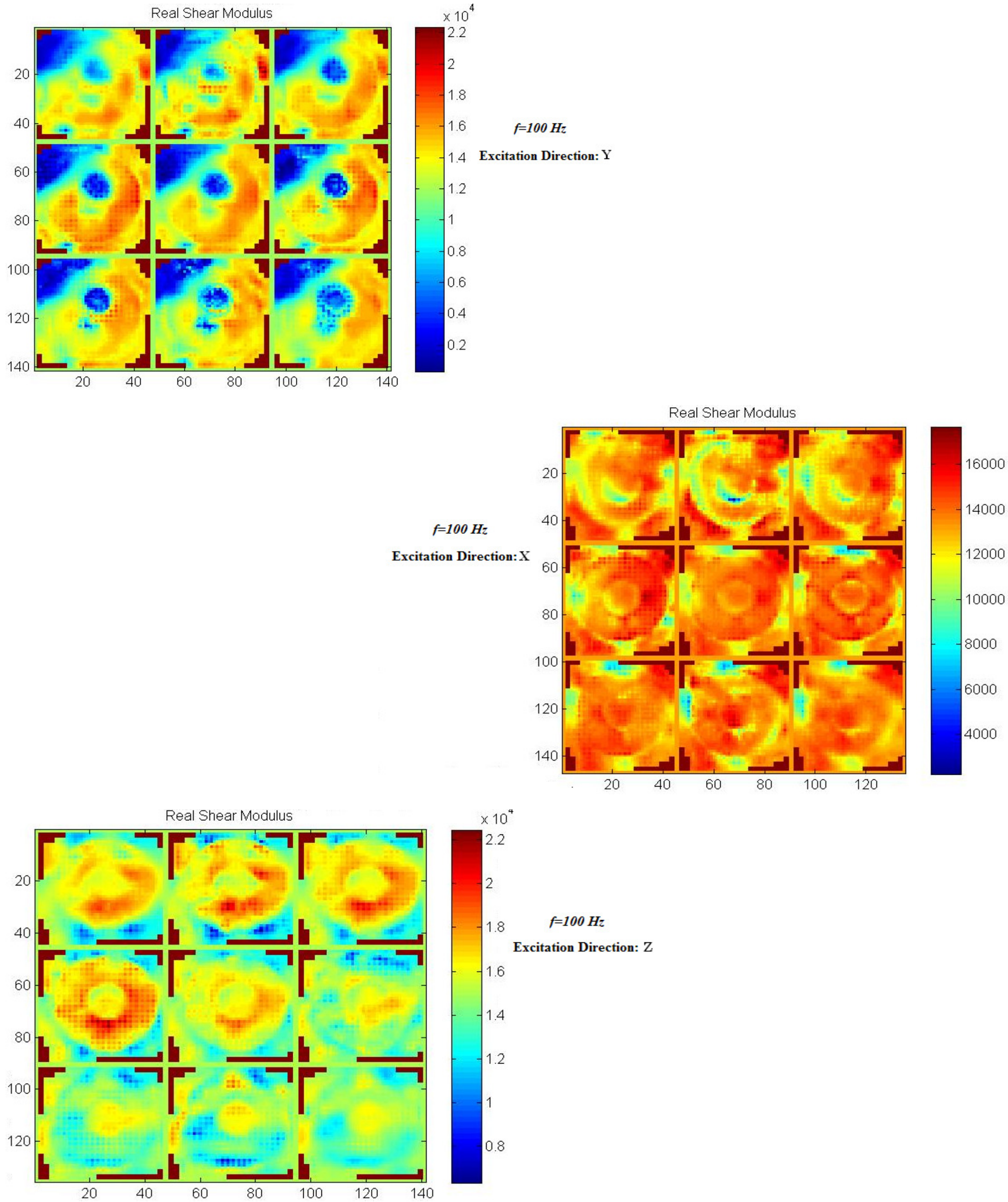

Figure 6- 34 Resulting isotropic shear modulus reconstructions in three dimensions obtained from the Rayleigh damping algorithm with a frequency of 100 Hz distributed in nine slices. The excitation directions in 3-D are shown. Almost all of the full circular pineapple inclusion with a fairly low level of artifact is visible when the excitation was in the Z direction. A high level of artifact can be seen in the X direction.

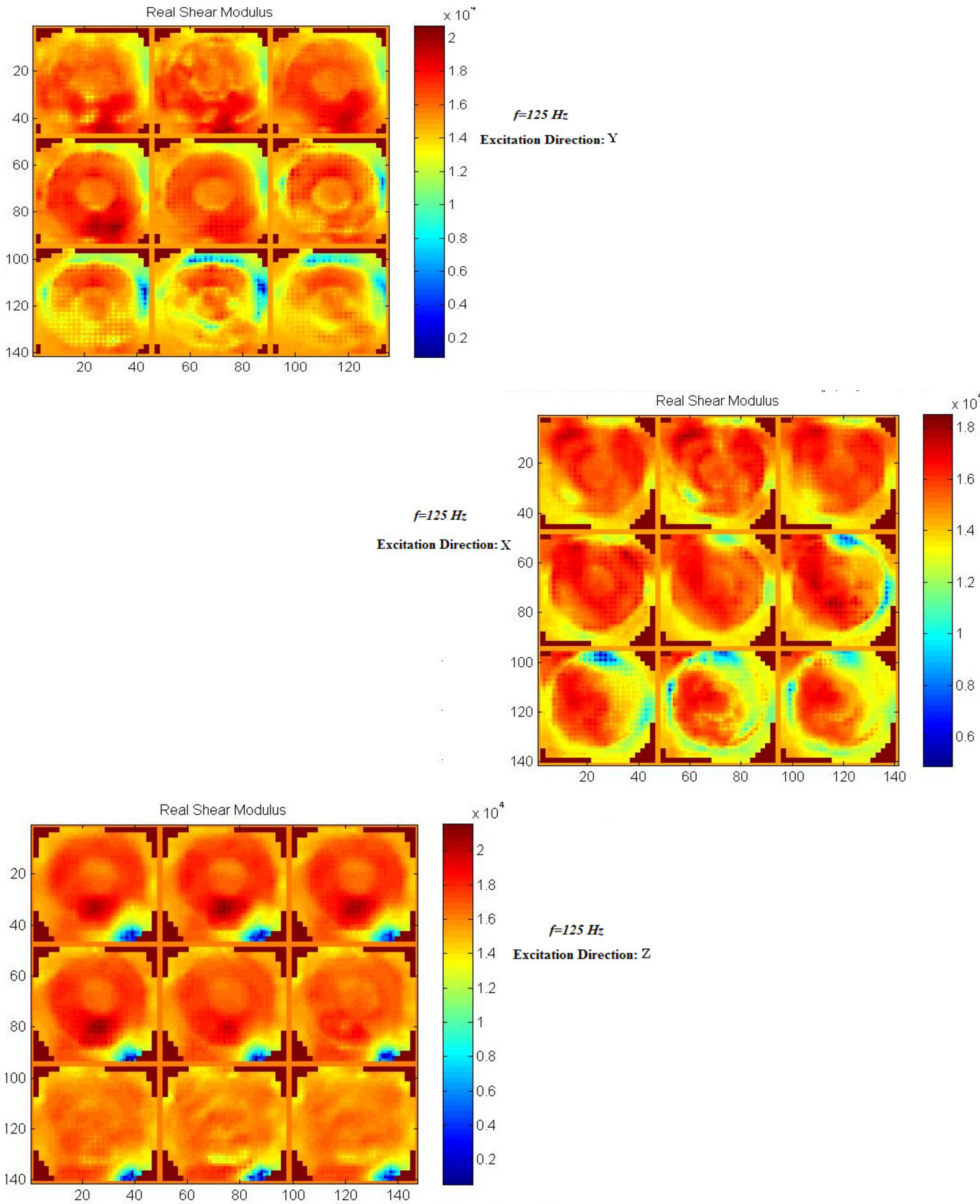

Figure 6- 35 These pictures show nine slices of the isotropic real shear modulus reconstructed by the Rayleigh damping algorithm with a frequency of 125 Hz captured from the full pineapple gelatin phantom MRE dataset with a circular shaped inclusion. The reconstructed shear modulus distribution with excitation directions (X, Y and Z) is depicted. The inclusion is fairly visible but with a high level of artifact in the background, which has almost covered the inclusion.

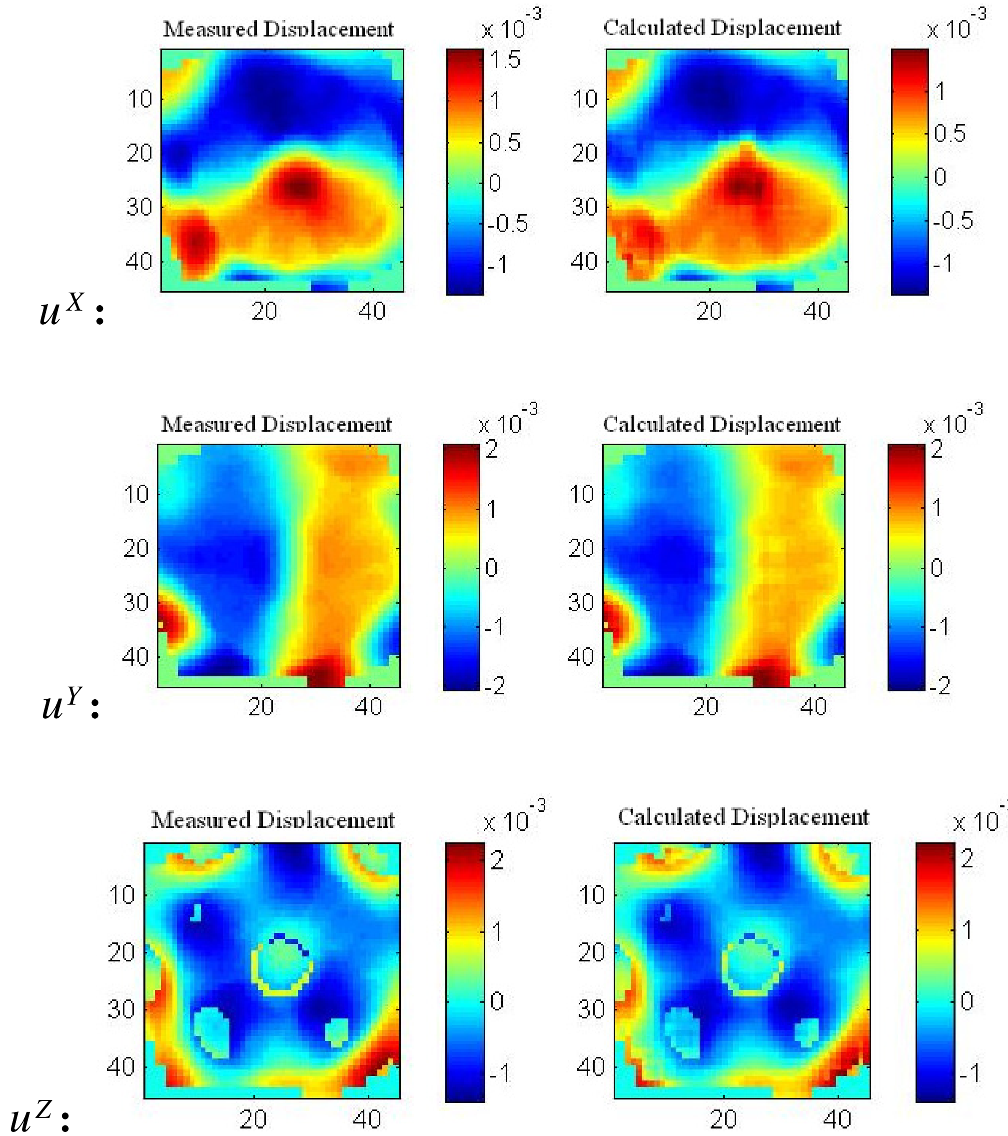

Figure 6- 36 Slice 7 of the correlation between the measured and the calculated displacement patterns in 3-D obtained from the pineapple gelatin phantom with a donut shaped inclusion. These pictures captured from a frequency of 85 Hz where the excitation was in the X direction. The irregular motion pattern is visible in the displacement field, while a few wrapped artifacts can be seen in the u^Z. (Note: a wrap artifact is a mis-mapping of signals which are outside the field of view (FOV) to the reverse side of the image. This causes some problems in recognizing the object which is inside the FOV and it happens in both frequency and phase encoding directions when the FOV is smaller than the object that is being imaged [209, 210]).

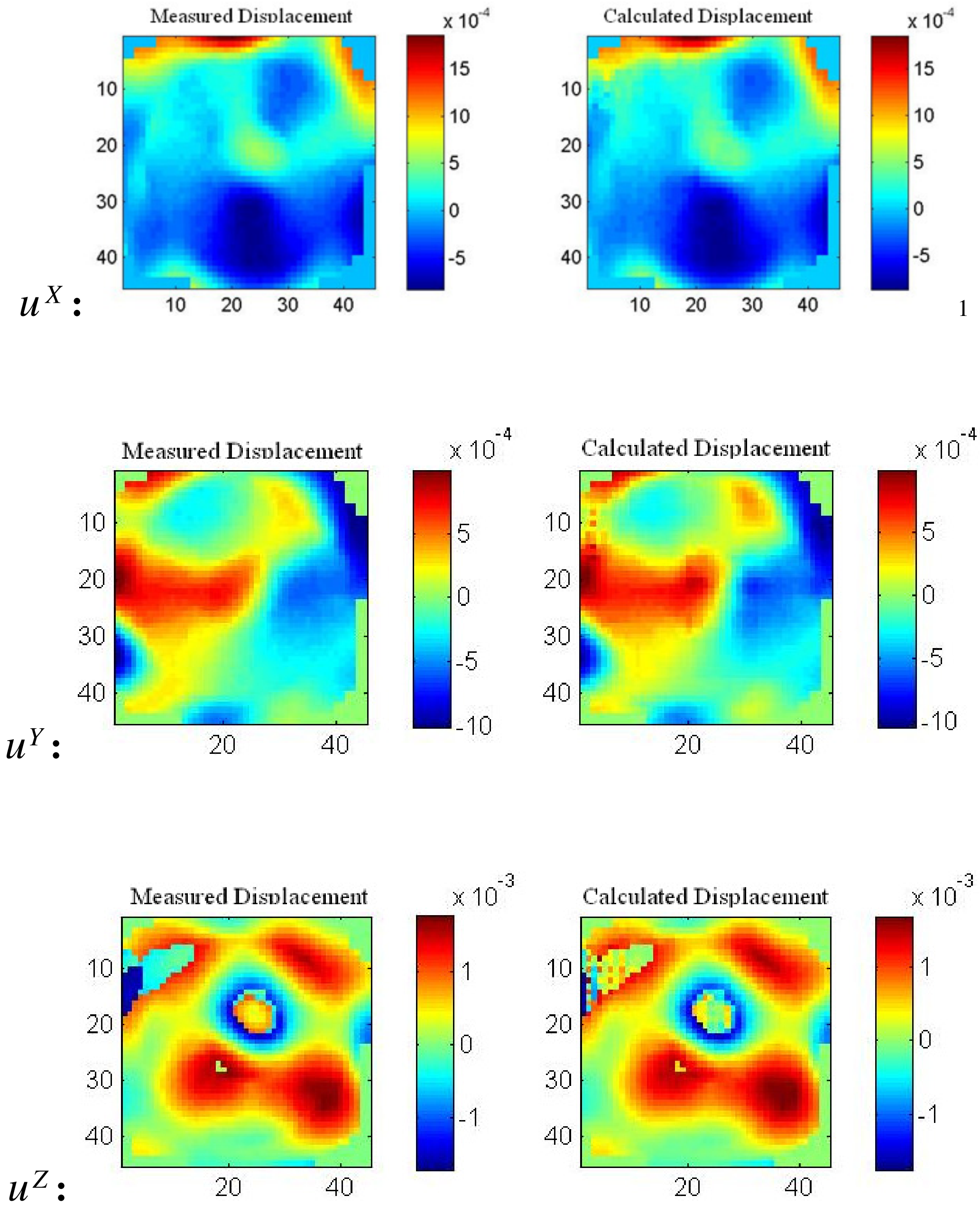

Figure 6- 37 The elastographic images show the correlation between the measured and the calculated displacements field obtained from slice 7 of the pineapple gelatin phantom with a donut shaped inclusion. These pictures were captured from the frequency of 100 Hz where the excitation was in the X direction. The displacement reconstructions in 3-D show a good perturbation motion pattern with a few wrapped artifacts in the Z direction, in both calculated and measured displacement images.

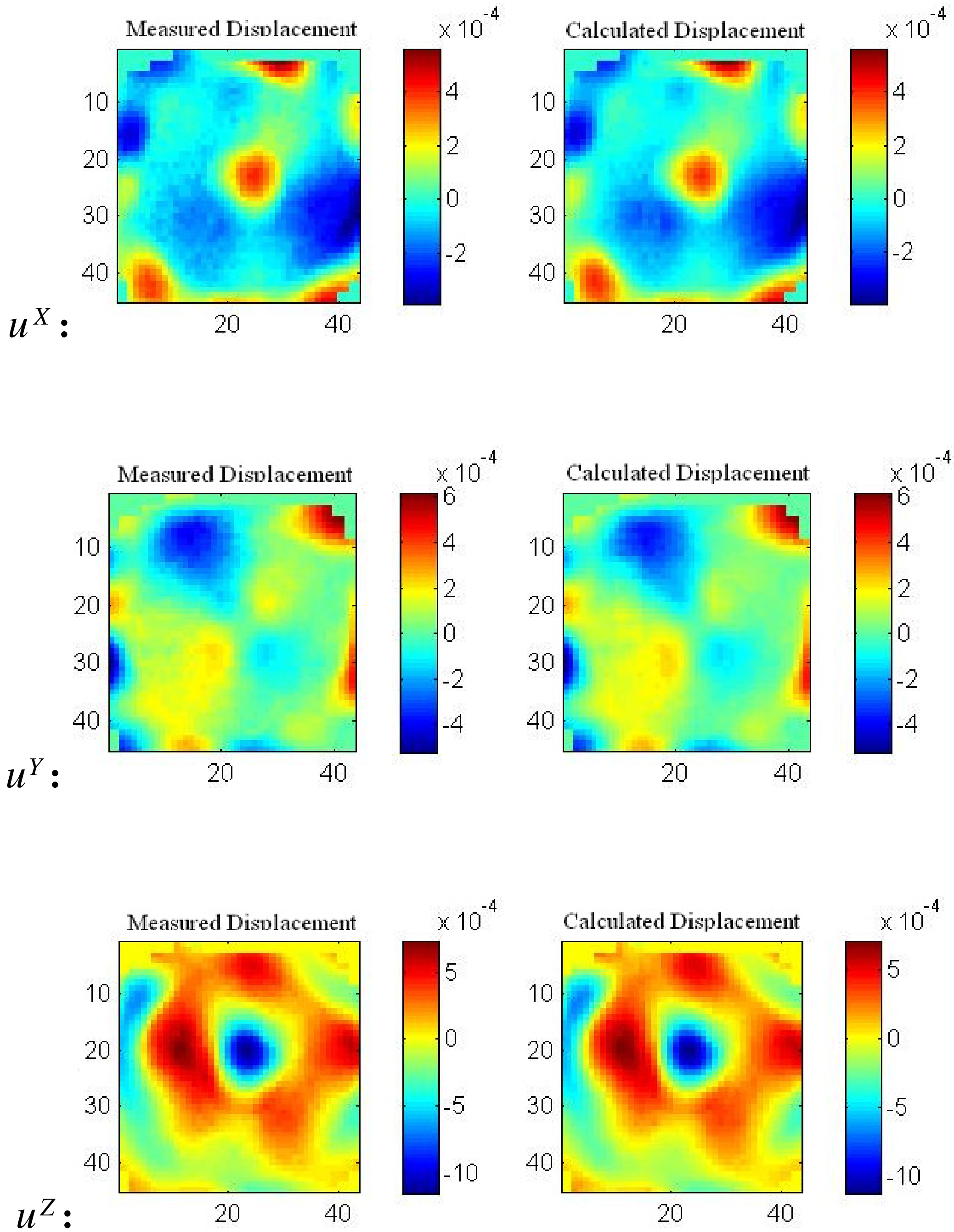

Figure 6- 38 The correlation between the real measured and calculated displacement patterns in three different directions for slice 7 of the pineapple gelatin phantom with a donut shaped inclusion is demonstrated. The displacements were captured from frequency of 125 Hz where excitation was in the X direction.. The images illustrate an irregular motion pattern. A high level of correlation is visible in all displacement directions.

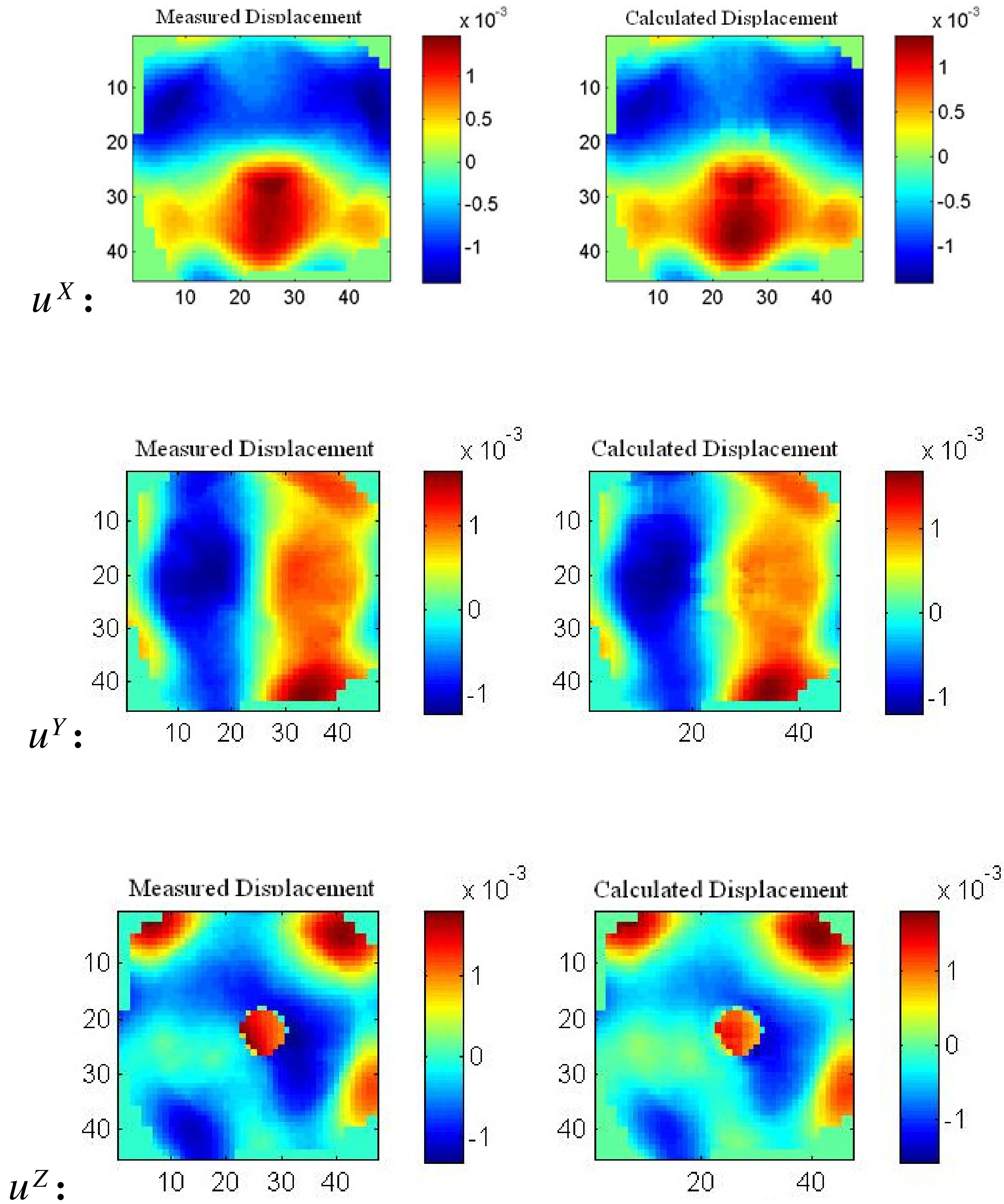

Figure 6- 39 The correlation between real measured and calculated displacement patterns in three different directions for slice 7 of the pineapple gelatin phantom with an arc shaped inclusion. The displacement dataset in 3-D were collected from the frequency of 85 Hz where the phantom was actuated in the Y direction. The motion directions, irregular pattern, and a high level of correlation, are visible in all images.

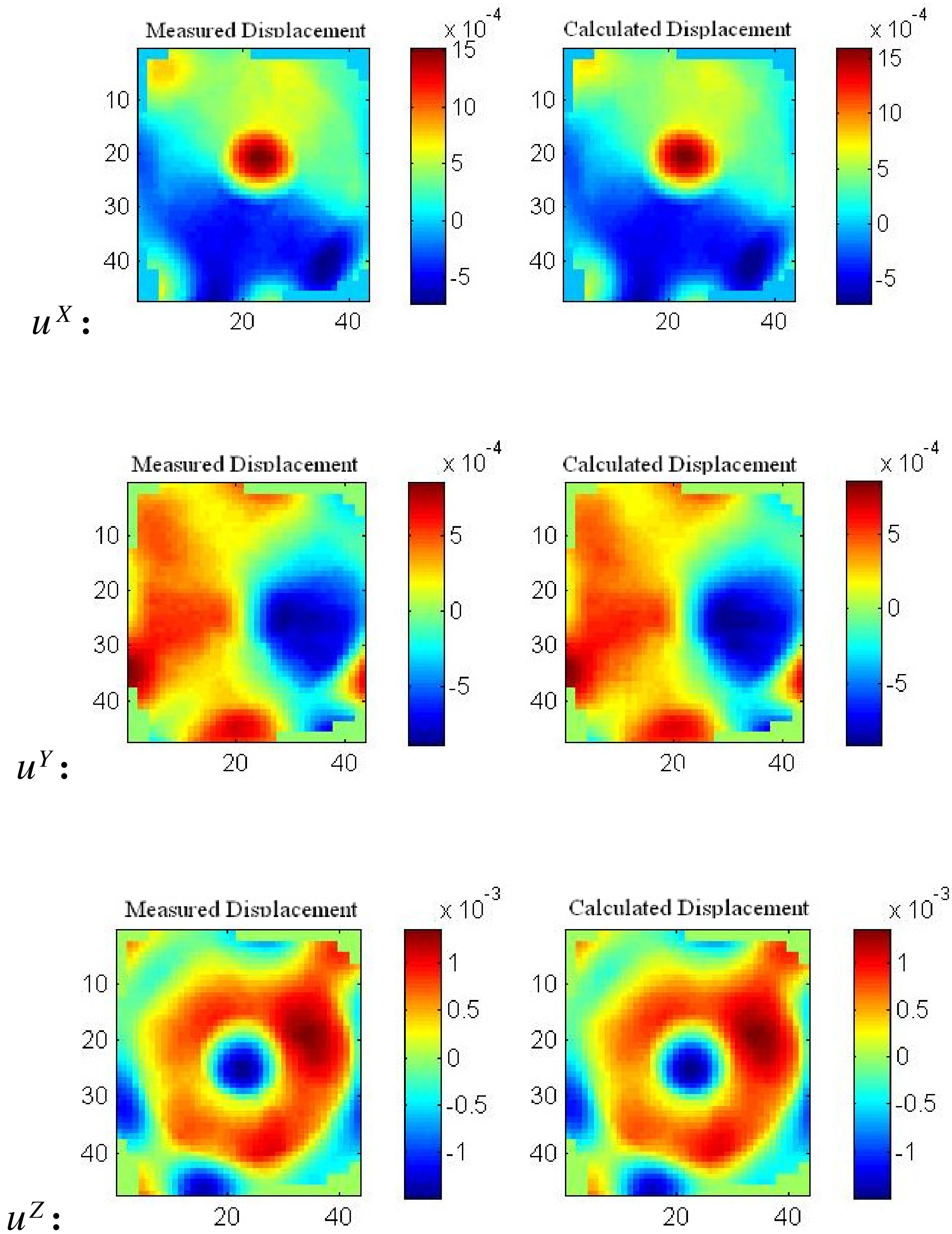

Figure 6- 40 The correlation between the measured and the calculated displacement field in three directions obtained from slice 7 of the donut shaped inclusion pineapple gelatin phantom is shown. These images were recorded from a frequency of 100 Hz where the excitation was in the Y direction.. A high level of correlation is observable in all directions, along with a good perturbation in the displacement pattern.

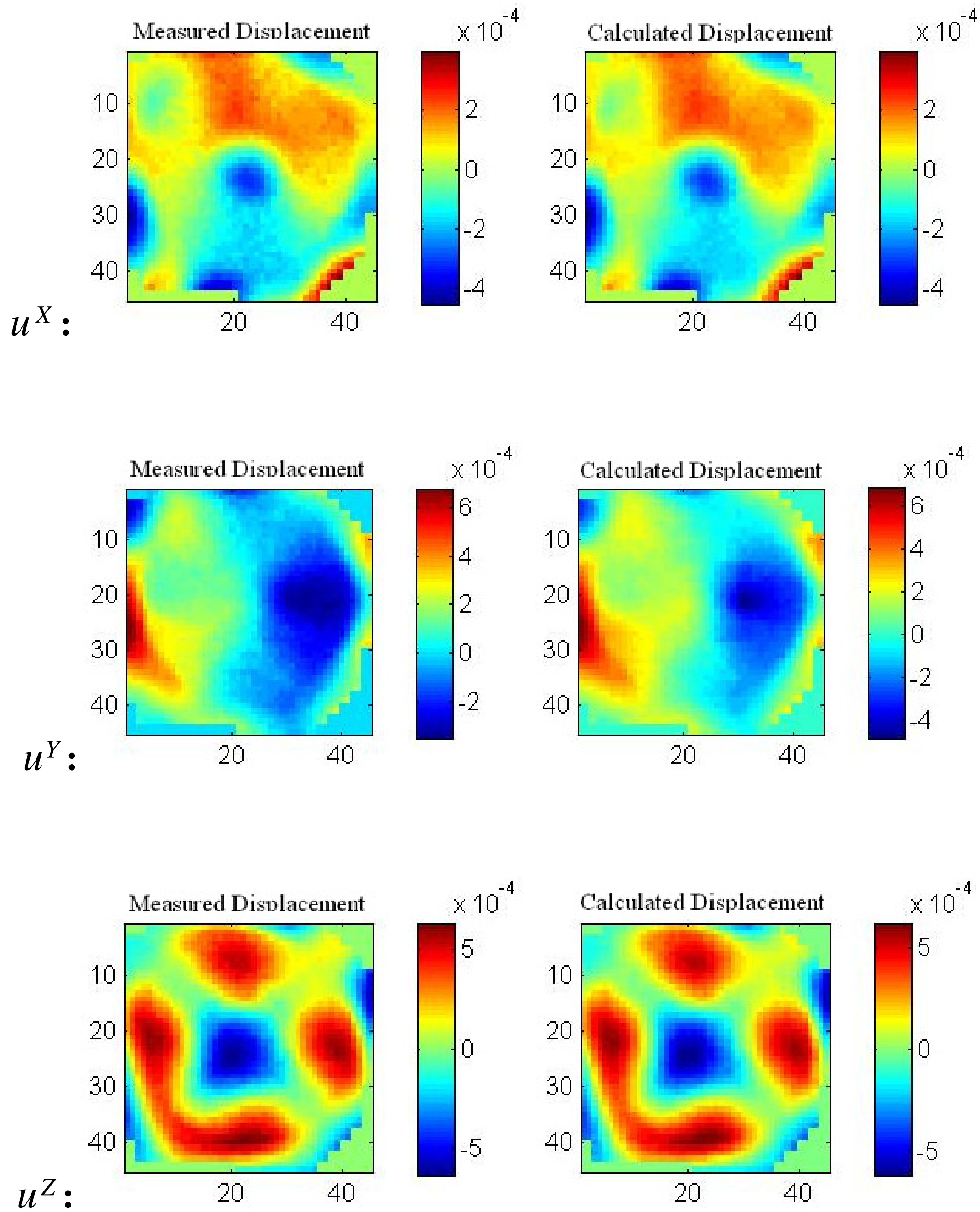

Figure 6- 41 The relationship between the measured and the calculated displacement patterns in three different directions are displayed for slice 7 of the pineapple gelatin phantom with a donut shaped inclusion. The MRE displacements were obtained from the frequency of 125 Hz where the actuation was in the Y direction. The directions of the irregular motion pattern with a good level of correlation are visible.

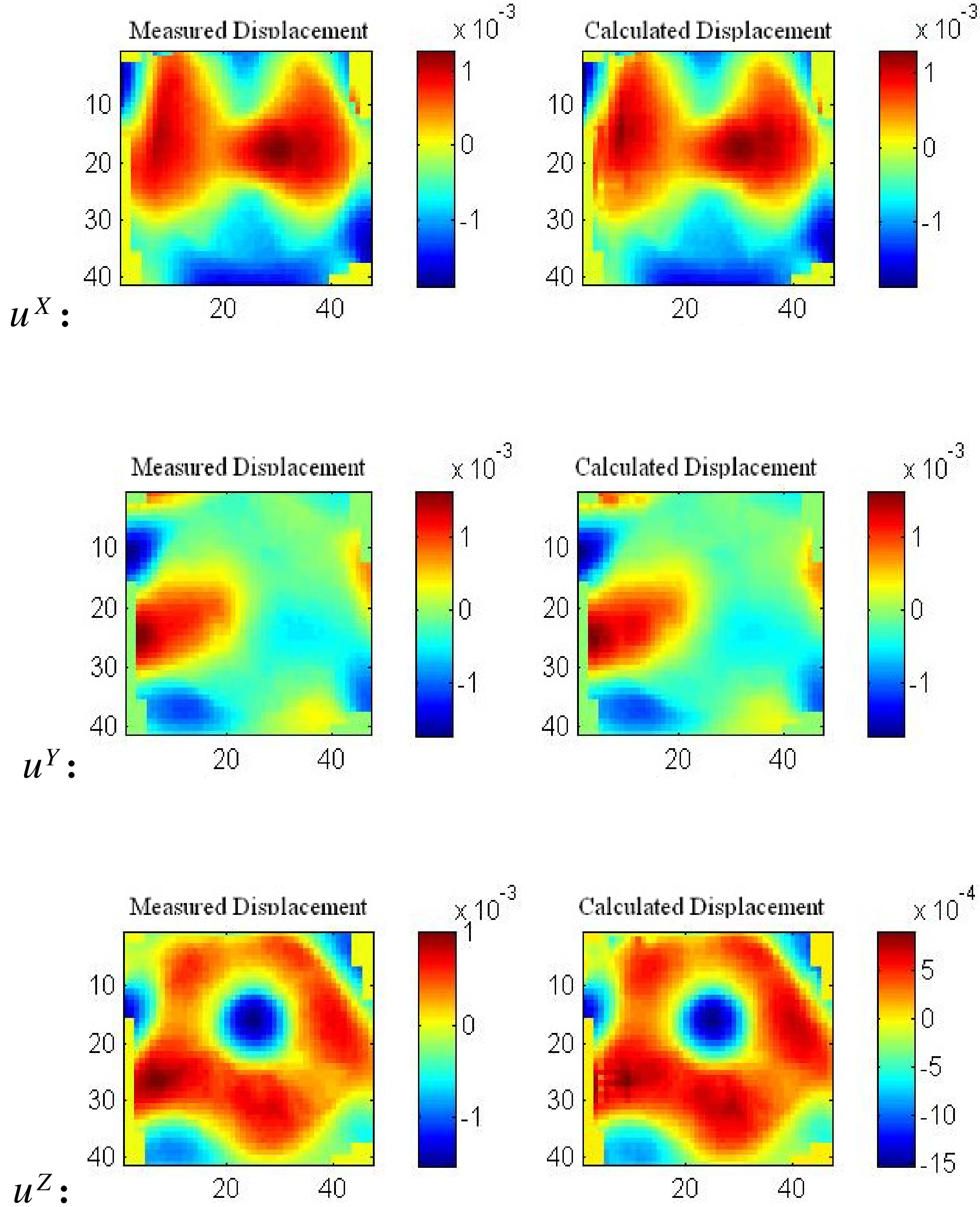

Figure 6- 42 Here the correlation between the isotropic measured and calculated displacement patterns in three directions, from slice 7 of the donut shaped pineapple inclusion are depicted. These images were obtained from the frequency of 85 Hz where excitation of the phantom was in the Z direction. The irregular pattern shows a good motion perturbation around the inclusion. The displacement images with a high level of correlation and a low level of artifact are illustrated.

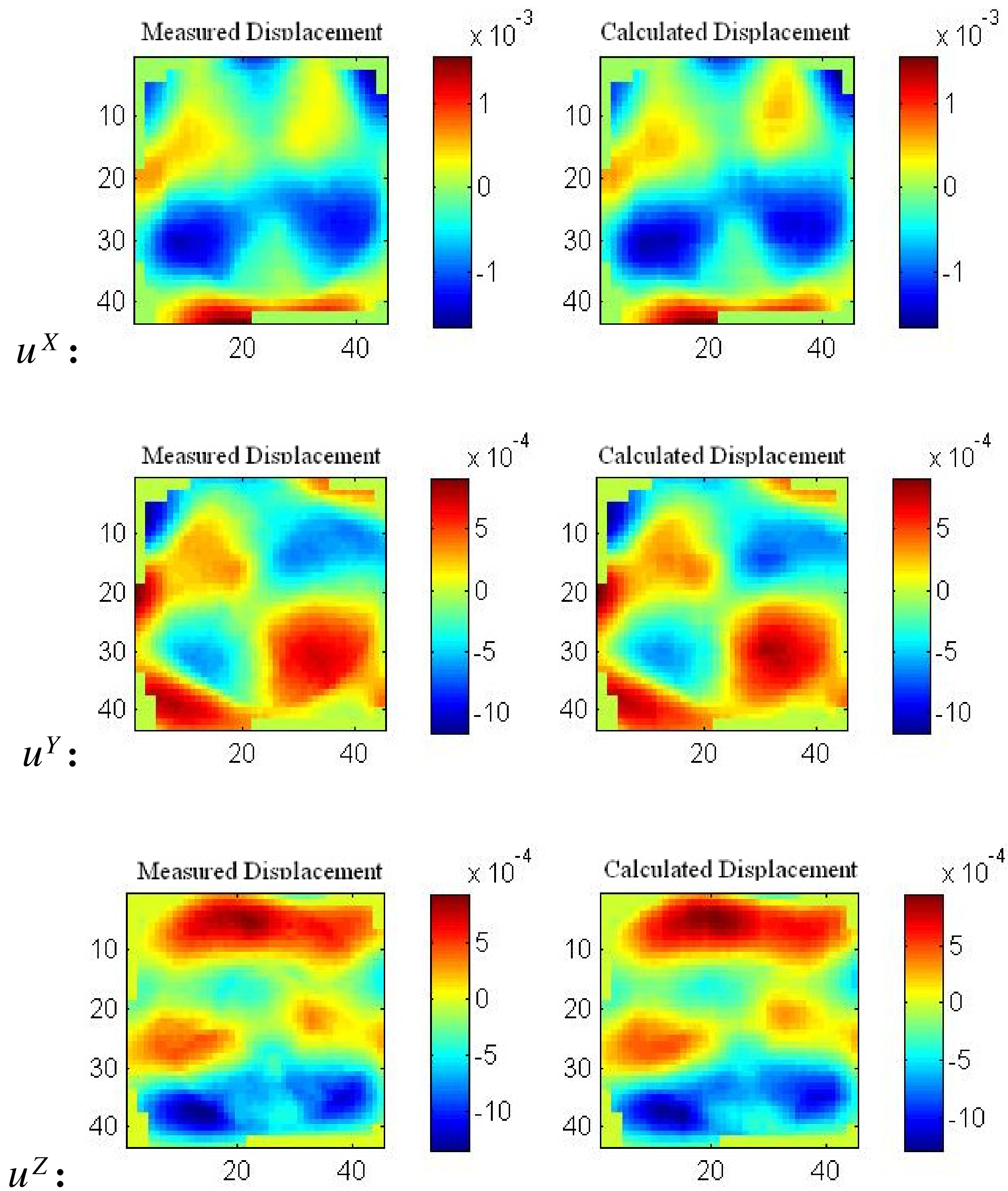

Figure 6- 43 These pictures depict the correlation between the measured and the calculated displacement patterns in three local directions for slice 7 of the pineapple gelatin phantom with a donut shaped inclusion. The MRE dataset for these reconstructions was captured from the frequency of 100 Hz where actuation was in the Z direction. The irregular motion pattern and the direction of the shear waves with a high level of correlation and a low level of artifact, indicate that the calculated displacements are in good symmetry with the measured displacements.

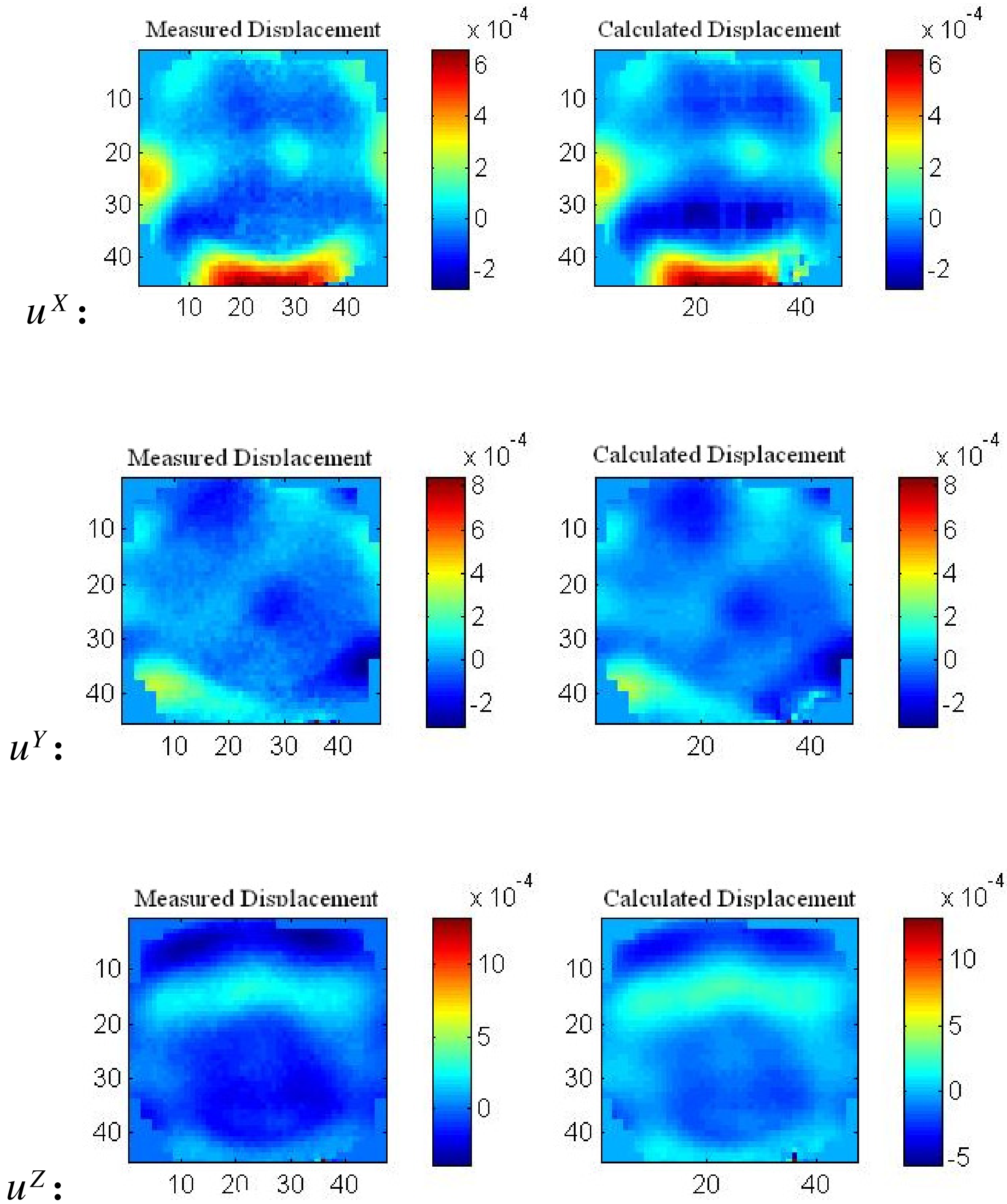

Figure 6- 44 The correlation between the measured and the calculated displacement patterns in three local directions for slice 7 of the pineapple gelatin phantom with a donut shaped inclusion is shown. These images come from the MRE motion dataset collected with a frequency of 125 Hz where the actuation was in the Z direction. The motion pattern shows the irregularity in the displacement field, while high motion signal strength cannot be seen. The direction of the waves with a high level of correlation and a low level of artifact are shown.

6.9.2 Rayleigh Damping Analysis for the Full Real MRE Dataset

In this study, the Rayleigh damping reconstruction results from the full real MRE dataset obtained from the pineapple gelatin phantom are evaluated.

Figures (6.33, 6.34 and 6.35) show enough evidence that the isotropic reconstruction algorithm could detect the whole (Fig. 6.34-Z direction and Fig. 6.33-X direction), or parts of the structure (Fig. 6.33 and 6.34, both in the Y direction) of the pineapple inclusion in three dimensions, with three different frequencies.

The inner and outer boundaries could be captured in the calculated shear modulus images (Fig. 6.33-X direction and Fig. 6.34-Z direction), along with significant artifacts (Figures 6.33-Z direction, 6.34-X direction, and 6.35- all dimensions). By focusing on slices 5 and 6 of Figure 6.34 the regions of the elevated shear stiffness in the Z direction fairly correspond to the pineapple's donut shaped inclusion.

Table 6.8 compares the displacement COR. CO. obtained from the Rayleigh damping image reconstruction for the frequency range between 85-125 Hz in three dimensions. Results are presented for slice 7 of the pineapple gelatin phantom with a donut shaped inclusion. In a general view on Table 6.8, it is found that the frequency of 100 Hz exhibits a higher displacement COR. CO. in both excitation directions of Y and Z for all displacement components in 3-D, while the frequency of 125 Hz illustrates a higher displacement COR. CO. where excitation was in the X direction, in comparison to other frequencies.

The evaluation of this table implies that there is an optimum frequency for each dimension. Taking the orthotropic datasets from these dimensions and considering the optimum frequency, leads to a more successful image reconstruction outcome.

Table 6.9 represents the percentage of the relative error ratio between measured and calculated displacements obtained from three dimensions of the orthotropic pineapple MRE dataset with three different frequencies (85, 100, and 125 Hz).

COR. CO. / Dimension		Frequency		
Excitation Direction	**Displacement Components**	**85 Hz**	**100 Hz**	**125 Hz**
X	u^X	0.9704	0.98237	0.99255
	u^Y	0.96993	0.96643	0.98805
	u^Z	0.97078	0.98074	0.99801
Y	u^X	0.98488	0.99541	0.99347
	u^Y	0.97885	0.99476	0.98632
	u^Z	0.98616	0.99896	0.99614
Z	u^X	0.99228	0.99594	0.97996
	u^Y	0.99257	0.99549	0.96991
	u^Z	0.99491	0.99834	0.99419

Table 6- 8 The displacement correlation coefficient (COR. CO.) results captured from the Rayleigh damping image reconstruction for the frequency range (85-125 Hz). These results obtained from three orthogonal excitation directions, with respect to the pineapple gelatin phantom with a donut shaped inclusion.

As this table shows, the frequency of 85 Hz shows the highest error in the dimension X as highlighted, while the frequency of 100 Hz demonstrates the lowest error in the dimension Y.

The minimum relative error rate in the excitation direction of X was found from the frequency of 125 Hz, while the minimum relative error in the Y and Z dimensions was captured from the frequency of 100 Hz. The frequency of 85 Hz shows the maximum relative errors in both X and Y dimensions.

Rel. Error % / Excitation	Frequency		
	85 Hz	100 Hz	125 Hz
X	14.5312	13.1072	7.0562
Y	9.2984	5.3947	8.7248
Z	8.6593	7.7073	13.3106

Table 6- 9 This table illustrates the percentage of the relative error (Rel. Error %) ratio between measured and calculated displacements obtained from the pineapple phantom with three excitation directions and including three different frequencies (85, 100, and 125 Hz). The frequency of 85 Hz shows the highest error where the excitation was in the X direction as highlighted, while the frequency of 100 Hz demonstrates the lowest error rate in the direction Y.

Unfortunately, the MRE dataset from the frequency of 85 Hz in the excitation direction of X which was randomly selected in the first place, was used for the orthotropic image reconstructions in this research (highlighted in the Table 6.9) . This may explain one of the reasons for the fairly poor results obtained from the orthotropic reconstruction described before throughout this chapter.

Successful initial elasticity image results obtained from the isotropic Rayleigh damping algorithm clarified that changing the frequency or excitation direction may lead to better results for the orthotropic reconstructions of the pineapple phantom. The pineapple inclusion could be captured in most cases, especially in the frequency of 100 Hz where the excitation was in the Z direction (Fig. 6.34). It is promising that by using a multiple displacement dataset with different frequencies, this may solve the non-uniqueness problem in the anisotropic reconstructions.

“The true philosophy is to learn again to see the world”

Morlean Ponty

Chapter 7

7.1 Conclusions

The orthotropic MRE was a novel technique which was launched for the first time throughout this project. The goals of this research were focused on establishing the methodology of orthotropic elastography imaging. These aims were categorized as:

- ❖ Developing an orthotropic phantom which would be able to mimic tissue by exhibiting a realistic orthotropic behavior.

- ❖ The collection of orthotropic data acquisition with multiple displacement measurements in one completed MRE dataset. The goal was to provide sufficient information for the boundary conditions to avoid the non-uniqueness problems, which can be highlighted in nonlinear orthotropic inverse problem.

- ❖ Validating the orthotropic incompressible algorithm which was developed for 3-D orthotropic materials and for the first time used as a robust algorithm through this project. This investigation into distributed orthotropic incompressible parameter reconstruction was performed to indicate how well this novel material property reconstruction algorithm will be able to differentiate the orthotropic incompressible shear stiffness parameters in three dimensions, as well as testing the capability of this orthotropic reconstruction program to generate accurate reconstruction results using real MRE data.

Also two different piezoelectric actuation systems were compared, introduced in this thesis as Type A and Type B in order to suggest a realistic design guideline for advanced MRE actuation systems.

Phantom experiments with these piezoelectric actuators have shown a potential source of artifact produced by constraints applied to the actuation system. In the comparison of the two piezoelectric actuators, Type-A and Type-B, with two different boundary conditions, a satisfactory shear modulus reconstruction with fewer artifacts was demonstrated with the Type-B actuation system.

Along with phantom fabrication, several modifications were made to the phantom-coil set up by considering three dimensional boundary conditions to improve the MRE data acquisition procedure suitable for orthotropic incompressible materials that can be a framework for future MRE clinical applications.

In addition, several investigations were attempted to reveal some artifact roots in elastographic image reconstructions. The approaches presented in this thesis investigated the role of the boundary condition and initial guess as two key factors for improved material property reconstructions, with fewer artifacts.

The initial guess study using orthotropic and isotropic image reconstructions along with the boundary condition examination applying isotropic reconstructions, were carried out to demonstrate the influence of these parameters in the improvement of the elastographic image reconstruction outcomes.

While results presented in this thesis have shown some evidence that the boundary condition and initial guess in MRE reconstruction may play important roles in the quality of reconstructed MRE images, more accurate tests are still required to determine the exact cause of the artifacts.

Results obtained from this research suggest that a good choice of initial guess and boundary condition can improve the elastic property imaging process.

The majority of this research was allocated to isotropic and orthotropic phantom development. The achieved fabricating protocols throughout this thesis can be used as a guideline for future MRE testing.

Recently, another study has been undertaken mentioned in 6.9 to investigate the full MRE dataset from the pineapple phantom with a toroid shaped inclusion, which was collected from three different frequencies and in three dimensions, with respect to the phantom. This investigation was carried out to find a perspective for the optimum frequency and dimension for the current, and for future MRE data recording.

Successful initial elasticity image results obtained from the isotropic Rayleigh damping algorithm clarified that changing the frequency or excitation direction may lead to better results for the orthotropic reconstructions of the pineapple phantom. It is also promising that by using a multiple displacement dataset with different frequencies, the non-uniqueness problem in the anisotropic reconstructions may be solved.

7.1.1 Orthotropic Phantom Developments

In this research, a technique based on the subzone error minimization through an optimization method has been presented to clarify the orthotropic elasticity behavior within biological and non-biological samples. For this purpose, several orthotropic and isotropic phantom manufacturing protocols were proposed, which can be used in advanced phantom fabrications.

The *in vitro* orthotropic gelatin phantom outputs included one biological (pineapple) and two non-biological (circular and vertical) bristle gelatin phantoms, which were successfully developed and tested for the MRE orthotropic data acquisition, although only the pineapple dataset was used for orthotropic image reconstructions in this research.

Fabricating biological gelatin phantoms using fruit (pineapple in this study) for orthotropic MRE *in vitro* testing was a novel technique which was specifically developed for this investigation. This method was easy regarding the phantom manufacturing, an inexpensive but efficient way to non-invasively measure the orthotropic elasticity parameters of a biological material *in vitro*.

In the developing of muscle phantoms, the satisfactory material property transformation using several techniques such as: laser transmission, electricity, electrosurgery devices, and chemical components, has shown that these methods are capable of creating a stiffer *ex vivo* inclusion within the bovine muscle phantom.

Questions still remain regarding the development of the optimum inclusion fabrication technique, improvement of the MRE data acquisition, and orthotropic image reconstructions for the *ex vivo* muscle phantoms, which will require more accurate testing to prepare a suitable orthotropic phantom with a stiffer inclusion, as well as its MRE dataset for orthotropic elastography experiments.

7.1.2 Multiple Measurement Developments for Orthotropic Boundary Conditions

For the first time, a complete MRE data set was successfully collected by developing phantom data recordings from one frequency to three different frequencies, in three dimensions, while in each dimension a set of these three different frequencies was applied.

This satisfactory improvement in the three dimensional orthotropic data acquisition from one specific frequency to three different frequencies collected in one set of MRE data was a novel approach which was developed for this project.

Multiple measurements from the pineapple gelatin phantom with several independent boundary conditions within the frequency range (85-125 Hz) in three orthogonal dimensions could provide a complete record of MRE motion information.

This is needed to capture all mechanical properties of this orthotropic phantom in 3-D during the orthotropic image reconstruction procedure. This full MRE dataset could cover three individual load conditions for different MRE problems with different boundary conditions.

These were categorized as: one specific frequency (i.e. 100Hz) in 3-D relative to the phantom, three different frequencies (i.e. 85 Hz, 100 Hz and 125 Hz) in 1-D, and three different frequencies in 3-D with respect to the phantom in which each frequency was assigned to one side of the phantom.

Although this effort was carried out to use a multiple displacement measurement set to provide sufficient information for the unique identification of material properties in 3-D, only one subset of the full MRE dataset with a single frequency (85 Hz) in the excitation direction X was used for orthotropic reconstructions in this research. The reason for this limitation was the long run time issue due to the slowness of the algorithm process.

7.1.3 Orthotropic Algorithm Validation

The ability of the non-linear 3-D orthotropic incompressible algorithm to detect differences in orthotropic incompressible shear stiffness parameters in three dimensions was investigated.

As this was the first time that the algorithm was tested for orthotropic incompressible reconstructions, a variety of settings for the various options was arranged to find the optimal configuration for an orthotropic image reconstruction.

Orthotropic image reconstructions were carried out to map orthotropic elasticity properties (shear moduli) in 3-D based on MR detected motion datasets captured from the pineapple gelatin phantom. The capability of the orthotropic reconstruction program to generate accurate results using the real MRE data is demonstrated through these reconstructions of the tissue-mimicking pineapple gelatin phantom.

The capability of the pineapple gelatin phantom to mimic the tissue with orthotropic properties was validated by evaluating the results obtained from orthotropic elasticity image reconstructions, which were discussed in the previous chapter.

The first generation of orthotropic image reconstruction results obtained from the initial guess of 10 KPa were promising, as areas of the pineapple inclusion were found to have higher real shear moduli than the surrounding gelatin background.

The recovered shear moduli and the displacement locations were also correlated with the real inclusion structure, although there were a few artifacts in the background and boundary regions.

Focusing on the initial guess of 10 KPa, the shear modulus and displacement COR. CO. obtained from Tables 6.5 and 6.6 indicated that orthotropic reconstructions were more successful in detecting the inclusion location with respect to a reference compared to the isotropic reconstructions.

Higher mean values found in Tables 6.1 and 6.3, and lower STDs obtained from Tables 6.2 and 6.4 have also led to the higher accuracy of the orthotropic incompressible algorithm, to distinguish the orthotropic elasticity parameter within an orthotropic phantom in comparison with the linear elasticity isotropic program.

These initial results are promising, and suggest that shear modulus obtained from common isotropic linear elasticity-based parameter reconstructions of displacement fields measured from the pineapple phantom may not be representative of the true orthotropic material parameter distributions.

While the elasticity image reconstruction analysis presented in this research enjoyed the advantage of the fastest optimization method (the CG combined with an adjoint residual technique), the orthotropic incompressible algorithm has shown that the procedure of the orthotropic inverse reconstruction is prohibitively slow.

For example, it took weeks for only a few iterations of the reconstructed image results. This was a serious issue which created numerous limitations for this research. Perhaps by applying more modifications in the algorithm, this problem can be solved in the future.

Although the orthotropic algorithm used in this research has not been given a chance to test a real patient dataset, this technique provided a promising approach to understanding the orthotropic behavior of non-linear incompressible materials such as breast tissue and hard tumors, and suggests a realistic design guideline for advanced MR elastography in the future.

7.2 Future Work

7.2.1 Orthotropic Phantom Modifications

There are several modification points which will lead to phantom improvement in the fabrication process. These can be listed as:

- Considering an inclusion with asymmetrical geometry during phantom manufacturing to prevent ambiguity in recognizing the shear moduli in the symmetrical plane.

- The geometry and the size of the inclusion should be proportional with the phantom box.

- The ratio between the phantom matrix and the inclusion should be considered so that sufficient gelatin matrix is surrounding the inclusion, to keep the inclusion far away from the phantom boundaries. Ignoring this issue will reduce the distance between the inclusion and the phantom boundaries, which can potentially cause the artifacts around the phantom boundaries in the image reconstruction procedure.

- ❖ Replacing the bovine muscle phantom with other animal muscle such as chicken muscle or fish, can be other alternatives used to make a harder inclusion using heat, as these may have better thermal conductivity to create a suitable inclusion within the phantom.

While the goal of elasticity property changing in order to generate a stiffer inclusion within the phantom using different techniques mentioned in 7.1.1 has been achieved, more modifications are still needed to create a qualified inclusion within the muscle phantom, and to capture a high quality orthotropic MRI dataset.

Selecting a suitable inclusion regarding the material type and its geometry for the *in vitro* orthotropic gelatin phantoms, whether biological or non-biological, which can mimic real tissue behavior, still needs more investigation.

Future work can be focused on generating more accurate *ex vivo* muscle phantoms, *in vitro* orthotropic gelatin phantoms, and MRE motion dataset acquisitions. These can be used as inputs to increase the accuracy of the orthotropic algorithm to create more sophisticated elastographic image results from orthotropic datasets.

7.2.2 Orthotropic Boundary Condition Modifications

As mentioned, the orthotropic reconstruction procedure requires the MRE datasets from multiple actuation directions along with multiple load conditions in 3-D, to generate a well conditioned formulation to avoid ambiguities due to non-unique inverse problem processes.

Owing to the orthotropic algorithm's slow optimization improvement, which in practice caused a serious time limitation issue for this project, only one sub displacement dataset was randomly chosen from the full MRE dataset, which comprised one single frequency (85 Hz) in the global actuation dimension X, to reconstruct the orthotropic behavior of the pineapple phantom.

However, Table 6.9 revealed that this specific frequency (85 Hz) demonstrated the highest relative error among other frequencies (100 Hz and 125 Hz).

For the future, the results can be improved by using the full MRE datasets obtained from the pineapple gelatin phantom, which includes multiple excitation directions with multiple frequencies in 3-D to produce a well-posed formulation for the inverse problem.

The results obtained from Tables 6.8 and 6.9 can be applied as a guide line to achieve satisfactory shear moduli reconstruction results. Using the frequency of 125 Hz in the X dimension and the frequency of 100 Hz in the Y and Z dimensions, may yield more success in producing accurate results with fewer artifacts.

While the pineapple model has been successful in generating the orthotropic MRE dataset using a frequency range between 85-125 Hz, little is known about the response of these materials to the dynamic loading.

This can be experienced during steady-state MRE to indicate the dynamic response of the pineapple in other available frequency ranges regarding the MRE equipment limitations to well characterize the orthotropic response of the pineapple to mechanical load conditions.

7.2.2 Orthotropic Algorithm Modifications

As mentioned in Chapter 3, to describe the incompressible orthotropic elastic behavior of the tissue-like materials such as the pineapple phantom, reconstructing all six independent coefficients E_i (E_1, E_2, and E_3), and μ_j (μ_4, μ_5, and μ_6), in the three directions is necessary.

As the procedure of the orthotropic reconstruction was slow, only three real shear moduli (μ_{XY}, μ_{ZY}, μ_{ZX}) in three dimensions were applied in this research. This limitation of conclusive evidence in the presented results reduced the certainty of proof needed to describe the nature of the orthotropic material.

One approach to improving the reliability of the orthotropic incompressible elasticity reconstruction parameters would be to set the problem for different optimization procedures, such as Gauss-Newton [200], Quasi-Newton [201, 202], and BFGS [203], as well as the CG method to be given different values for the regularization weight parameter in the TV regularization technique.

Although the orthotropic algorithm was able to distinguish three shear moduli in three directions successfully, more analysis is still needed to fully quantify the orthotropic behavior of a material.

The observed orthotropic effect presented in this research was related to the one single frequency in a specific direction. More anisotropic tests can be undertaken using the multiple displacement dataset from the full MRE dataset, developed for the orthotropic pineapple phantom.

The orthotropic algorithm used for this research is now capable of setting multiple displacement dataset input files in one inverse solution. In this process, the output generated from the orthotropic inverse problem solution will be the best approximation to the material properties given all of the provided input displacement data. This will help to improve the accuracy of the orthotropic results.

In parallel with other studies to find the artifact roots in the elastographic image reconstructions, an attempt was made to evaluate the role of the zone size to improve the orthotropic elasticity property outcomes.

Work is still underway to obtain the best ratio between internal and external nodes of a zone regarding the size of the zone. Setting a problem with a revised zone size may yield more success in producing desirable orthotropic results.

One avenue to verify the accuracy of the shear modulus value in all elasticity image reconstructions can be by using Dynamic Mechanical Analysis (DMA). This instrument is capable of determining a range of mechanical properties externally [204].

There are two important points in using DMA; first the sample should be prepared carefully and be less than 10mm square and be about 2mm in thickness, secondly the instrument must be calibrated precisely to determine the shear modulus values accurately.

The initial guess estimation can be established on the shear modulus value output collected from the DMA system. This method will provide a more accurate reconstruction, by directing the estimation of the correct initial guess, and will save time regarding the selection of the right value for the starting point in reconstructions.

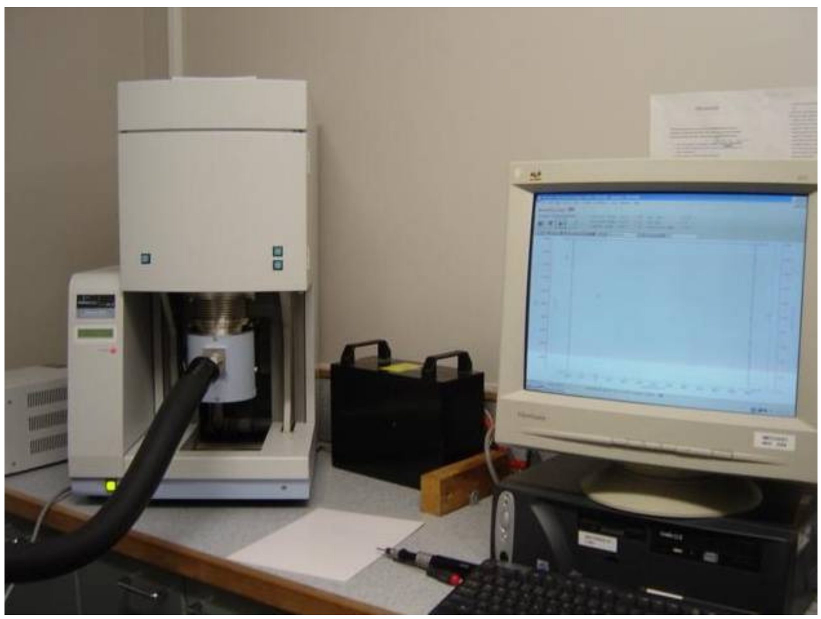

Figure 7- 1 A configuration of the Dynamic Mechanical Analysis (DMA) system

While an ideal robust algorithm should be insensitive to a range of initial guess values estimation and in the presence of the noise, image elastographic results in this study revealed a dramatic variation to the initial shear modulus distribution for the orthotropic reconstruction algorithm. In the reconstruction evaluation, it is found that none of the orthotropic solution process could meet the global iteration (100) set for the optimization convergence.

This can explain the reason for a greater error achieved from the early iterations in the error minimization of the objective function. This also clarifies the evidence for the larger relative error in the orthotropic reconstructions in comparison with isotropic cases (Table 6.7) as all isotropic reconstructions could converge to their highest global iteration (100).

However, it is still unknown how the orthotropic algorithm can be modified to reduce its sensitivity to the initial guess. At this stage, no certain judgment can be made regarding the orthotropic results obtained from the initial guess study presented in this research.

The ambiguities over some controversial results between orthotropic and isotropic tests remain that need more investigations to modify the orthotropic algorithm towards generating favorable images.

Simulations should also be carried out to implement a finite element model using an orthotropic incompressible algorithm for the pineapple gelatin phantom. This simulation study should involve tests on the pineapple gelatin's sample geometry to verify the functionality of the algorithms as well as validating the orthotropic results presented in this thesis.

7.3 Final Words

A meaningful mapping of the orthotropic shear moduli distributions in three directions has demonstrated enough evidence that the orthotropic MRE can be a feasible technique to determine orthotropic elasticity parameters of a biological tissue, noninvasively.

The orthotropic achievements throughout this project can be useful for future clinical cancer diagnostics by augmenting the information obtained from the orthotropic MRE reconstructions between normal tissue and tumors. To reach this aim, full examinations with real tissue are still required.

Although the orthotropic behavior for *in vivo* and *ex vivo* tests remains an unknown challenge for future trials, the MRE orthotropic-based fundamentals offered in this research opened a new horizon in the current medical image modalities, to approximate variations in the shear moduli distribution within an orthotropic media non-invasively, which may be helpful in monitoring the tissue pathology directed in cancerous tumors.

In this thesis, the main effort was to produce a strong foundation for all three orthotropic MRE basics: orthotropic phantom developing, orthotropic MRE dataset developing and validation of the orthotropic incompressible algorithm to generate meaningful orthotropic elastographic results.

This project was successful in developing the pineapple phantom as an orthotropic phantom, and in completing multiple measurements to produce an orthotropic MRE dataset including three different frequencies in three dimensions, with respect to the phantom. The validation of the orthotropic algorithm has demonstrated great potential to differentiate three shear moduli components in 3-D.

Results from the orthotropic elastographic reconstruction using real MRE datasets were promising, and they indicate that the algorithm is capable of detecting regions of stiffness elevation associated with the pineapple inclusion, as well as differentiating three shear muduli components in three orthogonal planes.

However, the orthotropic MRE as a novel technique has been surrounded by so many obstacles and more optimizations should be approached towards obtaining a satisfactory elastography image. This method needs more development of its fundamental bases established throughout this research, to improve its ability to perform as a reliable diagnostic image tool for future clinical MRE breast cancer examinations.

While little comprehensive reference regarding the error range in the MRE is available in literature, a series of different studies was performed to better understand the root cause of artifacts.

Several potential key factors were introduced throughout this thesis. Some of these image artifacts are relevant to the algorithm and can be called internal sources such as the initial guess, zone size etc.

In addition, other external error sources due to experimental works such as phantom fabrication processes, phantom-coil setups, boundary conditions (frequency of the actuation), and MRE data acquisition procedures, should also be considered. Modifying the MRE system in order to remove the source of errors will be another target in the future to improve the accuracy of elastographic results in this advanced medical image modality.

In conclusion, the results obtained from the experiments outlined in the previous chapters have not only illustrated that the main goals involved in this thesis have been achieved, but also the experimental work presented in this thesis provided a basic framework for future research in the orthotropic MRE field.

References

[1] World Health Organization International Agency for Research on Cancer (June 2003). "World Cancer Report" http://www.iarc.fr/en/Publications/PDFs-online/World-Cancer-Report/World-Cancer-Report, Retrieved on 2009-03-26.

[2] http://www.breastcancer.org/pictures/diagnosis/mammogram/mri_2.jsp

[3] World Health Organization, "Global cancer rates could increase by 50% to 15 million by 2020", World Health Organization, United Nations specialized agency for health, 2007

[4] Cancer Statistics Presentation, American Cancer Society, Inc, 2007

[5] Breast Cancer Facts & Figures, American Cancer Society, Inc, 2007-2008

[6] Kesteloot HE, Zhang J, "Differences in breast cancer mortality worldwide: unsolved problems", Eur J Cancer Prev, 15(5):416-23, 2006

[7] Mettlin C, "Global breast cancer mortality statistics", CA Cancer J Clin, 49(3):138-44, 1999

[8] New Zealand Health Information Service, "Cancer: New Registration and Death 1999", New Zealand Ministry of Health, 2002

[9] New Zealand Breast Cancer Foundation, "Facts on Breast Cancer", New Zealand Breast Cancer Foundation, 2006

[10] New Zealand statistics, "Cancer - leading cause of death among females", New Zealand's official statistics agency, Feb 2007

[11] Ashton Peters1, Stefan Wortmann, Rodney Elliott, Mark Staiger, J. Geoffrey Chase, Elijah Van Houten "Digital Image-based Elasto-Tomography: First experiments in surface based mechanical property estimation of gelatin phantoms", Japanese Society of Mechanical Engineers (JSME) International Journal Series C, 48(4), pp. 562-569, 2005

[12] Giordano SH, Hortobagyi GN "Inflammatory breast cancer: clinical progress and the main problems that must be addressed", Breast Cancer Res. **5** (6): 284–8, 2003

[13]Radiological Society of North America, Inc. (RSNA) http://www.radiologyinfo.org/en/info.cfmpg=mammo

[14] Craig A. Beam, Peter M. Lade, and Daniel C. Sullivan, "Variability in the interpretation of screening mammograms by us radiologists: Findings from a national sample", Archives of Internal Medicine, 156:209-213, 1996

[15] R. Sapir, M. Patlas, S. D. Strano, I. Hadas-Halpern, and N. I. Cherny, "Does mammography hurt?", Journal of Pain and Symptom Management, 25(1):53-63, 2003

[16] L. Tabar, M. F. Yen, Vitak B., H.H. Chen, R.A. Smith, and S.W. Dufy, "Mammography service screening and mortality in breast cancer patients: 20-year follow-up before and after introduction of screening", Lancet, 361(9367):1405-1410, 2003

[17] V. J. Robertson, K. G. Baker, "A Review of Therapeutic Ultrasound: Effectiveness Studies, Physical Therapy, Volume 81, Number 7, July 2001

[18] L. Bricker, J. Garcia, J. Henderson, et al, "Ultrasound screening in pregnancy: a systematic review of the clinical effectiveness, cost-effectiveness and women's views". Health technology assessment (Winchester, England) **4** (16): i-vi, 1–193, PMID 11070816, 2000

[19] DF Scollan, A. Alexander Holmes, Jianyang Zhang, Raimond L.Winslow, "Reconstruction of Myocardial Architecture at high Resolution using Diffusion Tensor MRI", Proceedings of The first Joint BMES/EMBS Conference Serving Humanity, Advancing Technology, USA, 13-19, 1999

[20] J. T. Bushberg, Seibert, J.A., Leidholdt, Jr., Edwin M., Boone, John M., "The Essential Physics of Medical Imaging", Second ed. New York: Lippincott Williams and Wilkins, 2002.

[21] L. Landini, V. Positano, and M. F. Santarelli, "Advanced Image Processing In Magnetic Resonance Imaging", CRC Press, 2005.

[22] E.M. Haacke, RW Brown, MR Thompson, and R. Venkatesan, Magnetic Resonance Imaging: Physical Principles and Sequence Design. 1999. New York: John Wiley & Sons, Inc.

[23] T. A. Krouskop, T. M. Wheeler, F. Kallet, B. S. Garra, and T. Hall, "Elastic moduli of breast and prostate tissue under compression", Ultrasonic Imaging, 20:260-274, 1998

[24] A. Samani, J. Bishop, C. Lunginbuhl, and D. B. Plewes, "Measuring the elastic modulus of ex vivo small tissue samples. Phys. Med. Biol., 48:2183-2198, 2003

[25] J. Ophir, I.Cespedes, H. Ponnekanti, Y. Yazdi, and X. Li, "Elastography: A quantitative method for imaging the elasticity of biological tissues", Ultrasonic Imaging, 13:111- 134, 1991

[26] M. M. Doyley, P. M. Meaney, and J. C. Bamber, "Evaluation of an iterative reconstruction method for quantitative elastography", Physics in Medicine and Biology, 45:1521-1540, 2000

[27] E. E. W. Van Houten, "Mechanical Property Reconstruction from MR Detected Harmonic Displacement Data", PhD thesis, Dartmouth College of Engineering, NH, USA, 2001

[28] E. E. W. Van Houten, M. I. Miga, J. B. Weaver, F. E. Kennedy, and K. D. Paulsen, " Three-dimensional subzone-based reconstruction algorithm for MR elastography", Magnetic in Resonance Medicine, 45(5): 827-837, 2001

[29] E. E. W. Van Houten, K. D. Paulsen, M. M. Doyley, F. E. Kennedy, and J. B. Weaver, "Confidence interval calculation for nonlinear reconstruction of elastic properties", In Proceedings of the 10th Scientific Meeting of the International Society for Magnetic Resonance in Medicine, 2002

[30] E. E. W. Van Houten, J. B. Weaver, M. I. Miga, F. E. Kennedy and K. D. Paulsen, "Elasticity reconstruction from experimental MR displacement data: Initial experience with an overlapping sub zone finite element inversion process. Medical Physics, 27(1): 101-107, 2000

[31] A. Peters, A. Milsant, J. Rouze, L. Ray, J. G. Chase, and E. E. W. Van Houten, "Digital-image based elasto-tomography: Proof of concept studies for surface based mechanical property reconstruction" , JSME International Journal, 47(4):1117-1123, 2004

[32] J. G. Chase, E. E. W. Van Houten, L. Ray, D. Bates, J. P. Henderson, C. Ewing, and C. Berg, "Digital image-based elasto-tomography for soft tissue imaging", In Proceedings of the first Asian Pacific Conference on Biomechanics, 2004

[33] R. Muthpillai, P. J. Rossman, D. J. Lomas, J. F. Greenleaf, S. J. Riederer, and R. L. Ehman, "Magnetic resonance elastography by direct visualization of propagating acoustic strain waves", Science, 269: 1854-1857, 1995

[34] T. Rago, F. Santini, M. Scutari, A. Pinchera and P. Vitti, "Elastography: New Developments in Ultrasound for Predicting Malignancy in Thyroid Nodules", Journal of Clinical Endocrinology & Metabolism Vol. 92, No. 8 2917-2922, 2007

[35] http://www.diagnosticimaging.com/ultrasound/content/article/113619/1191987?verify=0
[36] N. H. Gokhale, "A Fast Iterative Method for For Elastic Modulus Imaging", PhD thesis, Boston University, Boston, USA, 2003

[37] C. L. de Korte , A. F. W. Van der Steen, E. I. Céspedes, G. Pasterkamp, S. G Carlier , F. Mastik, A. H Schoneveld, P. W Serruys, N. Bom, "Characterization of plaque components and ulnerability with intravascular ultrasound elastography, J Phys. Med. Biol. Vol. 45, No 6, 1465, 2000

[38] E. E. W. Van Houten, M. M. Doyley, F. E. Kennedy, J. B. Weaver and K. D. Paulsen, "Initial in vivo experience with steady – state subzone – based MR elastography of the human breast", Journal of Magnetic Resonance Imaging, 17:72-85, 2003

[39] R. Sinkus and P. Bornet, "Real-time reduction of motion artefacts using k-space weighting in magnetic resonance imaging", Philips Journal of Research, 51:339-352, 1998

[40] R. Sinkus, J. Lorenzen, D. Schrader, M. Lorenzen, M. Dargatz, and D. Holz, "High-resolution tensor MR elastography for breast tumour detection", Phys. Med. Biol., 45:1649-1664, 2000

[41] Alexia L. McKnight, Jennifer L. Kugel, Phillip J. Rossman, Armando Manduca, Lynn C. Hartmann and Richard L. Ehman, "MR Elastography of Breast Cancer: Preliminary Results", American Journal of Roentgenology, 178:1411-1417, 2002

[42] Marvin M. Doyley, Seshadri Srinivasan, Sarah A. Pendergrass, Ziji Wu, and Jonathan Ophir, " Comparative evaluation of strain based and model based modulus elastography", Ultrasound in Med. and Biol., 31(6):787 -802, 2005.

[43] M. M. Doyley, J. B. Weaver, E. E. W. Van Houten, F. E. Kennedy, and K. D. Paulsen, "Thresholds for detecting and characterizing focal lesions using steady-state mr elastography", Medical Physics, 30(4):195-504, 2003.

[44] E. E. W. Van Houten, M. M. Doyley, F. E. Kennedy, K. D. Paulsen, and J. B. Weaver, "A three-parameter mechanical property reconstruction & algorithm for MR based elastic property imaging", IEEE Transactions on Medical Imaging, 2003

[45] E. E. W. Van Houten, M. M. Doyley, F. E. Kennedy, J. B. Weaver, and K. D. Paulsen, "Initial in vivo experience with steady-state subzone-based MR elastography of the human breast", Journal of Magnetic Resonance Imaging, 17(1):72-85, 2003

[46] J. B. Weaver, E. E. W. Van Houten, Michael L. Miga, Francis E. Kennedy and Keith D. Paulsen, "Magnetic resonance elastography using 3D gradient echo measurements of steady-state motion", Medical Physics, Volume 28, Issue 8, pp. 1620-1628, 2001

[47] Abbas Samani, Donald Plewes, "A method to measure the hyperelastic parameters of ex vivo breast tissue samples", Phys. Med. Biol, 49 4395-4405, 2004

[48] P. R. Perrinez "Determining the feasibility of reconstructing mechanical properties of living brain tissue using magnetic resonance elastography", Master of Science Thesis, Thayer School of Engineering, Dartmouth College, Hanover, NH, USA, March 2005

[49] Joseph P. Hornak, "The Basics of MRI", Department of Chemistry, Rochester Institute of Technology, Rochester, NY 14623-5603, 1996

[50] G. Morrow, "Progress In MRI Magnets", Inter-magnetic General Corporation, Latham, New York, USA

[51] S.R. Thomas, L.J. Busse, J.F. Schenck, "Gradient Coil Technology in Magnetic Resonance Imaging", Saunders, Philadelphia, USA, 1988

[52] S. A. Kruse et al, "characterization using magnetic resonance elastography: preliminary results", Phys. Med. Biol. 45 1579-1590, 2000

[53] R. Muthupillai, D. J. Lomas, P. J. Rossman, J. F. Greenleaf, A. Manduca, and R. L. Ehman, "Magnetic resonance elastography by direct visualization of propagating acoustic strain waves," Science, vol. 269, pp. 1854-7, 1995

[54] H.E. Engan, B.Y. Kim, J.N. Blake, H.J. Shaw, "Propagation and optical interaction of guided acoustic waves in two-mode optical fibers", Journal of Light wave Technology, 1988

[55] C. A. Eringen, E. S. Suhubi, "Elastodynamics", Academic Press, N.Y, USA, Vol 1& 2, 1974

[56] Zeynep Akalin, "Magnetic Resonance Elastography and Inverse problem solution in Elasticity", Proceeding of the first joint BMES/EMBS serving Humanity, Advancing technology, USA, 13-16, 1999

[57] J.C. Mosher, R.M. Leahy, P.S. Lewis, "EEG and MEG: Forward solutions for inverse methods", IEEE Transactions on Biomedical Engineering, Vol. 46, No 3, 1999

[58] M. D. J. McGarry, "Rayleigh Damped Magnetic Resonance Elastography", Master of Engineering Thesis, Mechanical Engineering dept, University of Canterbury, Christchurch, New Zealand., June 2008

[59] T. E. Oliphant, A. Manduca, R. L. Ehman, and J. F. Greenleaf, "Complex-valued stiffness reconstruction for magnetic resonance elastography by algebraic inversion of the differential equation", Magnetic Resonance in Medicine, 45:299–310, 2001.

[60] J. B. Weaver, E. E. Van Houten, M. I. Miga, F. E. Kennedy, and K. D. Paulsen, "Magnetic resonance elastography using 3D gradient echo measurements of steady-state motion," Medical Physics, vol. 28, pp. 1620-8, 2001

[61] K. J. Glaser, J. P. Felmlee, A. Manduca, and R. L. Ehman, "Shear stiffness estimation using intra voxel phase dispersion in magnetic resonance elastography," Magnetic Resonance in Medicine, vol. 50, pp. 1256-65, 2003

[62] D.J.N Wall, P. Olssen, and E.E.W Van Houten, "Some Results on the Conditioning of the Inverse Problem of Imaging in Magnetic Resonance Elastography" Snowbird, UT, USA: 5th International Conference on the Ultrasonic Measurement of Tissue Elasticity, 2006.

[63] K. D. Paulsen, P. M. Meaney, L. C. Gilman, "Alternative Breast Imaging; Four Model-Based Approaches", Springer Science & Business, Vol. 778, NY, USA, 2005

[64] M. Bertaja, S. Morigi, E. Loli Piccolomini, F. Sgallari, F. Zama, "Regularization of Large Discrete ill posed problems in image processing, Recent trends in Numerical analysis", Advances in the Theory of Computational Mathematics, vol. 3, Nova Science, Books and Journals, 2000

[65] T. Long-ji, "Estimate of the condition number for some discrete ill-posed equation", Journal of Computational Mathematics, Vol. 9, No. 1, 5-8, 1991

[66]A. M. Maniatty, and E. Park "Finite Element Approach to Inverse Problem in Dynamic Elastography", Proceedings of the 5th International Conference on Inverse Problems in Engineering: Theory and Practice, Cambridge, UK, 11-15th, July 2005

[67] Grandin, H., "Fundamentals of the Finite Element Method", Waveland Press, 1991

[68] C. Cuvelier, A. Segal, and A. A. Van Steenhoven, "Finite element methods and Navier-Stokes equation", D. Reidel Publishing Co, TA347.F5C88, chapter 6, 1986

[69] S. S. Rao, "The Finite Element Method in Engineering", Chapter 2, 3 & 12, Butterworth-Heinemann, MA, USA, 1999

[70] J. E. Akin, "Finite Element Analysis with Error Estimators", chapter 3, Elsevir, MA USA, 1988

[71] O.C. Zienkiewicz, R.L. Taylor, The Finite Element Method, vol. 1, 4th ed., McGraw Hill, New York, 1994

[72] E. K.P. Chong, S. H. Żak, "An introduction to optimization", Hoboken, N.J. Wiley-Inter-science, 3rd ed, Chapter 2& 3, 2008

[73] P. A. Absil, R. Mahony, R. Sepulchre, "Optimization algorithms on matrix manifolds", Princeton, N.J. Woodstock : Princeton University Press, 2008

[74] J. Nocedal, S. J. Wright, "Numerical Optimization", Springer-Verlag Inc, New York, 1999

[75] L. Liberti, N. Maculan, "Global optimization : from theory to implementation", New York, NY : Springer, chapter 1& 2, 2006

[76] I. Griva, S. G. Nash, A. Sofer, "Linear and nonlinear optimization", Philadelphia: Society for Industrial and Applied Mathematics, 2nd ed, 2009

[77] A.G. Buckley, J. L. Goffin, "Algorithms for constrained minimization of smooth nonlinear functions", Elsevier Science Pub., 1982

[78] M. C. Bartholomew-Biggs, "Nonlinear optimization with financial applications", Boston: Kluwer, 2005

[79] R. Baldick, "Applied optimization: formulation and algorithms for engineering systems", Cambridge, UK, New York : Cambridge University Press, 2006

[80] J. M. Ortega, W.C. Rheinboldt, "Iterative Solution of Nonlinear Equations in Several Variables", Society for Industrial and Applied Mathematics Philadelphia, PA, USA, 2000

[81] S. J. Norton, "Iterative inverse scattering algorithms: Methods of computing Fr´echet derivatives", The Journal of the Acoustical Society of America, 106:2653, 1999

[82] S. L. S. Jacoby, J. S. Kowalik, J. T. Pizzo, "Iterative methods for nonlinear optimization problems", Englewood Cliffs, N.J. : Prentice-Hall, 1972

[83] C.T. Kelley, "Iterative methods for optimization", Philadelphia: SIAM, 1999

[84] I. C.F. Ipsen, "Numerical matrix analysis: linear systems and least squares", Philadelphia: Society for Industrial and Applied Mathematics, 2009

[85] J. F. Epperson, "An introduction to numerical methods and analysis", New York: J. Wiley, 2002

[86] P. Whittle, "Prediction and regulation by linear least-square methods", Oxford: Blackwell, 2nd ed, 1983

[87] J. I. Trombka, R. L. Schmadebeck, "A numerical least-square method for resolving complex pulse height spectra", Washington: National Aeronautics and Space Administration, Scientific and Technical Information Division, 1968

[88] J. F. Epperson, "An introduction to numerical methods and analysis", New York: J. Wiley, 2002

[89] D. W. Marquadt, "An algorithm for least-squares estimation of non-linear parameters", J. Soc. Indust. Appl. Math., 11:431–441, 1953.

[90] A. R. Conn, Gould, I. M. Nicholas, Ph. L Toint, "Trust-region methods", Philadelphia, PA : Society for Industrial and Applied Mathematics, 2000

[91] B. Bartholomew, C. Michael, "Nonlinear optimization with engineering applications", New York : Springer, 2008

[92] J. M. Ortega, W. C. Rheinboldt, "Iterative Solution of Nonlinear Equations in Several Variables", Classics in Applied Mathematics, No 30, 2000

[93] J. A. Snyman, "Practical mathematical optimization: an introduction to basic optimization theory and classical and new gradient-based algorithms", Springer, 2005

[94] J.M. Lewis, S. Lakshmivarahan, S. Dhall, "Dynamic data assimilation: a least squares approach", Cambridge: Cambridge University Press, 2006

[95] J.C. Gilbert and J. Nocedal, "Global convergence properties of conjugate gradient methods for optimization", Journal on Optimization, 2(1):21–42, 1992

[96] P. Wolfe, "Convergence conditions for ascent methods", Review, 11(2):226– 235, 1969

[97] M. Fu, J. Qiang Hu, "Conditional Monte Carlo : gradient estimation and optimization applications", Boston : Kluwer Academic Publishers, 1997

[98] P. E. Gill, W. Murray, "Conjugate-gradient methods for large scale nonlinear optimization", Zillmere, Q. : BUSAR, 1979

[99] Y. Shapira, "Matrix-based multi-grid : theory and applications", N.Y. : Springer Verlag, 2nd ed, 2008

[100] L. Adams, J.L. Nazareth, "Linear and nonlinear conjugate gradient-related methods", Philadelphia: Society for Industrial and Applied Mathematics, Subject: Conjugate gradient methods – Congresses, 1996

[101] J.R. Shewchuk, "An introduction to the conjugate gradient method without the agonizing pain", unpublished paper.

[102] J. F. Epperson, "An introduction to numerical methods and analysis", New York : J. Wiley, 2002

[103] B. Kaltenbacher, A. Neubauer, O. Scherzer, "Iterative regularization methods for nonlinear ill-posed problems", Berlin; New York: Walter de Gruyter, 2008

[104] A. A. Samarskii, P. N. Vabishchevich, "Numerical methods for solving inverse problems of mathematical physics", Berlin, Germany; New York: Walter de Gruyter, 2007

[105] R. C. Aster, B. Borchers, C. H. Thurber, "Parameter estimation and inverse problem", Elsevier Academic Press, Vol. 90, 2005

[106] C.R. Vogel, "Computational Methods for Inverse Problems", Society for Industrial Mathematics, 2002

[107] H. A. Aly, “Image Up-Sampling Using Total-Variation Regularization with a New Observation Model”, IEEE Transactions on Image Processing, Vol., 14, No. 10, 2005

[108] D. Strong, T. Chan, “Edge-preserving and scale-dependent properties of total variation regularization”, J. Inverse Problems, 2003

[109] S. Osher, M. Burger, D. Goldfarb, J. Xu, W. Yin, “An Iterative Regularization Method for Total Variation –Based Image Restoration”, Multi-scale Model Simul, 2005

[110] H. Ling Liew and P.M. Pinsky, “Recovery of shear modulus in elastography using an adjoint method with B-spline representation”, Finite Elements in Analysis & Design, 41(7-8):778–799, 2005.

[111] A. A. Oberai, N. H. Gokhale, M. M. Doley, J. C. Bamber, “Evaluation of the adjoint equation based algorithm for elasticity imaging”, Phys. Med. Biol. 49:2955-2974, 2004

[112] A.A. Oberai, N.H. Gokhale, and G.R. Feij o, “Solution of inverse problems in elasticity imaging using the adjoint method”, Inverse Problems, 19(2):297–313, 2003

[113] EEW Van Houten, KD Paulsen, MI Miga, FE Kennedy, and JB Weaver, “An overlapping subzone technique for MR-based elastic property reconstruction”, Magnetic Resonance in Medicine, 42(4):779–786, 1999.

[114] E. E. W. van Houten, J. B. Weaver, M. I. Miga, F. E. Kennedy, and K. D. Paulsen, “Elasticity reconstruction from experimental MR displacement data: initial experience with an overlapping subzone finite element inversion process”, Medical Physics, 27:101–107, January 2000.

[115] E. E. W. Van Houten, M. I. Miga, J. B. Weaver, F. E. Kennedy, and K. D. Paulsen, “Three-dimensional subzone-based reconstruction algorithm for MR elastography”, Magnetic Resonance in Medicine, 45:827–837, 2001.

[116] Y. N. Zhu, T. J. Hall, and J. F. Jiang, “A finite-element approach for Young’s modulus reconstruction”, IEEE Trans. Med. Imag., vol. 22, no. 7, pp. 890–901, Jul. 2003

[117] H. B. Kang, E. Kim, and J. Y. Lee, “Identification of elastic inclusions and elastic moment tensors by boundary measurements”, Inverse Prob., vol. 19, pp. 703–724, 2003

[118] H. T. Liu, L. Z. Sun, G. Wang, and M. W. Vannier, “Analytic modelling of breast elastography”, Med. Phys., vol. 30, pp. 2340–2349, 2003

[119] S. J. Cox, M. Gockenbach, “Recovering planar Lame moduli from a single-traction experiment”, Math. Mech. Solids, vol. 2, pp. 297–306, 1997

[120] Y. C. Fung, “Biomechanics: Mechanical Properties of Living Tissues”, New York: Springer-Verlag, 1993

[121] R. Sinkus, J. Lorenzen, D. Schrader, M. Lorenzen, M. Dargatz, and D. Holz, “High-resolution tensor MR elastography for breast tumor detection,” Phys. Med. Biol., vol. 45, pp. 1649–1664, 2000

[122] J. Weaver, M. Doyley, E. Van Houten, M. Hood, X. C. Qin, F. Kennedy, S. Poplack, and K. Paulsen, “Evidence of the anisotropic nature of the mechanical properties of breast tissue,” Med. Phys., vol. 29, pp. 1291–1291, 2002

[123] J.R. Barber, “Elasticity”, Dordrecht ; Boston : Kluwer Academic Publishers, 1992

[124] D. François, A. Pineau, A. Zaoui, “Mechanical behaviour of materials”, Dordrecht; Boston: Kluwer Academic Publishers, 1998

[125] T.C.T. Ting, “Anisotropic Elasticity: Theory and Applications”, Oxford University Press; New York, 1996

[126] S.G. Lekhnitskii, “Theory of Elasticity of an Anisotropic Body”, Moscow: MIR, 1981

[127] S.A. Ambartsumyan, I. A. Kunin “Theory of anisotropic plates: strength, stability, and vibrations”, 2nd ed, New York : Hemisphere Pub. Corp, 1991

[128] W. C. Carter, “Models for Anisotropic materials”, MIT, Lecture 7, 2002, pruffle.mit.edu/3.00/Lecture_07_web/node3.html

[129] R. Sinkus, M. Tanter, S. Catheline, J. Lorenzen, C. Kuhl, E. Sondermann, and M. Fink, “Imaging anisotropic and viscous properties of breast tissue by magnetic resonance-elastography,” Magn. Reson. Med., vol. 53, pp. 372–387, 2005

[130] W.M. Lai, D. Runin, E. Krempl, “Introduction to Continuum Mechanics”, Program Press Inc., 660 White Plain Rd, NY 10591-5153, USA

[131] P. Haupt, J. A. Kurth, “Continuum mechanics and theory of materials”, 2nd ed, Berlin: Springer-Verlag, 2002

[132] A. E. Love, “A Treatise on the Theory of Elasticity”, New York: Dover Publications; 1944

[133] E. F. Chen, A. Saleeb, “Constitutive Equations for Engineering Materials”, New York: John Wiley & Sons, Inc; 1982

[134] C.S. Desai, H. J. Siriwardane, “Constitutive Laws for Engineering Materials -with Emphasis on Geologic Materials”, New Jersey: Prentice-Hall; 1984

[135] N. T. Mascia, F. A. R. Lahr, “Remarks on orthotropic elastic models applied to wood”, Mat. Res. vol.9 no.3 São Carlos July/Sept. 2006

[136] J.R. Goodman, J. Bodig, “Orthotropic Elastic Properties of Wood”, Journal of Structural Division, 96(11):2301-19, 1970

[137] D. Noack, V. W. Rooth, “On the Theory of Elasticity of Orthotropic Material", Wood Science and Technology, 10(1):97-110, 1976

[138] S. Valliappan, “Continuum mechanics: fundamentals”, Rotterdam: A. A. Balkema, 1981

[139] R.M. Jones, “Mechanics of Composite Materials”, Hemisphere Publishing Corporation, New York, 1975

[140] J. R. Vinson, R. L. Sierakowski, “The behavior of structures composed of composite materials”, 2nd ed, Dordrecht; Boston : Kluwer Academic Publishers, 2002

[141] L. R. Herrmann, “Elasticity equations for nearly incompressible materials by a variational theorem”, AIAA Journal, 3, 1896–1900, 1965

[142] S. W. Key, “A variational principle for incompressible and nearly-incompressible anisotropic elasticity, International Journal of Solids and Structures”, Vol. 5, PP.951-964, 1969

[143] L. M. Coley, A.T. Dolovich, “Finite Element Calculations for Perfectly Incompressible Materials and Displacements Prescribed on the Entire Boundary”, Submitted to CSME Transactions, February 2006

[144] M. F. Beatty, “Topics in finite elasticity: hyperelasticity of rubber, elastomers and biological tissues with examples”, Applied Mechanics Review Vol. 40, PP. 1699– 1734, 1987

[145] M. Mooney, “A Theory of Large Elastic Deformation”, Journal of Applied Physics, Vol.11, 582—592, 1940

[146] R. S. Rivlin, “Large elastic deformation of isotropic materials”, Philosophical Transactions of the Royal Society of London, Vol. A 195, PP 463-473, 1949

[147] R. W. Ogden, , Y.B. Fu, “Nonlinear elasticity: theory and applications”, Cambridge University Press, 2001

[148] R. L. Taylor, K. S. Pister, “On a variational theorem for incompressible and nearly-incompressible orthotropic elasticity”, Int. J. Solid Structure, Vol. 4, pp 875-8833, 1968

[149] About.com Filed In, “Incompressible Orthotropic Materials”, Composites / Plastics, 1999 http://composite.about.com/library/weekly/aa990916.htm

[150] M. Destrade, “Surface waves in orthotropic incompressible materials,” J. Acoust. Soc. Am. 110, 2001

[151] Y. Liu, L. Z. Sun and Ge Wang, “Tomography-Based 3-D Anisotropic Elastography Using Boundary Measurements”, IEEE Tranactions on Medical Imaging, Vol. 24, NO. 10, 2005

[152] G. Nakamura, G. Uhlmann, “Inverse problems at the boundary for an elastic medium”, SIAM J. Appl. Math., Vol. 26, pp. 263-279, 1995

[153] G. Nakamura, G. Uhlmann, “Layer stripping for transversely isotropic elastic medium”, SIAM J. Appl. Math., Vol. 59, pp. 1879-1891, 1999

[154] P. E. Barbone, J. C. Bamber, “Quantitative elasticity imaging: What can and cannot be inferred from strain images”, Phys. Med. Biol., Vol. 47, pp. 2147-2164, 2002

[155] A. L. Mazzucato, L. V. Rachele, “Partial uniqueness and obstruction to uniqueness in inverse problems for anisotropic elastic media”, Mathematical Science Research Institute (MSRI), 2003

[156] P. E. Barbone, N. H. Gokhale, “Elastic modulus imaging: on the uniqueness and non-uniqueness of the elastography inverse problem in two dimensions”, Inverse Prob., Vol. 20, pp. 283-296, 2004

[157] V. Kochervinskii, "Piezoelectricity in crystallizing ferroelectric polymers", Crystallography Reports, 48 (4): 649–675, 2003

[158] P. R. Perrinez “Determining the feasibility of reconstructing mechanical properties of living brain tissue using magnetic resonance Elastography”, MSc Thesis, Thayer School of Engineering, Dartmouth College, Hanover, NH, USA, March 2005

[159] James L. Flewellen, “Development of Clinically-Viable Applications of MR Elastography”, MSc thesis in Physics, University of Canterbury, Christchurch, New Zealand, May 2008

[160] Z. Barani Lonbani, M. Haghpanahi, H. Saeedi, “Computational models for diabetic insoles: An FEM approach”, MSc Thesis (in Persian), Islamic Azad University (Tehran Science and Research Branch), Tehran, Iran, 2000

[161] N. Hanafi, “Saline, silicone gel and alternative breast implants”, Guidance for industry and FDA staff, FDA, 5630 Fisher Lane, Rockville, USA, 2006

[162] E. L. Madesen, G. R. Frank, T. A. Krouskop, T. Varghese, F. Kallel, J. Ophir, “Tissue –mimicking oil-in-gelatine dispersions for use in heterogenous elastography phantoms”, Ultrasonic Imaging 25, 17-38, 2003

[163] Kevin J. Parker, Lawrence S. Taylor, and Sheryl Gracewski, "A unified view of imaging the elastic properties of tissue", School of Engineering and Applied Sciences, University of Rochester, P.O. Box 270126, Rochester, New York 14627-0127, 2005

[164] P. J. Chen. "Selected Topics in Wave Propagation", Noordhoff International Publishing, Leyden, 1976

[165] K. F. Graff, "Wave Motion in Elastic Solids", Ohio State University Press, Belfast, 1975

[166] I. G. Main, "Vibrations and Waves in Physics", Cambridge University Press, Cambridge, first edition, 1978

[167] H. J. Pain, "The Physics of Vibrations and Waves", John Wiley & Sons, Chichester, sixth edition, Ch. 9, 2005

[168] E.A. Brujan, T. Ikedaand, Y. Matsumoto, "On the pressure of cavitations bubbles", Elsevier Inc, doi:10.1016/j.expthermflusci, 2008.01.006, 2008

[169] C.-J.er Huang , H. H. Chang, "Wave-Induced Response in a Rigid Porous Bed", Proceedings of the Ninth (1999) International Offshore and Polar Engineering Conference, Brest, France, 1999

[170] S. S. Blemker, P. M. Pinsky, S. L. Delp, "A 3D model of muscle reveals the cause of nonuniform strains in the biceps brachii", J. Biomechanics, Vol.38, 657-665, 2005

[171] J. L. Flewellen, "Magnetic resonance elastography for breast cancer detection", 480 research report, Department of Physics and Astronomy, University of Canterbury, 2006.

[172] http://www.yourdictionary.com/laser

[173] American Heritage® Dictionary, http://education.yahoo.com/reference/dictionary/entry/laser

[174] Reference.com, "laser", http://dictionary.reference.com/browse/laser., Retrieved on 2008-05-15.

[175] G. R. Gordon , "The LASER, Light Amplification by Stimulated Emission of Radiation", in Franken, P.A. and Sands, R.H. (Eds.). The Ann Arbor Conference on Optical Pumping, the University of Michigan,. pp. 128, OCLC 02460155, 1959

[176] Donald Beaty et al, "Standard Handbook for Electrical Engineers 11th Ed.", McGraw Hill, 1978

[177] R. M. Black, "The History of Electric Wires and Cables", Peter Perigrinus, London 1983

[178] http://en.wikipedia.org/wiki/Direct_current

[179] B. L. Hainer, R. B. Usatine, "Electrosurgery for the Skin", Journal of the American Academy of Family Physicians, 66(7):1259-66, 2002

[180] B. L. Hainer, "Fundamentals of electrosurgery", Journal of the American Board of Family Practice, 4(6):419-26, 1991

[181] R.S. Boughton, S.K. Spencer, "Electrosurgical fundamentals", J. Am. Acad. Dermatology, 16(4):862-7, 1987

[182] M. J. Oringer, "Fundamentals of electrosurgery", J. Oral. Surg. Anesth. Hosp. Dent. Serv, 18:39-49, 1960

[183] Megadyne, The Electrosurgical Authority, TM, "Principles of electrosurgery", http://www.megadyne.com/pdf/Electrosurgery1.pdf

[184] A. Ryter, "Contribution of new cryomethods to a better knowledge of bacterial anatomy", Ann. Inst. Pasteur Microbiol. 139 (1): 33–44, 1988

[185] C. L. Friedrich, D. Moyles, T. J. Beveridge, R. E. W. Hancock, "Antibacterial Action of Structurally Diverse Cationic Peptides on Gram-Positive Bacteria", Antiomicrobial Agents and Chemotherapy, 44 (8): 2086–2092, 2000

[186] A. Lozano, B. Yip, R. K. Hanson "Acetone: a tracer for concentration measurements in gaseous flows by planar laser-induced fluorescence". Exp. Fluids, 13: 369–376, 1992

[187] S. S. Likhodii, I. Serbanescu, M. A. Cortez, P. Murphy, O.C. Snead, W. M. Burnham, "Anticonvulsant properties of acetone, a brain ketone elevated by the ketogenic diet". Ann. Neurol., 54 (2): 219–226, 2003

[188] T. Kaku , J. K. Ekem , C. Lindayen, D. J. Bailey , A. W. Van Nostrand , E. Farber , “Comparison of formalin- and acetone-fixation for immunohistochemical detection of carcinoembryonic antigen (CEA) and keratin”, Am. J. Clin. Pathol., 80(6):806-15, 1983

[189] P. Prento, H. Lyon, “Commercial formalin substitutes for histolopathology Biotech Histochem”, 72:273-282, 1997

[190] M. Werner, A. Chott, A. Fabiano, H. Battifora, “Effect of formalin tissue fixation and processing on immunohistochemistry” Am. J. Surg. Pathol., 24:1016-1019, 2000

[191] W. Salmhofer, E. Rieger, P. Soyer, J. Smolle, H. Kerl, “Influence of skin tension and formalin fixation on sonographic measurement of tumor thickness”, J. Am. Acad. Dermatol., 34:34-39, 1996

[192] R. Quester, R. Schroder, “The shrinkage of the human brain stem during formalin fixation and embedding in paraffin”, J. Neurosci. Methods, 75:81-89, 1997

[193] H. Chen, J. De Baerdemaeker, “Finite-element-based modal analysis of fruit firmness”, Transactions of the ASAE, 36(6): 1827-1833, 1993

[194] T. Srinag, V. B. K. Murthy, J. S. Kumar Suresh, “ Micromichanical analysis of hybrid discontinuous Fiber Reinforced Composite for Longitudinal Loading”, International Journal of Applied Engineering Research, Volume : 3, Issue : 7, 2008

[195] R.M. Christensen, “Mechanics of Composite Materials”, Wiley Interscience, N.Y., 1979

[196] Z. Hashin, C.T. Herakovich, “Mechanics of Composite Materials-Recent Advances”, Pergamon Press, N.Y., 1983

[197] S.W. Tsai, H.T. Hahn, “Introduction to Composite Materials”, Technomic Publ. Co., Inc., Lancaster, 1980

[198] J.M. Whitney, “Structural Analysis of Laminated Composites”, Technomic Publ. Co., Inc., Lancaster, 1987

[199] J.R. Vinson, R.L. Sierakowski, “The Behavior of Structures Composed of Composite Materials”, Kluwar Academic Publ., MA, 1985

[200] M. T. Hagan and M. Menhaj, “Training multilayer networks with the Marquardt algorithm,” IEEE Transactions on Neural Networks, vol. 5, no. 6, 1994, pp. 989-993

[201] P. E. Gill, W. Murray, “Quasi-Newton Methods for Unconstrained Optimization”, Journal of Applied Mathematics, 9(1):91-108, 1972

[202] P. T. Boggs, J. W. Tolle, and P. Wang, “On the Local Convergence of Quasi-Newton Methods for Constrained Optimization”, SIAM J. Control Optim. Volume 20, Issue 2, pp. 161-171, 1982

[203] D. C. Liu· J. Nocedal· “On the limited memory BFGS method for large scale optimization”, J Mathematical Programming, Springer Berlin, Heidelberg, Volume 45, Numbers 1-3, 1989

[204] T. E. Oliphant, A. Manduca, R. L. Ehman, and J. F. Greenleaf. Complex valued stiffness reconstruction for magnetic resonance elastography by algebraic inversion of the differential equation. Magnetic Resonance in Medicine, 45:299–310, 2001.

[205] R. Sinkus, M. Tanter, T. Xydeas, S. Catheline, J. Bercoff, and M. Fink. Viscoelastic shear properties of in vivo breast lesions measured by mr elastography. Magnetic Resonance Imaging, 23:159–165, 2005

[206] D. R. Bland. The Theory of Linear Viscoelasticity. Pergamon Press, Oxford, 1960

[207] W. Flugge. Viscoelasticity. Springer, Berlin, 1975 (second revised edition)

[208] http://www.usm.edu/mrsec/facilities/thermo.htm#dynamic

[209] http://www.imaios.com/en/e-Courses/e-MRI/Image-quality-and-artifacts/aliasing

[210] http://bme.yonsei.ac.kr/~biomecha/jinho/MRIArtifacts.htm

[211] Prof. David Wall, Mathematics and Statistics Dept, University of Canterbury, Christchurch, NZ

[212] G. P. Galdi, "An introduction to the mathematical theory of the Navier-Stokes equations" Springer-Verlag, NY, USA, 1994

[213] E. E. W. Van Houten, Mechanical Eng. Dept, University of Canterbury, Christchurch, NZ

Appendix A

The Equations of Linear Elasticity

Summary of Equations

Strain-displacement relations:

$$\varepsilon_{ij} = \frac{1}{2}(u_{i,j} + u_{j,i})$$

Constitutive Equations:

$$\sigma_{ij} = C_{ijkl} u_{k,l}$$

where
$$C_{ijkl} = \lambda \delta_{ij} \delta_{kl} + \mu(\delta_{ik} \delta_{jl} + \delta_{il} \delta_{jk})$$

Equilibrium equations/equation of motions when the body forces are ignored:

$$\sigma_{ij,i} = \rho \frac{\partial^2 u_i}{\partial t^2}$$

or symbolically

$$\nabla \cdot \sigma_{ij} = \rho \frac{\partial^2 u_i}{\partial t^2}$$

while

$$\sigma_{ij,i} = \lambda \delta_{ij} u_{k,ki} + \mu(u_{i,ji} + u_{j,ii}) + \lambda_{,i} \delta_{ij} u_{k,k} + \mu_{,i}(u_{i,j} + u_{j,i})$$

$$= \lambda u_{k,kj} + \mu(u_{i,ji} + u_{j,ii}) + \lambda_{,i} u_{k,k} + \mu_{,i}(u_{i,j} + u_{j,i})$$

Or in vector notation

$$\nabla \cdot \sigma_{ij} = (\lambda + \mu)\nabla(\nabla \cdot u) + \mu \nabla^2 u + \nabla \lambda (\nabla \cdot u) + \nabla \mu \cdot \nabla u + \nabla u \cdot \nabla \mu$$

Navier Equations:

Solve the equilibrium equations for the displacement gives:

$$(\lambda + \mu)\nabla(\nabla \cdot u) + \mu\nabla^2 u + \nabla\lambda(\nabla \cdot u) + \nabla\mu \cdot \nabla u + \nabla u \cdot \nabla\mu = \rho \frac{\partial^2 u}{\partial t^2}$$

[211, 212]

Appendix B

Caculating one of the orthotropic Poisson's ratios:

Recall (3.39) and rearrange that as:

$$\frac{1}{E_1} = \frac{\upsilon_{21}}{E_2} + \frac{\upsilon_{31}}{E_3} \tag{B.1}$$

Recall (3.34) and rewritten as: $\upsilon_{21} = 1 - \upsilon_{23}$ and then replacing it in the (B.1) gives:

$$\frac{1}{E_1} = \frac{(1-\upsilon_{23})}{E_2} + \frac{\upsilon_{31}}{E_3} \tag{B.2}$$

Recall (3.25) and rewriting as $\upsilon_{23} = \frac{E_2}{E_3} \cdot \upsilon_{32}$ and then replacing in the (B.2) yields:

$$\frac{1}{E_1} = \frac{1}{E_2}\left(1 - \upsilon_{32}\frac{E_2}{E_3}\right) + \frac{\upsilon_{31}}{E_3} \tag{B.3}$$

This leads to:

$$\frac{1}{E_1} = \frac{1}{E_2} - \frac{\upsilon_{32}}{E_3} + \frac{\upsilon_{31}}{E_3} \tag{B.4}$$

This gives:

$$\upsilon_{31} - \upsilon_{32} = \frac{E_3}{E_1} - \frac{E_3}{E_2} \tag{B.5}$$

By replacing υ_{32} with $1-\upsilon_{31}$, the equation (B.5) can be simplified as:

$$2\upsilon_{31} = \frac{E_3}{E_1} - \frac{E_3}{E_2} + 1 \tag{B.6}$$

This ultimately yields as:

$$\upsilon_{31} = \frac{E_3}{2}\left[\frac{1}{E_1} - \frac{1}{E_2} + 1\right] \tag{B.7}$$

This has been mentioned in (3.44). Other Poisson's ratio coefficients can be found with the same manner [213].